

Local structural effects in fiber-reinforced polymer web-core sandwich structures

THÈSE N° 7932 (2017)

PRÉSENTÉE LE 22 SEPTEMBRE 2017

À LA FACULTÉ DE L'ENVIRONNEMENT NATUREL, ARCHITECTURAL ET CONSTRUIT

LABORATOIRE DE CONSTRUCTION EN COMPOSITES

PROGRAMME DOCTORAL EN GÉNIE CIVIL ET ENVIRONNEMENT

ÉCOLE POLYTECHNIQUE FÉDÉRALE DE LAUSANNE

POUR L'OBTENTION DU GRADE DE DOCTEUR ÈS SCIENCES

PAR

Sonia YANES ARMAS

acceptée sur proposition du jury:

Prof. K. Beyer, présidente du jury

Prof. T. Keller, Dr J. de Castro San Roman, directeurs de thèse

Dr C. Paulotto, rapporteur

Dr W. Sebastian, rapporteur

Prof. E. Brühwiler, rapporteur



ÉCOLE POLYTECHNIQUE
FÉDÉRALE DE LAUSANNE

Suisse
2017

Para Davinia

Preface

Fiber-reinforced polymer web-core sandwiches are two-dimensional lightweight load-bearing structures composed of exterior face sheets and a complex core, the latter consisting of webs in different configurations and the resulting cell structure may be filled with foam. In bridge construction, such sandwich structures can offer durable and economic solutions. Prefabrication can minimize traffic interruptions and – in the case of the replacement of heavy concrete decks – their load-bearing capacity can be increased or existing bridges widened without overloading the substructure. In building construction, the potential integration of structural, building physics and architectural functions into large-scale and lightweight sandwich structures may lead to sustainable high-quality solutions and architecturally attractive freeform shapes.

The design of such sandwich structures is in most cases governed by the serviceability limit state, i.e. the structural stiffness, although there are cases where design is governed by the ultimate limit state. The quantification of the load-bearing capacity in the latter case is not that simple however, since the failure modes are driven by local effects, which are not yet fully understood. The aim of this research project was thus to extend the knowledge about such local structural effects in fiber-reinforced polymer web-core sandwich structures in order to promote the application of this promising technology.

Lausanne, July 2017

Prof. Dr. Thomas Keller
EPFL-CCLab

Acknowledgments

This doctoral thesis represents the conclusion of a four-and-a-half-year journey during which I was fortunate to receive the support, encouragement and goodwill of many people. To all of them, I would like to address my deep appreciation.

First and foremost, I would like to express all my gratitude to my supervisors, Prof. Thomas Keller and Dr. Julia de Castro. I owe much to their support and will always be obliged to them. Thank you Prof. Keller for the trust you placed in me from the very beginning and throughout all this time. I am grateful for your ever-valuable guidance, openness and undeniable dedication, and for the opportunity you gave me to participate in several other projects that have broadened my experience. Thank you also Dr. Julia de Castro for your continuous advice and confidence in my work, your sincere friendship and your tirelessly comforting attitude.

I wish to express my appreciation to my thesis defense jury for the time they devoted to examining my thesis and their feedback: Prof. Eugen Brühwiler (MCS-EPFL), Dr. Carlo Paulotto (Acciona, Spain), Dr. Wendel Sebastian (University of Bristol, UK) and Prof. Katrin Beyer (president of the jury, EESD-EPFL). I cherish fond memories of the times we met during my doctoral studies and I was honored by your participation in my thesis defense.

A large part of the work presented here was conducted and enjoyed in EPFL's Structural Engineering Laboratory and would not have been possible without the solid support and patience of the technicians. In particular, I would like to acknowledge Sylvain Demierre, for your contagious optimism, Patrice Gallay, for the custom fixtures you fabricated, and Gilles Guignet, for your assistance in all software-related matters.

Performing this research at the Composite Construction Laboratory (CCLab) enabled me to meet and share enriching time with numerous people from whose experience I have doubtlessly learned personally, professionally... and gastronomically. I wish to thank all "CCLabians" for this. Thank you to my longest-standing officemate Wei, for our early and quiet talks; Haifeng, Myrsini, Kyriaki, Maria (my fellows from the 2012–2017 PhD generation), Vahid and

Aida, for the moments we shared along our sometimes parallel, other times convergent paths; and Carlos, for the many smiles you elicited. Many thanks also to Margaret Howett for the thorough correction of the English text of my thesis.

Thanks also to all the people who have contributed to make life at EPFL and in Lausanne more pleasant, in one way or another. Special thanks to my French tandem Sarah for her friendship, which provided a good balance with academic life. A big thanks also to my friends Rocío and M^a José, whose support I always felt despite the distance.

I would probably have not started the PhD without the encouragement of Dr. David Sanz and Dr. José Luis Fernández Cabo (†). I would like to thank them for introducing me to research, and also my colleagues in IETcc-CSIC (Spain), where I got started.

Mi más profundo agradecimiento a mi familia, que me enseñó el valor del esfuerzo y me ha apoyado cualesquiera que fueran las circunstancias. Muchas gracias por su respaldo y amor incondicionales.

Lausanne, July 2017

Sonia Yanes Armas

Abstract

Glass fiber-reinforced polymer (GFRP) pultruded decks and sandwich panels currently represent two of the most extensive applications of FRP materials for load-bearing structural components in the bridge and building domains. Based on the state of the art, the global structural behavior of both systems has been fairly well investigated. Nonetheless, local effects governing in most cases the global behavior have been barely addressed. Selected local structural effects relevant to the global structural performance of pultruded GFRP bridge decks and GFRP-foam web-core sandwich structures are therefore investigated in this research.

The effect of the core geometry of pultruded GFRP decks on the system's behavior in its transverse-to-pultrusion direction was experimentally investigated. The experimental work conducted on two deck designs with trapezoidal- and triangular-cell cross sections showed that the transverse structural performance depends on the cell geometry. Furthermore, the systems' transverse bending and in-plane shear stiffness were evaluated and the results indicated that a triangular core causes a more pronounced bi-directional behavior of the deck when it is subjected to concentrated loads.

The local behavior of the web-flange junctions (WFJs) of the pultruded deck with trapezoidal cells was experimentally investigated regarding energy dissipation capacity and recovery subsequent to unloading. The experimental responses reported for two junction types with similar geometry and fiber architecture but different initial imperfections demonstrated that dissimilar imperfections could significantly affect WFJ behavior and change it from brittle to ductile. The time-dependent recovery and energy dissipation mechanisms of the WFJs exhibiting a ductile response were evaluated; the viscoelastic effects were found to be small in both cases. The rotational behavior of all WFJ types present in the trapezoidal-core deck was characterized. An experimental procedure based on three-point bending and cantilever experiments conducted on the web elements was developed and used for this purpose. The rotational stiffness, strength and failure modes of

the WFJs differed depending on the web type, location of the WFJ within the deck profile, existing initial imperfections and direction of the applied bending moment. Numerical simulations of the full-scale deck were performed to demonstrate the validity of the experimental moment-rotation ($M-\phi$) relationships and simplified $M-\phi$ curves provided.

The effects of creep on the load-bearing behavior of GFRP-foam web-core sandwich structures were investigated. A study of the creep behavior of polyurethane (PUR) foams was conducted and showed that in order to assess the long-term structural performance of the sandwich system, the foam anisotropy, density and loading type should be considered. The creep behavior of web-core sandwich panels, and specifically the structural aspects affected by the web-core interaction, were analyzed using the GFRP-PUR sandwich roof of the Novartis Campus Main Gate Building as case study and currently available design guidelines. The resulting sandwich designs depended on the applied design recommendations. Finally, provisions for the cross-sectional design of the hybrid web-core were proposed.

Keywords

Glass fiber-reinforced polymer, pultruded bridge deck, sandwich structure, local effect, transverse behavior, web-flange junction, rotational stiffness, creep behavior, polyurethane foam

Résumé

Les tabliers de ponts composés de profilés pultrudés et les panneaux sandwich en GFRP (polymères renforcés par des fibres de verre) représentent de nos jours deux des applications les plus étendues des matériaux composites renforcés par des fibres (FRP) en tant qu'éléments porteurs dans le domaine de la construction de ponts et de bâtiments. Selon l'état des connaissances actuel, le comportement structurel global de ces deux systèmes a été largement étudié. Néanmoins, les effets locaux déterminant dans la plupart des cas le comportement global n'ont guère été abordés. Cette recherche étudie des effets structurels locaux sélectionnés ayant une influence importante sur la performance structurelle globale des tabliers pultrudés en GFRP et des structures sandwich à base de GFRP dont le noyau en mousse est renforcé par des âmes intérieures en GFRP (web-core).

L'effet de la géométrie du noyau des tabliers pultrudés en GFRP sur le comportement du système dans la direction transversale à celle de la pultrusion a été investigué expérimentalement. Le travail expérimental effectué sur deux types de tablier avec des sections transversales constituées des cellules trapézoïdales et triangulaires a montré que la performance structurelle transversale dépend de la géométrie des cellules. En outre, les rigidités transversales à la flexion et au cisaillement dans le plan des deux systèmes ont été évaluées et ont indiqué que le noyau triangulaire engendre un comportement bidirectionnel du tablier plus prononcé lorsqu'il est soumis à des charges concentrées.

Le comportement local des jonctions âme-semelle (WFJ) du tablier pultrudé à cellules trapézoïdales en ce qui concerne la capacité de dissipation d'énergie et la recouvrance après déchargement a été investigué expérimentalement. Les résultats expérimentaux correspondant à deux types de jonction de géométrie et architecture de fibres similaires, mais présentant différents types d'imperfections initiales ont démontré que des imperfections dissemblables peuvent influencer le comportement des WFJ de manière significative et le transformer de fragile en ductile. La recouvrance en fonction

du temps et les mécanismes de dissipation d'énergie des WJF présentant un comportement ductile ont été évalués ; les effets viscoélastiques se sont avérés faibles dans les deux cas. Le comportement rotationnel des différents types de WFJ du tablier trapézoïdal a été étudié. Une procédure expérimentale basée sur des essais de flexion en trois points et en console menés sur les âmes du tablier a été conçue et utilisée à cet effet. La rigidité rotationnelle, la résistance et le mode de rupture des WFJ diffèrent en fonction du type d'âme, de l'emplacement de la WFJ dans le profilé pultrudé, des imperfections initiales existantes et de la direction du moment de flexion appliqué. Des simulations numériques du tablier à grande échelle ont été réalisées afin de démontrer la validité des courbes moment-rotation ($M-\varphi$) empiriques ainsi que des courbes $M-\varphi$ simplifiées également établies.

Les effets du fluage sur le comportement structurel des structures sandwich de type web-core en GFRP et mousse ont été investigués. Une étude sur le comportement au fluage des mousses en polyuréthane (PUR) a été menée et a montré la nécessité de considérer l'anisotropie et la densité de la mousse ainsi que le type de chargement appliqué lors de l'évaluation de la performance structurelle à long terme du système sandwich. Le comportement au fluage des panneaux sandwich web-core, et plus spécifiquement les aspects structurels influencés par l'interaction web-core (âme-noyau en mousse), ont été analysés à l'aide d'une étude de cas basée sur la toiture sandwich GFRP-PUR du Novartis Campus Main Gate Building et des recommandations de conception et dimensionnement en vigueur. Les dimensions de la structure sandwich en résultant ont dépendu des recommandations de dimensionnement appliquées. Finalement, une méthode de dimensionnement du noyau hybride web-core a été proposée.

Mots clés

Polymère renforcé par des fibres de verre, tablier pultrudé de pont, structure en sandwich, effet local, comportement transversal, jonction âme-semelle, rigidité rotationnelle, comportement au fluage, mousse de polyuréthane

Table of Contents

Preface	v
Acknowledgments	vii
Abstract	ix
Résumé	xi
Table of Contents	xiii
List of Figures	xvii
List of Tables	xxi
Chapter 1 Introduction	1
1.1 Context and motivation	1
1.2 Objectives	3
1.3 Methodology	3
1.4 Thesis organization	4
References	6
Chapter 2 System transverse in-plane shear stiffness	9
2.1 Introduction	9
2.2 Pultruded GFRP bridge deck systems	11
2.2.1 Description of system geometry	11
2.2.2 Material properties	12
2.3 Experimental program	13
2.3.1 Specimen dimensions and manufacture	13
2.3.2 Set-up and load equipment	14
2.3.3 Instrumentation and measurements	14
2.3.4 Experimental procedure	15
2.4 Experimental results and discussion	15

2.4.1	DS deck	15
2.4.2	AS deck	19
2.4.3	Comparison of experimental results	22
2.5	Conclusions	26
	References	27
Chapter 3 Energy dissipation and recovery in web-flange junctions		31
3.1	Introduction	31
3.2	Theoretical background	34
3.2.1	Recovery behavior of viscoelastic materials	34
3.2.2	Energy dissipation in viscoelastic materials	35
3.2.3	Ductility evaluation	35
3.3	Experimental program	36
3.3.1	Pultruded GFRP bridge deck system	36
3.3.2	Specimen description and preparation	36
3.3.3	Experimental set-up, instrumentation and procedure	38
3.4	Experimental results	40
3.4.1	<i>If-o</i> series response	40
3.4.2	<i>Ic-o</i> series response	42
3.4.3	Recovery behavior	43
3.5	Discussion	44
3.5.1	Comparison of <i>If-o</i> and <i>Ic-o</i> series	44
3.5.2	Recovery behavior	47
3.5.3	Energy dissipation capacity of <i>Ic-o</i> series	49
3.6	Conclusions	51
	References	52
Chapter 4 Rotational stiffness of web-flange junctions		57
4.1	Introduction	57
4.2	Experimental program	61
4.2.1	Experimental approach	61
4.2.2	Specimen description and preparation	64
4.2.3	Three-point bending experiments	66
4.2.4	Cantilever experiments	68
4.3	Experimental results and discussion	69
4.3.1	Three-point bending experiments	69
4.3.2	Cantilever experiments	71
4.3.3	Rotational stiffness of web-flange junctions	74
4.4	Modeling	78
4.4.1	Empirical modeling of rotational stiffness of web-flange junctions	78
4.4.2	Numerical modeling	79
4.5	Conclusions	83
	References	84
Chapter 5 Long-term design of FRP-PUR web-core sandwich structures		89
5.1	Introduction	89

5.2	Mechanical behavior of PUR foams used as sandwich core material	92
5.2.1	Anisotropy of rigid PUR foam properties	92
5.2.2	Creep behavior of rigid PUR foams	96
5.3	Time-dependent behavior of web-core sandwich panels	102
5.3.1	Distribution of shear forces	102
5.3.2	Shear resistance of webs	106
5.4	Design of web and core dimensions	112
5.4.1	Shear resistance of hybrid FRP-PUR core	112
5.4.2	Design provisions	114
5.5	Conclusions	115
	References	116
Chapter 6 Conclusions and future work		121
6.1	Conclusions	121
6.1.1	Effect of core geometry of pultruded GFRP decks on their transverse behavior	121
6.1.2	Energy dissipation capacity and recovery of web-flange junctions of pultruded GFRP decks	122
6.1.3	Rotational behavior of web-flange junctions of pultruded GFRP decks	122
6.1.4	Creep effects on the load-bearing behavior of web-core sandwich structures	122
6.2	Original contributions	123
6.3	Recommendations for future work	124
6.3.1	GFRP bridge decks as top chord of main girders	124
6.3.2	Ductility in pultruded GFRP members	125
6.3.3	Standardized experimental methods for WFJ behavior characterization	125
6.3.4	Wrinkling strength of GFRP laminates subjected to sustained loading	125
6.3.5	Partial safety factors for core materials	126
6.3.6	Shear resistance of web-core sandwich structures	126
	References	126
Appendix A Equations for beams with flexible shear connections		129
Appendix B DS beam experiments		133
Appendix C AS beam experiments		141
Appendix D DS web three-point bending experiments		151
Appendix E DS web-flange junction cantilever experiments		173
Appendix F Summary of experimental studies of the creep behavior of PUR foams		199
Curriculum Vitae		237

List of Figures

Chapter 1 | Introduction

- Figure 1.1 (a) Friedberg Bridge: road bridge with ASSET pultruded deck, Germany, 2008;⁹ (b) Schroon River Bridge in Warrensburg: replacement of filled steel grid deck with DuraSpan pultruded deck, USA, 2000.¹⁰ 2
- Figure 1.2 (a) Novartis Campus Entrance Building: GFRP-PUR sandwich roof, Switzerland, 2006;² (b) Yitzhak Rabin Center: GFRP-polyurethane sandwich roof, Israel, 2006. 3

Chapter 2 | System transverse in-plane shear stiffness

- Figure 2.1 Unit module geometry of (a) *DS* and (b) *AS* specimens; dimensions in mm. 11
- Figure 2.2 Typical fiber architecture of laminates from (a) *DS* and (b) *AS* specimens. 12
- Figure 2.3 Experimental set-up for (a) *DS* and (b) *AS* beams. 13
- Figure 2.4 Instrumentation system for correlation of images and recorded data in *AS* beams; (a) general view; (b) data acquisition screen view on computer, shown on tablet PC screen by means of web publishing tool. 15
- Figure 2.5 Load-deflection behavior of (a) *DS* beams; (b) *AS* beams; (c) crack sequence in *DS*-2 and *DS*-3; (d) failure location in *AS* beams. 16
- Figure 2.6 Failure pattern of *DS* beams; (a) deformed shape of specimen *DS*-3; (b) local failure of specimen *DS*-1 (8th web-top flange junction). 17
- Figure 2.7 Measured normalized strains in webs (*W*) and flanges (*TT*= top, top face; *TB*= top, bottom face; *BT*= bottom, top face; *BB*= bottom, bottom face) along span throughout beams' linear behavior range. 18
- Figure 2.8 Measured ratios of local bending strain to local axial strain in webs and flanges throughout beams' linear behavior range. 18
- Figure 2.9 Horizontal displacement across bottom flange at mid-span at 6-kN load in specimen *DS*-2. 19
- Figure 2.10 Load- Δu_x behavior of adhesively-bonded joint in bottom flange at mid-span in specimen *DS*-2. 19

Figure 2.11	Failure pattern of specimen AS-2; (a) first failure; (b) final failure.	20
Figure 2.12	Load-deflection behavior of AS beams at $0.4 L$ (δ_1), $0.5 L$ (δ_2) and $0.6 L$ (δ_3).	21
Figure 2.13	Opening of adhesively-bonded joint after first failure of AS-2 and AS-3.	21
Figure 2.14	Load-strain behavior of specimen AS-2 near failure location.	22
Figure 2.15	Load-strain behavior in top flange of AS beams at mid-span.	22
Figure 2.16	Local (a) axial forces and (b) bending moments in top flange.	24
Figure 2.17	Local (a) axial forces and (b) bending moments in webs / diagonals.	24
Figure 2.18	GFRP/GFRP composite beam; (a) elevation; (b) cross section.	25
Figure 2.19	Calculated transverse system in-plane shear modulus for (a) DS series and (b) AS series.	26

Chapter 3 | Energy dissipation and recovery in web-flange junctions

Figure 3.1	Load-deflection behavior of full-scale DS-3 beam. ²⁴	33
Figure 3.2	Behavior of viscoelastic materials; (a) recovery; energy dissipation under monotonic loading, (b) without and (c) with residual deformation.	35
Figure 3.3	Unit module geometry of DS bridge deck system; dimensions in mm.	36
Figure 3.4	(a) Local bending moments in webs of DS deck panel subjected to transverse bending. (b) WFJ specimens; dimensions in mm.	37
Figure 3.5	Fiber architecture and crack initiation of (a) <i>If-o</i> and (b) <i>Ic-o</i> series; dimensions in mm.	38
Figure 3.6	Initial imperfections of (a) <i>If-o</i> and (b) <i>Ic-o</i> series.	38
Figure 3.7	Experimental set-up; (a) general view; (b) front view; (c) cross section; dimensions in mm.	39
Figure 3.8	Specimen instrumentation: arrangement of target points for video extensometer measuring system; dimensions in mm.	39
Figure 3.9	Load-displacement response of (a) <i>If-o</i> specimens and (b) <i>Ic-o</i> specimens.	40
Figure 3.10	Crack pattern at peak load of (a) <i>If-o2</i> and (b) <i>Ic-o6</i> specimens; post-peak crack pattern of (c) <i>If-o2</i> and (d) <i>Ic-o6</i> specimens.	41
Figure 3.11	Delayed recovered deflection of specimens (a) <i>Ic-o4</i> , <i>Ic-o5</i> and <i>Ic-o6</i> ; (b) <i>Ic-o8</i> ; (c) <i>Ic-o9</i> .	43
Figure 3.12	Differential rotation in (a) web and (b) flange elements.	44
Figure 3.13	Contribution of pre-crack to total deflection in <i>Ic-o</i> series.	45
Figure 3.14	Recovered deflection throughout cycles in <i>Ic-o</i> series.	47
Figure 3.15	Total and dissipated energies per unit width during monotonic loading.	50
Figure 3.16	Ratio of hysteretic to total dissipated energy throughout cycles.	50
Figure 3.17	Ductility index for <i>Ic-o</i> WFJs throughout displacement. $\mu = 1$ indicates rigid-plastic behavior.	51

Chapter 4 | Rotational stiffness of web-flange junctions

Figure 4.1	Unit module geometry of DS bridge deck system; dimensions in mm.	58
------------	--	----

Figure 4.2	Experimental configuration for <i>DS</i> deck specimens subjected to transverse (a) three-point bending and (b) in-plane shear; load-displacement behaviors under (c) three-point bending and (d) in-plane shear. ^{6,7}	59
Figure 4.3	Fiber architecture and structural idealization of WFJs with (a) inclined and (b) vertical webs.	62
Figure 4.4	Models of (a) simply supported beam under symmetric three-point bending; (b) cantilever beam with fixed end; (c) cantilever beam with semi-rigid end.	63
Figure 4.5	(a) WFJ specimens; (b) location of WFJ specimens within <i>DS</i> deck panel when subjected to transverse bending (local bending moments in webs are shown); dimensions in mm.	65
Figure 4.6	Set-up for three-point bending experiments; (a) general view (<i>Ic-o</i> specimen); (b) front view (<i>Ic-a</i> specimen); (c) cross section; dimensions in mm.	66
Figure 4.7	Instrumentation for three-point bending/cantilever experiments in (a)/(b) <i>I</i> and (c)/(d) <i>V</i> specimens; dimensions in mm.	67
Figure 4.8	Set-up for cantilever experiments; (a) general view (<i>Ic-o</i> specimen); (b) front view (<i>Ic-a</i> specimen); (c) cross section; dimensions in mm.	68
Figure 4.9	Load-strain behavior of <i>If-o</i> and <i>If-a</i> specimens in three-point bending experiments.	69
Figure 4.10	Load-deflection response of (a) <i>If-</i> , (b) <i>Ic-</i> and (c) <i>V</i> -WFJs during three-point bending (3pb) and cantilever experiments.	70
Figure 4.11	Crack pattern at peak load of (a) <i>If-o1</i> , (b) <i>Ic-o1</i> , (c) <i>V-d1</i> , (d) <i>If-a1</i> , (e) <i>Ic-a3</i> and (f) <i>V-s3</i> specimens.	73
Figure 4.12	Calculated moment-rotation behavior of (a) <i>If-</i> , (b) <i>Ic-</i> and (c) <i>V</i> -WFJs.	75
Figure 4.13	Comparison of moment-rotation behavior of WFJs of <i>DS</i> deck and pultruded GFRP H-profiles. ^{21,22}	76
Figure 4.14	Idealized moment-rotation behavior; (a) <i>RP</i> model; (b) <i>TL</i> model.	78
Figure 4.15	Idealized moment-rotation behavior of (a) <i>If-</i> , (b) <i>Ic-</i> and (c) <i>V</i> -WFJs.	80
Figure 4.16	Schema of FE frame models developed for full-scale (a) three-point bending and (b) in-plane shear experiments.	81
Figure 4.17	Comparison of measured and calculated load-deflection behavior in four-module specimens subjected to three-point bending.	82
Figure 4.18	Comparison of measured and calculated load-displacement behavior in (a) three-module and (b) four-module specimens subjected to in-plane shear.	83

Chapter 5 | Long-term design of FRP-PUR web-core sandwich structures

Figure 5.1	Compressive stiffness and strength anisotropy ratios of commercially available rigid PUR foams of 30–240 kg/m ³ : (a) influence of foam density; (b) comparison; from references 44–48.	95
Figure 5.2	Effect of anisotropy on compressive creep behavior of a 60-kg/m ³ PUR foam, calculated from Fig. 8 in reference 50.	98
Figure 5.3	Effect of density on shear creep behavior of rigid PUR foams, calculated from Fig. 5 in reference 21.	98

Figure 5.4	Comparison of compressive and shear creep behavior of rigid PUR foams, calculated from references 22 and 51.	99
Figure 5.5	Comparison of shear modulus reduction factor for 50-kg/m ³ PUR foam calculated according to BÜV ¹⁵ and experimentally determined from reference 27.	101
Figure 5.6	Cross-sectional geometry of web-core sandwich panel (not to scale).	103
Figure 5.7	Shear moduli reduction factors for GFRP webs and PUR foam core.	104
Figure 5.8	(a) Time-dependent contribution of GFRP webs to bearing shear forces and (b) increase with time.	105
Figure 5.9	Contribution of GFRP webs to bearing shear forces depending on normalized web area.	106
Figure 5.10	Overall material factors over time applicable to GFRP webs in case study.	110
Figure 5.11	Design shear and shear wrinkling strength of GFRP webs from case study.	111
Figure 5.12	Design shear wrinkling and critical shear buckling strengths of GFRP webs from case study according to EUR 27666. ³⁵	111
Figure 5.13	(a) Time-dependent contribution of web-core components to shear stiffness and resistance; (b) time-dependent normalized shear resistance of hybrid core and individual components from case study.	113
Figure 5.14	(a) Time-dependent contribution of web-core components to shear stiffness and resistance; (b) time-dependent normalized shear resistance of hybrid core and individual components from case study 2.	114
Figure 5.15	Time-dependent normalized shear resistance of hybrid core from case study 2 depending on normalized web area.	115
Figure 5.16	Increase of web thickness in case study 2 resulting from neglect of foam core load-bearing capacity.	115

List of Tables

Chapter 1 | Introduction

Table 1.1	Thesis organization.	5
-----------	----------------------	---

Chapter 2 | System transverse in-plane shear stiffness

Table 2.1	Material properties of <i>DS</i> and <i>AS</i> unit modules.	12
Table 2.2	Adhesive properties of <i>DS</i> and <i>AS</i> deck systems.	12
Table 2.3	Calculated apparent bending stiffness of <i>DS</i> beams.	16
Table 2.4	Calculated apparent bending stiffness of <i>AS</i> beams.	20

Chapter 3 | Energy dissipation and recovery in web-flange junctions

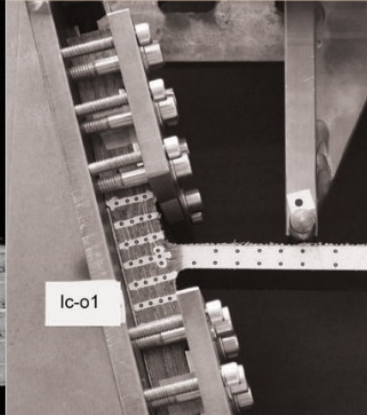
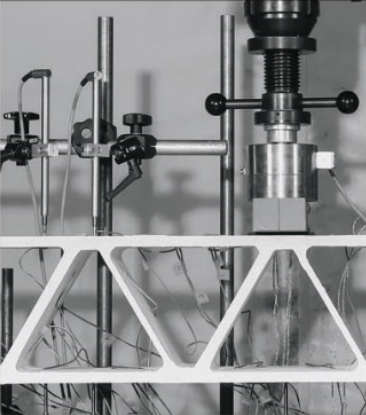
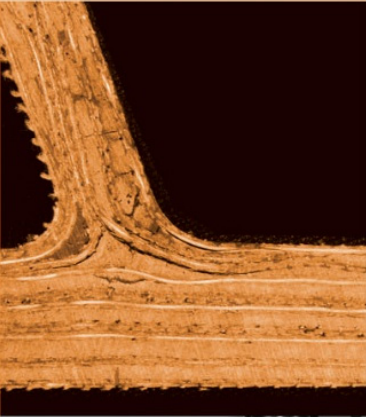
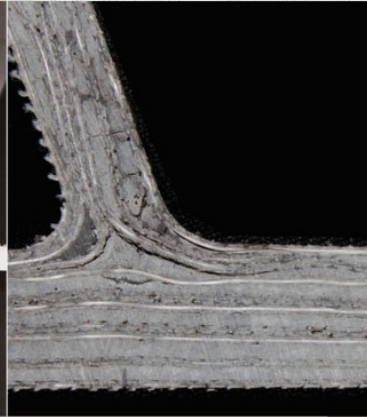
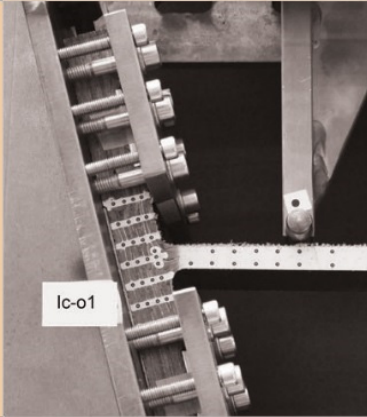
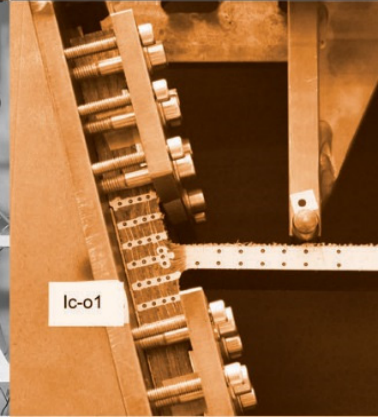
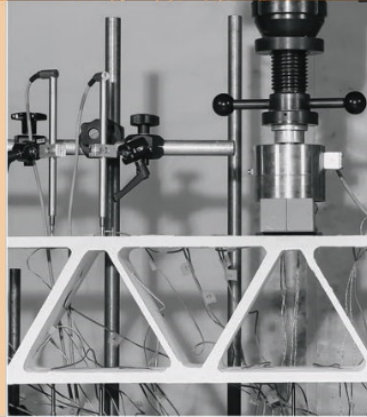
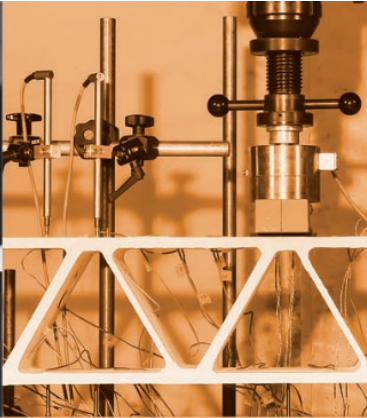
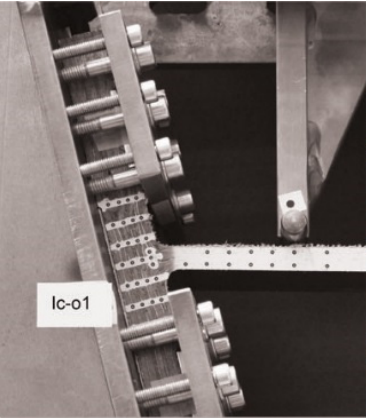
Table 3.1	Material properties of <i>DS</i> . ²⁹	37
Table 3.2	Overview of performed experiments.	40
Table 3.3	Experimental peak loads and corresponding displacements; calculated ultimate moments.	41
Table 3.4	Obtained Weibull distribution function parameters and $\delta_{r,del}^{\infty}$ to model time-dependent recovered deflection.	48

Chapter 4 | Rotational stiffness of web-flange junctions

Table 4.1	Material properties of <i>DS</i> . ²⁸	65
Table 4.2	Average dimensions of WFJ specimens.	66
Table 4.3	Calculated transverse elastic flexural moduli of web laminates.	71
Table 4.4	Experimental peak loads and corresponding displacements; calculated ultimate moments and corresponding rotations; calculated rotational stiffness.	72
Table 4.5	Parameters of idealized moment-rotation relationships.	78

Chapter 5 | Long-term design of FRP-PUR web-core sandwich structures

Table 5.1	Shape-anisotropy ratio and mechanical anisotropy of PUR foams.	95
Table 5.2	Characteristic material properties of GFRP web laminates and PUR foam core. ²	104
Table 5.3	Effects taken into account in material factors by partial safety coefficients or influence / conversion factors.	107
Table 5.4	Partial safety coefficients and material factors from Eurocomp ¹⁸ applicable to case study.	108
Table 5.5	Material and modification factors from BÜV ¹⁵ applicable to case study.	108
Table 5.6	Material and conversion factors from EUR 27666 ³⁵ applicable to case study.	108
Table 5.7	Design shear, shear wrinkling and critical shear buckling strength equations.	109



Chapter 1

Introduction

1.1 Context and motivation

Civil engineering projects relating to new construction and rehabilitation of bridge and building structures are, to an increasing extent, demanding construction methods that can contribute to accelerating construction processes. Enhanced time performance in the construction phase leads to earlier project delivery and reduced return-on-investment times, thus more rapidly fulfilling users' needs and contributing to productivity improvement. The acceleration of on-site works is of special relevance in the case of replacement and rehabilitation projects where minimum traffic disruption and building closure times are a primary requirement and for new constructions in built environments to reduce inconvenience to residents and disruption of their everyday lives to a minimum. As a result, prefabrication technologies and off-site construction techniques, which in addition provide superior quality control compared to conventional on-site methods, are being increasingly employed.

Major current challenges concerning bridge construction also include low maintenance and durability issues. Long-term funding provisions required to perform intensive maintenance works are difficult to ensure and in view of present day high traffic volumes, interruptions for maintenance may result in annoyance and unacceptable delays for users. Public administrations and bridge engineers therefore attach increasing importance to the development of bridge designs that entail lower maintenance costs. Aside from increasing traffic demands, deficiencies commonly identified in the existing bridge inventory, frequently causing the need for repair or replacement operations, include corrosion of steel members and steel reinforcement of concrete, deck deterioration due to wear, de-icing salts, freeze-thaw cycles, and concrete aging and degradation.¹ Materials and construction systems and detailing that offer improved corrosion resistance are hence constantly being sought.

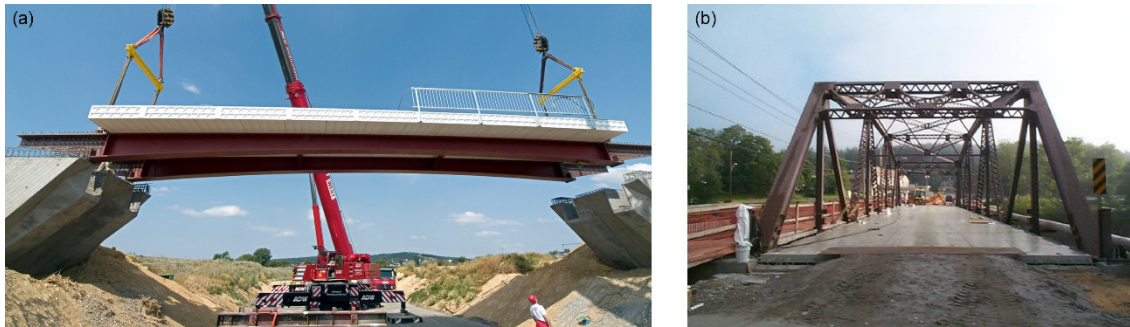


Figure 1.1 – (a) Friedberg Bridge: road bridge with ASSET pultruded deck, Germany, 2008;⁸ (b) Schroon River Bridge in Warrensburg: replacement of filled steel grid deck with DuraSpan pultruded deck, USA, 2000.⁹

In the building construction domain, the development of digital technologies has in recent years fostered the so-called freeform, ‘liquid design’ or ‘blob’ architecture, which is arousing growing interest among architects. The realization of architectural concepts based on these emerging geometrically complex shapes, for which traditional construction techniques are not adapted, constitutes a new challenge for the construction industry.

Fiber-reinforced polymer (FRP) composite materials, in this context, offer advantageous properties for use in bridge and building construction, such as high strength- and stiffness-to-weight ratios, good resistance against environmental actions and fatigue, and low thermal conductivity in the case of glass fiber-reinforced polymers (GFRPs). Lightweight large-scale elements, which can adopt complex shapes, can be prefabricated and then easily transported to and rapidly installed on the construction site.²⁻⁵

In bridge construction, GFRP decks have been increasingly used during the last two decades in newly built bridges and to upgrade existing ones by replacing reinforced-concrete decks (see Figure 1.1).^{6,7} A commercially available deck concept consists of individual pultruded profiles that are adhesively bonded together to form an orthotropic slab. Several cross-sectional geometries exist, in which different web arrangements result in dissimilar cellular shapes that influence the structural behavior in the transverse-to-pultrusion direction, i.e. Vierendeel frame or truss behavior for trapezoidal/rectangular or triangular cells, respectively.¹⁰

Regarding building construction, GFRP-foam sandwich structures enable the integration of structural, building physics and architectural functions (see Figure 1.2).^{2,3} In larger span roof and floor structures, the shear resistance and stiffness of the foam core may not be sufficient and a reinforcing GFRP web system thus needs to be integrated into the core.² The sandwich face sheet and web laminates are generally thin-walled compared to pultruded bridge deck components and therefore sensitive to local stability problems when subjected to compressive loading, i.e. buckling and wrinkling. In this respect, the foam acts as a structural stabilizing element in addition to fulfilling the thermal insulation function.

A significant amount of research work has been conducted in recent years on the global structural behavior of pultruded decks¹¹⁻¹⁵ and web-core sandwich structures.^{2,16,17} These studies have shown that the global structural performance is in most cases governed by local effects.^{10,12-17} In pultruded bridge decks, failure normally initiates in the web-flange junctions; depending



Figure 1.2 – (a) Novartis Campus Entrance Building: GFRP-PUR sandwich roof, Switzerland, 2006;² (b) Yitzhak Rabin Center: GFRP-polyurethane sandwich roof, Israel, 2006.

on the cellular cross-sectional geometry, this results in brittle or (pseudo-) ductile global behavior.¹⁰ In sandwich structures subjected to sustained loading, creep of the foam may result in a reduction of the stabilization provided to the compressed face sheet and web laminates.¹⁸ Despite the significant influences of local effects on global structural behavior as described above, few studies are available¹⁹ and further research is therefore required.

1.2 Objectives

The aim of this research is to investigate selected local structural effects occurring in pultruded GFRP bridge decks and GFRP-foam web-core sandwich structures, as described above. The following objectives were thus defined:

1. Investigation of the effect of the core geometry of pultruded decks on the system's behavior in the transverse-to-pultrusion direction.
2. Investigation of the energy dissipation capacity and recovery after unloading of the web-flange junctions of a pultruded deck system.
3. Characterization and modeling of the rotational behavior of the web-flange junctions of a pultruded deck system.
4. Investigation of creep effects on the load-bearing behavior of web-core sandwich structures, with emphasis on the creep-stability interaction.

1.3 Methodology

The methodology adopted to attain the objectives of this research is as follows:

- 1.a Experimental investigation of the static transverse behavior of two pultruded deck systems with trapezoidal and triangular cellular cross-sectional geometries.
- 1.b Analysis of experimental results to obtain the transverse in-plane shear moduli of both systems, using analytical models for composite girders with flexible shear connections.
- 2.a Experimental investigation of the local bending behavior, recovery subsequent to unloading and energy dissipation capacity of the web-flange junctions of a pultruded deck system.
- 3.a Establishment of an experimental procedure to characterize the rotational behavior of the web-flange junctions of pultruded decks.
- 3.b Experimental investigation of the local bending behavior of web

- components and web-flange junctions to characterize the rotational stiffness of all types of web-flange junctions of a pultruded deck.
- 3.c Numerical simulations of full-scale deck experiments to validate the experimental and modeled rotational stiffnesses.
 - 4.a Analysis of the mechanical behavior of polyurethane (PUR) foams with a focus on creep, based on experimental results obtained from the literature.
 - 4.b Design of GFRP-PUR web-core sandwich roof examples according to current guidelines and comparison of these guidelines and the resulting designs.

1.4 Thesis organization

The research presented in this thesis is divided into four main chapters, which address the four objectives defined in Section 1.2, and an additional chapter presenting the main conclusions of the research. The general organization of the thesis is shown in Table 1.1.

The main content of each chapter is summarized as follows:

- Chapter 2: The static behavior in the transverse-to-pultrusion direction of two GFRP deck systems with trapezoidal and triangular cellular cross-sectional geometries is experimentally investigated. The behavior of both deck designs with regard to stiffness, strength and failure mode is compared. The systems' in-plane shear moduli are estimated from the experimental deflection results.
- Chapter 3: The energy dissipation capacity resulting from progressive cracking and the recovery after unloading of the web-flange junctions of a pultruded GFRP deck are experimentally investigated. Two junction types with similar geometry and fiber architecture but different initial imperfections are examined; their influence on the junctions' behavior is assessed. The sensitivity of the response to different loading and unloading rates is evaluated. The ductility index of the junctions is calculated and compared to that of the full-scale deck.
- Chapter 4: The rotational behavior of the web-flange junctions of a pultruded GFRP deck is characterized. For this purpose an experimental procedure based on three-point bending and cantilever experiments conducted on the web elements and simple analytical models is proposed and used. Simplified expressions to model the rotational behavior are provided. The experimental and modeled rotational responses are validated by numerical simulations of full-scale deck experiments.
- Chapter 5: The structural behavior of GFRP-PUR web-core sandwich structures subjected to sustained loading is investigated. A study of the creep behavior of PUR foams used as core materials is conducted. The creep effects on the load-bearing behavior of the web-core sandwich structure are analyzed. In particular, the structural design aspects affected by the web-core interaction and the influence of creep on local

Main chapters	Structural element	Local effect	Methodology	Appendices	Paper
2 System transverse in-plane shear stiffness	Pultruded deck	Effect of core geometry	- Experimental investigation - Analytical determination of in-plane shear modulus	A, B, C	1
3 Energy dissipation and recovery in web-flange junctions	Pultruded deck	Energy dissipation and recovery	- Experimental investigation	E	2
4 Rotational stiffness of web-flange junctions	Pultruded deck	Rotational behavior of junctions	- Experimental investigation - Modeling of junction rotational stiffness - Numerical modeling of full-scale decks	D, E	3
5 Long-term design of FRP-PUR web-core sandwich structures	Web-core sandwich	Creep and creep-stability interaction	- Analysis of PUR foam behavior - Eurocomp, BÜV and EUR 27666 designs	F	4

Table 1.1 – Thesis organization.

stability phenomena are investigated. The effects of applying particular design recommendations on the resulting design are assessed based on the example of a real GFRP-PUR sandwich roof. A design procedure to take creep effects into account in the design of the web and core dimensions is presented.

- Chapter 6: The conclusions of the conducted research are summarized and suggestions for future research are formulated.

Supplementary information concerning the main chapters of the thesis is provided in six appendices (see Table 1.1):

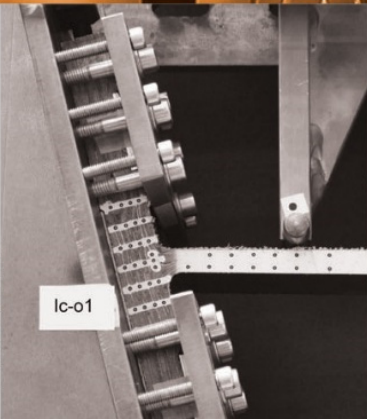
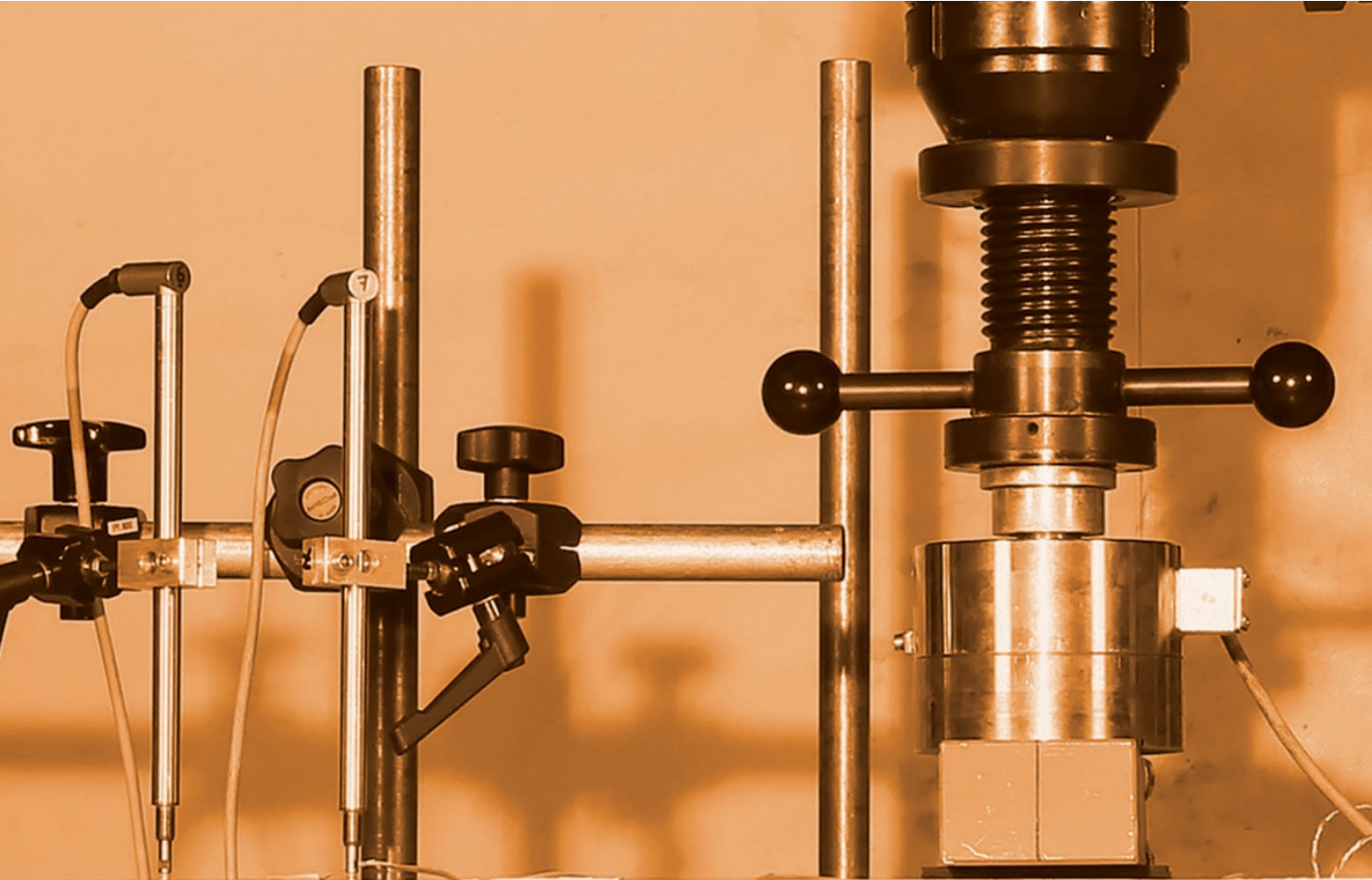
- Appendix A: Equations for beams with flexible shear connections
- Appendix B: *DS* beam experiments
- Appendix C: *AS* beam experiments
- Appendix D: *DS* web three-point bending experiments
- Appendix E: *DS* web-flange junction cantilever experiments
- Appendix F: Summary of experimental studies of the creep behavior of PUR foams

The results of this thesis have been presented in four journal papers – three published and one submitted for publication. The four papers are listed below and correspond to the four main chapters of the thesis (see Table 1.1):

1. Yanes-Armas S, de Castro J, Keller T. System transverse in-plane shear stiffness of pultruded GFRP bridge decks. *Eng Struct* 2016;107:34–46. doi:10.1016/j.engstruct.2015.11.003
2. Yanes-Armas S, de Castro J, Keller T. Energy dissipation and recovery in web-flange junctions of pultruded GFRP decks. *Compos Struct* 2016;148:168–180. doi:10.1016/j.compstruct.2016.03.042
3. Yanes-Armas S, de Castro J, Keller T. Rotational stiffness of web-flange junctions of pultruded GFRP decks. *Eng Struct* 2017;140:373–389. doi:10.1016/j.engstruct.2017.03.003
4. Yanes-Armas S, de Castro J, Keller T. Long-term design of FRP-PUR web-core sandwich structures in building construction. Submitted to *Compos Struct* in June 2017.

References

1. Karbhari VM, Zhao L. Use of composites for 21st century civil infrastructure. *Comput Methods Appl Mech Eng* 2000;185(2–4):433–454.
2. Keller T, Haas C, Vallée T. Structural concept, design, and experimental verification of a glass fiber-reinforced polymer sandwich roof structure. *J Compos Constr* 2008;12(4):454–468.
3. Eekhout M. The GRP shell structures for the Rabin Center in Tel Aviv. In: Scheublin F, Westra J, Pronk A (eds.) *Proceedings of the International Conference on Adaptable Building Structures, Adaptables 2006*, 3–5 July 2006, Eindhoven, The Netherlands. p.3-237.
4. Lee SW, Hong KJ, Park S. Current and future applications of glass-fibre-reinforced polymer decks in Korea. *Struct Eng Int* 2010;20(4):405–408.
5. Keller T, Rothe J, de Castro J, Osei-Antwi M. GFRP-balsa sandwich bridge deck: concept, design, and experimental validation. *J Compos Constr* 2013;18(2):04013043-1.
6. Keller T. *Use of fibre reinforced polymers in bridge construction*. Structural engineering documents, 7. Zurich: International Association for Bridge and Structural Engineering IABSE; 2003.
7. Hollaway L. A review of the present and future utilisation of FRP composites in the civil infrastructure with reference to their important in-service properties. *Constr Build Mater* 2010;24(12):2419–2445.
8. Knippers J, Cremers J, Gabler M, Lienhard J. *Construction manual for polymer + membranes: materials, semi-finished products, form-finding design*. Basel: Birkhäuser; 2011.
9. Triandafilou L, O'Connor J. FRP composites for bridge decks and superstructures: state of the practice in the U.S. In: *Proceedings of International Conference on Fiber Reinforced Polymer (FRP) Composites for Infrastructures Applications*, 2009, Stockton, Canada.
10. Gürtler HW. *Composite action of FRP bridge decks adhesively bonded to steel main girders* [PhD Thesis]. Ecole Polytechnique Fédérale de Lausanne, Switzerland; 2004.
11. Jeong J, Lee YH, Park KT, Hwang YK. Field and laboratory performance of a rectangular shaped glass fiber reinforced polymer deck. *Compos Struct* 2007;81(4):622–628.
12. Hayes MD, Ohanehi D, Lesko JJ, Cousins TE, Witcher D. Performance of tube and plate fiberglass composite bridge deck. *J Compos Constr* 2000;4(2):48–55.
13. Keller T, Schollmayer M. Plate bending behavior of a pultruded GFRP bridge deck system. *Compos Struct* 2004;64(3):285–295.
14. Zhou A, Coleman JT, Temeles AB, Lesko JJ, Cousins TE. Laboratory and field performance of cellular fiber-reinforced polymer composite bridge deck systems. *J Compos Constr* 2005;9(5):458–467.
15. Lee J, Kim Y, Jung J, Kosmatka J. Experimental characterization of a pultruded GFRP bridge deck for light-weight vehicles. *Compos Struct* 2007;80(1):141–151.
16. Correia JR, Garrido M, Gonilha JA, Branco FA and Reis LG. GFRP sandwich panels with PU foam and PP honeycomb cores for civil engineering structural applications: Effects of introducing strengthening ribs. *Int J Struct Integrity* 2012; 3(2):127–147.
17. Fam A, Sharaf T. Flexural performance of sandwich panels comprising polyurethane core and GFRP skins and ribs of various configurations. *Compos Struct* 2010;92(12):2927–2935.
18. Hamed E, Frostig Y. Influence of creep on the geometrically nonlinear behavior of soft core sandwich panels. *Int J Mech Sci* 2016;105:398–407.
19. Sebastian WM, Keller T, Ross J. Influences of polymer concrete surfacing and localized load distribution on behavior up to failure of an orthotropic FRP bridge deck. *Compos Part B* 2013;45(1):1234–1250.



Chapter 2

System transverse in-plane shear stiffness

2.1 Introduction

Glass fiber-reinforced polymer (GFRP) bridge decks are one of the most developed applications of FRP structural materials in the civil engineering domain. During the last decades, GFRP bridge decks have been increasingly employed in vehicular and pedestrian bridges, both for new construction and rehabilitation purposes, owing to favorable characteristics compared to traditional reinforced concrete (RC) decks. Advantages of GFRP decks comprise high specific strength, corrosion resistance, light weight (about 10–20% of the structurally equivalent RC deck,¹ which in replacement applications enables increase of the live load capacity through dead load reduction), easy and rapid assembly, short field installation times with minimum traffic disruption, and lower life-cycle costs. Several all-FRP and hybrid FRP-concrete deck systems have been designed, experimentally studied and implemented. Reviews regarding their development and use have been presented by several authors and can be found in the literature.^{1–5}

Based on the manufacturing and assembly process, GFRP decks can be classified into two categories: sandwich and pultruded decks. Sandwich bridge decks are composed of two GFRP face sheets and a lightweight material core (e.g. foam, honeycomb panel, balsa wood). Pultruded deck systems consist of an assembly of hollow shapes (also called profiles) manufactured by the pultrusion process and adhesively bonded together to form the slab. Unit profiles with different cell geometries (e.g. triangular, rectangular, trapezoidal, hexagonal) and profile-to-profile joint configurations have been proposed. The shapes' pultrusion direction is generally aligned transversely to the traffic direction, with the profiles spanning across the bridge's longitudinal girders.⁶

Pultruded GFRP decks exhibit orthotropic structural behavior due to material orthotropy and different load-bearing mechanisms in their

longitudinal (parallel to pultrusion) and transverse (perpendicular to pultrusion) directions. In the longitudinal and main working direction, the deck system can be considered as a group of contiguous box or I-beams formed by the deck's webs and flanges.^{7,8} In its transverse direction, the deck's load transfer mechanism depends on the system's cellular cross-sectional geometry. Truss and Vierendeel frame load-bearing mechanisms have been found to govern the transverse in-plane shear behavior of pultruded deck systems with triangular and trapezoidal core geometries, respectively.⁹ The characteristics of the web-flange junctions and joints between adjacent profiles also influence the deck's transverse structural performance.¹⁰ Numerous laboratory and field experimental investigations have been conducted, for several pultruded deck systems, to study their global stiffness, strength, failure modes and fatigue performance under vehicular loads.^{8,11-14} Experimental research has also focused on the characterization of the deck's longitudinal behavior by means of beam tests on specimens composed of one to three single profiles.¹⁴⁻¹⁶ Few experimental studies are available for the transverse-to-pultrusion direction however, notwithstanding the influence of the deck's transverse behavior on its performance in two structural functions, namely: (i) the transmission of concentrated traffic loads to the underlying superstructure (i.e. the bi-directional bending action depends on the transverse behavior) and (ii) the participation in transferring loads in the bridge's longitudinal direction when acting as the upper chord of the hybrid main girders.

Pultruded bridge decks distribute and transmit the traffic loads to the main girders. The deck's structural performance as a slab and its orthotropy ratio are influenced by the contribution of the transverse-to-pultrusion direction to carrying applied concentrated loads. The deck's response to concentrated loading is influenced by the applied wearing surface and its failure mode governed by local effects.¹⁷ Park et al.¹⁶ conducted bending tests in the transverse-to-pultrusion direction of a bridge deck with rectangular cell cross section; contrary to the response in the longitudinal direction, the observed load-displacement behavior was strongly nonlinear and failure was caused by the flexural failure of the web-flange junctions. Analogous findings have been reported for another pultruded GFRP deck with rectangular cells by Zi et al.¹⁸

Additionally, pultruded GFRP decks can participate in transferring loads in the bridge's longitudinal direction, acting as the top chord of the main girders when there is sufficient composite action between the girder and the deck, which is dependent on the shear performance of the deck-to-beam connection. The contribution of the GFRP deck has been proven to be significant in terms of stiffness and strength in GFRP deck-steel/RC beam hybrid members with bonded connections.^{9,19} Furthermore, the participation of GFRP decks as the upper chord of main girders also depends on the shear transmission within the deck itself (from its bottom to its top flange) in the bridge's longitudinal direction, i.e., the deck's transverse direction. The level of composite action within the deck depends on its transverse in-plane shear stiffness and load transfer mechanisms, both related to the core configuration. Experimental research conducted on composite beams with pultruded GFRP

decks has shown that a triangular cell core is able to provide almost full composite action between the deck flanges²⁰ while a trapezoidal/rectangular cross-sectional geometry only enables partial contribution of the deck's upper flange.^{21,22} The transverse in-plane shear behavior of the deck has also been found to influence a more/less ductile response of the hybrid beams (the trapezoidal core, with nonlinear in-plane shear stiffness, enhanced the ductility of the hybrid beam system by local failures in the deck, occurring during the yielding of the steel girder).⁹ Transverse in-plane shear modulus values for pultruded GFRP deck systems have been experimentally obtained via in-plane shear tests and included in analytical equations for composite girders, assimilating the core to a flexible shear connection and abstracting from its actual geometry.⁹ Nevertheless, the aforementioned experimental approach is restricted to the deck's behavior as the upper chord of composite beams but not adapted to evaluate its performance as a slab, as global bending effects in the deck are not considered.

The objective of this work was to experimentally investigate the effect of the core geometry on the system transverse in-plane shear stiffness of pultruded GFRP decks and to understand the locally occurring load distribution and failure mechanisms – in order to establish a basis for the evaluation of (i) the bi-directional behavior of decks (effective width) and (ii) the composite action behavior of hybrid beams. To achieve this objective, three-point bending experiments were conducted on deck specimens transverse to the pultrusion direction. Stiffness, strength, failure modes and load transfer mechanisms were investigated. Lastly, the experimental results were analyzed to obtain the transverse in-plane shear moduli of both systems.

2.2 Pultruded GFRP bridge deck systems

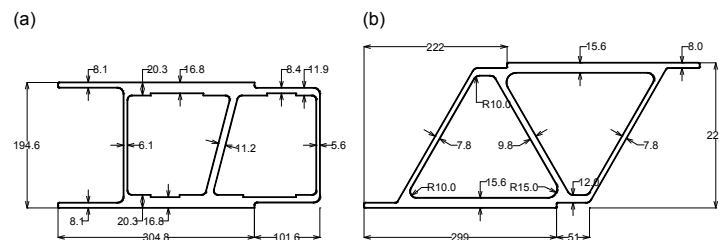
2.2.1 Description of system geometry

Two pultruded GFRP bridge deck systems with different transverse cross sections were investigated: DuraSpan (DS) and Asset (AS).

The DS unit module profile cross-sectional geometry comprises two trapezoidal cells formed by vertical and slightly inclined webs connected to the deck's flanges. The adjacent unit module profiles are bonded along their vertical webs. A tongue-and-groove connection between panels is provided by lip extensions and steps in the deck's flanges. Detailed dimensions of the DS unit shape are shown in Figure 2.1(a).

The cross section of the AS unit profile consists of a parallelogram with an inner diagonal which creates two triangular cells. Dual-cell profiles are bonded to the adjacent ones along their outer diagonals. Lip extensions are provided

Figure 2.1 – Unit module geometry of (a) DS and (b) AS specimens; dimensions in mm.



in the flanges in two of the profile corners and grooves in the two opposite ones in order to facilitate the bonded profile-to-profile connection. The unit shape geometry is depicted in Figure 2.1(b).

2.2.2 Material properties

The DS and AS decks are composed of E-glass fibers embedded in an isophthalic polyester resin. The fiber architecture of the DS laminates consists of a sequence which alternates unidirectional roving, multi-ply structural fabrics and additional non-structural mats. The AS laminates comprise a core of unidirectional roving in between multi- and/or cross-ply structural fabrics on each side; additional mats are used for the unit shape outer layer. The typical fiber architectures of the laminates from both deck types are shown in Figure 2.2. The in-plane material properties for the flanges, webs and/or diagonal elements are given in Table 2.1. Table 2.2 lists the properties of the adhesives employed for the profile-to-profile joints.

Figure 2.2 – Typical fiber architecture of laminates from (a) DS and (b) AS specimens.

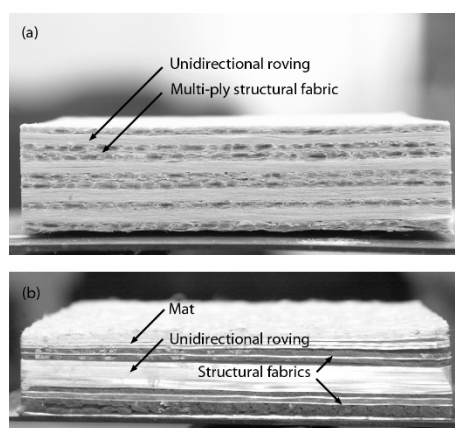


Table 2.1 – Material properties of DS and AS unit modules.

Deck type	Element	Longitudinal elastic modulus E_x (MPa)	Transverse elastic modulus E_y (MPa)
DS	Flanges	21 240 ^(a)	11 790 ^(a) [12 980 ^(c)]
	Vertical (bonded) webs	17 380 ^(a)	9 650 ^(a) [14 910 ^(c)]
	Inclined (single) webs	17 380 ^(a)	9 650 ^(a) [16 350 ^(c)]
AS	Flanges	27 000 ^(b)	19 000 ^(b)
	Outer (bonded) diagonals	20 000 ^(b)	23 000 ^(b)
	Inner (single) diagonals	17 000 ^(b)	26 000 ^(b)

x = pultrusion direction, y = perpendicular to pultrusion direction, in-plane

^(a) Data reported by Gürtler.⁹

^(b) Data reported by Sebastian et al.¹⁹

^(c) Own values, experimentally obtained for 0-0.20% strain range

Table 2.2 – Adhesive properties of DS and AS deck systems.

Deck type	Adhesive type	Elastic modulus E (MPa)	Poisson's ratio ν (-)
DS	Polyurethane	388 ^(a)	0.40 ^(c)
AS	Epoxy	9 800 ^(b)	0.35 ^(b)

^(a) Data reported by Gürtler.⁹

^(b) Data reported by Sebastian et al.¹⁹

^(c) Data reported by manufacturer.²⁶

2.3 Experimental program

2.3.1 Specimen dimensions and manufacture

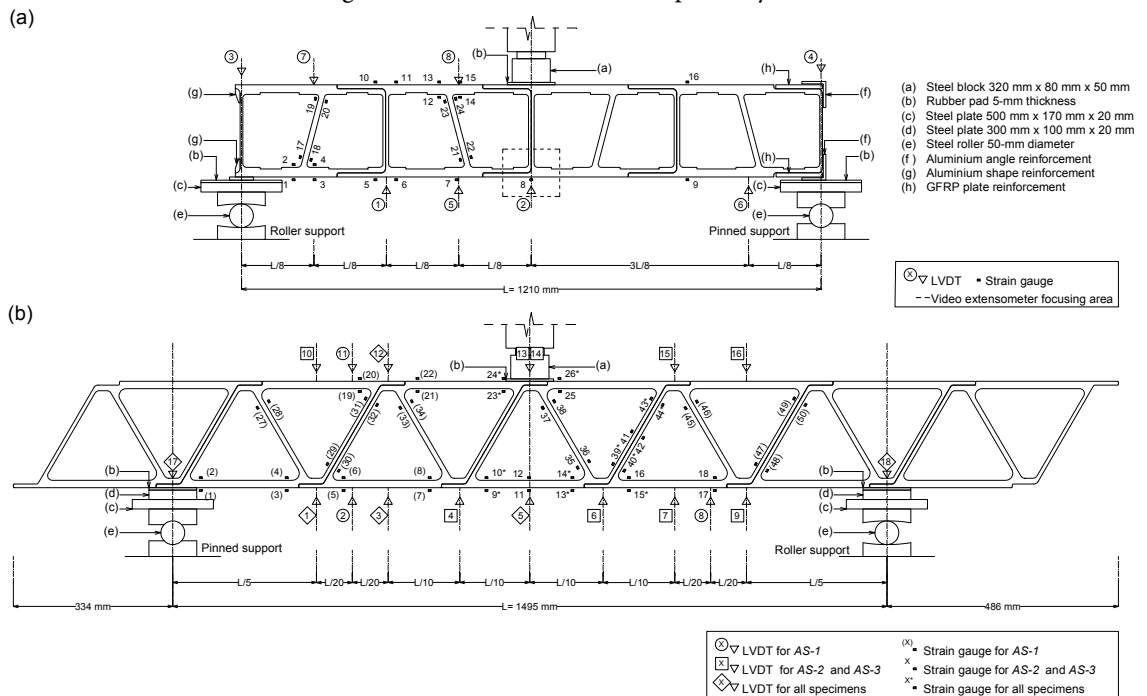
The experimental program was conducted on three beams from each deck design. Specimens were labeled *DS-1*, *DS-2*, *DS-3* and *AS-1*, *AS-2*, *AS-3* for the *DS* and the *AS* series, respectively.

A 3500-mm-long deck panel composed of four *DS* unit module profiles had been provided for a previous investigation.²³ The dual-cell shapes were bonded using a structural polyurethane adhesive. Three 200-mm-wide specimens were cut from the aforementioned panel perpendicularly to its pultrusion direction. The transverse cross section of each *DS* specimen therefore comprised eight cells, see Figure 2.3(a). The *DS* specimens' global length and height were 1230 and 194.6 mm, respectively.

The *DS* specimens did not exhibit constant height at one end due to steps in the flanges intended for the tongue-and-groove profile-to-profile connection. Additional GFRP plates were bonded in those areas to prevent premature failure in the support location. Moreover, the *DS* specimens' outer vertical webs – simple webs – exhibited a smaller thickness than their inner vertical webs – double-bonded webs – due to the absence of contiguous profiles to complete the specimens' ends. Aluminum reinforcements were bonded in the top and bottom edges of the external webs to prevent premature local failures.

The *AS* specimens were produced by the deck's manufacturer. Each *AS* specimen was fabricated by adhesively bonding seven single profile units of 200-mm length – the specimens' width – with a structural two-component epoxy adhesive. The *AS* specimens' transverse cross section therefore consisted of fourteen triangular cells, see Figure 2.3(b). Their global length and height were 2315 and 225 mm, respectively.

Figure 2.3 – Experimental set-up for (a) *DS* and (b) *AS* beams.



2.3.2 Set-up and load equipment

Both the *DS* and *AS* beams were loaded in a three-point bending configuration. The experimental set-ups of the *DS* and *AS* series are depicted in Figure 2.3. The *DS* specimens were simply supported on their edges with the supports' axis vertically coinciding with the outer webs' middle plane. Each support consisted of a 50-mm-diameter steel roller located between two steel plates. Rotation and horizontal displacement were permitted in the left support whereas only rotation was permitted in the right one. Steel plates and 5-mm-thick rubber pads were placed below the specimens' bottom face. The clear span length L was 1210 mm, which corresponds to a span-to-depth ratio of 6.2. The concentrated load was applied at mid-span, on the top of the middle vertical web (see Figure 2.3(a)).

The *AS* specimens were simply supported with a clear span length L of 1495 mm (span-to-depth ratio of 6.6). The supports were placed under the joints between the 1st/2nd and 6th/7th specimens' unit shapes. Support fixtures from the *DS* series were used. The left support only allowed rotation while the right support allowed both rotation and horizontal displacement. A concentrated load was applied to the specimens' top surface at mid-span, coinciding with the joint area between the 3rd/4th profiles (see Figure 2.3(b)).

The concentrated load was applied in both experimental series using a hydraulic jack of 300-kN capacity via a 320-mm x 80-mm x 50-mm steel block to assure uniform pressure distribution across the beams' width. The steel block rested on a 5-mm-thick hard rubber pad placed on the specimens' top surface.

2.3.3 Instrumentation and measurements

Specimens were equipped with linear vertical displacement transducers (LVDTs) and 120- Ω -resistance/6-mm-length electrical strain gages to measure vertical deflections and axial strains along their length (parallel to span), respectively. Strain gages were placed both on flanges and webs elements. Pairs of gages were mounted on several sections – one gage on each side – to allow the decoupling of local axial from local flexural effects. Deflection and strain data were automatically recorded at regular intervals by an HBM UPM 60 data acquisition system connected to a computer. A data acquisition program allowed the evolution of the recorded data to be followed on the computer screen during the experiments.

The instrumentation of the *DS* series is detailed in Figure 2.3(a). The *DS* specimens were instrumented with eight LVDT and 24 strain gages. Deflections were measured in the specimens' centerline. The strain gages were also positioned on the specimen's centerline in *DS-1* and 50 mm away from it in *DS-2* and *DS-3*. In the latter specimens, the location of the strain gages offset from the centerline facilitated their installation in the cells and thus assured their alignment. A video extensometer was used for experiments on *DS-2* and *DS-3* to study the behavior of the adhesively-bonded joints. Its measurement region focused on the bottom part – web-flange junction – of the profile-to-profile connection between the 2nd/3rd specimens' unit shapes (see Figure 2.3(a)). The arrangement of the LVDTs and strain gages for the *AS*

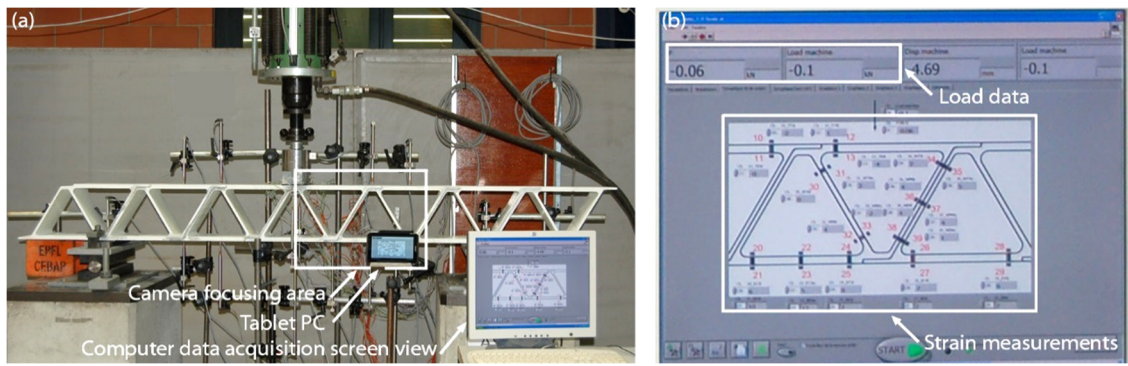


Figure 2.4 – Instrumentation system for correlation of images and recorded data in AS beams; (a) general view; (b) data acquisition screen view on computer, shown on tablet PC screen by means of web publishing tool.

series is shown in Figure 2.3(b). AS-1/AS-2/AS-3 were instrumented with 9/15/15 LVDTs to measure the vertical deflection of the specimens along the span on their top and bottom sides. 38/24/24 strain gages, mounted in pairs – one on each side of the instrumented section – were used in AS-1/AS-2/AS-3. LVDTs and strain gages – except LVDT-13 and -14 (see Figure 2.3(b)) – were located on the specimens' centerline. Instrumentation of AS-2 and AS-3 included a digital camera whose position was fixed during the experiments and which focused on the expected failure area (see Figure 2.4(a)). A remote-controlled software was used for automatically capturing and saving images at a frequency of 0.5 Hz. A tablet PC was located in the camera focusing area and therefore appeared in the pictures. A web publishing tool was used to synchronize the information shown on the screen of the tablet PC with the screen view of the computer connected to the data acquisition system. As a result, correlation between images and recorded data was possible. The system is illustrated in Figure 2.4. Targets were installed in the specimens' bottom flange to monitor the horizontal distance between the vertical axis passing through 13-14 and 15-16 strain gage pairs (see Figure 2.3(b)) throughout the experiments by means of this system.

2.3.4 Experimental procedure

All experiments were performed under displacement control up to failure. The loading rate was 0.05 mm/s for the DS specimens. AS-1/AS-2/AS-3 were loaded at a rate of 0.010/0.005/0.005 mm/s, respectively. Three loading-unloading cycles were conducted in both series prior to failure. Maximum loads for the 1st/2nd/3rd cycles were 3/6/10 kN (3/6/11.5 kN) for the DS-1, DS-2 (DS-3) specimens and 10/10/15 kN for the AS specimens. During DS-2, DS-3 and AS-1 experiments the cracks' appearance was sketched on the specimens' front surface based on visual observation.

2.4 Experimental results and discussion

2.4.1 DS deck

Load-deflection response

The load-deflection responses at mid-span (δ_2) and quarter-span (δ_1) measured for the DS beams, in their bottom face, are shown in Figure 2.5(a). Deflection data were measured in specimen DS-1 up to a 7-kN load, when

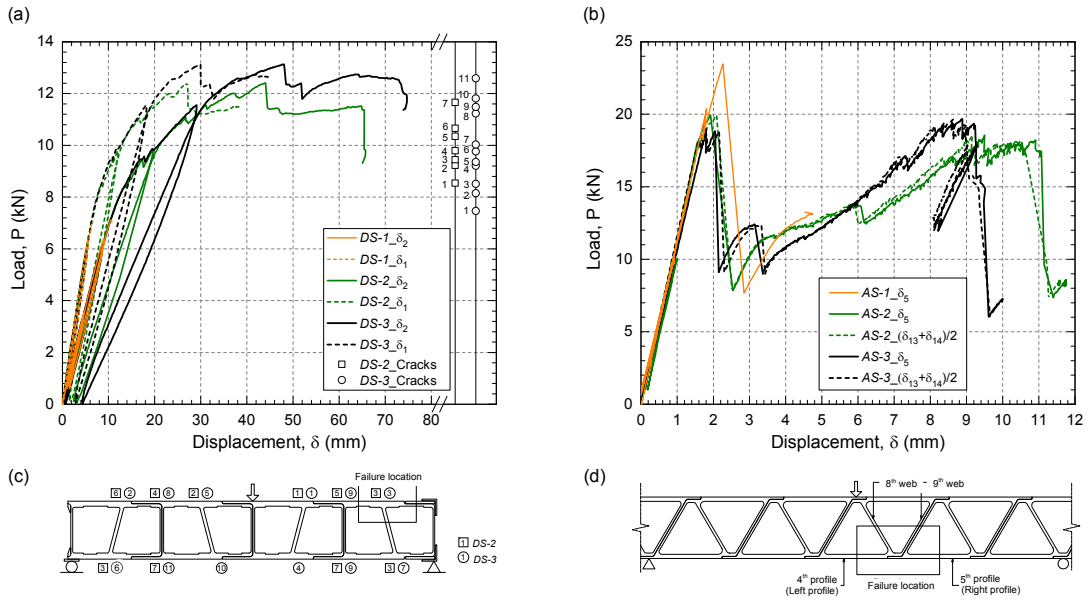


Figure 2.5 – Load-deflection behavior of (a) DS beams; (b) AS beams; (c) crack sequence in DS-2 and DS-3; (d) failure location in AS beams.

LVDT-1 and -2 were removed; deflections in specimens DS-2 and DS-3 were recorded up to failure. The three beams exhibited linear elastic behavior up to a load of approximately 7 kN, when the first audible cracks were heard in the 3rd cycles. No changes in stiffness were observed in the loading-unloading cycles performed prior to reaching that load. The initially linear response turned to nonlinear and the stiffness decreased. Progressive delamination cracking was meanwhile detected in the web-flange junctions without causing the specimens' final failure. The sequence of observed cracks in specimens DS-2 and DS-3, their location and the associated load levels are indicated in Figure 2.5(a), on the right side, and Figure 2.5(c). The cracks observed at the ends of the inclined webs preceded those observed in the vertical webs, except the cracks observed in sixth and tenth place for specimens DS-2 and DS-3, respectively. In the inclined webs, cracks were generally noticed first in their top part and then in their bottom part. Exceptions were attributed to the limitations of the crack recording procedure based on visual observation.

The initial apparent bending stiffness (EI_{app}) of the DS beams, which includes deformations related to frame behavior of the flange and web elements (subjected to shear, bending and axial forces), and local deformations in the adhesively-bonded joints, was derived from the experimental deflection data throughout the specimens' linear behavior range, before any crack was noticed, by: (i) conducting a linear regression analysis

Table 2.3 – Calculated apparent bending stiffness of DS beams.

Specimen	Reference deflection	Apparent bending stiffness EI_{app} ($\times 10^{10}$ Nmm ²)	$EI_{app} / EI_{nom,full}$ (%)
DS-1	δ_2	2.69	3.6
	δ_1	2.99	4.0
DS-2	δ_2	2.67	3.6
	δ_1	3.00	4.0
DS-3	δ_2	2.69	3.6
	δ_1	2.98	4.0

on the measured load-deflection responses; (ii) conjointly using the thus calculated load-deflection relationships and corresponding deflection equations of the beam axis from the classical beam theory to evaluate EI_{app} . The bottom face deflections at mid-span (δ_2) and quarter-span (δ_1) were used separately in the calculations. The calculated EI_{app} values for the *DS* specimens are listed in Table 2.3.

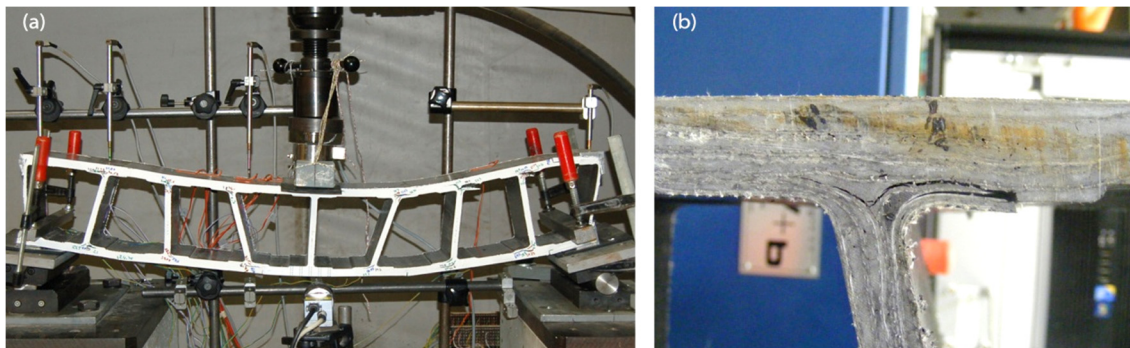
Failure mode

Failure, defined as the inability of the specimen to bear any further load increase, occurred at 12.9/12.4/13.1 kN in specimens *DS-1/DS-2/DS-3*, respectively. Noticeable load drops and the development of large displacements were subsequently recorded, see Figure 2.5(a). A general view of the failed specimens' deformed shape is shown in Figure 2.6(a).

The *DS* beams' failures were governed by local failures in the web-flange junctions. Failure of specimens *DS-1* and *DS-2* occurred due to the propagation of previously formed cracks and subsequent local failure in the top junction of the inclined 8th web, see Figure 2.5(c). In-plane delamination cracks in the top flange, in the 8th web's right side, had appeared during the specimens' nonlinear behavior range due to through-thickness tension caused by Vierendeel action and exceeding the rather low through-thickness tensile strength of the laminate. Cracks progressed towards the flanges' bottom face and caused the webs, on their right side, to separate from the flange (see Figure 2.6(b)). The load decreased from 12.9 to 11.7 kN – 9% – and from 12.4 to 11.5 kN – 7% – for *DS-1* and *DS-2*, respectively. The failure pattern was influenced by the fiber architecture – multi-ply fabrics from the webs were prolonged towards the flanges, whose thickness is consequently greater close to web junctions; the crack opening in the flanges coincided with the interruption of these continuous fabrics.

Specimen *DS-3* failed due to local bending failures in the reinforced outer webs. Significant bending deformation was observed in the outer webs – with reduced thickness – close to the failure load level, see Figure 2.6(a). Nevertheless, specimen *DS-3* showed the highest load capacity of the *DS* series. Two consecutive load drops (from the maximum 13.1-kN load to 12.4 kN – 5% – and from 12.4 to 11.8 kN – 5% –) resulted from local failures in the 9th and 1st webs' bottom part, respectively. A subsequent load peak of 12.7 kN – 97% of the maximum load – was reached before a third local failure, exhibiting the same location and pattern as those exhibited in *DS-1* and *DS-2*, was produced.

Figure 2.6 – Failure pattern of *DS* beams; (a) deformed shape of specimen *DS-3*; (b) local failure of specimen *DS-1* (8th web-top flange junction).



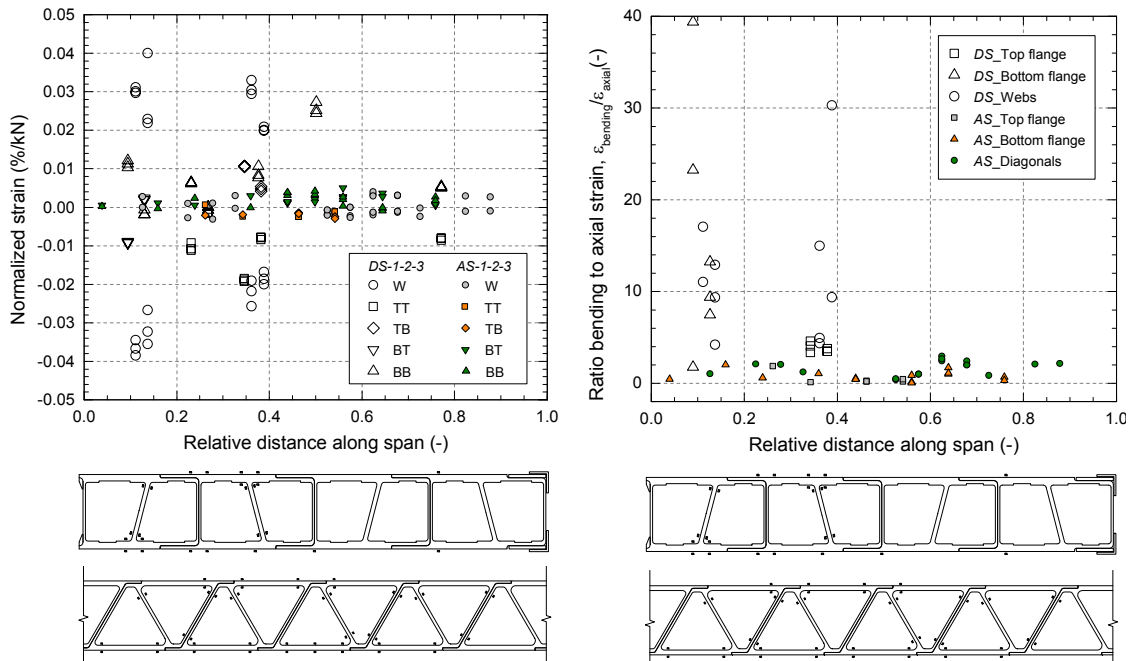
Strain distribution and load transfer mechanism

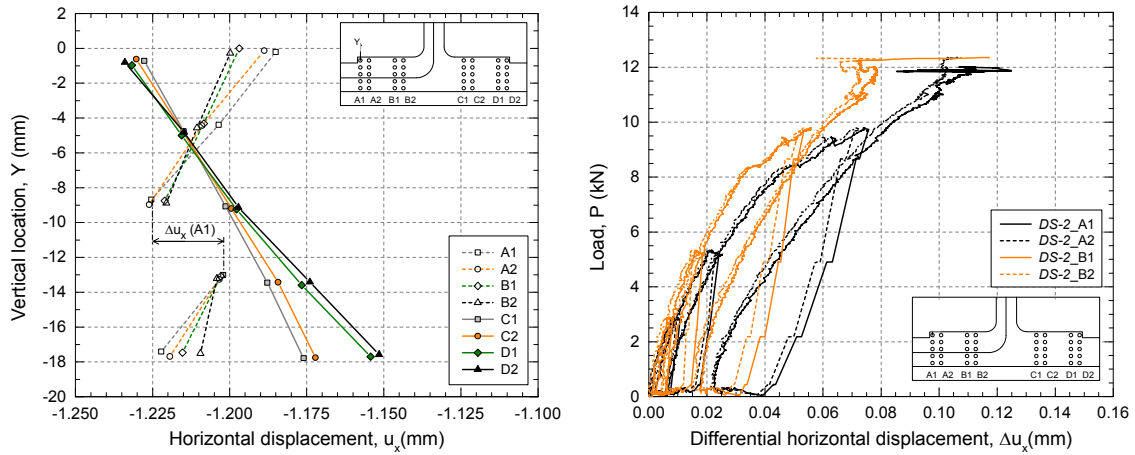
The normalized values (strain per unit load) of measured strains in the DS beams during their initial linear behavior are shown in Figure 2.7. No influence of the strain gages' location along (DS-1) or offset (DS-2 and DS-3) from the specimen's centerline on the recorded strains was observed. Comparison of strains in web-flange junctions where strains were recorded in all elements – 2nd web bottom junction and 4th web top junction – showed that significantly higher strains developed in the webs than in the flanges. The magnitude of the maximum normalized strain measured in the flanges in the bottom junction of the 2nd web / top junction of the 4th web was 30–37% / 61–86% of the values measured from gages installed on the webs.

Figure 2.7 shows that positive and negative strain values appeared in both the top and bottom flanges of the beams and in the two instrumented webs. Differences in strain data from gages mounted on the same section but opposite surfaces (ϵ_i, ϵ_j) were found. This showed that, in addition to compression (top flange, 2nd web) and tension (bottom flange, 4th web) axial forces related to truss action, local bending moments and shear forces appeared in the elements. Strains due to local flexural effects, $\epsilon_{bending}$, related to the difference between the (ϵ_i, ϵ_j) values, were significantly higher than strains due to axial forces, ϵ_{axial} , linked to the (ϵ_i, ϵ_j) average value, in the flanges as well as in the webs. This showed that the transfer of forces in the DS beams is governed by the frame mechanism (Vierendeel action), with the load transmitted from mid-span to the supports by local bending moment and shear forces in the elements. The calculated $\epsilon_{bending}/\epsilon_{axial}$ ratios are given in Figure 2.8. $\epsilon_{bending}/\epsilon_{axial}$ ranged from 1.8 to 39.4 in the flanges and from 4.2 to 30.3 in the webs for the measured locations. The considerably higher $\epsilon_{bending}/\epsilon_{axial}$ values observed in the bottom flange than in the top flange were attributed to the position of the measured locations along the span – regarding

< Figure 2.7 – Measured normalized strains in webs (W) and flanges (TT= top, top face; TB= top, bottom face; BT= bottom, top face; BB= bottom, bottom face) along span throughout beams' linear behavior range.

> Figure 2.8 – Measured ratios of local bending strain to local axial strain in webs and flanges throughout beams' linear behavior range.





< Figure 2.9 – Horizontal displacement across bottom flange at mid-span at 6-kN load in specimen *DS-2*.

> Figure 2.10 – Load- Δu_x behavior of adhesively-bonded joint in bottom flange at mid-span in specimen *DS-2*.

truss action, lower ε_{axial} were expected in the $\varepsilon_1 - \varepsilon_2$ and $\varepsilon_3 - \varepsilon_4$ pairs than in the $\varepsilon_{12} - \varepsilon_{13}$ and $\varepsilon_{14} - \varepsilon_{15}$ pairs owing to their closer location to supports.

Adhesively-bonded joint behavior

Figure 2.9 shows the horizontal displacements measured across the flange thickness in the 5th web – middle web – bottom junction of specimen *DS-2* at a 6-kN load. In the left part of the junction, the flange element comprised the adhesively-bonded joint between the 2nd/3rd unit module profiles of the specimen.

Horizontal displacements across the flange thickness were almost linearly distributed on the right side of the junction, see C1, C2, D1 and D2 in Figure 2.9. On the left side, however, a discontinuity between targets from the 3rd/4th rows was detected, showing that slip through the adhesive occurred in the profile-to-profile joints, see A1, A2, B1 and B2 in Figure 2.9. The measured differential horizontal displacement between targets from the 3rd/4th rows, Δu_x , is shown in Figure 2.10. A nonlinear load- Δu_x relationship was observed. *DS-3* exhibited analogous behavior.

2.4.2 AS deck

Load-deflection response

The load-deflection plots at mid-span recorded for the AS beams in their top (δ_{13} , δ_{14}) and bottom (δ_5) faces are shown in Figure 2.5(b). The three beams exhibited almost linear elastic behavior until first failure occurred abruptly. No stiffness changes were detected in the loading-unloading cycles conducted before failure.

The initial EI_{app} of the AS beams was calculated from the experimental deflection results as for the *DS* series. The bottom face deflection (δ_5) and average top face deflection (δ_{13} , δ_{14}) at mid-span were used separately in the calculations. The obtained EI_{app} values are given in Table 2.4.

Table 2.4 – Calculated apparent bending stiffness of AS beams.

Specimen	Reference deflection	Apparent bending stiffness	$EI_{app} / EI_{nom,full}$ (%)
		EI_{app} ($\times 10^{10}$ Nmm ²)	
AS-1	δ_5	75.2	57.8
AS-2	δ_{13}, δ_{14}	77.3	59.4
	δ_5	77.3	59.4
AS-3	δ_{13}, δ_{14}	80.8	62.1
	δ_5	73.8	56.7

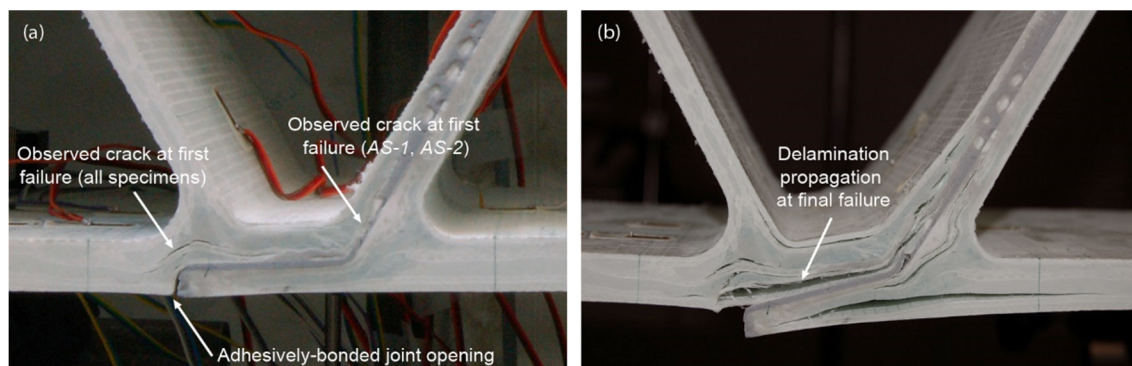
Failure mode

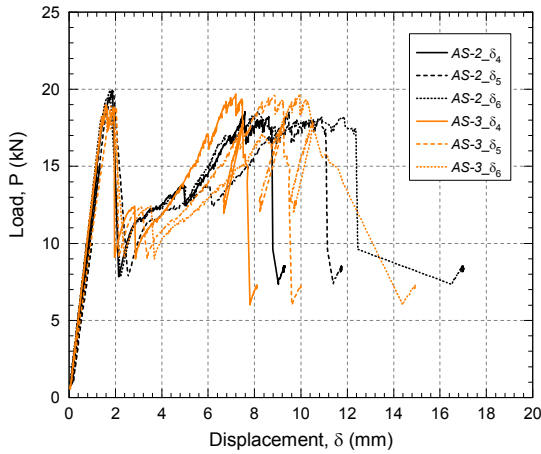
The AS-1, AS-2 and AS-3 beams exhibited a sudden first failure at 23.5, 20.0 and 18.8-kN loads, respectively. The opening of the adhesively-bonded joint in the bottom flange between the 4th/5th profiles and a crack perpendicular to the 8th web in its bottom part (see Figure 2.5(d)) were observed at that point for all specimens, see Figure 2.11(a). A crack parallel to the 9th web in its bottom part, 4th profile, was also observed in specimens AS-1 and AS-2, see Figure 2.11(a). Load decreases of 67/61/52% were recorded for AS-1/AS-2/AS-3 after the first failure.

Subsequently, all specimens were able to bear an increasing load, however with initial stiffness reductions of between 80 and 85%. Subsequent peaks of 20.8/18.6/19.7-kN loads for AS-1/AS-2/AS-3 were reached, see Figure 2.5(b). The appearance and development of other cracks in the damaged webs-flange junction area had meanwhile been observed before final failure took place abruptly. All the beams showed a similar failure pattern with delamination propagating parallel to the adhesively-bonded joint between the 4th/5th profiles above and on the left side of the outer mat layer of the left profile, see Figure 2.11(b). The delamination initiation was caused by through-thickness tensile stresses resulting from the local bending moments of the elements due to their end partial restraint to rotation at the junctions. The profile-to-profile bond exhibited superior through-thickness strength than the internal mat-resin bond strength of the GFRP laminate.

Asymmetric deflection behavior near mid-span was detected as from the first failure in AS-3 and close to final failure in AS-2 due to the opening of the adhesively-bonded joint. Higher deflections developed at $0.6 L$ (specimens' right side (δ_6)) than at $0.5 L$ (δ_5), followed by the left side deflection at $0.4 L$ (δ_4), see Figure 2.12.

Figure 2.11 – Failure pattern of specimen AS-2; (a) first failure; (b) final failure.

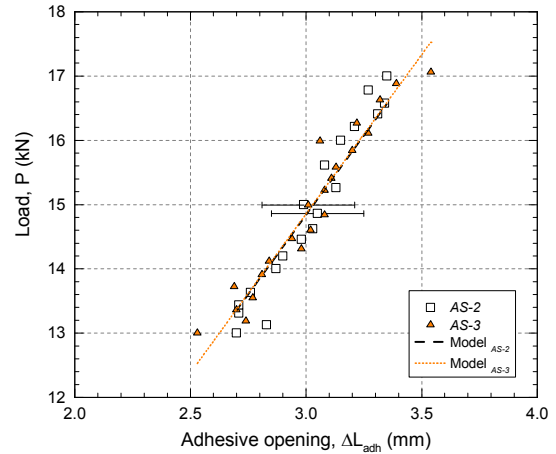




< Figure 2.12 – Load-deflection behavior of AS beams at $0.4 L$ (δ_4), $0.5 L$ (δ_5) and $0.6 L$ (δ_6).

> Figure 2.13 – Opening of adhesively-bonded joint after first failure of AS-2 and AS-3.*

*Note: uncertainty of ΔL_{adh} experimental data is constant and of ± 0.2 mm.

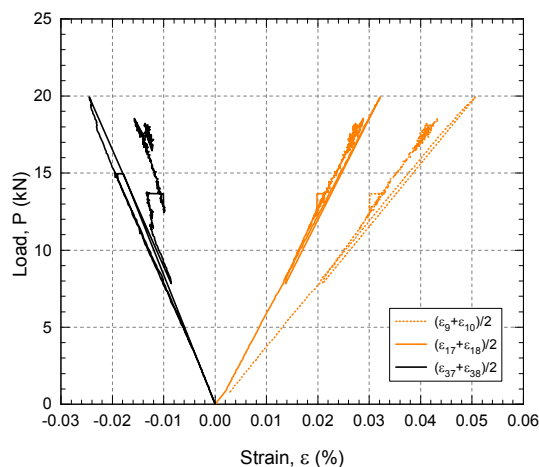


The opening of the adhesively-bonded joint resulted in an additional axial deformation in the corresponding bottom flange section. It can be modeled as a spring whose axial stiffness equals the ratio between the acting axial force and the opening length, ΔL_{adh} . The ratio of the applied load, P , to ΔL_{adh} between first failure and final failure was calculated. Optic measurements from the camera-tablet PC system – targets placed in the vertical axis passing through 13-14 and 15-16 strain gage pairs – in the 13-17-kN load range were used. Constant $P/\Delta L_{adh}$ was assumed. The $P/\Delta L_{adh}$ value obtained performing linear regression on the $P-\Delta L_{adh}$ data was 4950 ± 350 N/mm ($R^2 = 0.93$) for both specimens AS-2 and AS-3, see Figure 2.13.

Strain distribution and load transfer mechanism

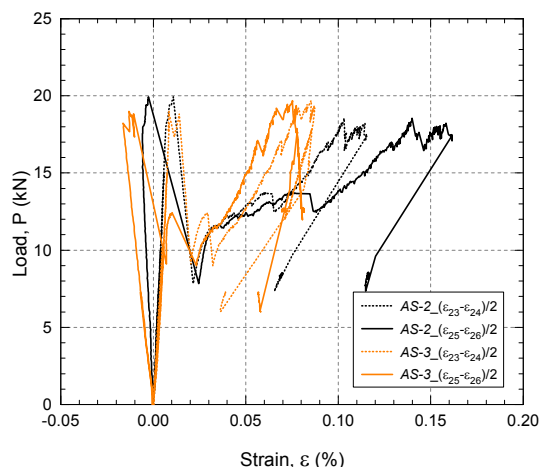
The strains per unit load measured in the AS specimens during their initial linear range, before first failure was produced, are illustrated in Figure 2.7. Figure 2.7 shows that mainly positive strain values were recorded in the bottom flange and in the single (inner) / bonded (outer) diagonals of the beams' left/right sides, while predominantly negative strain values were recorded in the top flange and the bonded/single diagonals of the beams' left/right side.

Absolute normalized strains in the flanges increased from the supports towards mid-span; on the other hand, comparable values were measured in the bonded or single diagonals in the left and right sides of the beams, independently of their location along the span (see Figure 2.7). Figure 2.7 shows that the truss mechanism – with increasing tension/compression axial forces in the flanges towards mid-span and alternatively tensioned/compressed diagonals, with constant axial force – dominated the AS beams' transverse behavior. However, strain measurements showed that local bending moments and shear forces appeared both in the flanges and the diagonals. Figure 2.8 shows the calculated $\varepsilon_{bending}/\varepsilon_{axial}$ values, before first failure occurred, for the instrumented locations. They ranged from 0.0 to 2.0, from 0.4 to 1.2 and from 2.0 to 3.0 in the flanges, single diagonals and bonded diagonals, respectively. Slip through the adhesive layer between pairs of gages could however have influenced this decoupling of strains in the bonded diagonals.



< Figure 2.14 – Load-strain behavior of specimen AS-2 near failure location.

> Figure 2.15 – Load-strain behavior in top flange of AS beams at mid-span.



The load transfer mechanism did not seem to change significantly after first failure. Figure 2.14 shows the average strains, $(\varepsilon_i + \varepsilon_j)/2$ (related to the axial forces), measured in several pairs of gages ($\varepsilon_i, \varepsilon_j$) mounted on diagonal/bottom flange elements connected to the failure joint in the AS-2 specimen. The slope of the load-strain plots measured in the bottom flange ($(\varepsilon_9 + \varepsilon_{10})/2$ and $(\varepsilon_{17} + \varepsilon_{18})/2$) did not exhibit any significant changes before and after first failure was recorded. This showed that the axial forces per unit load borne by the pertinent elements were hardly influenced by the first failure. A decrease in the compression force per unit load borne by the 8th web, see $(\varepsilon_{37} + \varepsilon_{38})/2$ in Figure 2.14, was however observed. On the other hand, a redistribution of local bending moments was noticed after first failure. Figure 2.15 shows the strain differences $(\varepsilon_{23} - \varepsilon_{24})/2$ and $(\varepsilon_{25} - \varepsilon_{26})/2$ (related to the local bending moment) measured in two locations and on opposite sides of the top flange near to the load application point. Sign changes in $(\varepsilon_{25} - \varepsilon_{26})/2$ – from negative to positive – and significant increases of $(\varepsilon_{23} - \varepsilon_{24})/2$ and $(\varepsilon_{25} - \varepsilon_{26})/2$ – therefore of the local bending moment in the pertinent sections – were detected. The latter showed that after first failure more load was transferred from mid-span towards the supports by local shear forces in the top flange. This is in agreement with the aforementioned decrease in the compression force borne by the 8th web.

2.4.3 Comparison of experimental results

Deflection, apparent transverse bending stiffness and failure load

The DS beams exhibited non-linear behavior with an elastic limit at approximately 55% of their failure load. The AS beams exhibited linear elastic behavior up to failure. The calculated initial EI_{app} values, which included the influence of the load arrangement and span length, were significantly higher (24 to 30 times) for the AS deck system than for the DS system, see Tables 2.3 and 2.4. The higher EI_{app} in the AS series than in the DS series was mainly attributed to the influence of the core geometry – triangular vs. trapezoidal. A 19% higher lever arm between the flanges (see Figure 2.1) and a 46–61% higher transverse elastic modulus in the flange laminates (see Table 2.1) in the AS beams than in the DS beams also contributed.

The EI_{app} to $EI_{nom,full}$ ratio isolates the effect of the core geometry in the apparent transverse stiffness of the deck systems. $EI_{nom,full}$ represents the nominal bending stiffness of the 200-mm-wide DS and AS beams, assuming full composite action between the deck flanges. The $EI_{nom,full}$ values obtained for the DS and AS beams were $7.49 \cdot 10^{11}$ Nmm² and $13.02 \cdot 10^{11}$ Nmm², respectively. The calculated EI_{app} to $EI_{nom,full}$ ratios are shown in Tables 2.3 and 2.4 and confirm the effect of the webs' arrangement on the apparent transverse stiffness of the deck. The DS beams showed a negligible degree (less than 4%) of composite action between both flanges while the $EI_{app}/EI_{nom,full}$ values obtained for the AS beams were approximately 60%. The triangular core geometry (AS) provided a significantly higher degree of composite action between the flanges than the trapezoidal core geometry (DS).

The AS series exhibited 43 to 89% higher failure loads than the DS series in spite of the 19% shorter DS-span. Failure occurred in an abrupt manner in the AS beams, while it was preceded by a large displacement development in the DS beams. This was attributed to a higher system redundancy in the deck with trapezoidal cross section, which exhibited progressive failure in the web-flange junctions.

Load transfer mechanism

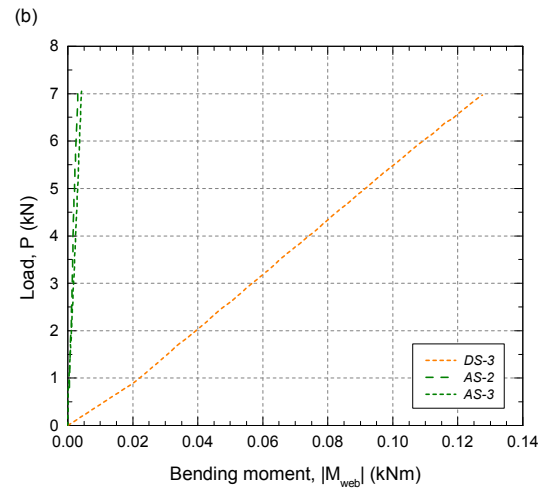
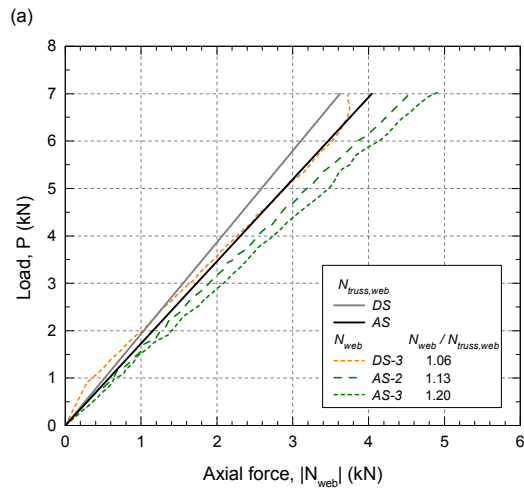
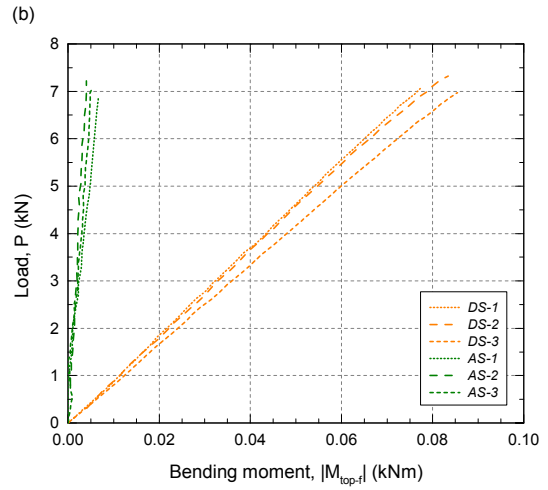
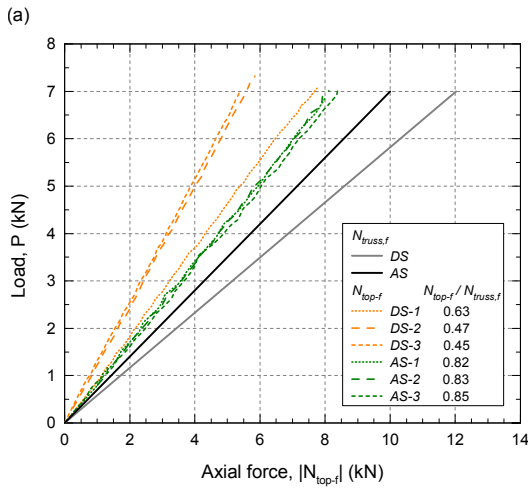
Strain measurements indicated that the transverse-to-pultrusion flexural behavior of the DS beams was frame dominated while it was truss governed in the case of the AS beams. The results of the strain measurements, the geometrical properties of the sections (Figure 2.1) and the material properties listed in Table 2.1 were conjointly used to obtain the axial forces and local bending moments in the decks' face sheets and webs. A symmetric fiber distribution about the mid-depth of the laminates was assumed.

Figures 2.16(a) and 2.17(a) show the magnitude of the resulting axial forces in the top flange (N_{top-f}), near the load application point (14-15 / 23-24 gage pairs for the DS/AS beams), and in the top part of the web/diagonal elements (N_{web}) closest to mid-span (23-24 / 37-38 gage pairs for the DS/AS specimens), respectively, up to a 7-kN load before any local failure was produced. The theoretical axial forces for 100% truss mechanisms (load transferred only by means of axial forces in the elements) are also shown and were determined using Equation (2.1) for the flanges and Equation (2.2) for the webs/diagonals:

$$N_{truss,f} = \frac{M}{h} = \frac{PL}{\beta(h_{deck} - t_f)} \quad (2.1)$$

$$N_{truss,web} = \frac{V}{\sin\alpha} = \frac{P}{2\sin\alpha} \quad (2.2)$$

where M = global bending moment of the beam, V = global shear of the beam, P = applied load, L = span length (see Figure 2.3), h = lever arm, h_{deck} = deck height (see Figure 2.1), t_f = flange thickness (see Figure 2.1), α = angle between the web and the flange elements (75° for the DS series, 60° for the AS series), β = factor to consider the location of the cutting plane – the method of sections



^ Figure 2.16 – Local (a) axial forces and (b) bending moments in top flange.

√ Figure 2.17 – Local (a) axial forces and (b) bending moments in webs/diagonals.*

* Note: values corresponding to DS-1 and DS-2 beams are not shown due to measuring problems detected in gages 23/24 during experiments.

was employed – for the analysis in each case (four for the DS series (at 0.5 L), five for the AS series (at 0.4 L)).

The axial forces in the analyzed locations in the flanges were closer to the axial forces calculated assuming the truss mechanism in the AS series than in the DS series, see Figure 2.16(a). The N_{top-f} to $N_{truss,f}$ ratios, representing the contribution of the truss mechanism, were 63/47/45% and 82/83/85% for specimens DS-1/DS-2/DS-3 and AS-1/AS-2/AS-3, respectively; the N_{web} to $N_{truss,web}$ ratio was approximately 115% in the AS series and approximately 106% in the DS-3 beam for the examined elements (see Figure 2.17(a)). This confirmed that in the AS system the global shear force was nearly equilibrated by the vertical component of the diagonals' axial force and that the global bending moment was mainly borne by axial forces in the flanges (truss mechanism). In the DS system, however, low N_{top-f} to $N_{truss,f}$ ratios suggested that non-negligible local bending moments appeared in the elements in addition to axial forces to equilibrate the global bending moment of the beam – the amount of the global bending moment borne by local bending moments is related to the $(1 - N_{top-f}/N_{truss,f})$ value. Accordingly, considerably higher local bending moments were obtained in the examined flange (M_{top-f}) and web/diagonal (M_{web}) elements for the DS beams than for the AS beams, as shown in Figures 2.16(b) and 2.17(b), respectively.

Systems' transverse in-plane shear moduli

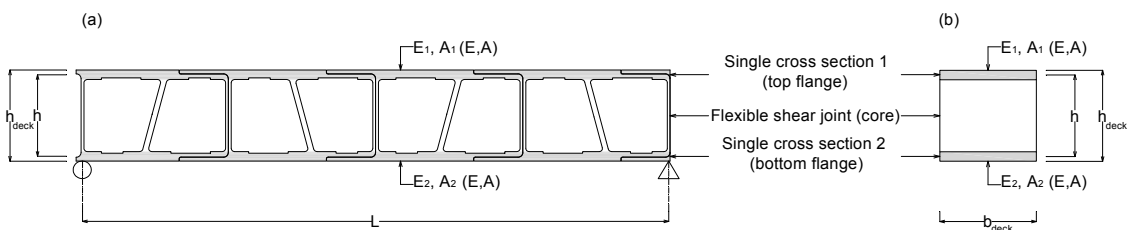
In their transverse direction, GFRP pultruded bridge decks can be modeled as two-component composite beams with a flexible shear connection, see Figure 2.18. The cross section of the GFRP transverse beams is composed of two partial cross sections corresponding to the top – *single cross section 1* – and bottom – *single cross section 2* – flanges of the deck. The core structure of the deck, which connects the upper and lower flanges, can be considered as a flexible shear connection whose shear stiffness (k) can be expressed in terms of the depth (h_{deck}), width (b_{deck}) and system in-plane shear modulus of the deck in its transverse direction (G_{yz}), see Equation (A.6) in Appendix A.

Several design methods exist for composite girders comprising two or more components connected with flexible or partial shear connections. The method developed by Natterer and Hoefl²⁴ for single-span timber-concrete composite beams was employed in this study. It allows the obtaining of the deflections of the beam, the differential displacement of the two partial cross sections and their internal forces under different loading conditions, based on the cross-sectional geometry, the elastic modulus of the components, the in-plane shear stiffness of the connection and the loading configuration. The analytical method to predict deflections is detailed in Appendix A.

The inverse procedure was followed in this study. Experimental load-deflection data, material and geometrical properties were conjointly used with the deflection equations to back calculate the in-plane shear stiffness – hence G_{yz} – of both deck systems, see Appendix A. The bottom face deflections at mid-span (δ_2) and quarter-span (δ_1) were used separately in the calculations for the DS series. The average mid-span deflection (bottom – δ_5 – and top – δ_{13} , δ_{14} – faces) was used for the AS series. The calculated G_{yz} results for the DS specimens, before any crack was noticed, and for the AS beams, before first failure occurred, are shown in Figures 2.19(a) and 2.19(b), respectively. Decreasing G_{yz} values with increasing load in the DS series were attributed to the limitations of the procedure used to record the damage onset based on visual observation. The effect of the flanges' shear deformation, which is not considered in the aforementioned method, has not been eliminated from the deflection data. The given G_{yz} values therefore constitute a lower bound of the actual in-plane shear moduli.

The system in-plane shear modulus of the DS beams (approximately 5.5 to 6 MPa) represented 2–3% of the modulus of the AS beams (approximately 250–280 MPa), which is in accordance with the results discussed in the first part of Section 2.4.3. The AS triangular cell cross-sectional geometry provided

Figure 2.18 – GFRP/GFRP composite beam; (a) elevation; (b) cross section.



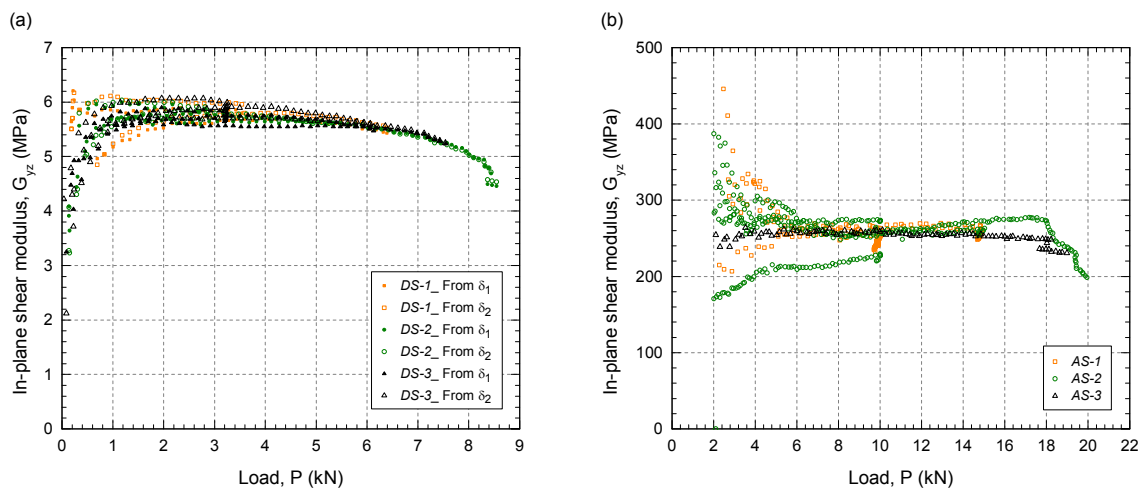


Figure 2.19 – Calculated transverse system in-plane shear modulus for (a) DS series and (b) AS series.

a significant degree of composite action between the bottom and top flanges, while the degree of composite action in the DS beams, with trapezoidal-cell cross section, was considerably lower.

Experimentally determined G_{yz} values of 5/47 MPa for the DS/AS deck system are available in the investigations conducted by Keller and Gürtler.^{20, 21} For the DS series, the calculated system in-plane shear modulus agreed well with experimentally obtained G_{yz} – an approximately 10–20% difference was found. The calculated G_{yz} results for the AS series were five to six times higher than the experimental values reported by Keller and Gürtler.²⁰

2.5 Conclusions

The static transverse behavior of two GFRP pultruded bridge deck systems with different cross-sectional geometry (trapezoidal DS and triangular AS) was experimentally studied. Three beams from each series were investigated under symmetric three-point bending to evaluate their stiffness, strength, failure modes and load transfer mechanisms. The behavior in the transverse-to-pultrusion direction of both deck designs was compared. The following conclusions may be drawn from this work:

1. The DS deck system exhibited initial linear elastic behavior up to approximately 55% of the failure load followed by nonlinear behavior. The latter was caused by progressive cracking in the web-flange junctions prior to final failure. The AS deck system exhibited linear elastic behavior up to first failure, which occurred abruptly. Subsequently, comparable peak loads were achieved with decreased stiffness.
2. Load transfer mechanisms in the transverse direction differed in the DS and AS specimens and depended on their cross-sectional geometry. Frame behavior was more dominant in the DS system (trapezoidal cells) than in the AS system (triangular cells), which was truss governed.
3. The DS deck system exhibited a significantly lower apparent bending stiffness in its transverse direction than the AS deck system (24 to 30 times less) owing to the considerably lower in-plane shear stiffness – therefore lower

degree of composite action between the flanges – provided by the trapezoidal (*DS*) compared to the triangular (*AS*) core geometry.

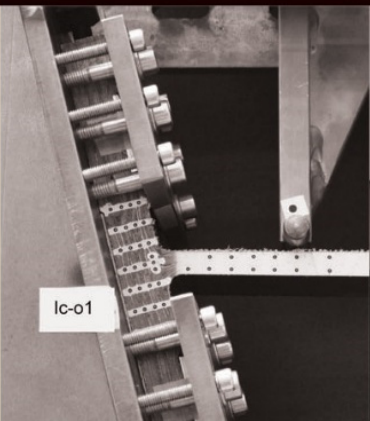
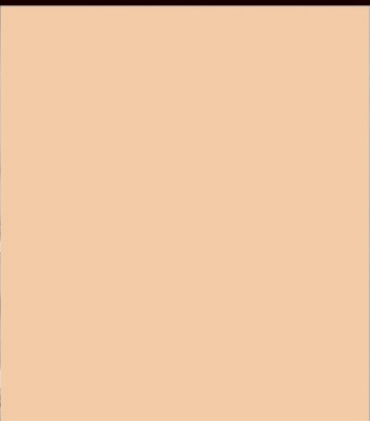
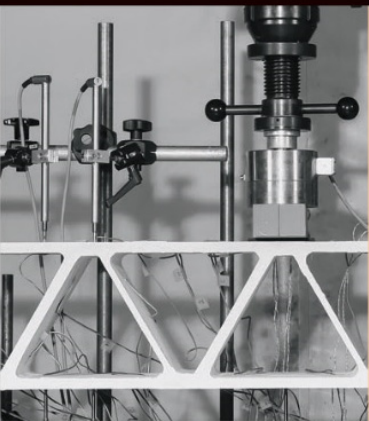
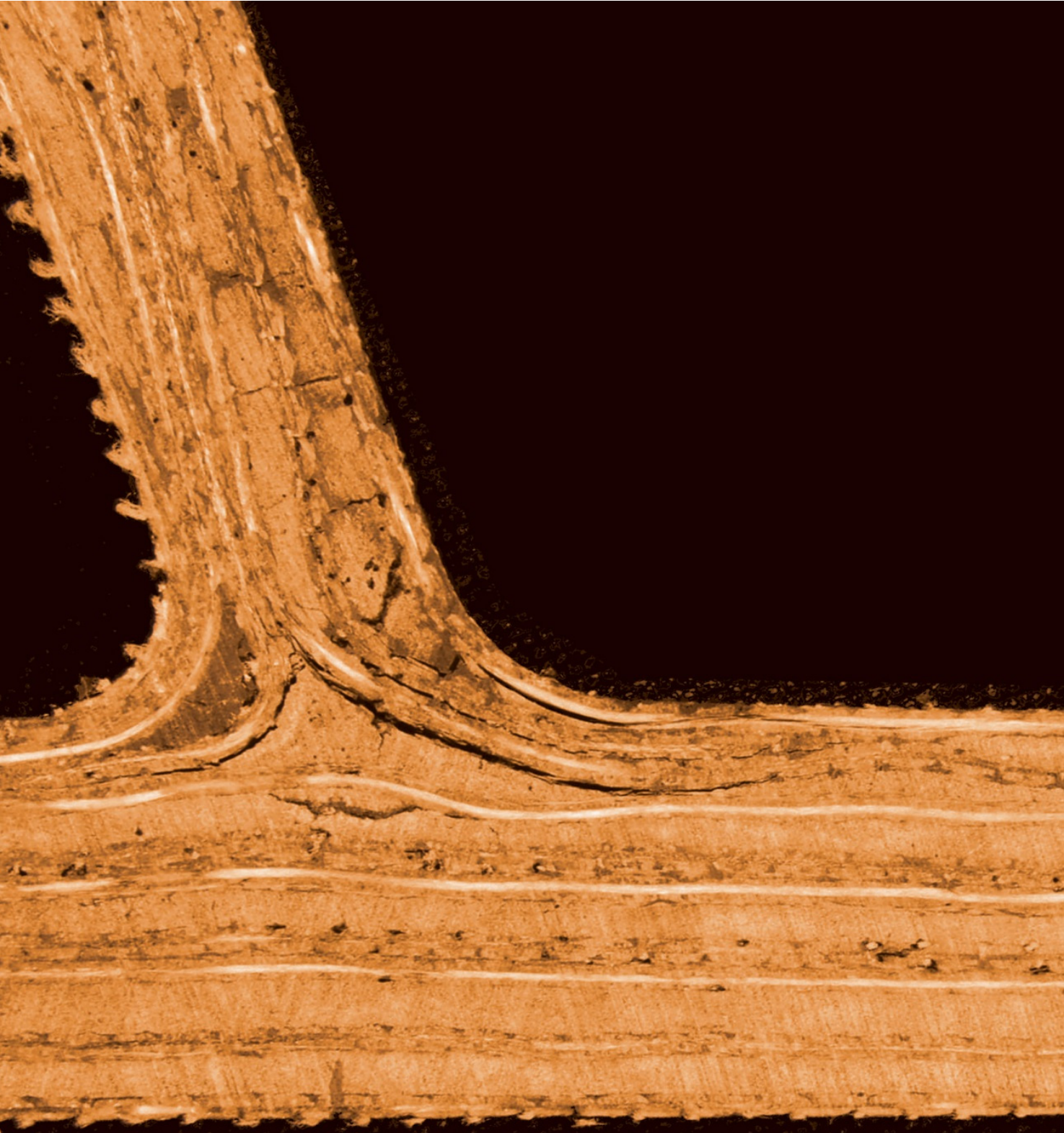
4. The lower bound values for the *DS* and *AS* decks' system in-plane shear moduli in their transverse direction were estimated from the experimental deflection results using existing equations for timber-concrete composite beams with flexible shear connections. The *DS* deck system showed substantially lower values than the *AS* deck system (the thus calculated system in-plane shear modulus of *DS* represented approximately 2–3% of the modulus of *AS*).

The aforementioned approach to calculate the transverse in-plane shear modulus is limited to the linear elastic range behavior. Nevertheless, the modulus of *DS* can be nonlinear due to progressive local failures. Further work will consider the complete characterization of the system in-plane shear modulus up to failure and its effects on the global performances of both the slab and composite girder.

References

- Hollaway L. A review of the present and future utilisation of FRP composites in the civil infrastructure with reference to their important in-service properties. *Constr Build Mater* 2010;24(12):2419–2445.
- Keller T. *Use of fibre reinforced polymers in bridge construction*. Structural engineering documents, 7. Zürich: International Association for Bridge and Structural Engineering IABSE; 2003.
- Chen DN, El-Hacha R. Hybrid FRP-concrete structural member: research and development in North America. In: Lieping Y, Feng P, Yue Q (eds.) *Advances in FRP composites in civil engineering: Proceedings of the 5th International Conference on FRP Composites in Civil Engineering, CICE 2010*, 27–29 September 2010, Beijing, China. Heidelberg: Springer; 2011. p.185–190.
- Chen DN, El-Hacha R. Hybrid FRP-concrete structural member: research and development in Europe and Asia. Lieping Y, Feng P, Yue Q (eds.) *Advances in FRP composites in civil engineering: Proceedings of the 5th International Conference on FRP Composites in Civil Engineering, CICE 2010*, 27–29 September 2010, Beijing, China. Heidelberg: Springer; 2011. p.191–196.
- Cheng L, Karbhari VM. New bridge systems using FRP composites and concrete: a state-of-the-art review. *Prog Struct Eng* 2006;8(4):143–154.
- Bakis C, Bank LC, Brown V, Cosenza E, Davalos J, Lesko J, et al. Fiber-reinforced polymer composites for construction — state-of-the-art review. *J Compos Constr* 2002;6(2):73–87.
- Qiao P, Davalos JF, Brown B. A systematic analysis and design approach for single-span FRP deck/stringer bridges. *Compos Part B* 2000;31(6):593–609.
- Keller T, Schollmayer M. Plate bending behavior of a pultruded GFRP bridge deck system. *Compos Struct* 2004;64(3):285–295.
- Gürtler HW. *Composite action of FRP bridge decks adhesively bonded to steel main girders* [PhD Thesis]. Ecole Polytechnique Fédérale de Lausanne, Switzerland; 2004. doi:10.5075/epfl-thesis-3135
- Zi G, Kim BM, Hwang YK, Lee YH. The static behavior of a modular foam-filled GFRP bridge deck with a strong web-flange joint. *Compos Struct* 2008;85(2):155–163.
- Hayes MD, Ohanehi D, Lesko JJ, Cousins TE, Witcher D. Performance of tube and plate fiberglass composite bridge deck. *J Compos Constr* 2000;4(2):48–55.

12. Zhou A, Coleman JT, Temeles AB, Lesko JJ, Cousins TE. Laboratory and field performance of cellular fiber-reinforced polymer composite bridge deck systems. *J Compos Constr* 2005;9(5):458–467.
13. Jeong J, Lee YH, Park KT, Hwang YK. Field and laboratory performance of a rectangular shaped glass fiber reinforced polymer deck. *Compos Struct* 2007;81(4):622–628.
14. Lee J, Kim Y, Jung J, Kosmatka J. Experimental characterization of a pultruded GFRP bridge deck for light-weight vehicles. *Compos Struct* 2007;80(1):141–151.
15. Luke S, Canning L, Collins S, Knudsen E, Brown P, Taljsten B, et al. Advanced composite bridge decking system — Project ASSET. *Struct Eng Int* 2002;12(2):76–79.
16. Park KT, Kim SH, Lee YH, Hwang YK. Pilot test on a developed GFRP bridge deck. *Compos Struct* 2005;70(1):48–59.
17. Sebastian WM, Keller T, Ross J. Influences of polymer concrete surfacing and localised load distribution on behaviour up to failure of an orthotropic FRP bridge deck. *Compos Part B* 2013;45(1):1234–1250.
18. Zi G, Kim BM, Hwang YK, Lee YH. An experimental study on static behavior of a GFRP bridge deck filled with a polyurethane foam. *Compos Struct* 2008;82(2):257–268.
19. Sebastian W, Gegeshidze G, Luke S. Positive and negative moment behaviours of hybrid members comprising cellular GFRP bridge decking epoxy-bonded to reinforced concrete beams. *Compos Part B* 2013;45(1):486–496.
20. Keller T, Gürtler H. Quasi-static and fatigue performance of a cellular FRP bridge deck adhesively bonded to steel girders. *Compos Struct* 2005;70(4):484–496.
21. Keller T, Gürtler H. Composite action and adhesive bond between fiber-reinforced polymer bridge decks and main girders. *J Compos Constr* 2005;9(4):360–368.
22. Park KT, Kim SH, Lee YH, Hwang YK. Degree of composite action verification of bolted GFRP bridge deck-to-girder connection system. *Compos Struct* 2006;72(3):393–400.
23. Keller T, Schollmayer M. Through-thickness performance of adhesive joints between FRP bridge decks and steel girders. *Compos Struct* 2009;87(3):232–241.
24. Natterer J, Hoefl M. *Zum Tragverhalten von Holz-Beton-Verbundkonstruktionen*. Lausanne: Ecole Polytechnique Fédérale de Lausanne, Chaire de Construction en Bois; 1987. Report No.1345.
25. Keller T, Gürtler H. Design of hybrid bridge girders with adhesively bonded and compositely acting FRP deck. *Compos Struct* 2006;74(2):202–212.
26. Ashland. *Data Sheet Pliogrip 6660*. Columbus: Ashland; 1999.



Chapter 3

Energy dissipation and recovery in web-flange junctions

3.1 Introduction

Glass fiber-reinforced polymer (GFRP) bridge decks constitute one of the most widely developed applications of FRP structural materials in the civil engineering field. Since the 1990s, GFRP bridge decks have been increasingly used in road and footbridges, both for new structures and the upgrading of existing ones, due to advantageous properties compared to decks composed of traditional materials – e.g. reinforced concrete (RC) and steel. The main advantages of GFRP materials when employed for bridge slabs include high specific strength, low self-weight (10-20% of that of a comparable RC deck),¹ high corrosion and fatigue resistance, rapid installation times with minimum traffic disruption and low life-cycle costs.^{1,2}

Despite the good potential of FRP materials for structural applications, other features have delayed their more widespread use, including their lack of inherent ductility.^{3,4} Structural safety considerations require structures to be robust, i.e., to be capable of sustaining unforeseen loads to which they might reasonably be subjected.⁵ Robustness is related both to strength and deformability capacities. Inherent material ductility represents a main advantage to provide robustness⁵ with which structural engineers are familiar. Ductile materials permit the redistribution of internal forces and dissipation of energy under impact and seismic actions. Material ductility also results in large structural deformations although without any decrease in load-bearing capacity prior to ultimate failure, therefore representing a warning of possible structural problems. However, unexpected brittle failure is unacceptable in civil structures, which consequently results in the large safety margins required in the design procedure. FRPs typically used in civil engineering consist of non-ductile components – they comprise brittle fibers embedded in a brittle polymeric matrix. The material's brittle behavior results in reduced

structural ductility and prevents an optimized use of their strength properties. Given the lack of ductility of FRP material constituents, alternative approaches have to be developed. Ductility can be provided on the material and/or the structural system level, referred to as material and system ductility respectively. Two different sub-concepts can be distinguished on each level: (i) ductility, referring to the combination of ductile and brittle constituents or components; (ii) pseudo-ductility, comprising only brittle constituents or components.³

A primary strategy to provide material ductility is the incorporation of new ductile constituents (matrices and fibers), which still requires extensive development.⁶ Material pseudo-ductility includes material hybridization; a recent review on this topic has been presented by Swolfs et al.⁷ A nonlinear inelastic behavior, with decreasing stiffness at higher load levels, similar to ductile materials, can be achieved through gradual failure of/between the constituents by appropriately mixing different types of fibers with different ultimate strains in the composite material.^{6,8-10} The ratio between the different fibers and their dispersion state are crucial aspects in the behavior of the resulting hybrid material. A similar pseudo-ductile stress-strain behavior can be attained by using different fiber orientations and/or the use of alternative manufacturing techniques, e.g. braiding.^{11,12} Pseudo-ductility can be improved by controlling the damage mechanisms.^{8,13}

Reviews on the ductility and pseudo-ductility of FRP composites on the system level have been presented by Keller and De Castro³ and Bank.⁴ System ductility can be achieved through the integration of ductile structural components or connections. Examples of the former are hybrid beams with GFRP bridge decks adhesively bonded to main steel girders, for which failures in the deck, occurring during the yielding of the steel, have been reported.^{14,15} Ductile adhesive joints, using adhesives with visco-elastoplastic behavior, for brittle FRP components were proposed by Keller and De Castro.^{3,16}

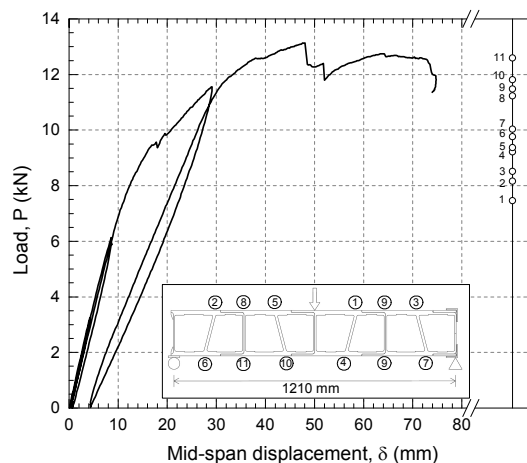
In the absence of ductile components, system pseudo-ductility can be achieved by progressive failure in the brittle components/connections. System pseudo-ductility can be attained providing that structural redundancy in the system (static indeterminacy), in the cross section and/or at the component level exists. The structural system redundancy provides alternative load paths and force redistribution as local failures occur in the components or in the connections. Nonetheless, pseudo-ductile structures become statically determinate after a certain number of internal failures and a further failure would result in abrupt collapse. The truss structure of the Pontresina Pedestrian Bridge,² with crossed diagonals supplying alternative load transfer paths in the case of failure of one or several components or joints, represents an example of system redundancy. At the cross-sectional level, redundancy can be provided in multi-component cross sections, using one or several materials. Failure of the first material/component or connection between the components does not necessarily lead to failure of the whole section, and internal force redistribution functions as in statically indeterminate systems. Similar to hybridization at the material level, combinations of GFRP sections and carbon fiber-reinforced polymer (CFRP) laminates have been proposed

to obtain pseudo-ductile characteristics in the flexural behavior of the hybrid beams.^{17,18} The beams were designed to have a first failure occurring in the CFRP laminates – leading to internal stress redistribution and a global stiffness decrease – which could be interpreted as a warning of future flexural collapse of the cross section. Nonlinear, inelastic behavior providing pseudo-ductility by means of progressive internal failures can also be found at the component level. Experimental research on the transverse in-plane shear performance of pultruded GFRP bridge decks showed that progressive failure in the web-flange junctions led to behavior comparable to that of a ductile material.¹⁹

Other approaches to obtain gradual and controlled failure in FRP structural components, allowing the development of a nonlinear, inelastic increase in deformation and leading to the dissipation of internal strain energy, consist of a design for non-catastrophic failure modes (e.g. sustained crushing load in FRP tubes subjected to axial loads; tearing failure at the junctions in pultruded members). The energy dissipation ability of tubular FRP profiles under bending through material fragmentation due to progressive tearing failure in the web-flange junctions was experimentally investigated by Mertens.²⁰ The effect of different lengths of initiator slits showed that with their length increase, the ratio of the peak load to the stable crushing load decreased, therefore producing a less catastrophic failure. A similar tensile tearing failure mode, leading to flange separation, has also been observed after buckling of the flange(s) and/or web of pultruded I-profiles subjected to bending or axial compression.^{21,22} These local tearing failures have been found to result in a nonlinear pseudo-ductile load-deflection behavior for entire frame structures.²³

In a previous investigation,²⁴ the load transfer mechanism and failure mode of a GFRP deck system, *DS*, with trapezoidal cell cross section in its transverse-to-pultrusion direction were experimentally studied. Figure 3.1 illustrates the loading configuration and load-deflection response measured at mid-span. The deck exhibited a frame-dominated behavior whereby the load was mainly transmitted by local shear and bending moments in the web and flange elements (Vierendeel frame mechanism). Gradual cracking in the web-flange junctions (WFJs) was detected and led to a stiffness reduction without

Figure 3.1 – Load-deflection behavior of full-scale *DS-3* beam.²⁴



causing the deck's final failure. The sequence of the observed cracks, their location and the associated load levels are indicated on the right side of Figure 3.1. A non-brittle failure was observed and sustained load-bearing capacity under the development of large displacements was registered. This was attributed to the system redundancy – progressive local bending failures occurred in the WFJs. The unloading cycles performed after the initiation of damage in the WFJs and prior to final failure demonstrated that the deck was able to dissipate internal energy through the inelastic increase in deformation caused by the internal local failures.

The objective of this work is the experimental investigation of the energy dissipation capacity resulting from progressive cracking of the WFJs of the *DS* deck. Two types of WFJs with similar geometry but different locations within the deck profile were investigated. A visual examination of the deck had revealed that, despite the similar geometry of the two WFJ types, slight dissimilarities in the fiber architecture and different initial imperfections existed. Their influence on the WFJs' behavior was studied. Given the viscoelastic character of FRP materials – FRPs may exhibit viscoelastic behavior because of the polymeric nature of their matrix – the sensitivity of the response to different loading/unloading rates was also assessed. Web-cantilever bending experiments up to failure were performed on 50-mm-wide specimens. The response of both series is compared and discussed. The energy dissipation capacity of the WFJs under monotonic loading was evaluated using existing ductility indices.

3.2 Theoretical background

3.2.1 Recovery behavior of viscoelastic materials

FRP materials may exhibit viscoelastic behavior owing to the polymeric nature of their matrix. Hence, viscoelastic effects in FRPs are most pronounced in their matrix-dominated responses.²⁵ The delayed recovery upon unloading is one of the principal manifestations of viscoelastic behavior in structural materials. After a loading process, once the load is partially or entirely removed, viscoelastic materials undergo strain recovery (ϵ_r) in two stages: instantaneous (elastic) recovery ($\epsilon_{r,0}$) is followed by time-dependent, i.e. delayed, recovery ($\epsilon_{r,del}$) which takes place gradually and at a decreasing rate as time elapses. Hence, the total recovered strain (ϵ_r) equals the sum of $\epsilon_{r,0}$ and $\epsilon_{r,del}$. A residual deformation (ϵ_{res}) from viscous flow effects, corresponding to the viscous nature of the material, may remain upon unloading even in the absence of any damage. In the case of materials exhibiting damage or plasticity, the residual deformation ϵ_{res} also includes the effects of the latter and cannot be exclusively attributed to the material's viscous properties.

For a homogeneous viscoelastic material subjected to bending, an analogous approach can be adopted for the deflection recovery (δ_r), since the flexural deflection δ can be expressed as a function of the maximum strain ϵ_{max} . Figure 3.2(a) shows the deflection recovery, including the instantaneous ($\delta_{r,0}$) and delayed ($\delta_{r,del}$) components, and the residual deflection (δ_{res}) over time. The maximum delayed recovery, $\delta_{r,del}^{\infty}$, is obtained at infinite recovery time t_r .

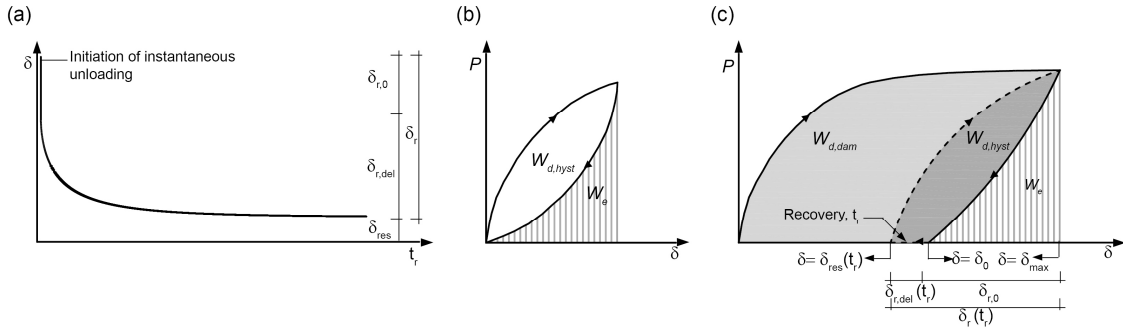


Figure 3.2 – Behavior of viscoelastic materials; (a) recovery; energy dissipation under monotonic loading, (b) without and (c) with residual deformation.*

*Note: indicated $W_{d,dam}$ and $W_{d,hyst}$ are subject to $t_r = \infty$.

The experimental determination of the actual $\delta_{r,0}$ and $\delta_{r,del}^{\infty}$ values requires instantaneous unloading and infinite t_r .

3.2.2 Energy dissipation in viscoelastic materials

Viscoelastic materials are able to both store and dissipate energy under load owing to their viscous properties, in contrast to ideal Hookean elastic solids, which are capable of energy storage but not energy dissipation. During the deformation of an ideal viscoelastic material with no residual deformation (see Figure 3.2(b)), the total energy supplied during loading through the work of the external loads, W_t , can be formulated as:

$$W_t = W_e + W_{d,hyst} \quad (3.1)$$

where W_e = elastic energy, i.e. energy elastically stored during loading and released upon instantaneous unloading; $W_{d,hyst}$ = energy dissipated through viscosity-related friction losses, also referred to as hysteretic energy.²⁶ The elastic energy is represented by the area below the unloading path and the hysteretic energy is related to the area within the hysteretic loop, see Figure 3.2(b).

In viscoelastic materials subjected to plasticity or damage, besides $W_{d,hyst}$, part of the total energy is dissipated through plasticity and damage mechanisms, $W_{d,dam}$, leading to a non-recoverable, permanent deformation δ_{res} (see Figure 3.2(c)). The total energy provided to the system can be expressed as:

$$W_t = W_e + W_{d,hyst} + W_{d,dam} \quad (3.2)$$

where the addition of $W_{d,hyst}$ and $W_{d,dam}$ represents the total dissipated energy, W_d . The decoupling of these terms requires: (i) enabling the delayed recovery, $\delta_{r,del}$, to develop entirely and (ii) performing a reloading cycle.

3.2.3 Ductility evaluation

Ductile structural materials, elements or systems are characterized by their ability to sustain inelastic deformation without loss of their load-bearing capacity and dissipate energy during impact and reverse cyclic loading. Ductility can be expressed, following this definition, in terms of deformation or energy dissipation. A large energy dissipation capacity, as well as large deflections, deformations, rotations and curvatures, can be considered as ductility indicators. The ratio of the energy dissipated at failure, W_d , to the total energy supplied by the work of the external loads, W_t , has been proposed as a ductility index μ :^{27,28}

$$\mu = \frac{W_d}{W_t} \quad (3.3)$$

The ductility index thus defined would be equal to zero for ideal elastic behavior, equal to 1 for rigid-plastic behavior and range between 0 and 1 in the general case of elasto-plastic behavior. For viscoelastic materials showing residual deformation, Equation (3.3) can be formulated as:

$$\mu = \frac{W_{d,hyst} + W_{d,dam}}{W_t} \quad (3.4)$$

3.3 Experimental program

The investigation is based on small-scale experiments conducted on the web-flange junctions (WFJs) of the DuraSpan (*DS*) pultruded GFRP bridge deck system,²⁹ manufactured by Martin Marietta Composites Inc. (Raleigh, United States).

3.3.1 Pultruded GFRP bridge deck system

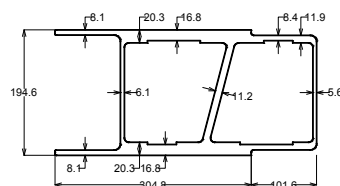
The cross section of the *DS* unit module profile consists of two trapezoidal cells shaped by vertical and slightly inclined webs connected to the deck's face sheets (flanges), as shown in Figure 3.3. The dual-cell unit profiles are bonded together along their vertical (outer) webs using a structural polyurethane adhesive to form the slab, see Figure 3.4(a). A tongue-and-groove connection between adjacent profiles is provided by lip extensions and steps in the deck's face sheets, on opposite sides of the unit profile. Mirror symmetry about a horizontal axis is used for every other unit so that the direction of the inclined web alternates in each element.

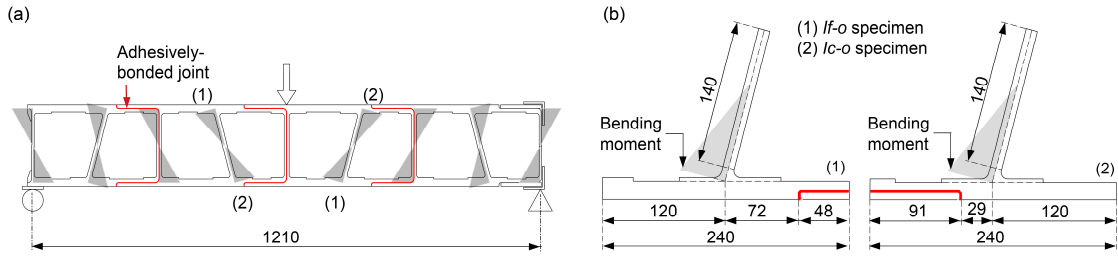
The *DS* deck is composed of E-glass fibers embedded in an isophthalic polyester resin. The fiber stacking sequence of the laminates alternates roving in the pultrusion direction, triaxial multi-ply fabrics and additional non-structural mats. The material properties for the flange and web laminates are listed in Table 3.1. The total fiber content by weight is 60%.²⁹

3.3.2 Specimen description and preparation

The *DS* deck's WFJs can be classified into two groups according to the corresponding web geometry: vertical (*V*) and inclined (*I*). Two *I* WFJ types can be differentiated depending on the closer (*c*) / farther (*f*) location of the adhesively-bonded profile-to-profile joint in the flange in regard to the WFJ itself. The three WFJ types (*V*, *Ic*, *If*) were investigated under local bending moment, in relation to the frame-dominated behavior exhibited by the *DS* deck in its transverse-to-pultrusion direction.²⁴ Nevertheless, within the framework of this investigation, the study is focused on the *Ic* and *If* types.

Figure 3.3 – Unit module geometry of *DS* bridge deck system; dimensions in mm.





Property	Unit	Flanges	Vertical webs	Inclined webs
E_x	MPa	21 240	17 380	17 380
E_y	MPa	11 790	9 650	9 650
E_z	MPa	[12 980 ^(a)]	[14 910 ^(a)]	[16 350 ^(a)]
G_{xy}	MPa	5 580	7 170	7 170
$G_{xz} = G_{zy}$	MPa	600	600	600
ν_{xy}	-	0.32	0.30	0.30
$\nu_{xz} = \nu_{zy}$	-	0.30	0.30	0.30

x = pultrusion direction; y = perpendicular to pultrusion direction, in-plane; z = through-thickness direction

^(a) Own values, experimentally obtained for 0-0.20% strain range

Note: applicable strain ranges for properties from DARPA²⁹ were not available.

^ Figure 3.4 – (a) Local bending moments in webs of DS deck panel subjected to transverse bending. (b) WFJ specimens; dimensions in mm.

√ Table 3.1 – Material properties of DS.²⁹

The experimental program was conducted on three *If* and five *Ic* specimens. The specimens were labeled *If-om* ($m = 1-3$) and *Ic-on* ($n = 4-6$ and $8-9$). The third character (*o*) of the specimens' nomenclature denotes the direction of the local bending moment in the web element – *o* indicates the tensioned side of the web towards the obtuse angle of the WFJ (see Figure 3.4(b)). The specimens' location within the deck panel and their overall geometry are shown in Figures 3.4(a) and 3.4(b), respectively.

The typical fiber architecture of both WFJs examined is schematically illustrated in Figure 3.5. Two thirds of the triaxial multi-ply fabrics from the web laminate are prolonged into the flange. As a result, the flange thickness is greater close to the WFJ – 20.3 mm versus 16.8 mm, see also Figure 3.3. At the center of the WFJ there is an approximately triangular-shaped roving core. A visual examination of the specimens was conducted and showed that, due to initial imperfections, differences existed between their actual fiber arrangement and the fiber architecture design, see Figure 3.6. In the *If-o* specimens, these imperfections consisted of: (i) a resin pocket in the WFJ, towards the WFJ's acute angle and (ii) the uneven distribution of the triaxial fabrics, concentrated towards the acute angle side, across the web thickness, see Figure 3.6(a). In the *Ic-o* series, the observed flaws comprised: (i) the prolongation of the continuous web-flange triaxial fabrics into the 16.8-mm thickness region of the flange and (ii) the wrinkling of the innermost fabric (obtuse angle side) in the radius area, see Figure 3.6(b). Furthermore, during the visual inspection, a small crack (referred as *pre-crack* in the following) of 20–40-mm length was observed in the flange of every *Ic-o* specimen, see also Figure 3.5(b). The pre-crack was located towards the obtuse angle side of the WFJ, had an average length of approximately 30 mm and ran parallel to

Figure 3.5 – Fiber architecture and crack initiation of (a) *If-o* and (b) *lc-o* series; dimensions in mm.

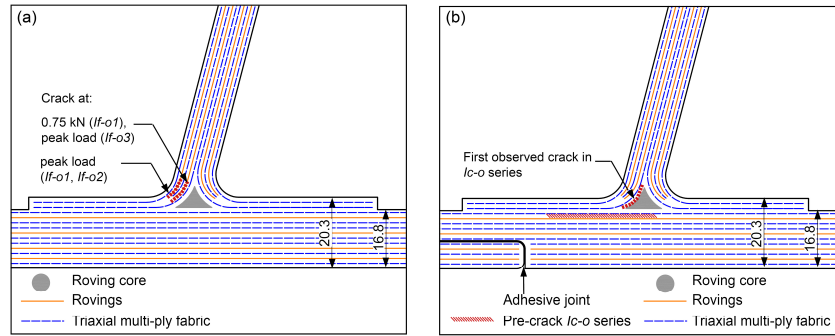
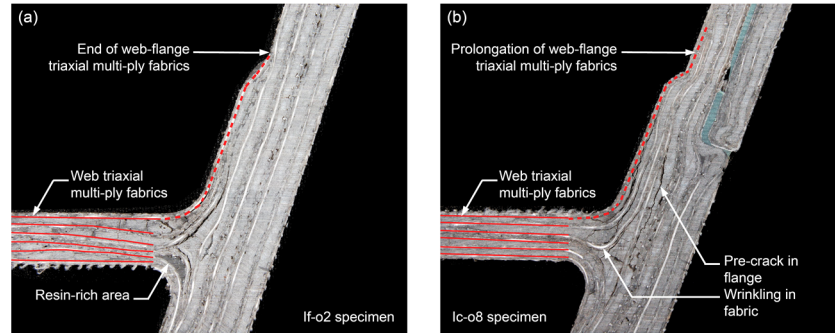


Figure 3.6 – Initial imperfections of (a) *If-o* and (b) *lc-o* series. Note: view of specimens after experiments; web triaxial multi-ply fabrics marked in red continue towards the flange.

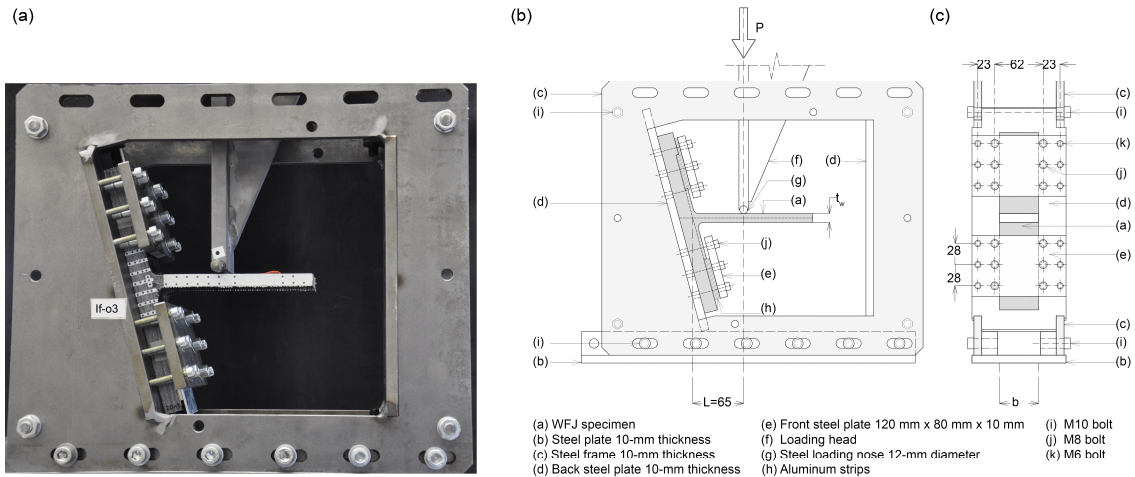


the flange element at an approximately 8-mm depth from the laminate's surface.

3.3.3 Experimental set-up, instrumentation and procedure

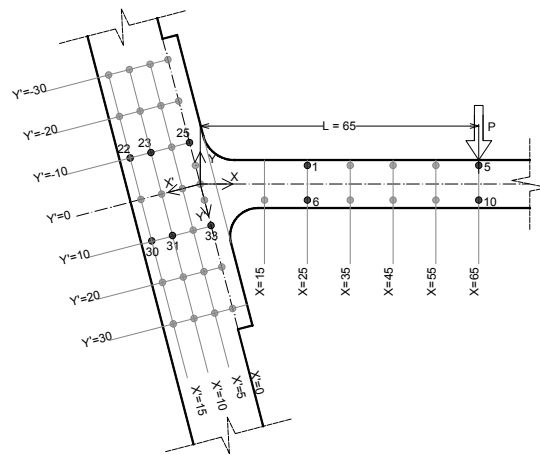
The WFJ specimens were loaded under local bending applied to the web element. The specimens' webs were loaded as a cantilever with a 65-mm lever arm and clamped flange, see Figure 3.7(a). A single support fixture allowing the conducting of the web-cantilever experiments on all WFJ types using a universal testing machine was designed and manufactured. The set-up is shown in Figures 3.7(b) and 3.7(c). The test rig consisted of a two-layer steel frame fixed to the lower platen of the testing machine and transversely connected with 10-mm-diameter bolts and 10-mm-thick welded steel plates. The flange of the specimen was clamped to one of these steel plates so that the web element was placed horizontally. Two additional steel plates and two sets of 8-mm-diameter bolts were used to laterally clamp the specimen's flange on both sides of the WFJ without drilling it. In order to take into account any unevenness in the specimen's flange thickness, aluminum strips were placed between the flange and the front fixing plates; the 20.3-mm-thickness flange area close to the WFJ (see Figure 3.7) remained unclamped. The assembly could be adjusted horizontally in the testing machine to set the load application point. The vertical load was introduced through a triangular-shaped loading head bolted to the upper platen of the testing machine. Contact between the loading fixture and the upper face of the specimen's web was via a 12-mm-diameter steel bar and across the whole width of the web.

The rotations of the specimen's flange and web and the vertical deflections along the length of the latter were measured by means of a video extensometer throughout the experiments. For this purpose, black dots were marked on the specimen's lateral surface: (i) in an array arrangement on the flange, at equal



^ Figure 3.7 – Experimental set-up; (a) general view; (b) front view; (c) cross section; dimensions in mm.

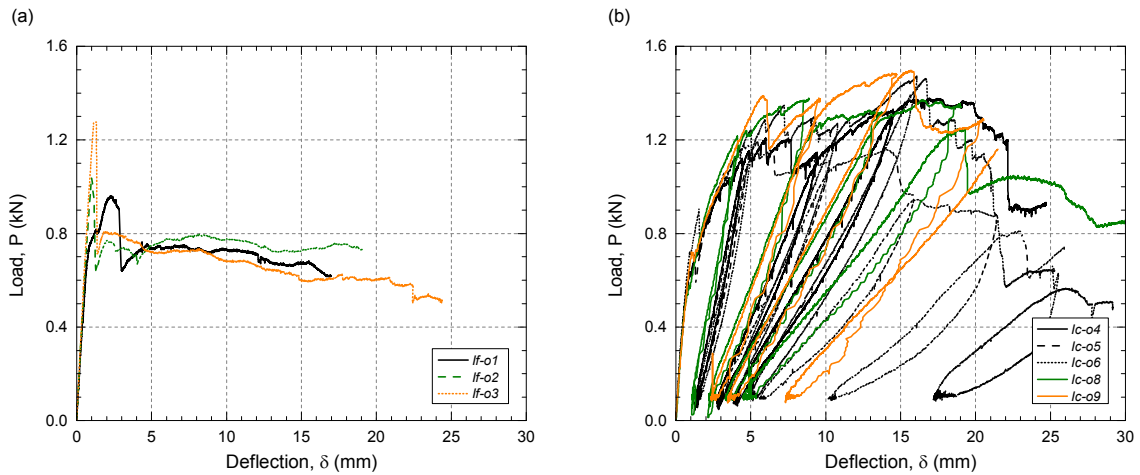
> Figure 3.8 – Specimen instrumentation: arrangement of target points for video extensometer measuring system; dimensions in mm.



intervals of around $\Delta X' \approx 5$ mm across its thickness and $\Delta Y' \approx 10$ mm along its length; (ii) in pairs on the upper and lower sides of the web, at $\Delta X \approx 10$ -mm intervals, see Figure 3.8. The X - Y coordinates of these target points were monitored by a video extensometer camera and recorded with an accuracy of $5 \cdot 10^{-7}$ m by a LabVIEW application at a 2–10-Hz frequency. They were subsequently processed with a simple data processing module to determine the rotations and deflections. The video extensometer system was also used to automatically capture and save images of the specimen at regular intervals during the experiments. In addition, the vertical displacement of the testing machine was continuously recorded at a 2–5-Hz frequency by a DOLI EDC 60/120 data-acquisition device. Load and time were registered in both systems.

An overview of the experiments carried out is given in Table 3.2. All experiments were conducted under displacement control up to failure. The *If-o* specimens were monotonically loaded at a rate of 0.01 mm/s. The *Ic-o* specimens were subjected to several unloading-reloading cycles delimited by previously defined maximum machine displacements, δ_{max} ranging from 5 to 20 mm. The influence of the displacement rates during loading/unloading and the recovered deflections were investigated with regard to the potential viscoelastic behavior of the material. The displacement rates during loading/reloading,

Series	Specimen	Number of cycles	Displacement at unloading δ_{max} (mm)	Loading/reloading rate v_l (mm/s)	Unloading rate v_u (mm/s)	Recovery time t_{max} (min)
<i>If-o</i>	<i>If-o1</i>	0	-	0.01	-	-
	<i>If-o2</i>	0	-	0.01	-	-
	<i>If-o3</i>	0	-	0.01	-	-
<i>Ic-o</i>	<i>Ic-o4</i>	3	5, 10, 15	0.01	0.01	5
	<i>Ic-o5</i>	4	5, 10, 15, 20	0.01	0.01	10
	<i>Ic-o6</i>	4	5, 10, 15, 25	0.01	0.01	60
	<i>Ic-o8</i>	4	5, 10, 15, 20	0.10	0.50	60
	<i>Ic-o9</i>	3	10, 15, 20	0.10	1.50	60



△ Table 3.2 – Overview of performed experiments.

√ Figure 3.9 – Load-displacement response of (a) *If-o* specimens and (b) *Ic-o* specimens.

v_l , ranged from 0.01 to 0.10 mm/s and the rates during unloading, v_u , from 0.01 mm/s to 1.50 mm/s. After unloading, the load was sustained at 0.1 kN for a period of time t_{max} (see Table 3.2) during which the deflection recovery was measured.

3.4 Experimental results

3.4.1 *If-o* series response

The load-deflection (P - δ) responses registered for the *If-o* series are shown in Figure 3.9(a). A small rotation in the flange element, on its rear side, was registered (see section defined by targets 22-30 in Figure 3.8). Its contribution to the total deflection was subtracted from the measured vertical deflections of the WFJ specimen's web under the load application δ point, in order to eliminate the effect of the unclamped flange area from the web's response.

All the *If-o* specimens showed similar initial stiffness, as indicated by coincident P - δ plots. Specimen *If-o1* displayed a linear P - δ relationship up to an approximately 0.75-kN load, when the first crack was observed in the upper (tensioned) fillet of the WFJ, parallel to its surface. The first crack appeared adjacent to a triaxial fabric of the web without continuity into the flange, towards the inner part of the WFJ, see Figures 3.5(a) and 3.10(a). The stiffness decreased and the initially linear response became slightly nonlinear up to failure, which occurred suddenly at a 0.96-kN load when a second crack was

Figure 3.10 – Crack pattern at peak load of (a) *If-o2* and (b) *Ic-o6* specimens; post-peak crack pattern of (c) *If-o2* and (d) *Ic-o6* specimens.

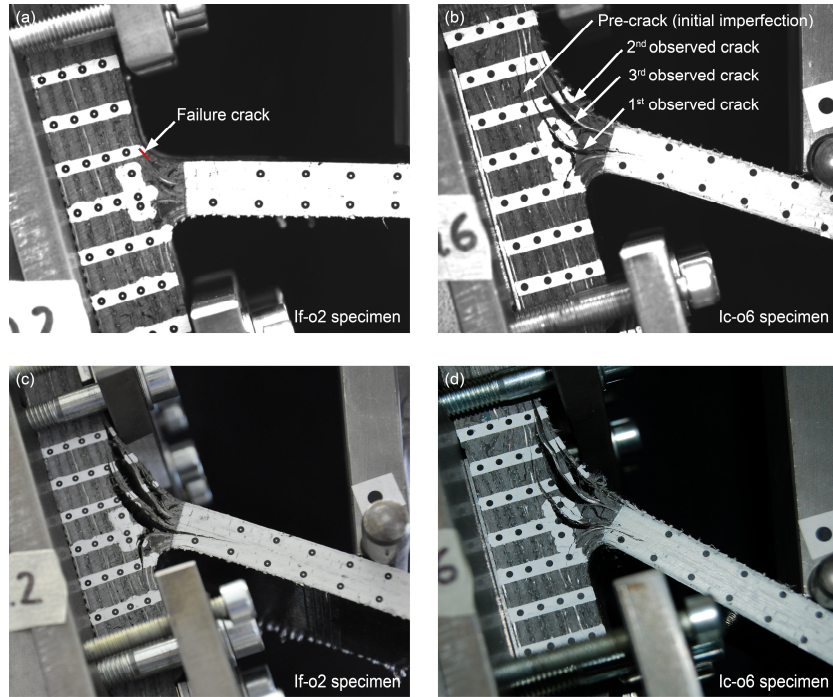


Table 3.3 – Experimental peak loads and corresponding displacements; calculated ultimate moments.

Series	Specimen	P_{ult} (kN)	δ_{ult} (mm)	P_{ult}/b (N/mm)	M_{ult}/b (Nmm/mm)
<i>If-o</i>	<i>If-o1</i>	0.96	2.8	19.5	1270
	<i>If-o2</i>	1.05	1.1	21.1	1375
	<i>If-o3</i>	1.28	1.3	25.9	1684
	Mean		$1.7 \pm 0.9^{(a)}$	$22.2 \pm 3.3^{(a)}$	$1443 \pm 215^{(a)}$
<i>Ic-o</i>	<i>Ic-o4</i>	1.38	19.9	28.5	1853
	<i>Ic-o5</i>	1.20	14.4	24.8	1610
	<i>Ic-o6</i>	1.47	16.3	30.0	1950
	<i>Ic-o8</i>	1.38	19.3	27.8	1806
	<i>Ic-o9</i>	1.50	15.7	29.8	1934
	Mean		$17.1 \pm 2.4^{(a)}$	$28.2 \pm 2.1^{(a)}$	$1831 \pm 137^{(a)}$

^(a) Standard deviation.

observed, parallel to the first one and closer to the WFJ surface. It also occurred adjacent to the abovementioned fabric but towards the outer side of the WFJ (see Figure 3.5(a)). Specimens *If-o2* and *If-o3* exhibited linear behavior up to failure, which occurred abruptly at 1.05- and 1.28-kN loads, respectively. At the peak load, a delamination crack was observed in a similar location to either the pre-failure or failure crack of *If-o1*, see Figure 3.5(a). No damage had been previously detected.

Failure was governed by transverse (through-thickness) tension in the fillet region of the WFJs under tension. The average ultimate load per unit width (P_{ult}/b) was 22.2 ± 3.3 N/mm, see Table 3.3. Load decreases of $38 \pm 6\%$ were registered after failure. Subsequently, specimens were able to bear an approximately constant (0.58–0.80-kN), slightly decreasing load under large displacement development, see Figure 3.9(a). As the displacement increased,

other delamination cracks appeared and propagated near the continuous web-flange triaxial fabrics in the WFJs' tensioned side, as shown in Figure 3.10(c).

The ultimate bending moment of the WFJs, M_{ult} , was calculated as the product of the experimental ultimate load, P_{ult} , and the distance from the load application point to the WFJ (lever arm), L , see Figures 3.7(b) and 3.8. The M_{ult}/b mean value was 1443 ± 215 Nmm/mm, see Table 3.3. The flexural strength of the WFJs, σ_f , defined as the surface stress at failure at the beginning of the web's constant cross section (at the intersection with the flange's surface, disregarding the fillet), was also determined. An homogeneous cantilever beam of ($b \cdot t_w$) rectangular cross section was assumed. A σ_f average value of 62.5 ± 8.7 MPa was obtained.

3.4.2 *Ic-o* series response

The load-deflection responses measured for the *Ic-o* series are shown in Figure 3.9(b). The deflection caused by the rotation of the flange was discounted as for the *If-o* series. The overall behavior of the five *Ic-o* specimens was analogous regardless of their different loading programs. All the specimens exhibited linear behavior up to a load of approximately 0.50–0.70 kN (proportional limit) in the first cycle. The propagation of the pre-existing crack in the specimens' flange (see Section 3.3.2) was then noticed. The behavior changed to nonlinear, with a marked reduction of stiffness and large displacement development towards failure. Progressive delamination cracks were observed in the upper (tensioned) fillet of the WFJs as from the proportional limit without producing the specimens' final failure. The appearance and propagation of cracking occurred with increasing displacement throughout the cycles – no crack onset/development was detected during reloading before the maximum displacement of former cycles was reached. The first cracking – apart from the pre-crack in the flange – initiated between the triangular-shaped roving core, in the WFJs' tensioned side, and the adjacent triaxial web-flange fabric, as indicated in Figures 3.5(b) and 3.10(b). Before the peak load was reached, other delamination cracks appeared in the tensioned fillet, adjacent to the triaxial fabric of the web without continuity into the flange, in the same locations as those observed in the *If-o* series at peak load (see Figures 3.5(a) and 3.10(b)). Due to the progressive cracking, the specimens showed decreasing stiffness during reloading with increasing displacement at unloading. Reloading paths deviated from the unloading paths in the cycles conducted on all the specimens.

Failure, defined as the peak load (representing the inability of the specimens to bear any further load increment), occurred at 1.20–1.50 kN in the *Ic-o* specimens, which corresponds to a 28.2 ± 2.1 -N/mm load per unit width, see Table 3.3. The corresponding displacement ranged from 14 to 20 mm. Noticeable load drops were afterwards observed under increasing displacement, see Figure 3.9(b). The *Ic-o* specimens failed due to the propagation of the previously formed delamination cracks (as from a 0.55-kN load in the first cycle) caused by transverse tension in the upper fillet of the WFJs. No differences were detected in the *Ic-o* specimens' failure modes

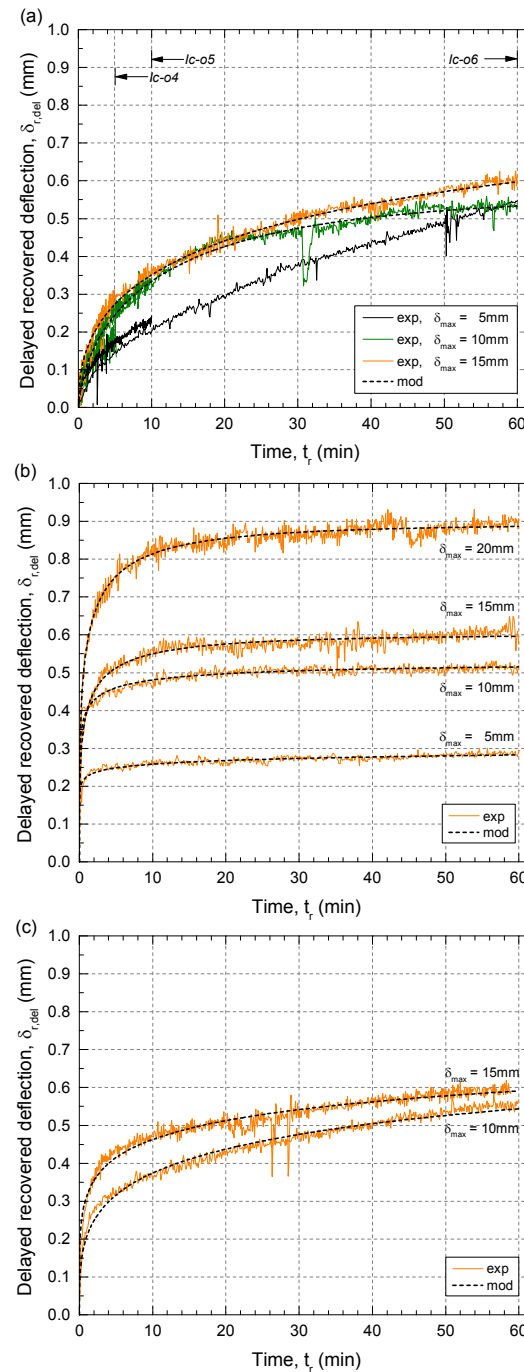
irrespective of the dissimilarities in the experimental procedure. Figure 3.10(d) illustrates the typical post-peak crack pattern of the *Ic-o* series.

The ultimate bending moment per unit width of the *Ic-o* WFJs is given in Table 3.3. The resulting M_{ult}/b average value was 1831 ± 137 Nmm/mm. An average flexural strength σ_f of 80.1 ± 5.3 MPa, calculated as for the *If-o* specimens, was obtained for the *Ic-o* series.

3.4.3 Recovery behavior

The development of the measured deflection recovery in the *Ic-o* specimens after unloading, $\delta_{r,del}$, against the unloading time, t_r , up to $t_r = t_{max}$ is shown in Figure 3.11. The results displayed comprise only unloading cycles conducted

Figure 3.11 – Delayed recovered deflection of specimens
(a) *Ic-04*, *Ic-05* and *Ic-06*;
(b) *Ic-08*; (c) *Ic-09*.



prior to failure. When a certain t_r had elapsed after unloading, the corresponding $\delta_{r,del}(t_r)$ value was calculated as:

$$\delta_{r,del}(t_r) = \delta_0 - \delta_{res}(t_r) \tag{3.5}$$

where δ_0 and $\delta_{res}(t_r)$ are the deflections registered immediately and at a time t_r after unloading, respectively. The rate of recovery after unloading, denoted by the slope of the $\delta_{r,del}-t_r$ plot, decreased with increasing unloading period t_r , see Figure 3.11. The decrease occurred faster for specimens *Ic-08* and *Ic-09*, with higher loading and unloading rates, than for the *Ic-04/5/6* specimens – e.g. *Ic-06* recovered 80% of the maximum measured recovery, $\delta_{r,del}(t_{max})$, in 18–40 minutes after unloading while for *Ic-08/9* this recovery occurred after 1–23 minutes. One hour after unloading, $\delta_{r,del}$ had almost stabilized (except for *Ic-06* on its 5-mm cycle) and approached a threshold whose value increased with the cycle’s maximum displacement δ_{max} .

3.5 Discussion

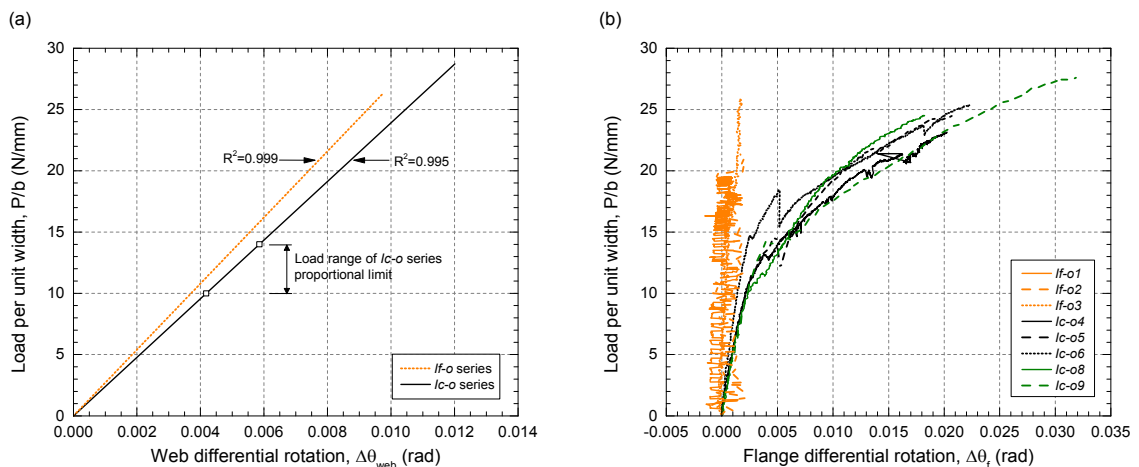
3.5.1 Comparison of *If-o* and *Ic-o* series

The *If-o* and *Ic-o* specimens had similar geometry, which only differed in the location of the adhesively-bonded profile-to-profile joint in the flange element in respect to the WFJ itself. Furthermore, their fiber architecture design was equal, although visual inspection of the specimens had revealed that differences existed between the two series due to initial imperfections. The different load-displacement behavior, failure mode and strength registered for the two series are now discussed and compared with regard to the aforesaid dissimilarities.

The *If-01/2/3* specimens exhibited linear behavior up to 78/100/100% of their peak load. The *Ic-o* specimens displayed nonlinear behavior with the proportional limit at approximately 35–50% of their peak load. The average tangent initial stiffness of the *If-o* and *Ic-o* specimens, defined as the load per unit width to be applied to produce a unit vertical displacement under the load application point, was 26.1 ± 1.4 and 20.2 ± 1.9 N/mm mm respectively, which represents an approximately 25% difference. This difference increased as from the proportional limit of the *Ic-o* specimens due to the initiation of their nonlinear behavior. Figure 3.12(a) shows the difference of rotation ($\Delta\theta_{web}$)

Figure 3.12 – Differential rotation in (a) web and (b) flange elements.*

*Note: measured results for $P/b-\Delta\theta_{web}$ were approximated using linear regression.

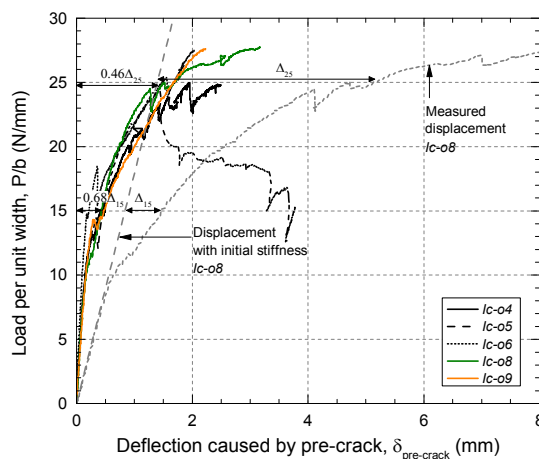


between two sections of the specimens' webs located at 25 and 65 mm from the WFJ (see in Figure 3.8 the vertical lines defined by targets 1-6 and 5-10) during the first loading cycle, which exceeded the proportional limit of the *Ic-o* series. Linear relationships with load were registered in both series, with a 13% difference between them. This showed that the web element remained undamaged and that the stiffness decrease in the *Ic-o* specimens was not related to the web – its fiber stacking sequence was equal in the *If-o* and *Ic-o* specimens, see Figure 3.5.

The effect of the *Ic-o* specimens' pre-crack (see Figures 3.5(b) and 3.6(b)) on their nonlinear behavior was further analyzed. Figure 3.12(b) illustrates the differential rotation in the flange, $\Delta\theta_f$, between two sections located 10 mm apart across its thickness (see Figure 3.8, sections defined by targets 23-31 and 25-33). The *Ic-o* pre-crack was flanked by these two sections. Figure 3.12(b) shows that in the *If-o* series, where no pre-crack existed, both sections rotated conjointly ($\Delta\theta_f \approx 0$) while in the *Ic-o* specimens a non-linear differential rotation, corresponding to the opening of the pre-crack, was registered. The contribution of the pre-crack to the total deflection, $\delta_{pre-crack}$, was calculated as the product of $\tan(\Delta\theta_f)$ and the horizontal distance from the pre-crack to the load application point (the latter was estimated from the *X* coordinate measurements). Figure 3.13 shows that the *Ic-o* specimens' stiffness decrease was partially caused by the flange's pre-existing crack – e.g. in *Ic-08*, at 15/25 N/mm loads, $\delta_{pre-crack}$ represented 68/46% of the difference between the measured displacement and the expected deflection if the initial stiffness had remained constant up to failure. The pre-crack was thus considered as being the origin of the initial nonlinearity of the *Ic-o* series, but not of its sustained load-bearing capacity under increasing displacement – the influence of the pre-crack opening reduced with increasing load levels.

Failure occurred due to transverse (through-thickness) tension in the upper (tensioned) fillet, where the first cracks were noticed in both series. However, and regardless of their similar fiber architecture, the *If-o/Ic-o* specimens displayed different crack formation sequences – the first cracks were observed in different interfaces and closer/farther from the laminate's surface – and peak loads. This was ascribed to the fiber arrangement in the

Figure 3.13 – Contribution of pre-crack to total deflection in *Ic-o* series.



web element and in the WFJ itself. In the studied configuration, the load was mainly borne by the triaxial multi-ply fabrics – rovings ran perpendicularly to the plane containing the resulting bending moment. The triaxial fabrics were evenly distributed across the thickness of the *Ic-o* specimens' webs, whereas in the *If-o* specimens and close to the WFJ, they were concentrated towards their lower (compressed) side, see Figure 3.6. The neutral axis of the web was therefore located closer to its lower face in *If-o* than in *Ic-o*. Hence, at a same load value (thus equal bending moment), the tension stress in the upper fabrics, and therefore the transverse tension stress in the fillet, was higher in *If-o* than in *Ic-o*. The first cracking appeared in the *If-o* series close to the surface due to the higher tensile force borne by and higher curvature of the outer fabric, and thus maximum through-thickness stress in that location, see Figure 3.10(a). In the *Ic-o* specimens, which bore a lower tensile force in the outer fabric, the first cracking (see Figure 3.10(b)) was registered adjacent to the inner fabric next to the roving core, where the maximum curvature, resulting from some apparent wrinkling, was observed (see Figure 3.6(b)). Moreover, this area could be influenced by the proximity of the pre-crack and show lower strength.

The different crack sequences observed in the *If-o/Ic-o* series resulted in different load capacities and failure modes in the two series: the *If-o* specimens exhibited approximately 22% lower peak loads per unit width than the *Ic-o* specimens and sudden failure, whereas in the *Ic-o* series failure was preceded by a large displacement development. Additionally, a resin-rich area in the compressed fillet of the *If-o* WFJs (see Figure 3.6(a)) might have also contributed to their lower strength compared to the *Ic-o* WFJs. Owing to the appearance of the first crack, the delaminated outer thin fabric layer in the *If-o* series no longer contributed to the section's bending stiffness. The bending stiffness reduction, considering the uneven fabric distribution shown in Figure 3.6(a), was however significant (approximately 50%) in the web element and close to the WFJ. As a result, a sharp load drop was registered at the peak load displacement δ_{ult} . Further crack development occurred in the post-peak phase with almost sustained but lower load capacity, see Figures 3.9(a) and 3.10(c). In the *Ic-o* specimens, the first cracking resulted in a decrease of the bending stiffness, as shown in Figure 3.9(b). The triaxial fabrics above the first crack remained active, enabling the WFJs to bear an increasing load. Subsequently, cracking occurred in the same locations as those registered for the cracks in the *If-o* specimens, although at higher deflections. The upper fabrics were straightened and acted as tensioned ties, which allowed the peak load to be sustained at an approximately constant level. Figure 3.10(b) shows the crack pattern at the peak load level in the *Ic-o* specimens. Further crack propagation, resulting in a similar crack pattern to that observed in the *If-o* series (see Figure 3.10 (d)), led to the progressive inactivation of the upper fabrics and resulted in a lower post-peak capacity comparable to that of the *If-o* specimens, see Figure 3.9.

The average flexural strength values calculated for both the *If-o/Ic-o* WFJs represented 75/97% and 38/49% of the experimentally obtained tensile (83 MPa) and compressive (163 MPa) strength values of the web laminate²⁹ –

experimental results for its flexural strength are not available. Lower bending strength of the WFJs compared to that of the web element has been also reported by Turvey and Zhang³¹ and attributed to the differences in the fiber architecture of the two locations.

3.5.2 Recovery behavior

The recovered deflection of the *Ic-o* specimens throughout the cycles is shown in Figure 3.14. The values for the deflection recovery occurring during ($\delta_{r,0}$) and after unloading ($\delta_{r,del}$) and their addition, which represents the total recovered deflection (δ_r) are shown. The $\delta_{r,0}$, $\delta_{r,del}$ and δ_r values were calculated from the measured deflections as follows:

$$\delta_{r,0} = \delta_{max} - \delta_0 \quad (3.6)$$

$$\delta_{r,del} = \delta_0 - \delta_{res}(t_{max}) \quad (3.7)$$

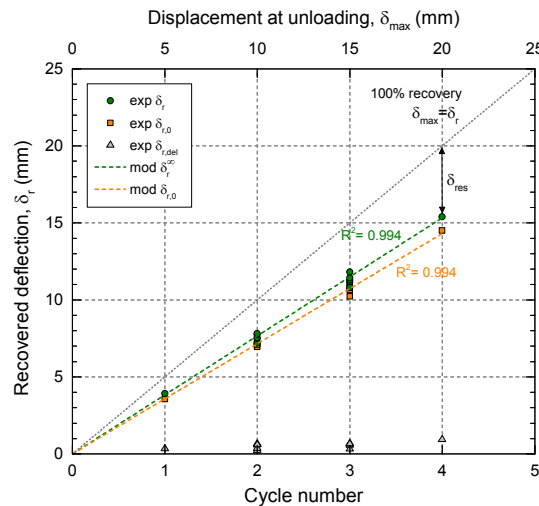
$$\delta_r = \delta_{max} - \delta_{res}(t_{max}) \quad (3.8)$$

where δ_{max} is the displacement at unloading of the relevant cycle, δ_0 is the deflection registered immediately after unloading, and $\delta_{res}(t_{max})$ is the deflection recorded after a t_{max} time (see Table 3.2) subsequent to unloading, thus immediately before reloading, see Figure 3.2(c).

The measured δ_r , $\delta_{r,0}$ and $\delta_{r,del}$ values constitute approximations of the actual total, instantaneous and delayed recoveries, respectively, since a non-instantaneous unloading was conducted, whose fastest rate (for *Ic-o9*) was restricted by limitations in the data registration and experimental set-up; hence, the obtained $\delta_{r,0}$ includes part of the delayed recovery and the calculated $\delta_{r,del}$ represents a lower bound limit of the actual $\delta_{r,del}$. Increasing values of δ_r , $\delta_{r,0}$ and $\delta_{r,del}$ were registered with increasing displacement at unloading; a linear trend with δ_{max} was observed for both δ_r and $\delta_{r,0}$.

The delayed recovered deflection of the *Ic-o* specimens was approximated using the Weibull distribution function, which has been used to fit the strain recovery data of polymers and polymer-matrix composites.^{32,33} Based on the equation proposed by Fancey³² to express the time-dependent strain recovery,

Figure 3.14 – Recovered deflection throughout cycles in *Ic-o* series.*
*Note: $\delta_{max} = 10$ mm in cycle 1 for *Ic-o9* specimen.



and since the flexural deflection δ can be expressed as a function of the maximum strain ϵ_{max} , $\delta_{r,del}$ was formulated as:

$$\delta_{r,del}(t_r) = \delta_{r,del}^{\infty} \left[1 - e^{-(t_r/\eta_r)^{\beta_r}} \right] \quad (3.9)$$

where $\delta_{r,del}^{\infty}$ = maximum time-dependent recovered deflection, t_r = recovery time, η_r = characteristic life parameter representing the t_r value at which 63% of the maximum delayed recovery occurs (if $t_r = \eta_r$, then $\delta_{r,del}(\eta_r) = 0.63 \delta_{r,del}^{\infty}$), β_r = non-dimensional shape parameter related to the recovery rate (lower β_r indicates a faster decreasing recovery rate). Equation (3.9) was used to fit the experimental $\delta_{r,del}$ values throughout the unloading period. The obtained Weibull parameters, $\delta_{r,del}^{\infty}$ and coefficients of determination, R^2 , are shown in Table 3.4 and the corresponding models represented in Figure 3.11. The Weibull distribution function allowed the close matching of the measured delayed deflection recovery values ($R^2 \geq 0.9$ except for *Ic-o8* at $\delta_{max} = 5$ mm).

The maximum time-dependent recovery, $\delta_{r,del}^{\infty}$, increased with the imposed displacement, see Table 3.4 – $\delta_{r,del}(t_r)$ equals $\delta_{r,del}^{\infty}$ when t_r tends to infinity and consequently $\delta_{r,del}^{\infty}$ would represent the upper bound of the delayed recovered deflection. The calculated $\delta_{r,del}^{\infty}$ values were up to 30% higher than the maximum time-dependent recovery measured, $\delta_{r,del}(t_{max})$. Higher $\delta_{r,del}^{\infty}$ values were expected for lower loading rates (v_l) due to the longer loading times and therefore greater viscoelastic deflection. However, the influence of v_l on $\delta_{r,del}^{\infty}$ could not be assessed by the performed experiments since different unloading rates (v_u) were also used and the v_l and v_u effects could thus not be decoupled. On the other hand, lower unloading rates were expected to result in lower $\delta_{r,del}^{\infty}$ values since part of the viscoelastic recovery occurred during the non-instantaneous unloading. The lower $\delta_{r,del}^{\infty}$ values for *Ic-o8* compared to *Ic-o9* are in agreement with the expected effect of the unloading rate – v_u was three times lower for *Ic-o8* than for *Ic-o9* while v_l was equal for both of them, see Table 3.2.

Table 3.4 – Obtained Weibull distribution function parameters and $\delta_{r,del}^{\infty}$ to model time-dependent recovered deflection.

Specimen	$\delta_{max} = 5$ mm				$\delta_{max} = 10$ mm			
	$\delta_{r,del}^{\infty}$ (mm)	η_r (min)	β_r (-)	R^2 (-)	$\delta_{r,del}^{\infty}$ (mm)	η_r (min)	β_r (-)	R^2 (-)
<i>Ic-o4/5/6</i>	(a)	(a)	(a)	(a)	0.566	11.95	0.650	0.98
<i>Ic-o8</i>	0.347	0.68	0.117	0.78	0.530	0.24	0.230	0.88
<i>Ic-o9</i>	(b)	(b)	(b)	(b)	0.820	46.17	0.324	0.98
Specimen	$\delta_{max} = 15$ mm				$\delta_{max} = 20$ mm			
	$\delta_{r,del}^{\infty}$ (mm)	η_r (min)	β_r (-)	R^2 (-)	$\delta_{r,del}^{\infty}$ (mm)	η_r (min)	β_r (-)	R^2 (-)
<i>Ic-o4/5/6</i>	0.864	41.99	0.454	0.99	(c)	(c)	(c)	(c)
<i>Ic-o8</i>	0.602	0.83	0.360	0.91	0.894	0.99	0.380	0.95
<i>Ic-o9</i>	0.823	22.32	0.238	0.93	(c)	(c)	(c)	(c)

(a) Recovery time t_{max} was insufficient in all specimens to apply Equation (3.9).

(b) The $\delta_{max} = 5$ mm cycle was not performed on *Ic-o9* specimen.

(c) Failure occurred prior to a 20-mm machine displacement.

For the same cycle, the η_r and β_r parameters were higher for the *Ic-04/5/6* specimens than for the *Ic-08/9* specimens – η_r for *Ic-09* in the 10-mm cycle excepted. This is in accordance with the higher v_1 of *Ic-08/9* (lower η_r and β_r values resulted from the shorter loading times and hence smaller viscoelastic effects).

The measured $\delta_{r,0}$ values and the δ_r^∞ values calculated by adding the estimated $\delta_{r,det}^\infty$ (see Table 3.4) were approximated by linear regression models (see *mod* δ_r and *mod* $\delta_{r,0}$ in Figure 3.14, respectively). The models showed that the $\delta_{r,0}/\delta_{max}$ and $\delta_r^\infty/\delta_{max}$ ratios were constant. The latter suggested that the rate of total recovery and accumulated damage – linked to the irreversible deflection δ_{res}^∞ , i.e. to the difference between δ_{max} and δ_r^∞ – were constant regardless of the maximum displacement reached and of the loading/unloading rates. The resulting δ_r - δ_{max} slope indicated that before final failure approximately 77% of the maximum deflection attained was reversible and thus only up to approximately 23% was irrecoverable. The closeness of the δ_r and $\delta_{r,0}$ model results demonstrated that deflection recovery mainly occurred instantaneously ($\delta_{r,0} \approx 0.93\delta_r$) and that the viscoelastic effect on the recovery of the WFJs was small for the studied configuration.

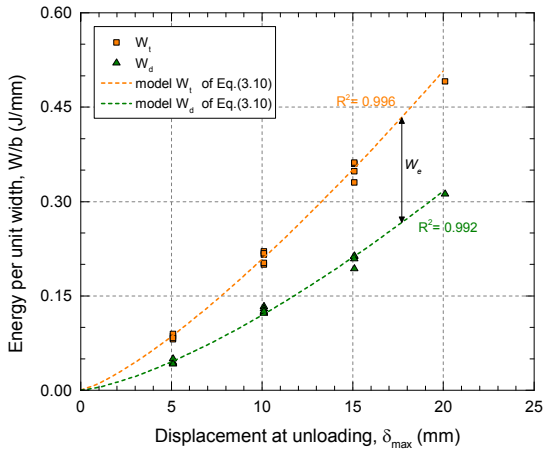
3.5.3 Energy dissipation capacity of *Ic-0* series

The *Ic-0* specimens exhibited nonlinear behavior and development of large deflections towards failure with sustained load-bearing capacity (see Sections 3.4.2 and 3.5.1). In addition, the unloading-reloading cycles conducted revealed that the *Ic-0* series response was not elastic and that inelastic, irrecoverable deflections took place; its behavior could therefore be described as ductile. The capability of the *Ic-0* WFJs to dissipate energy under local bending, for a monotonic loading case and taking into consideration their viscoelastic behavior, is analyzed to assess their ductility.

Figure 3.2(c) can serve to schematically illustrate the energy dissipation behavior of the WFJs under monotonic loading. The envelopes of the experimental load-deflection relationships from Figure 3.9(b) were assumed to be representative of the monotonic behavior and were thus considered to obtain the total energy provided to the WFJs, W_t , up to the considered displacement δ_{max} . The unloading paths were used to obtain the dissipated energy, W_d (W_d equals the area enclosed by the loading and unloading paths). The calculated W_t and W_d per unit width are represented in Figure 3.15. The W_t/b and W_d/b values, in J/mm, can be approximated as a function of δ_{max} (mm) by power functions as follows:

$$\frac{W_i}{b}(\delta_{max}) = a_i \cdot \delta_{max}^{c_i} \quad (3.10)$$

where $i = t$ (total energy) or d (dissipated energy) and a_i and c_i are calibration parameters fitted to the experimental results ($c_i = 1.285/1.405$ and $a_i = 0.0108/0.0047$ J/mm^(1+c) for $i = t/d$, respectively). The obtained c values indicated that W_t/b and W_d/b augmented with increasing cycle displacement ($c > 0$) at an increasing rate ($c > 1$), showing that for the same displacement increment more work has to be performed and more energy is dissipated at



< Figure 3.15 – Total and dissipated energies per unit width during monotonic loading.

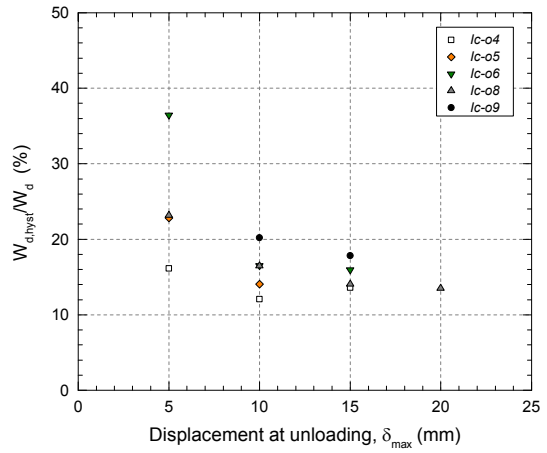


> Figure 3.16 – Ratio of hysteretic to total dissipated energy throughout cycles.

higher than at lower deflection levels. Figure 3.15 shows that good agreement existed between the experimental results and the power empirical model from Equation (3.10) and indicates that the elastic energy W_e per unit width increased with increasing cycle displacement. The augmentation of W_d/b was related to the decrease of stiffness and increase of recovered deflection throughout the cycles (see Sections 3.4.2 and 3.5.2).

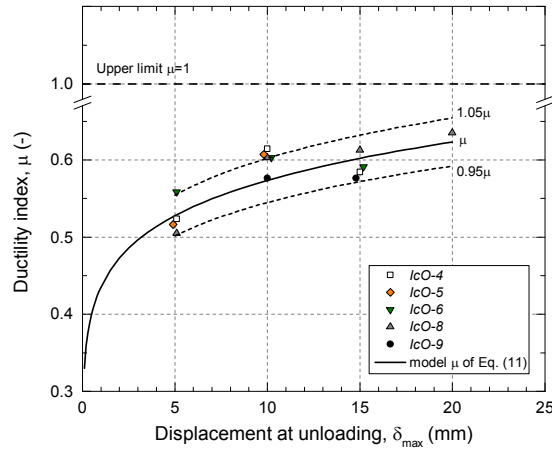
The ratio of the hysteretic energy to the total dissipated energy up to the relevant cycle, $W_{d,hyst} / W_d$, is given in Figure 3.16 throughout the conducted cycles. Figure 3.16 shows that the energy dissipation due to the viscoelastic behavior (related to $W_{d,hyst}$) was below 40% of the total dissipated energy at early displacement stages and that this ratio decreased rapidly with increasing maximum cycle displacement down to approximately 15% at failure. This showed that damage and the associated crack development represented the main dissipation mechanism of the WFJs, whereas the amount of energy dissipated through viscoelasticity was low except for small displacements, when cracking was still incipient.

The ductility index for the $Ic-o$ WFJs throughout loading ($0 \leq \delta_{max} \leq 20$ mm) was calculated using the energy values per unit width and hence substituting Equation (3.10) into Equation (3.3) as follows:

$$\mu = \frac{a_d}{a_t} \cdot \delta_{max}^{c_d - c_t} \tag{3.11}$$

where d and t subscripts denote the dissipated and total energy, respectively. The model from Equation (3.11) is represented in Figure 3.17. A good agreement with the experimental results was observed – they were within $\pm 5\%$ of the modeled values. The modeled ductility index increases with increasing maximum displacement, although at a decreasing rate ($0 < (c_d - c_t) < 1$). As a result, the predicted ductility index for specimens failing at a 10-mm displacement (e.g. $Ic-06$) represented approximately 91% of the predicted value for those failing at 20 mm (e.g. $Ic-08$) – ductility indices of 0.57 and 0.62 corresponded to 10- and 20-mm δ_{max} , respectively. This suggests that the ratio between the dissipated and total energies – and therefore the ratio between any two of the dissipated, elastic and total energies – did not significantly vary after a certain displacement was attained (9% increase for W_d/W_t from

Figure 3.17 – Ductility index for *Ic-o* WFJs throughout displacement. $\mu = 1$ indicates rigid-plastic behavior.



10- to 20-mm δ_{max} at an approximately constant rate of 0.049/mm). This was attributed to the constant recovery and damage rates observed: nearly constant $\delta_{r,o}/\delta_{max} \approx 0.72$, $\delta_{r,del}/\delta_{max} \approx 0.05$ and $\delta_{res}/\delta_{max} \approx 0.23$ ratios, related to W_e , $W_{d,hyst}$ and $W_{d,dam}$ respectively, were obtained (see Section 3.5.2).

The ductility index of the *DS* deck in its transverse-to-pultrusion direction was compared to that of the *Ic-o* WFJs. The load-deflection response of the *DS* beams under three-point bending is shown in Figure 3.1. The last cycle providing data on the unloading path prior to failure was conducted at an approximately 30-mm displacement and 11.5-kN load, which correspond to 88% of the beam's failure load and 40% of its ultimate mid-span displacement. The ductility index for the full-scale beam, μ_{beam} was calculated according to Equation (3.3) for that cycle. A value of $\mu_{beam} = 0.43$ was obtained. The ductility index of the *Ic-o* WFJs at 40% of its displacement at the peak load (see δ_{ult} in Table 3.3), i.e. at $\delta_{max} \approx 7$ mm, was $\mu = 0.55$ according to Equation (3.11) and Figure 3.17. The μ_{beam} value represented 78% of the corresponding ductility index of the *Ic-o* WFJs. The lower μ_{beam} may be attributed to the existence of several WFJ types in the *DS* deck. The studied *DS* beams comprise only two *Ic-o* WFJs (see Figure 3.4); other WFJ types may exhibit a different behavior – e.g. the *If-o* WFJs studied here showed a brittle behavior.

3.6 Conclusions

The behavior under local bending of two types of web-flange junctions (WFJs) from the *DS* deck (*If-o* and *Ic-o* series), the recovery subsequent to unloading and the energy dissipation capacity, under monotonic loading, of one of them showing progressive failure (*Ic-o*) were experimentally studied. The following conclusions were drawn:

1. Initial imperfections can significantly affect the local behavior of WFJs in pultruded GFRP decks. For the *DS* deck, dissimilar initial imperfections resulted in different local bending behavior in two WFJ types with similar geometry and fiber architecture (*If-o*, *Ic-o*). The WFJ response changed from brittle (*If-o*) to ductile (*Ic-o*).

2. The WFJs failed due to transverse (through-thickness) tension in their tensioned fillet. The *If-o* specimens showed a 22% lower peak load than the *Ic-o* specimens due to a less even distribution of the load-bearing fabrics across the web element thickness.
3. The *Ic-o* specimens showed significant recovery: approximately 77% of the attained deflection was reversible. A small influence of the FRP viscoelastic properties was observed (nearly 7% of the total recovery did not occur instantaneously). The damage rate in the *Ic-o* series, associated with the irreversible deflection, was constant throughout the loading process.
4. The delayed recovered deflection was modeled using the Weibull distribution function. The model agreed well with the experimental results.
5. A power model was developed for modeling the total and dissipated energies of the *Ic-o* WFJs under monotonic loading. Higher rates at higher displacement levels were obtained for both the total and dissipated energies.
6. The *Ic-o* WFJs dissipated at failure up to 62% of the total energy provided. The ductility index, defined as the ratio of the dissipated to the total energy, did not significantly increase as from a 10-mm displacement. This was related to the constant recovery and damage rates of the specimens with increasing deflection.
7. The main energy dissipation mechanism of the *Ic-o* WFJs was related to the crack development. Given the viscoelastic nature of FRP materials, dissipation through viscoelastic losses did also occur. The viscoelastic contribution to energy dissipation was significant at low deflection levels, when cracking was still incipient; however, it rapidly decreased to approximately 15% with increasing displacement and progression of cracking.

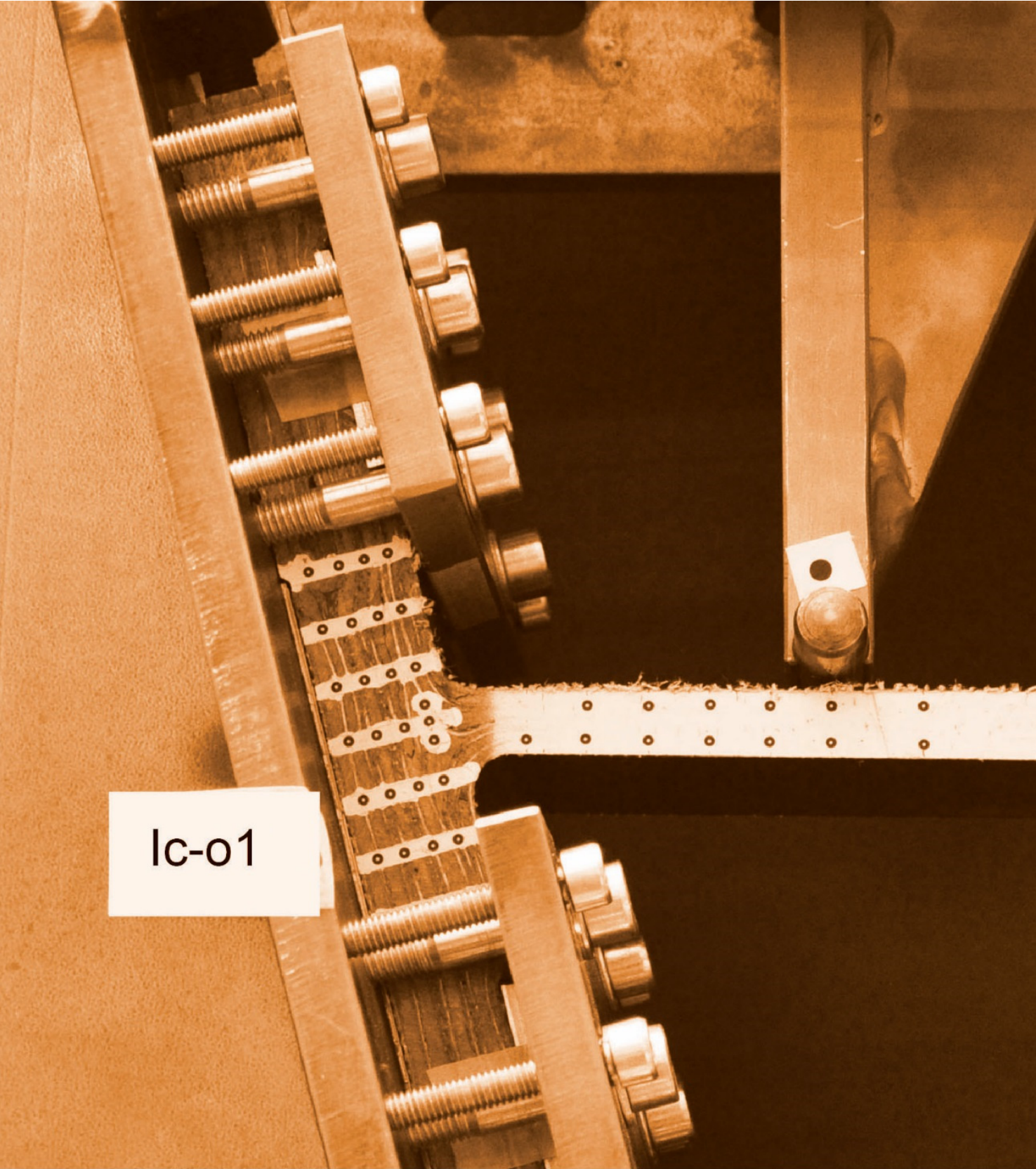
Further research is required to evaluate the influence of the viscoelastic character of the FRP material on the energy dissipation capability of the WFJs when subjected to cyclic loading. Under cyclic loading up to a previously established load/displacement level, dissipation through viscosity-related losses can occur without any damage increase; thus, the energy dissipation owing to the material viscoelasticity may be better exploited.

References

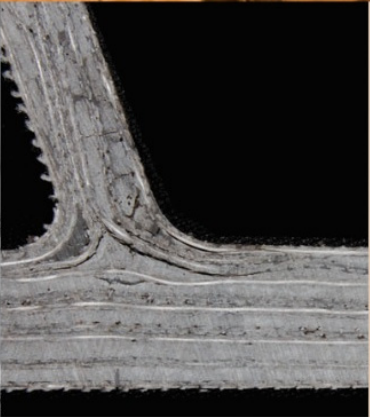
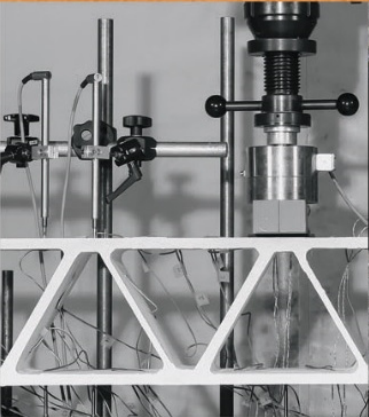
1. Hollaway L. A review of the present and future utilisation of FRP composites in the civil infrastructure with reference to their important in-service properties. *Constr Build Mater* 2010;24(12):2419–2445.
2. Keller T. Recent all-composite and hybrid fibre-reinforced polymer bridges and buildings. *Prog Struct Eng* 2001;3(2):132–140.
3. Keller T, de Castro J. System ductility and redundancy of FRP beam structures with ductile adhesive joints. *Compos Part B* 2005;36(8):586–596.
4. Bank LC. Progressive failure and ductility of FRP composites for construction: review. *J Compos Constr* 2013;17(3):406–419.
5. Van Erp GM. Robustness of fibre composite structures loaded in flexure. In: Teng JG (ed.) *FRP composites in civil engineering: Proceedings of the International Conference on FRP Composites in Civil Engineering*, 12–15 December 2001, Hong Kong, China. Amsterdam: Elsevier; 2001. p.1421–1426.

6. Czél G, Wisnom MR. Demonstration of pseudo-ductility in high performance glass/epoxy composites by hybridisation with thin-ply carbon prepreg. *Compos Part A* 2013;52:23–30.
7. Swolfs Y, Gorbatiikh L, Verpoest I. Fibre hybridisation in polymer composites: a review. *Compos Part A* 2014;67:181–200.
8. Bunsell AR, Harris B. Hybrid carbon and glass fibre composites. *Composites* 1974;5(4):157–164.
9. Bakis CE, Nanni A, Terosky JA, Koehler SW. Self-monitoring, pseudo-ductile, hybrid FRP reinforcement rods for concrete applications. *Compos Sci Technol* 2001;61(6):815–823.
10. Yu H, Longana ML, Jalalvand M, Wisnom MR, Potter KD. Pseudo-ductility in intermingled carbon/glass hybrid composites with highly aligned discontinuous fibres. *Compos Part A* 2015;73:35–44.
11. Tepfers R, Tamužs V, Apinis R, Vilks U, Modniks J. Ductility of nonmetallic hybrid fiber composite reinforcement for concrete. *Mech Compos Mater* 1996;32(2):113–121.
12. Harris HG, Somboonsong W, Ko FK. New ductile hybrid FRP reinforcing bar for concrete structures. *J Compos Constr* 1998;2(1):28–37.
13. Fuller JD, Wisnom MR. Pseudo-ductility and damage suppression in thin ply CFRP angle-ply laminates. *Compos Part A* 2015;69:64–71.
14. Keller T, Gürtler H. Quasi-static and fatigue performance of a cellular FRP bridge deck adhesively bonded to steel girders. *Compos Struct* 2005;70(4):484–496.
15. Keller T, Gürtler H. Composite action and adhesive bond between fiber-reinforced polymer bridge decks and main girders. *J Compos Constr* 2005;9(4):360–368.
16. de Castro J, Keller T. Ductile double-lap joints from brittle GFRP laminates and ductile adhesives, Part I: Experimental investigation. *Compos Part B* 2008;39(2):271–281.
17. Triantafillou T, Meier U. Innovative design of FRP combined with concrete. In: Neale K, Labossière P (eds.) *Advanced composite materials in bridges and structures. ACMBBS: 1st international conference*. 1992, Sherbrooke, Canada. Montréal: Canadian Society of Civil Engineers; 1992. p.491–499.
18. Chen D, El-Hacha R. Damage tolerance and residual strength of hybrid FRP-UHPC beam. *Eng Struct* 2013;49:275–283.
19. Keller T, Gürtler H. In-plane compression and shear performance of FRP bridge decks acting as top chord of bridge girders. *Compos Struct* 2006;72(2):151–162.
20. Mertens KO. *Experimental studies of the progressive tearing failure of pultruded FRP composite tubes in flexure* [M.S. thesis]. University of Wisconsin-Madison, USA; 2003.
21. Bank LC, Nadipelli M, Gentry TR. Local buckling and failure of pultruded fiber-reinforced plastic beams. *J Eng Mater Technol* 1994;116(2):233–237.
22. Turvey GJ, Zhang Y. A computational and experimental analysis of the buckling, postbuckling and initial failure of pultruded GRP columns. *Comput Struct* 2006;84(22-23):1527–1537.
23. Mosallam AS, Bank LC. Short-term behavior of pultruded fiber-reinforced plastic frame. *J Struct Eng* 1992;118(7):1937–1954.
24. Yanes-Armas S, de Castro J, Keller T. System transverse in-plane shear stiffness of pultruded GFRP bridge decks. *Eng Struct* 2016;107:34–46.
25. Gibson RF. *Principles of composite material mechanics*. Boca Raton: CRC Press; 2011.
26. Widyatmoko I, Ellis C, Read JM. Energy dissipation and the deformation resistance of bituminous mixtures. *Mater Struct* 1999;32(3):218–223.
27. Grace NF, Soliman AK, Abdel-Sayed G, Saleh KR. Behavior and ductility of simple and continuous FRP reinforced beams. *J Compos Constr* 1998;2(4):186–194.
28. De Lorenzis L, Galati D, La Tegola A. Stiffness and ductility of fibre-reinforced polymer-strengthened reinforced concrete members. *Proc ICE-Struct Build* 2004;157(1):31–51.
29. DARPA. Advanced composites for bridge infrastructure renewal - Phase II, Task 16 - Modular composite bridge. USA: Defense Advanced Research Projects Agency; 2000.

30. Keller T, Schollmayer M. Through-thickness performance of adhesive joints between FRP bridge decks and steel girders. *Compos Struct* 2009;87(3):232–241.
31. Turvey GJ, Zhang Y. Characterisation of the rotational stiffness and strength of web-flange junctions of pultruded GRP WF-sections via web bending tests. *Compos Part A* 2006;37(2):152–164.
32. Fancey KS. A mechanical model for creep, recovery and stress relaxation in polymeric materials. *J Mater Sci* 2005;40(18):4827–4831.
33. Jia Y, Peng K, Gong XI, Zhang Z. Creep and recovery of polypropylene/carbon nanotube composites. *Int J Plasticity* 2011;27(8):1239–1251.



lc-01



Chapter 4

Rotational stiffness of web-flange junctions

4.1 Introduction

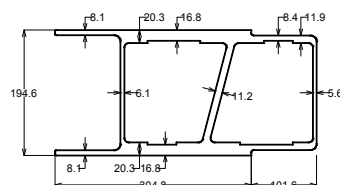
Glass fiber-reinforced polymer (GFRP) bridge decks nowadays constitute one of the most developed and extended applications of FRP materials for primary, load-bearing structural members in the civil engineering domain. Since the 1990s, GFRP bridge decks have been increasingly employed in road and footbridges, both for new construction and rehabilitation purposes, due to favorable characteristics in comparison with decks composed of traditional structural materials – e.g. reinforced concrete (RC) or steel. Advantages of GFRP materials when used for bridge slabs include high specific strength and low self-weight. GFRP decks weight about 10–20% of the structurally equivalent RC deck,¹ which in replacement applications allows increase of the live load capacity via dead load reduction. Other main advantages of GFRP materials for deck applications comprise high fatigue resistance, improved durability and corrosion resistance, which result in low bridge maintenance and reduced life-cycle costs. Furthermore, GFRP decks offer manufacturing versatility (the cross-sectional geometry can be designed and/or the material constituents and fiber architecture tailored to meet structural requirements) and allow high construction speed with minimized traffic disruption times.^{1,2} Reviews regarding the development and implementation of several all-FRP and hybrid FRP-concrete deck systems have been presented by several authors and can be found in the literature.^{1–4}

GFRP bridge decks fulfill two structural functions, namely: (i) distribution and transmission of the traffic loads applied to the bridge to the underlying superstructure; (ii) participation in load transfer in the bridge's longitudinal direction by acting as the top chord of the main girders when there is sufficient composite action between the girder and deck. The latter function is particularly relevant in the case of concrete deck replacement – supplementary

strengthening of the main girders is required if the upper chord function is not maintained. Pultruded GFRP deck systems exhibit orthotropic behavior owing to material orthotropy and different load-bearing mechanisms in their longitudinal (parallel to pultrusion) and transverse (perpendicular to pultrusion) directions. Their performance concerning the above-mentioned two structural functions is influenced by the deck's transverse behavior. The deck system's orthotropy ratio and therefore its structural performance as a slab depend on the contribution of the transverse-to-pultrusion direction to carrying applied concentrated loads.⁵ The deck's participation as the upper chord of main girders is affected by its transverse in-plane shear stiffness, which governs the shear transmission within the deck (from its bottom to its top flange) in the bridge's longitudinal direction.⁶

In a previous investigation,⁷ the behavior in the transverse-to-pultrusion direction of a GFRP deck with trapezoidal cell geometry, *DS*, was experimentally studied. The cross section of the *DS* unit module profile consists of a rectangle shaped into two trapezoidal cells by a slightly inclined inner web connected to the deck's flanges, as shown in Figure 4.1. The slab is formed by adhesively bonding the dual-cell unit profiles along their vertical (outer) webs using a structural polyurethane adhesive, see Figure 4.2(a). The loading configuration used and the load-deflection response recorded at mid-span are illustrated in Figures 4.2(a) and 4.2(c), respectively. The load transfer mechanism, failure mode and system transverse in-plane shear stiffness were investigated. The deck exhibited a frame-governed behavior whereby the load was mainly transmitted by local shear and bending moments in the web and flange elements (Vierendeel frame mechanism). Progressive cracking occurring in the web-flange junctions (WFJs) resulted in a stiffness reduction without leading to the deck's final failure. The sequence of the cracks observed, their location and the corresponding load levels are shown in Figures 4.2(a) and 4.2(c), on the right side. A non-brittle failure was observed and a sustained load-bearing capacity under the development of large displacements was recorded owing to the system redundancy – gradual local bending failures occurred in the WFJs. The system transverse in-plane shear modulus, before any local failure was detected, was estimated from the experimental deflection data based on existing equations for composite beams with flexible shear connections that were originally developed for timber-concrete composite girders. The thus calculated in-plane shear modulus agreed well with the experimentally determined value reported by Gurtler from in-plane shear experiments,⁶ see Figures 4.2(b) and 4.2(d).

Figure 4.1 – Unit module geometry of *DS* bridge deck system; dimensions in mm.



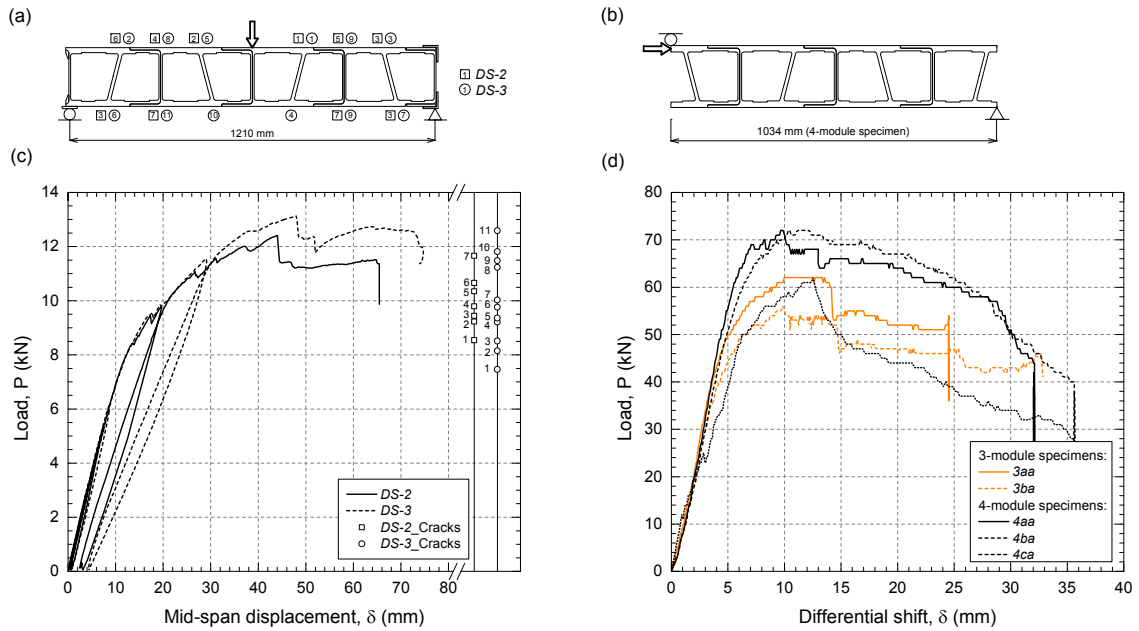


Figure 4.2 – Experimental configuration for *DS* deck specimens subjected to transverse (a) three-point bending and (b) in-plane shear; load-displacement behaviors under (c) three-point bending and (d) in-plane shear.^{6,7}

The aforementioned research provided a comprehensive basis for the evaluation, by means of further models, of the bidirectional behavior of decks and the composite behavior of hybrid beams with GFRP decks acting as their top chord. Prospective models for the *DS* deck should consider additional local features, i.e. the rotational behavior of the WFJs, since the nonlinearity of its global transverse bending behavior originated from progressive cracking in the WFJs prior to final failure. Moreover, the above-mentioned procedure to calculate the transverse in-plane shear modulus is restricted to the linear elastic range behavior. Nevertheless, the in-plane shear modulus of *DS* may not be constant (nonlinear in-plane shear behavior) due to gradual local failures in the WFJs.^{6,7} The local rotational response and strength of the *DS* WFJs is unknown, however. The characterization of the WFJ rotational behavior is therefore required in order to develop reliable numerical models for accurately predicting both the initially linear (before any cracking occurrence) and subsequently nonlinear transverse behavior of the deck.⁸ Once the models are developed, the complete characterization of the system in-plane shear modulus up to failure would be possible and its effects on the global performances of both the slab (orthotropy ratio) and hybrid girder (composite action) could be assessed.

The WFJ characterization has been highlighted as a topic of interest for research on FRP pultruded profiles. The local behavior of the WFJs, with distinctive fiber architecture and material properties, has been found to be crucial for the global performance of both steel-like open-/closed-section elements and multicellular closed-section profiles for bridge decks. Experimental investigations, computational studies and analytical models of GFRP pultruded beams and short columns have shown that the WFJ local behavior may affect the overall pre-buckling/post-buckling behavior of the element as well as its local buckling response.^{9–14} In the investigation conducted by Wu and Bai,¹⁵ failures at the WFJs were observed as first failure

modes, limiting the load-bearing capacity of GFRP square hollow sections subjected to concentrated transverse loading. Similarly, shear failure at the WFJs was reported by Borowicz and Bank¹⁶ for pultruded GFRP I-beams subjected to concentrated loads in the plane of the web and constrained in the lateral direction to prevent any lateral/torsional instability. Local failures at the WFJs of angle sections used for moment-resisting connections (e.g. beam-to-column and base-to-column connections) can be critical for their stiffness and strength.¹⁷ Failure of the web-flange junctions has been reported by several researchers as the governing failure mechanism of pultruded decks with rectangular cross section subjected to transverse bending;^{18,19} a later study by Zi et al.²⁰ demonstrated that strengthening the web-flange junction could change the failure mode to delamination in the profile-to-profile bondline.

The mechanical properties of the FRP material in the WFJ area may differ from those of the flat web/flange laminates owing to a number of specific fiber architecture features: (i) the fiber layers in the junction area are curved and (ii) thus more prone to wrinkling than those in the flat laminates; (iii) there is a roving-/resin-rich region at the WFJ; (iv) the WFJ region may be subject to a higher risk of local imperfections.^{13,21,22} Experimental studies of the mechanical behavior of the WFJs of pultruded beams have demonstrated that the tensile tearing, shear and flexural strengths in the junction area may be lower than the corresponding strength values of the web/flange laminates.^{21,23,24} The need of characterizing the mechanical properties of the WFJ region and their consideration for the structural design of FRP pultruded members have been stated by various researchers.^{11,22,25}

In the last decade, several experimental investigations aiming to characterize the axial,^{23,26} shear²⁴ and rotational^{21,22,27} behavior of the WFJs of pultruded profiles have been conducted. With regard to the rotational behavior, Turvey and Zhang²¹ investigated the rotational stiffness and strength of the WFJs of pultruded H-profiles by means of bending experiments performed in the web element under simply supported and clamped flange conditions. A test fixture to load the WFJ area of H- and L- profiles under local bending moment in order to evaluate its rotational strength and moment-rotation behavior was proposed in a more recent experimental study by Mosallam et al.²² The experimental results obtained are limited to the investigated profiles and, in the author's view, conditioned by the experimental approaches used. In the investigation conducted by Turvey and Zhang,²¹ final failure of the specimens did not occur in the WFJs – it took place in the web element due to flexural tension cracking, as propagation of early cracking occurring in the WFJ was prevented by the clamping of the flange close to the junction – and the calculated rotational stiffness values included the effect of the web's shear deformation. Furthermore, the experimental procedure simultaneously involved the two WFJs of each profile and assumed that they exhibited equal behavior. The test rig employed by Mosallam et al.²² was considered not to represent the actual boundary conditions for the flange element of an H-profile – it was pre-compressed in its through-thickness direction, which may have affected both the strength and observed failure mode. In a recent investigation by Xin et al.,²⁷ the WFJ rotational behavior was

characterized by performing cantilever experiments on the web elements. The proposed experimental set-up overcame the abovementioned limitations of the experimental configurations previously used by other researchers.^{21,22} However, the deflection component(s) used for the calculation of the relative rotation between the web and the flange elements are not explicitly defined; it is therefore not clear if other effects else than the WFJ rotational flexibility (i.e. bending/shear deformation of the web, rotation of the unclamped flange area near the junction) are included in the thus calculated WFJ rotational stiffness.

The objective of this work was to characterize the rotational behavior of the *DS* WFJs. Taking into account the *DS* unit profile's detailed geometry shown in Figure 4.1, three types of WFJs can be identified, corresponding to the adhesively-bonded vertical outer webs and the top/bottom part of the inclined inner web. The three WFJ types were investigated in two bending moment directions each. A method to experimentally obtain the rotational stiffness of the WFJs based on simple analytical models was used. The experimental approach comprised three stages: (i) first, three-point bending experiments with simply supported end conditions were conducted on the web elements; (ii) then, web-cantilever bending experiments were performed; (iii) finally, the WFJ moment-rotation relationships were calculated from the load-deflection data. Simplified expressions to model the WFJ rotational behavior were derived. Lastly, the validity of the obtained moment-rotation relationships was assessed by means of numerical simulations of the abovementioned full-scale experiments conducted on the *DS* deck.

4.2 Experimental program

The investigation is based on small-scale experiments conducted on the web-flange junctions (WFJs) of the DuraSpan (*DS*) pultruded GFRP bridge deck system,²⁸ manufactured by Martin Marietta Composites Inc. (Raleigh, United States). The cross section of the *DS* unit module profile is shown in Figure 4.1. The *DS* deck is composed of E-glass fibers embedded in an isophthalic polyester resin; the total fiber content by weight is 60%.²⁸

4.2.1 Experimental approach

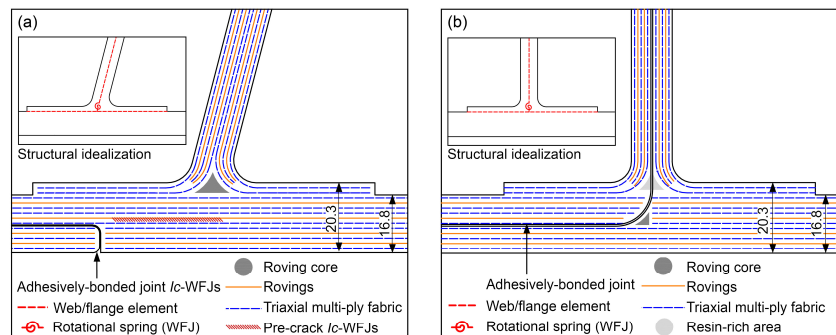
Each *DS* WFJ may be defined by three convergent elements (one web and two flange segments). The typical fiber architecture of the WFJ area, consisting of three types of fiber reinforcements (rovings in the pultrusion direction, triaxial multi-ply fabrics and additional non-structural mats), is illustrated in Figure 4.3. The triaxial multi-ply fabrics run parallel to the flange laminate without any direction change; they are continuous within each unit profile and interrupted at the bondline between adjacent profiles, see bottom/top part of the flange laminate in Figure 4.3(a)/(b). Two thirds of the triaxial multi-ply fabrics from the web laminate are prolonged into the flange; hence, the flange thickness is larger close to the WFJ – 20.3 mm versus 16.8 mm. There is an approximately triangular-shaped roving core (inclined webs) or resin-rich area (vertical webs) at the center of the WFJ.

Based on the described fiber architecture, the flange can be considered as being continuous across the WFJ, i.e. no relative rotation occurs between the ends of the two converging flange segments – no direction change occurs in the flange fabrics and at least approximately half of them are uninterrupted at the WFJ. The adhesively-bonded joint in the flange element in itself was not expected to affect the flange behavior at the WFJ intersection – it is situated away from that location in the inclined webs; in the case of the vertical webs, independent movements of the two adhesively-bonded flange laminates may be restrained close to the WFJ by the reciprocal constraints between adjacent profiles. On the other hand, the web's end may exhibit a certain rotational flexibility due to: (i) the lack of fiber continuity towards the flange; (ii) the change of direction of the prolonged fabrics, whose radii of curvature vary from infinite in the flange/web laminates to finite close to the junction; (iii) the roving core / resin-rich area, see Figure 4.3. The end condition of the web can thus be considered as a semi-rigid joint whose rotational behavior is described by the relationship between the local bending moment applied to the web's end, M , and the relative rotation between the web and the flange elements, φ . Hence, the web's end can be modeled in the form of a rotational spring represented by the moment-rotation (M - φ) relationship.

Rotational springs exhibiting linear elastic behavior obey the rotational form of Hooke's law and their M - φ relationship can be formulated using a constant factor, K^{rot} , the rotational stiffness of the spring – K^{rot} is defined as the moment to be applied to the spring to produce a unit rotation in it. The rotational stiffness thus defined would be equal to zero for a simply supported end condition (pinned), equal to infinity for a rigid end condition (fixed) and equal to a finite value different from zero in the general case of a semi-rigid end condition. Rotational springs showing nonlinear behavior cannot be described by using a single and constant K^{rot} value. The entire M - φ relationship throughout loading is required instead.

The DS WFJs were expected to exhibit nonlinear rotational behavior – previous studies showed that progressive cracking occurred in the WFJ region.^{7,29} The complete M - φ relationship characterizing the rotational stiffness of the WFJs can be determined from the experimental data (load, deflection, set-up geometry) of symmetric three-point bending beam and cantilever experiments conducted on the web element, providing that the two following conditions are satisfied: (i) the cantilever span length, L_{cants} , equals half of the beam span length, L_{3pb} ; (ii) the ratio of the maximum beam load

Figure 4.3 – Fiber architecture and structural idealization of WFJs with (a) inclined and (b) vertical webs; dimensions in mm.



to the maximum cantilever load is equal to or higher than two. Span lengths of $L_{3pb} = 130$ mm and $L_{cant} = 65$ mm were defined based on the webs' lengths and the dimensional requirements of the experimental set-ups. The rotational stiffness can be derived from the experimental responses obtained by using simple analytical beam models applicable to the above-mentioned experimental configurations. The first model is that of a simply supported beam under three-point bending, which can be analyzed as two fixed cantilever beams symmetrically placed in relation to mid-span; the second analysis model is that of a cantilever with semi-rigid end condition, whose rotational stiffness equals that of the WFJ.

Simply supported beam model

Figure 4.4(a) illustrates a simply supported beam of L_{3pb} span length subjected to symmetric three-point bending. The applied load, the vertical reactions at the supports and the mid-span deflection are denoted by P_{3pb} , R_{3pb} and δ_{3pb} , respectively.

The simply supported beam shown in Figure 4.4(a) can be considered as two cantilevers of $L_{cant} = L_{3pb}/2$ length with fixed end and symmetrically placed about mid-span, see Figure 4.4(b). The applied load, the vertical reaction at the support and the deflection under the load application point in the cantilever configuration are denoted by P_{cant} , R_{cant} and $\delta_{cant,f}$ respectively.

The comparison of Figures 4.4(a) and 4.4(b) shows that equal deflections are obtained for both configurations given that $P_{cant} = R_{3pb}$, i.e., $P_{cant} = P_{3pb}/2$. This equality can be expressed as:

$$\delta_{cant,f}(P_{cant}) = \delta_{3pb}(2P_{cant}) \quad (4.1)$$

Semi-rigid end cantilever model

Figure 4.4(c) illustrates a cantilever beam with semi-rigid end condition. The semi-rigid end is modeled as a rotational spring. The deflection of the partially fixed cantilever under the load application point, $\delta_{cant,sr}$, can be formulated as:

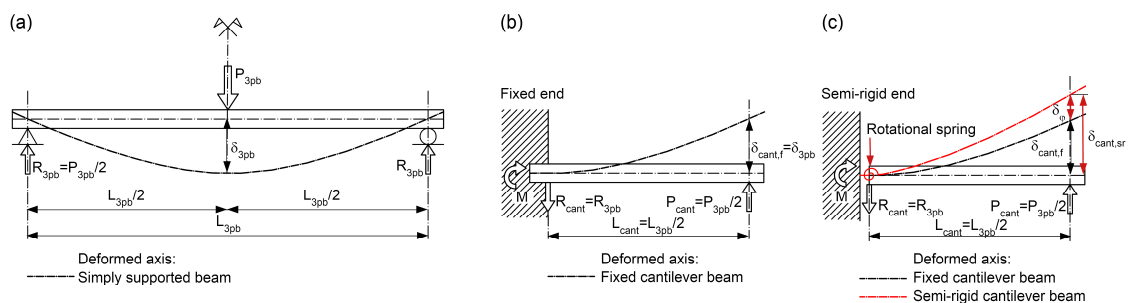
$$\delta_{cant,sr}(P_{cant}) = \delta_{cant,f}(P_{cant}) + \delta_{\varphi}(P_{cant}) \quad (4.2)$$

where $\delta_{cant,f}$ = deflection of the fixed end counterpart (same span length, L_{cant} , and subjected to the same load, P_{cant}), δ_{φ} = deflection caused by the rotation in the semi-rigid end.

Rotational stiffness from simply supported beam and semi-rigid end cantilever models

Equation (4.2) shows that two cantilever beams of the same span length (L_{cant}) and subjected to the same load (P_{cant}), but with different end conditions (fixed

Figure 4.4 – Models of (a) simply supported beam under symmetric three-point bending; (b) cantilever beam with fixed end; (c) cantilever beam with semi-rigid end.



and semi-rigid, respectively), exhibit a difference in deflection equal to δ_φ at the P_{cant} load level, hence dependent on the rotational stiffness of the semi-rigid end:

$$\delta_{cant, sr}(P_{cant}) - \delta_{cant, f}(P_{cant}) = \delta_\varphi(P_{cant}) \quad (4.3)$$

Substituting Equation (4.1) in Equation (4.3), δ_φ at a given P_{cant} load can be expressed as:

$$\delta_\varphi(P_{cant}) = \delta_{cant, sr}(P_{cant}) - \delta_{3pb}(2P_{cant}) \quad (4.4)$$

Additionally, δ_φ can be calculated as a function of the rotation in the semi-rigid end, φ , as:

$$\delta_\varphi = L_{cant} \cdot tg(\varphi) \quad (4.5)$$

Therefore, by replacing Equation (4.4) in Equation (4.5), φ can be formulated as a function of the deflections, under the load application points, in the simply supported beam and the semi-rigid end cantilever configurations as:

$$\varphi = arctg\left(\frac{\delta_\varphi(P_{cant})}{L_{cant}}\right) = arctg\left(\frac{\delta_{cant, sr}(P_{cant}) - \delta_{3pb}(2P_{cant})}{L_{cant}}\right) \quad (4.6)$$

The bending moment acting in the semi-rigid end, M (see Figure 4.4(c)), can be calculated as the product of the applied load and the distance from the load application point to the support (lever arm):

$$M = P_{cant} \cdot L_{cant} \quad (4.7)$$

The rotational stiffness of the WFJs is characterized by the complete M - φ relationship. The web element is considered to be semi-rigidly connected to the flange element, which is continuous across the WFJ. In accordance with the preceding explanations, the M - φ relationship of the WFJ can be obtained from the recorded loads, measured deflections and set-up geometry of three-point bending beam and cantilever experiments performed on the web element, providing that $L_{cant} = L_{3pb}/2$. First, the web is subjected to three-point bending with simply supported end conditions and a $L_{3pb} = 130$ -mm span length (model explained in the first subsection of Section 4.2.1). Subsequently, the web-cantilever experiment is conducted with a $L_{cant} = 65$ -mm lever arm – the WFJ is considered as a rotational spring and the experiment responds to the model referred to in the second subsection of Section 4.2.1. Finally, the WFJ moment-rotation relationship is calculated from the load-deflection data, by applying Equations (4.6) and (4.7) throughout the whole P_{cant} - $\delta_{cant, sr}$ range and the corresponding P_{3pb} - δ_{3pb} ($2P_{cant}$ - δ_{3pb}) range.

4.2.2 Specimen description and preparation

Two groups of WFJs can be differentiated in the *DS* deck depending on the corresponding web geometry: vertical (*V*) and inclined (*I*). The latter can be classified into two types according to the closer (*c*) / farther (*f*) location of the adhesively-bonded profile-to-profile joint in the flange in relation to the web, see Figure 4.5(a).

The rotational stiffness of the three WFJ types (*Ic*, *If*, *V*) was investigated. Both directions of the local bending moment applied to the web element were

considered. An additional character is used for specimen appellation to indicate the direction of the web's bending moment: the tensioned side of the web towards the obtuse/acute angle (*I*-WFJs) or towards the double (adhesively-bonded) / single flange laminate (*V*-WFJs) is denoted by *o/a* and *d/s*, respectively, see Figure 4.5(a). The experimental program was performed on three specimens from each of the six series. Figure 4.5(a) shows the specimens' overall geometry and Figure 4.5(b) their location within the deck panel of the preceding beam experiments.⁷ The material properties of the flange and web elements²⁸ are listed in Table 4.1.

The WFJ specimens were prepared from a *DS* deck panel comprising four unit module profiles supplied for a previous investigation.³⁰ The specimens were machined in two phases by means of a diamond-coated disk-saw: (i) four

Figure 4.5 – (a) WFJ specimens; (b) location of WFJ specimens within *DS* deck panel when subjected to transverse bending (local bending moments in webs are shown); dimensions in mm.

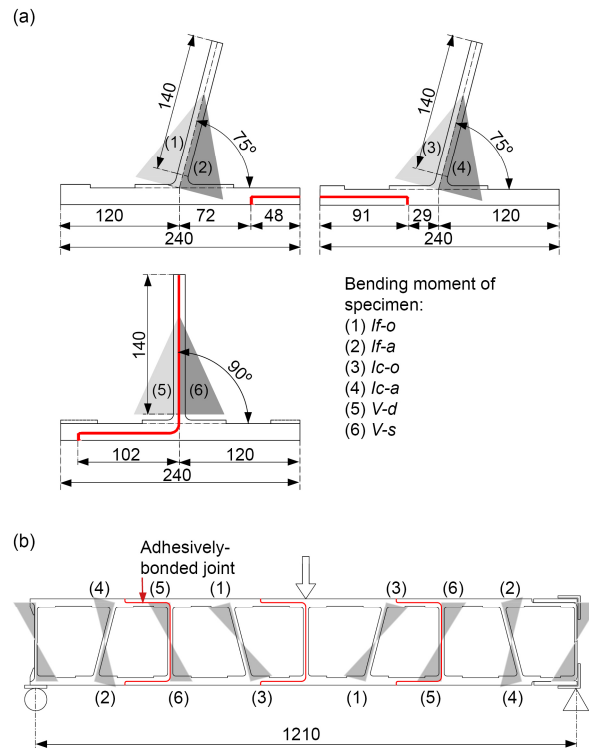


Table 4.1 – Material properties of *DS*.²⁸

Property	Unit	Flanges	Vertical (bonded) webs	Inclined (single) webs
$E_{t,x}$	MPa	21 240	17 380	17 380
$E_{t,y}$	MPa	11 790	9 650	9 650
		[12 980 ^(a)]	[14 910 ^(a)]	[16 350 ^(a)]
$E_{t,z}$	MPa	4 140	4 140	4 140
G_{xy}	MPa	5 580	7 170	7 170
$G_{xz} = G_{zy}$	MPa	600	600	600
ν_{xy}	-	0.32	0.30	0.30
$\nu_{xz} = \nu_{zy}$	-	0.30	0.30	0.30

x = pultrusion direction; y = perpendicular to pultrusion direction, in-plane; z = through-thickness direction

^(a) Own values, experimentally obtained for 0-0.20% strain range

Note: applicable strain ranges for properties from DARPA²⁸ were not available.

50-mm-wide pieces were cut from the panel perpendicularly to its pultrusion direction; (ii) the WFJ specimens were then cut from these four pieces (each one provided a maximum of three *V*- and three *I*-WFJs). The width (*b*) and thickness (*t_w*) of the specimens' webs were measured prior to conducting the experiments. The average dimensions per series are listed in Table 4.2. The visual inspection of the specimens revealed that initial imperfections existed in the WFJ specimens. Partially bonded areas were apparent in the adhesive layer of the *V*-WFJs and a small crack (referred to as *pre-crack* in the following) existed in the flange of every *I_c* specimen, see Figure 4.3(a). Differences in the actual fiber arrangement of the *I_f*- and *I_c*-WFJs were observed, despite their identical fiber architecture design; these are detailed in a previous work.²⁹

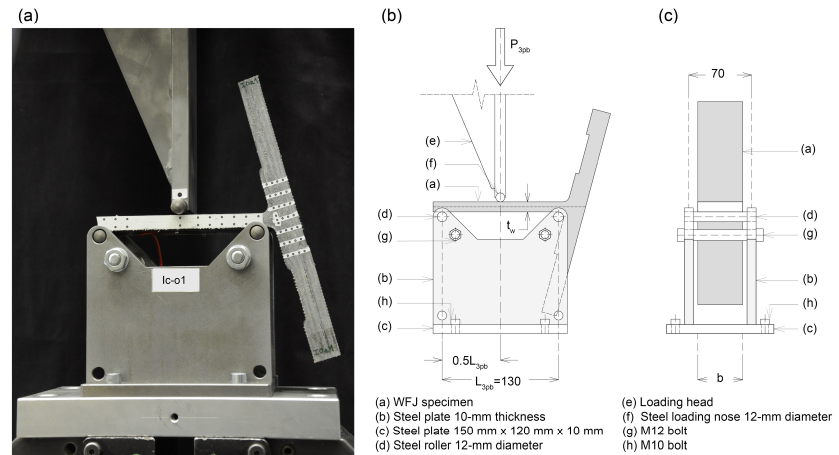
4.2.3 Three-point bending experiments

The webs of the WFJ specimens were loaded in a symmetric three-point bending configuration with simply supported end conditions and a 130-mm span length (*L_{3pb}*), which corresponds to a slenderness ratio ranging from 10.3 to 11.4. The set-up for the three-point bending experiments is shown in Figure 4.6. The test rig consisted of two 10-mm-thick parallel steel plates fixed to the lower platen of the testing machine and transversely connected with 12-mm-diameter bolts. The web was supported across its whole width and perpendicularly to its longitudinal axis on 12-mm-diameter steel rollers spanning between both plates. The vertical load was applied at mid-span via a triangular-shaped loading head bolted to the upper platen of the testing ma-

Table 4.2 – Average dimensions of WFJ specimens.

Series	Web width	Web thickness
	<i>b</i> (mm)	<i>t_w</i> (mm)
<i>I_f-o</i>	49.4±0.2	11.4±0.1
<i>I_f-a</i>	50.5±0.7	11.4±0.1
<i>I_c-o</i>	50.1±1.2	11.4±0.0
<i>I_c-a</i>	50.6±0.6	11.4±0.0
<i>V-d</i>	50.3±1.0	12.6±0.1
<i>V-s</i>	50.4±0.8	12.4±0.1

Figure 4.6 – Set-up for three-point bending experiments; (a) general view (*I_c-o* specimen); (b) front view (*I_c-a* specimen); (c) cross section; dimensions in mm.

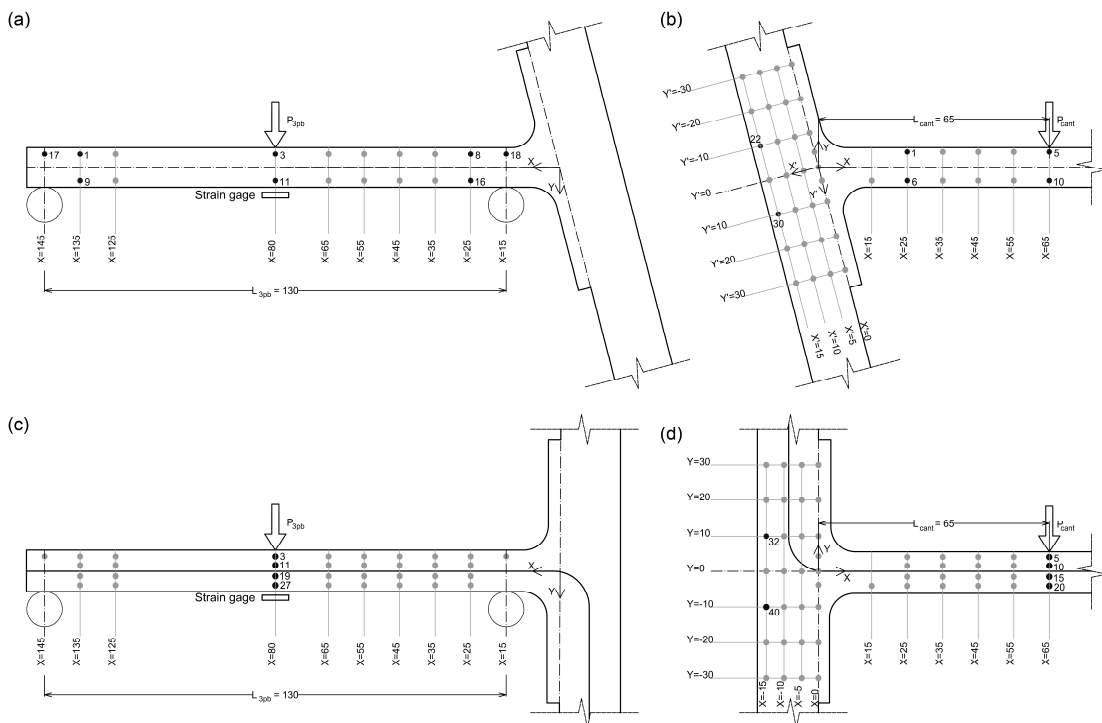


chine. Contact between the loading fixture and the upper face of the specimen's web was via a 12-mm-diameter steel bar and across the whole width of the web. The centerline of the specimen's web was aligned with the middle plane of the experimental set-up to avoid any torsion effect.

Each specimen was equipped with a 120- Ω -resistance/6-mm-length electrical strain gage to measure the axial strain (parallel to span) in the soffit of the web under the load application point, see Figures 4.7(a) and 4.7(c). The rotations and the vertical deflections along the specimen's web were measured by means of a video extensometer. For this purpose, pairs/quartets of black dots were marked along the web on the *I/V* specimen's lateral surface, see Figures 4.7(a) and 4.7(c). A video extensometer camera was used to monitor the targets' *X-Y* coordinates, which were continuously recorded by a LabVIEW application with an accuracy of $5 \cdot 10^{-7}$ m at a 2-Hz frequency. The rotations and deflections were thereafter determined using a simple data processing module. The cross-head displacement of the testing machine and the strain data were recorded at a 2-Hz frequency by a DOLI EDC 60/120 data-acquisition device throughout the experiments. Load and time were recorded in both systems.

All experiments were performed under displacement control at a rate of 0.01 mm/s. The specimens were loaded until the strain recorded in the soffit of the web reached a limit value of 0.6% and were subsequently unloaded at a 0.02-mm/s rate. The strain limit value was selected to assure that the web remained undamaged for the subsequent cantilever experiment on the same specimen. Furthermore, three loading-unloading cycles were conducted on each specimen, with a 15-s time interval after unloading, to verify that no changes in stiffness occurred.

Figure 4.7 – Instrumentation for three-point bending/cantilever experiments in (a)/(b) *I* specimens and (c)/(d) *V* specimens; dimensions in mm.



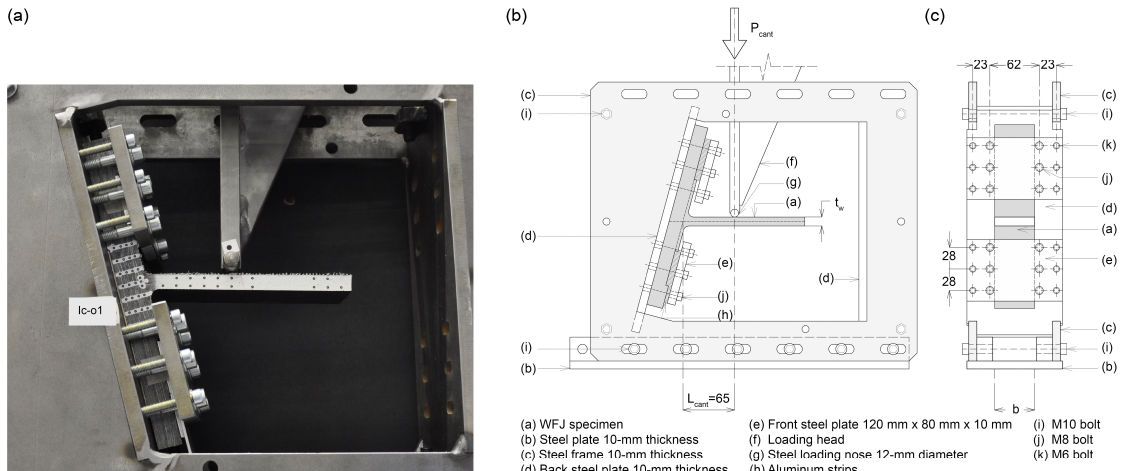
4.2.4 Cantilever experiments

Cantilever experiments with a 65-mm lever arm (L_{cant}) were performed on the specimens' webs to investigate the response of the WFJs when loaded under local bending moment applied to the web element and, conjointly with the three-point bending experiments, allow their rotational stiffness to be obtained. To ensure that the tensioned/compressed sides of the web remained the same in both experimental configurations, the three-point bending specimens were rotated 180° around a horizontal axis normal to their middle plane for the conducting of the cantilever experiments.

A single test rig was designed and manufactured so that the web-cantilever experiments could be conducted on the six WFJ series using a universal testing machine, see Figure 4.8. The fixture comprised a two-layer steel frame transversely connected with 10-mm-diameter bolts and two 10-mm-thick welded steel plates (one vertical and one inclined). The *I/V* specimen's flange was clamped to the inclined/vertical plate so that the web element was placed horizontally. The frame, when necessary, was turned upside down so that the web's side to be tensioned, according to the relevant bending moment direction, was located upwards. The specimen's flange was laterally clamped on both sides of the WFJ, without being drilled, by means of two steel plates of 10-mm thickness and two sets of 8-mm-diameter bolts. Aluminum strips were placed between the flange and the front fixing plates, where necessary, so that an even contact surface was achieved despite the flange's thickness change; the 20.3-mm-thickness flange area close to the WFJ remained unclamped, see Figure 4.8. The assembly was fastened to the lower platen of the testing machine and could be adjusted horizontally to set the load application point. The vertical load was introduced via the same loading head used for the three-point bending experiments.

A video extensometer was used to measure the rotations of the specimen's flange and web and the vertical deflections along the length of the latter. The arrangement of the target points is detailed in Figures 4.7(b) and 4.7(d) for the *I* and *V* specimens, respectively. On the web, the target points layout from the three-point bending experiments, with pairs/quartets of dots at intervals of around $\Delta X \approx 10$ mm along its length, was used. On the flange, dots were

Figure 4.8 – Set-up for cantilever experiments; (a) general view (*Ic-o* specimen); (b) front view (*Ic-a* specimen); (c) cross section; dimensions in mm.



marked in an array arrangement, at equal intervals of $\Delta X' \approx 5$ mm across its thickness and $\Delta Y' \approx 10$ mm along its length. The same data acquisition details as for the three-point bending experiments applied. Additionally, the video extensometer system was used for automatically capturing and saving images of the specimen at regular intervals during the experiments.

All experiments were conducted under displacement control. The specimens were monotonically loaded at a 0.01-mm/s rate up to failure.

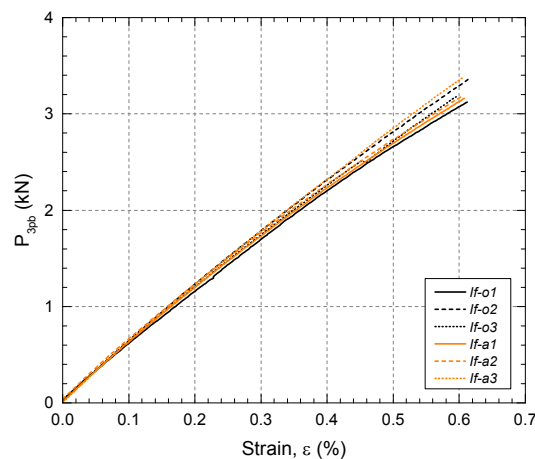
4.3 Experimental results and discussion

4.3.1 Three-point bending experiments

Figure 4.9 shows the load-strain ($P_{3pb}-\varepsilon$) behavior measured at mid-span for the *If-o* and *If-a* series up to the experiments' reference strain (0.6%) during the first cycle. The reloading paths of the second and third cycles slightly deviated from the loading path of the first cycle for all the specimens; no decrease of stiffness was observed, however. This was related to the viscoelastic material behavior and attributed to the short time lapse between two consecutive cycles, which was insufficient to allow the delayed recovery to entirely develop. These effects had been investigated in a previous work.²⁹ Only measurements from the first cycle are therefore analyzed in the following for all series. The *If-o* and *If-a* specimens' load-strain response was nearly linear. Negligible scattering was registered within each series. A similar behavior was observed for the *Ic-o* and *Ic-a* series, whereas the *V-d* and *V-s* specimens showed a mildly nonlinear response and higher scattering. The latter was ascribed to the variability of the adhesive layer's imperfections (partially glued areas).

The load-deflection ($P_{3pb}-\delta_{3pb}$) responses measured for all the specimens during the first cycle are given in Figures 4.10(a) to 4.10(c), on the left side. The average deflections at mid-span (targets 3-11 and 3-11-19-27 for *I* and *V* specimens respectively, see Figures 4.7(a) and 4.7(c)) are shown. The *If* and *Ic* specimens exhibited linear behavior throughout the experiments. The response of the *I*-WFJs displayed insignificant scattering irrespective of the series – it was not related to the WFJ characteristics but only to the web element, whose fiber architecture was identical in all the *I*-type specimens. The

Figure 4.9 – Load-strain behavior of *If-o* and *If-a* specimens in three-point bending experiments.



$V-d$ and $V-s$ specimens showed slightly nonlinear behavior and more significant scattering than the I series, as observed for the load-strain responses, due to the imperfections noticed in the adhesive layer.

The method proposed in this study to obtain the rotational stiffness of the WFJs by loading the web element first as a simply supported beam under three-point bending and then as a cantilever assumes symmetric behavior in the former case. However, the WFJ specimens were asymmetric due to the

Figure 4.10 – Load-deflection response of (a) I -, (b) Ic - and (c) V -WFJs during three-point bending (3pb) and cantilever experiments.

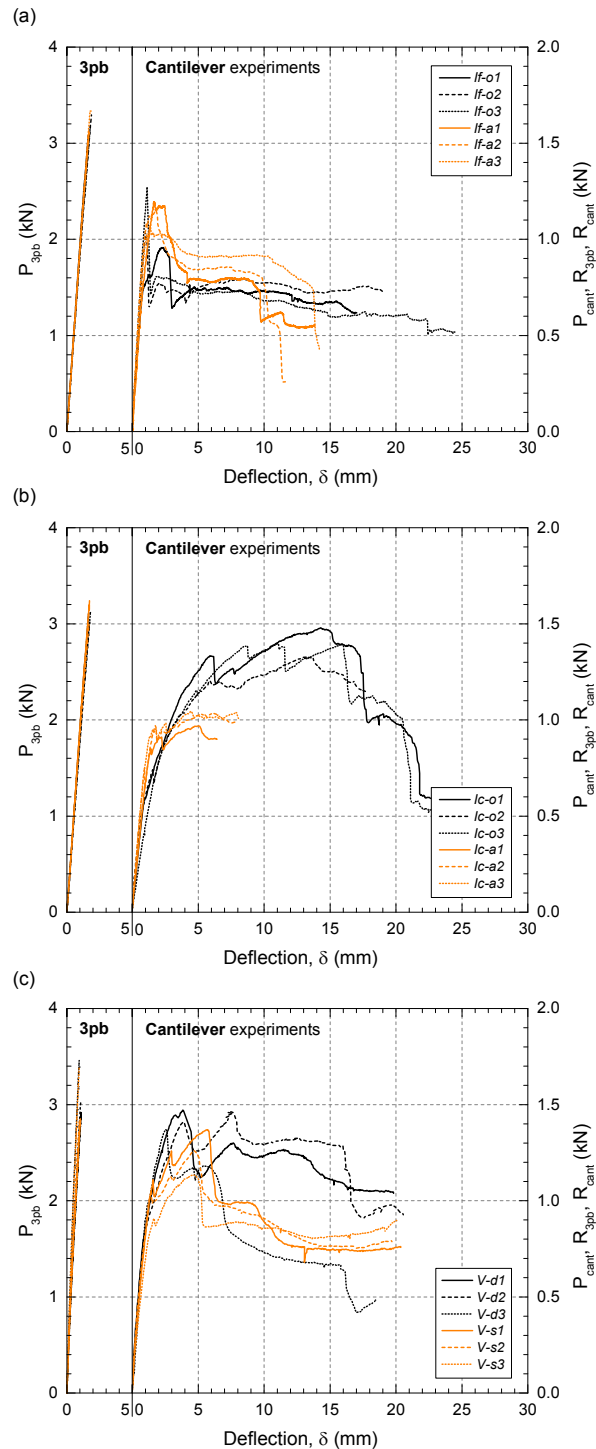


Table 4.3 – Calculated transverse elastic flexural moduli of web laminates.

Series	$E_{f,y}$ (MPa)
<i>If-o</i>	17 790±610
<i>If-a</i>	17 780±320
<i>Ic-o</i>	17 420±560
<i>Ic-a</i>	17 420±340
<i>V-d</i>	14 630±1810
<i>V-s</i>	14 990±1010

attachment of the web, on one of its sides, to the flange element, i.e. to the WFJ itself. In order to verify the fulfillment of the symmetry assumption, the rotation of two triangular areas located near the left and right supports and symmetrically placed about mid-span was compared (e.g. for *I*-type specimens, see triangles formed by targets 1-9-17 and 8-16-18 in Figure 4.7(a)). No discernible differences were found between the left and right side rotations for the *I*-WFJs, which confirmed that their behavior was symmetric regardless of the WFJ. The *V* specimens exhibited slightly asymmetric behavior, which was attributed to the discontinuities observed in the adhesive layer.

The load and strain data from the three-point bending experiments were used to evaluate the elastic flexural moduli in the transverse-to-pultrusion direction ($E_{f,y}$) of the webs. The $E_{f,y}$ values were derived by (i) conducting a linear regression analysis on the measured $P_{3pb}-\epsilon$ responses throughout the 0–0.20% strain range; (ii) conjointly using the thus calculated relationships, the web cross-sectional dimensions (b , t_w) and the loading configuration to evaluate $E_{f,y}$. The average values for all series are listed in Table 4.3. The calculated $E_{f,y}$ values for the inclined webs (*I*-WFJs) were 6–9% higher than the transverse elastic modulus obtained from tensile experiments, $E_{t,y}$, in the same strain range, ($E_{t,y} = 16\,350$ MPa, see Table 4.1). For the vertical webs (*V* WFJs), nearly the same values were obtained for $E_{f,y}$ and $E_{t,y}$ ($E_{t,y} = 14\,910$ MPa, see Table 4.1).

4.3.2 Cantilever experiments

The load-deflection responses registered for all the series during the cantilever experiments, $P_{cant}-\delta_{cant}$, are shown in Figures 4.10(a) to 4.10(c), on the right side. A small rotation on the rear side of the flange element was measured (see sections defined by targets 22-30/32-40 for *I/V* specimens in Figure 4.7(b)/(c), respectively). In order to isolate the web's response excluding the effect of the unclamped flange zone, the contribution to deflections of the above-mentioned rotation was subtracted from the recorded vertical displacements.

Although the *If* and *Ic* specimens had similar geometry – differing only in the location of the adhesively-bonded profile-to-profile joint in the flange element in relation to the web – and identical fiber architecture design, they exhibited different behavior. The *If-o* specimens generally exhibited linear behavior up to their peak load, after which sudden load decreases of approximately 40% were recorded; subsequently, the specimens were able to bear an almost constant, slightly decreasing load, with increasing

displacement, see Figure 4.10(a). On the other hand, the *Ic-o* specimens exhibited initial linear behavior up to 35–40% of their peak load, which then changed to markedly nonlinear. A nearly sustained load-bearing capacity under the development of large displacements preceded failure, see Figure 4.10(b). The differences between the *Ic-o* and *If-o* responses were attributed to dissimilar initial imperfections in the *If* and *Ic* WFJs; detailed explanations are given in a previous work.²⁹ Similar differences in the $P_{cant}-\delta_{cant}$ responses were observed when the *I*-WFJs were subjected to a local bending moment in the opposite direction (*If-a* and *Ic-a* specimens, with the web's tensioned side towards the acute angle of the WFJ). The *If-a* series exhibited linear behavior up to the peak load; a progressive load decrease towards a nearly constant post-peak load followed. The *Ic-a* specimens also exhibited linear behavior almost up to the peak load, although with lower stiffness than the *If-a* specimens. Thereafter, a sustained load-bearing capacity at approximately the peak load value, without any significant load decrease, was recorded. The *V-d* specimens displayed initial linear behavior up to about 55–70% of their maximum load, followed by nonlinear behavior preceding a first peak load at which noticeable load drops occurred. A second local peak load was afterwards recorded, which was lower/marginally higher than the first one for (*V-d1*, *V-d3*)/*V-d2* specimens, see Figure 4.10(c). The scatter of both peak values was attributed to the WFJs' local imperfections, which differ from specimen to specimen. A roughly constant load was subsequently borne under large displacement development. Similarly to the *V-d* series, nonlinear behavior, with the proportional limit at about 60–75% of the peak load, and approximately constant post-peak capacity were recorded for the *V-s* specimens. The *V-s* series exhibited however a more pronounced pre-peak nonlinearity and lower post-peak capacity than the *V-d* series. Specimens of the same WFJ type (*If*, *Ic*, *V*) exhibited similar initial stiffness and an analogous shape of their overall load-deflection curves regardless of the direction of the local bending moment applied.

The specimens' failure loads, P_{ult} , defined as the peak load (representing the inability of the specimens to bear any further load increment), are given in Table 4.4. The average corresponding displacement, δ_{ult} , and ultimate load per unit width, P_{ult}/b , for all series are also listed. Failure was governed by transverse (through-thickness) tension in the upper (tensioned) fillet of the WFJs, where the first cracks were noticed in all series. However, different crack

Table 4.4 – Experimental peak loads and corresponding displacements; calculated ultimate moments and corresponding rotations; calculated rotational stiffness.

Series	$P_{ult}^{(a)}$ (kN)	$\delta_{ult}^{(b)}$ (mm)	$P_{ult}/b^{(b)}$ (N/mm)	$M_{ult}/b^{(b)}$ (Nmm/mm)	$\varphi_{M,ult}^{(b)}$ (rad)	$K_{rot}/b^{(b)}$ (kN/rad)	$K_{rot}/b^{(b)}$ (kN/rad)
<i>If-o</i>	0.96/1.05/1.28	1.7±0.9	22.2±3.3	1 443±215	0.007±0.011	∞	∞
<i>If-a</i>	1.20/1.15/1.08	1.6±0.1	22.6±1.2	1 468±75	0.006±0.003	∞	∞
<i>Ic-o</i>	1.48/1.33/1.40	14.5±1.4	28.0±0.9	1 821±57	0.195±0.022	189±87	59±14
<i>Ic-a</i>	0.97/1.04/1.05	4.9±0.5	20.2±0.8	1 310±55	0.059±0.007	628±277	262±104
<i>V-d</i>	1.47/1.47/1.38	4.6±2.5	28.6±0.8	1 859±53	0.056±0.037	212±80	160±27
<i>V-s</i>	1.37/1.26/1.14	5.0±0.6	24.9±2.3	1 620±150	0.064±0.007	178±46	110±33

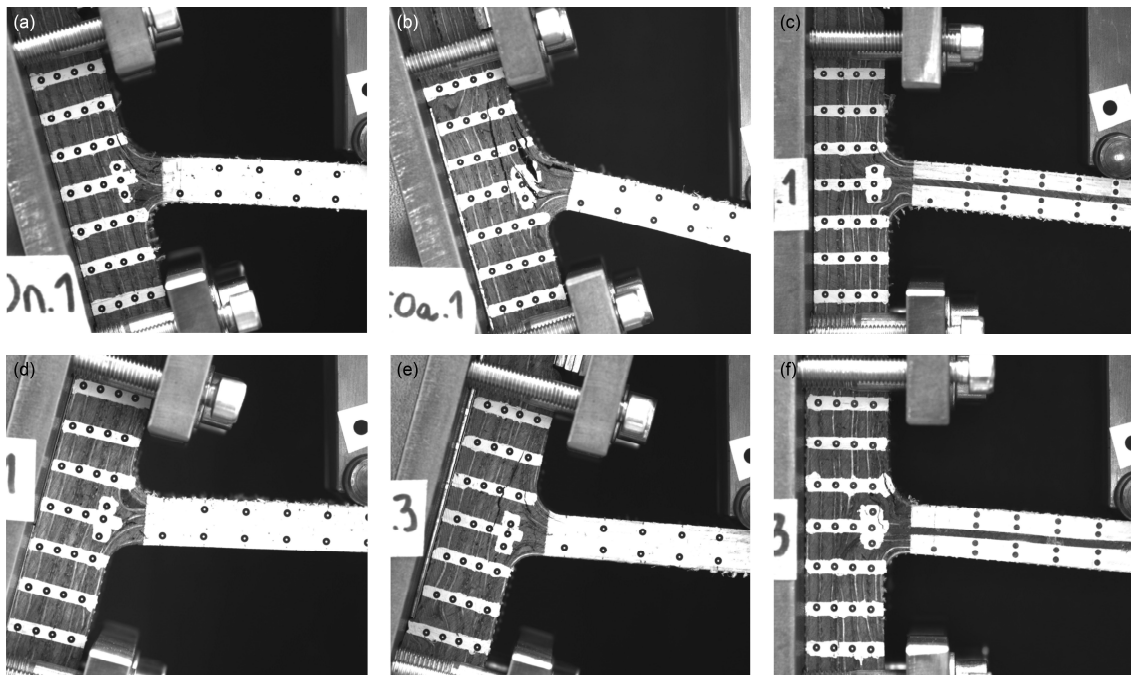
^(a) Indicated values correspond to specimens 1/2/3 respectively

^(b) Mean±Standard deviation

formation and development sequences were observed and resulted in different failure modes and load capacities – see previous work²⁹ for a detailed comparison between the *If-o* and the *Ic-o* series. The typical crack patterns of all series at the peak load level are shown in Figure 4.11. Specimens from series exhibiting a less pronounced nonlinear pre-peak behavior and a more sudden failure (*If-o*, *If-a*, *V-d*) showed only incipient cracking at the peak load level, whereas specimens exhibiting markedly pre-peak nonlinearity (*Ic-o*, *Ic-a*, *V-s*) showed a higher degree of cracking. Further crack propagation occurred during the sustained peak load / post-peak regimes. The *If*-WFJs reached comparable peak loads irrespective of the direction of the applied local bending moment. This was related to the fiber arrangement in their web elements. The triaxial multi-ply fabrics, bearing the load in the studied configuration, were unevenly distributed across the web thickness and concentrated towards the acute angle side²⁹ – the neutral axis of the web was therefore located closer to its lower compressed / upper tensioned side in *If-o*/*If-a*, respectively. Had the fabrics been evenly distributed, *If-a* would have exhibited a lower capacity than *If-o* due to the higher curvature, hence higher transverse tensile stress in the fillet, of their outer tensioned fabrics (acute angle). However, as a result of the asymmetrical neutral axis location, smaller tensile forces were borne by the outer fabrics in *If-a* than in *If-o*, counterbalancing the effect of the curvature. In contrast, for the *Ic*-WFJs, where the triaxial fabrics were uniformly distributed across the web thickness, significantly lower (21–35%) peak loads were recorded for *Ic-a* than for *Ic-o* owing to the higher curvature of the upper fabrics – at a same load value, the tensile forces borne by the upper fabrics are equal in *Ic-a* and *Ic-o*, but the transverse tensile stresses in the fillet are higher in the former.

Figure 4.11 – Crack pattern at peak load of (a) *If-o1*, (b) *Ic-o1*, (c) *V-d1*, (d) *If-a1*, (e) *Ic-a3* and (f) *V-s3* specimens.

The ultimate bending moment of the WFJs, M_{ult} , was calculated as the product of the experimental ultimate load, P_{ult} , and the distance from the load



application point to the WFJ (lever arm), L_{cant} , see Figure 4.8(b). The M_{ult}/b mean value per series is given in Table 4.4. The *If-/Ic-/V*-WFJs showed a 2/33/14% difference in the average M_{ult}/b value depending on the direction of the applied bending moment. Differences in the post-peak moment capacities were also observed in the *If-o/If-a* and *V-d/V-s* series, see Figures 4.10(a) and 4.10(c), respectively – the bending moment capacity is proportional to the load capacity. The modeling of the rotational stiffness of each WFJ type should therefore reflect the different behavior in both directions of the applied bending moment.

The flexural strength of the WFJs, σ_f , defined as the web's surface stress, at the peak load level, at the intersection with the flange's surface – disregarding the fillet – was determined. A homogeneous cantilever beam of $(b \cdot t_w)$ rectangular cross section was assumed. The calculated σ_f values ranged from 55.4–72.1 / 54.4–81.6 / 53.8–68.5 MPa for the *If-/Ic-/V*-WFJs, respectively. The thus calculated σ_f represented 65–98% and 33–50% of the experimental tensile (83 MPa) and compressive (163 MPa) strength values of the flat web laminate²⁸ – experimental values for the flexural strength are not available. Lower flexural strength of the WFJs compared to that of the relevant web element has been also reported by Turvey and Zhang²¹ and ascribed to the dissimilarities in the fiber architecture of the two locations.

4.3.3 Rotational stiffness of web-flange junctions

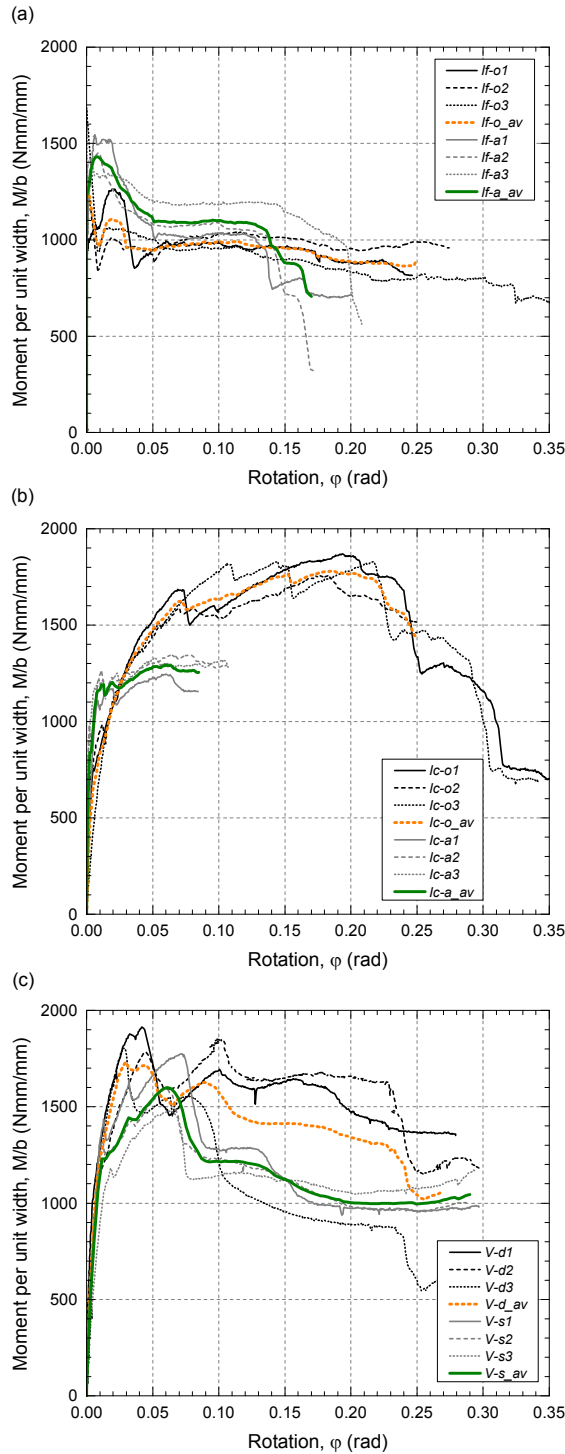
Moment-rotation behavior of DS web-flange junctions

The procedure referred to in Section 4.2.1 was applied to calculate the moment-rotation (M - φ) relationships of the WFJs. Figure 4.12 shows the M - φ curves obtained for all specimens and the average (av) response for all series. The normalized M values (moment per unit width, M/b) are displayed. The av curves were calculated by averaging M/b (P -related) at regular φ intervals (δ -related) within each series – the experiments were conducted under displacement control. The M_{ult}/b mean value per series and the corresponding rotation, $\varphi_{M,ult}$, are listed in Table 4.4. The initial tangent rotational stiffness per unit width, K_0^{rot}/b , defined as the slope at the origin of the M - φ curve, was calculated. A linearized value for the rotational stiffness, K_I^{rot} , was also determined from the slope of the straight line fitted to the M - φ curve corresponding to the 0.05–0.25% strain range²¹ measured in the three-point bending experiments. Table 4.4 lists the average K_0^{rot} and K_I^{rot} per unit width for all series.

The *If*-WFJs initially displayed perfectly rigid behavior ($K_0^{rot}/b = \infty$; $\varphi = 0$), irrespective of the direction of the local bending moment applied to the web element, almost up to their maximum ultimate bending moment. Their rotation at failure, $\varphi_{M,ult}$, was negligible (see Table 4.4). The maximum moment capacity of both series was similar regardless of the examined bending direction – there was less than 2% difference between the M_{ult}/b mean values of *If-o* and *If-a*, see Table 4.4. Nevertheless, after the peak moment, a sudden moment decrease occurred in the *If-o* specimens while the *If-a* specimens showed a progressive softening branch. A nearly constant post-peak (residual) moment capacity followed in both series, which was approximately 10%

higher in *If-a* than in *If-o*, although it developed up to an around 40% smaller maximum rotation. On the other hand, the *Ic*-WFJs initially exhibited semi-rigid ($0 < K_0^{rot}/b < \infty$), nonlinear behavior preceding the maximum moment capacity, which occurred at rotation values significantly larger than in the *If*-WFJs. The rotational flexibility of the *Ic*-WFJs was related to their lower stiffness and initial nonlinearity in the cantilever configuration, associated with the flange's pre-crack.²⁹ The *Ic-o* specimens, where the applied local bending moment

Figure 4.12 – Calculated moment-rotation behavior of (a) *If*-, (b) *Ic*- and (c) *V*-WFJs.



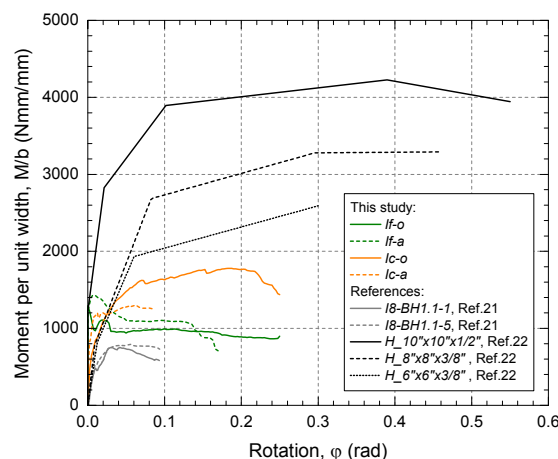
produced tension in the WFJ's obtuse angle and hence opening of the pre-crack, displayed a more pronounced nonlinearity and a lower rotational stiffness – the average K_0^{rot}/b of *Ic-o* represented approximately 30% of that of *Ic-a*, see Table 4.4. The *Ic-o* specimens exhibited a considerably higher peak moment (approximately 40%) and relative rotation at failure (3.3 times) than the *Ic-a* specimens. The *V*-WFJs showed a non-rigid, slightly nonlinear initial $M-\varphi$ response with comparable rotational stiffness irrespective of the applied bending moment direction, as indicated by nearly coincident $M-\varphi$ plots in the *V-d* and *V-s* series – a 17% difference in K_0^{rot}/b was found between the *V-d* and *V-s* series. However, the *V-s* specimens exhibited a more pronounced nonlinearity and significant stiffness reduction as from approximately 70-80% of their maximum moment. A roughly constant post-peak moment capacity was exhibited by both the *V-d* and the *V-s* specimens. The average value of the residual moment-bearing capacity was approximately 30% higher in the *V-d* series than in the *V-s* series, although it developed up to an about 20% smaller maximum rotation. Differences in the rotational stiffness and/or strength of the six WFJ specimen types indicated that their characterization should be considered separately and that prospective modeling should take the dissimilarities into account.

Comparison to other experimental results

The rotational behavior of WFJs of pultruded H-profiles with similar web thickness (t_w) to the *DS* WFJs was investigated in previous studies by other researchers.^{21,22} Figure 4.13 shows the moment-rotation relationships obtained for the *DS I*-WFJs compared to those reported by Turvey and Zhang²¹ and Mosallam et al.²² The $M-\varphi$ relationships displayed for the profiles investigated by Turvey and Zhang²¹ were back calculated by conjointly using the published load-deflection data and E-modulus values and a semi-rigid beam model. The $M-\varphi$ curves corresponding to the study conducted by Mosallam et al.²² were adapted from the presented linearized rotational stiffness expressions.

Semi-rigid rotational behavior, with values of K_1^{rot}/b in the 6.1–7.5 kN/rad range, was reported by Turvey and Zhang²¹ for pultruded H-profiles with a 9.6-mm-thick web. The significantly higher values obtained in this study for K_1^{rot}/b (one to two orders of magnitude higher for the *Ic*- and *V*-WFJs and infi-

Figure 4.13 – Comparison of moment-rotation behavior of WFJs of *DS* deck and pultruded GFRP H-profiles.^{21,22}



nite for the *If*-WFJs, see Table 4.4) in the same strain range were mainly attributed to substantial differences in the fiber architecture of the *DS* deck laminates compared to the profiles investigated by Turvey and Zhang.²¹ The latter consist of roving in the pultrusion direction and non-structural continuous filament mats, therefore their behavior was resin-dominated (rovings ran perpendicularly to the analyzed plane); the former also contain triaxial multi-ply structural fabrics which greatly contributed to bearing the moment in the studied configuration. The greater web thickness of the *DS* WFJs (see Table 4.2) may have also contributed. Nonlinear moment-rotation relationships, with overall shapes analogous to those of the *Ic* series, were obtained, see Figure 4.13. The peak bending moments per unit width, M_{ult}/b , in the *DS I*-WFJs were 55–160% greater than those calculated for the H-profile WFJs studied by Turvey and Zhang.²¹ However, comparable flexural strength at the WFJs was obtained (σ_f values in the 62–116 / 54–82 MPa ranges corresponding to failure initiation / final failure were reported by Turvey and Zhang²¹ / in this study), despite the above-mentioned differences in the fiber architecture between the *DS* deck laminates and the profiles investigated by Turvey and Zhang.²¹ This was related to the similar WFJ failure patterns observed, which were associated with resin- and not fiber-dominated behaviors – delamination cracking in the WFJs appeared due to transverse (through-thickness) tensile stresses in both cases.

Initial rigid rotational behavior ($K_o^{rot}/b = \infty$), as exhibited by the *If*-WFJs, was observed by Mosallam et al.²² for the WFJs of a profile with a 12.7-mm-thick web, whereas for WFJs with smaller web thickness ($t_w = 9.5$ mm) a semi-rigid behavior was detected, with finite K_o^{rot}/b calculated values in the 66–87-kN/rad range. The intermediate K_o^{rot}/b values obtained for the *Ic*-WFJs (see Table 4.4) were attributed to their in-between thickness ($t_w = 11.4$ mm, see Table 4.2). The overall rotational responses of the WFJs were markedly nonlinear, with large rotation development recorded at moment levels close to the maximum, similar to the behavior observed in the *Ic* series, see Figure 4.13. However, these plateaux may have been affected by the test fixtures employed – clamping of the flanges close to the WFJ may have prevented the cracking appearing in the junction from propagating. The peak bending moments per unit width, M_{ult}/b , of the *DS I*-WFJs represented only 30–70% of the maximum values recorded for the WFJs investigated by Mosallam et al.²² The calculated σ_f values for the latter (157–214 MPa) were 1.9–4.0 times higher than those obtained for the *DS I*-WFJs; furthermore, they were 2.3–3.1 times higher than the material's flexural strength in the transverse-to-pultrusion direction quoted by the manufacturer (68.9 MPa).²² The significantly higher values of ultimate bending moments reported by Mosallam et al.²² and of the corresponding WFJ's strength and the large plateaux were attributed to the limitations of the test rigs used – the flange element of the H-profile was pre-compressed in its through-thickness direction, which may have enabled higher moments and rotations to be reached by preventing crack propagation towards the flange.

4.4 Modeling

The experimental results showed that the behavior of the *DS* WFJs when subjected to local bending was generally non-rigid and nonlinear. In order to take the WFJs' rotational flexibility into account, the webs' end conditions can be modeled as rotational springs responding to the moment-rotation ($M-\varphi$) curves. For a realistic modeling, the experimental $M-\varphi$ relationships can be used. Simplified expressions may also be employed to facilitate the modeling; their validity for accurately simulating the global response should be evaluated.

First, linearized $M-\varphi$ relationships for the experimental $M-\varphi$ curves are proposed to model the *DS* WFJ rotational behavior. Then, numerical simulations of the full-scale deck experiments mentioned above (Figure 4.2), incorporating the developed WFJ models, are performed to assess their validity.

4.4.1 Empirical modeling of rotational stiffness of web-flange junctions

Based on the average $M-\varphi$ curves obtained from the three-point bending and cantilever experimental results (see Figure 4.12), two idealized models were derived for the moment-rotation behavior of the WFJs: (i) a rigid-plastic model and (ii) a trilinear model, referred to as *RP* and *TL*, respectively. These are schematically illustrated in Figure 4.14.

The *RP* model (see Figure 4.14(a)) presumes that no relative rotation exists for moments per unit width lower than the assumed maximum bending capacity, M_{pl}/b ($M/b < M_{pl}/b \rightarrow \varphi = 0$). Increasing rotation takes place at a constant M_{pl}/b moment level and up to a φ^{av}_{max} maximum rotation at which failure occurs. The peak bending moment or the upper boundary of the nearly

Figure 4.14 – Idealized moment-rotation behavior; (a) *RP* model; (b) *TL* model.

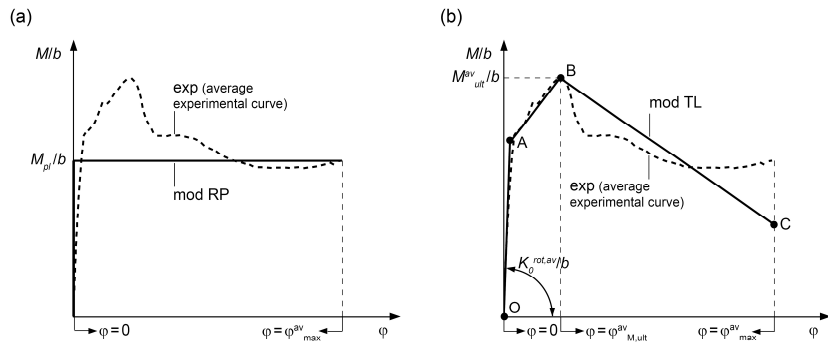


Table 4.5 – Parameters of idealized moment-rotation relationships.

Series	RP model		TL model			
	M_{pl}/b (Nmm/mm)	φ^{av}_{max} (rad)	$K^rot,av}/b$ (kN/rad)	M^{av}_{ult}/b (Nmm/mm)	$\varphi^{av}_{M,ult}$ (rad)	φ^{av}_{max} (rad)
<i>If-o</i>	992	0.250	∞	1107	0.020	0.250
<i>If-a</i>	1102	0.170	∞	1431	0.007	0.170
<i>Ic-o</i>	1779	0.250	189	1779	0.185	0.250
<i>Ic-a</i>	1294	0.085	628	1294	0.060	0.085
<i>V-d</i>	1416	0.270	212	1733	0.030	0.270
<i>V-s</i>	1045	0.290	178	1601	0.061	0.290

constant post-peak capacity of the experimental M - φ curves, normalized per unit width, was taken as M_{pl}/b , depending on whether the relevant WFJ exhibited sustained bending capacity prior ($Ic-o$, $Ic-a$) or subsequent ($If-o$, $If-a$, $V-d$, $V-s$) to reaching its ultimate moment, respectively; φ^{av}_{max} was taken as being equal to the maximum rotation of the series' average plot (see av curves in Figure 4.12), reached by all specimens of the relevant series. Table 4.5 lists the M_{pl}/b and φ^{av}_{max} used in the RP model for all series.

In the TL model, a three-segment (OA , AB , BC) piecewise linear function, composed of two ascending branches and one softening, descending branch, is used to represent the moment-rotation behavior, see Figure 4.14(b). The average M - φ curves from Figure 4.12 and their corresponding $K_0^{rot,av}/b$, M^{av}_{ult}/b , $\varphi^{av}_{M,ult}$ and φ^{av}_{max} are the input parameters to define the TL relationship – superscript av is used to denote the aforesaid curves. The following assumptions were made: (i) the idealized initial rotational stiffness is equal to $K_0^{rot,av}/b$ – the slope of the first segment, OA , is defined by $K_0^{rot,av}/b$; (ii) the M^{av}_{ult}/b and the corresponding $\varphi^{av}_{M,ult}$ are respected – they define point B , considered as the softening initiation; (iii) the φ^{av}_{max} value is respected – it defines the φ coordinate of point C , taken as the softening end; (iv) AB and BC slopes are defined on the basis of the energetic balance between the idealized and the average M - φ experimental curves up to the $\varphi^{av}_{M,ult}$ and φ^{av}_{max} rotations, respectively. The M - φ coordinates of the TL model are listed in Table 4.5 for all series.

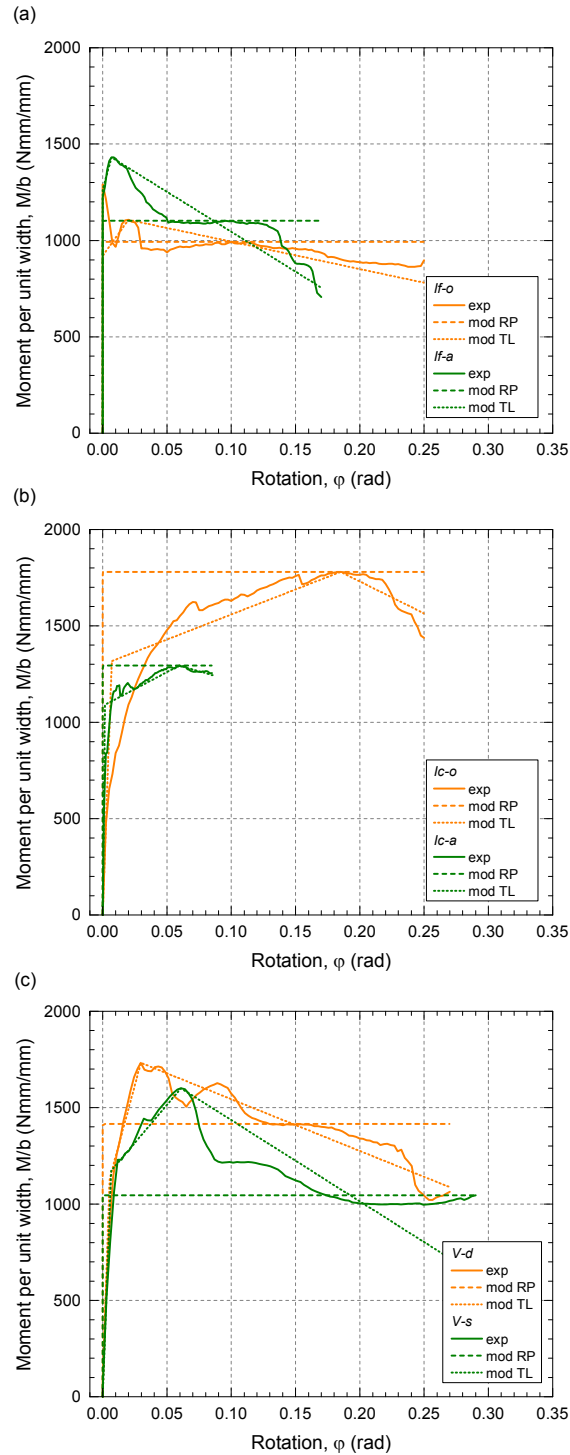
The RP and the TL models for the moment-rotation relationships are represented in Figures 4.15(a), 4.15(b) and 4.15(c) for the If -, Ic - and V -WFJs, respectively. The RP model significantly underestimates the maximum moment of the WFJs exhibiting constant post-peak capacity – the M_{pl}/b values for the If - and V -WFJs were 10–35% lower than the corresponding M^{av}_{ult}/b values, see Table 4.5. On the other hand, the initial rotational stiffness is overestimated – perfectly rigid rotational behavior was assumed for all WFJ types, whereas experimental results showed that $0 < K_0^{rot}/b < \infty$ for Ic and V , see Table 4.4. The pre-peak behavior may be more appropriately represented by the TL model, which is better adapted to the experimentally obtained curves.

4.4.2 Numerical modeling

In order to support the WFJ moment-rotation relationships calculated from the experimental results (see first part of Section 4.3.3) and validate the idealized models derived (see Section 4.4.1), two-dimensional finite element (FE) models were established of full-scale DS deck specimens composed of three to four unit profiles and subjected to three-point bending⁷ and in-plane shear⁶ in their transverse-to-pultrusion direction. The experimental configurations modeled and the corresponding experimental results are shown in Figure 4.2.

The FE-software SAP2000 and the Frame element were used. The thickness of the flange/web laminates (see Figure 4.1) and the width of the deck specimens (200/600 mm for three-point bending⁷/in-plane shear⁶ experi-

Figure 4.15 – Idealized moment-rotation behavior of (a) *If*-, (b) *lc*- and (c) *V*-WFJs.



ments) were taken as the depth and width of the frame elements, respectively. The adhesively-bonded profile-to-profile joints were not modeled – single laminates of 16.8–20.3-mm / 11.7-mm thickness were considered for the adhesively-bonded flange/web elements where appropriate. The web-to-flange connections were modeled as rotational springs using the multilinear elastic Link element, see Figure 4.16. Their behavior corresponded to the moment-rotation relationships shown in Figure 4.15, except for the external

webs' junctions (above the supports) in the three-point bending experiments – the $M-\varphi$ behavior of the corresponding vertical webs, consisting of single, non-glued laminates and aluminum reinforcements at the edges,⁷ was not studied. The following assumptions were made for the latter: (i) their initial $M-\varphi$ behavior is perfectly rigid; (ii) a perfect hinge ($M = 0$) is formed when the reinforced web's moment capacity is reached. The moment capacity was estimated taking into account the aluminum reinforcement (the homogenized section was used) and assuming that bending failure of the WFJ occurred when the surface tensile/compressive stress in the GFRP material reached the tensile/compressive strength of the web laminate (83/163 MPa,²⁸ respectively). Three different models were established for each experimental configuration to separately consider the experimentally-based $M-\varphi$ curves (*exp*) and the idealized relationships (*RP* and *TL*). The same appellation as for the $M-\varphi$ relationships is used for the corresponding FE models. The orthotropic elastic material properties listed in Table 4.1 were used for the web and flange laminates. Displacement-controlled nonlinear static analyses considering geometric nonlinearities were performed.

Figure 4.17 shows the comparison of the measured load-displacement ($P-\delta$) behavior of the deck under three-point bending and the corresponding numerical results obtained from the FE analysis (FEA). The vertical deflection at mid-span is shown. No differences were detected in the numerical results irrespective of the $M-\varphi$ relationships used (nearly coincident $P-\delta$ plots were obtained for *exp*, *RP* and *TL* FE models) and a limited agreement with the experimental data was observed. Initial linear behavior up to a load of approximately 6 kN, matching the experimental results well, was predicted by the FE simulations. A slight nonlinearity followed, although it progressively deviated from the recorded load-displacement data, which showed a more pronounced stiffness reduction. At an approximately 14-kN load, sudden load drops of 20% can be observed in the numerical predictions, corresponding to two simultaneous local failures appearing at the bottom junctions of the inclined 8th web and of the right external (9th) web. Local failure at the top junction of the 8th web, producing failure of the DS deck specimens at a 12.8-kN

Figure 4.16 – Schema of FE frame models developed for full-scale (a) three-point bending and (b) in-plane shear experiments.*
*Note: rotational springs are of zero length.

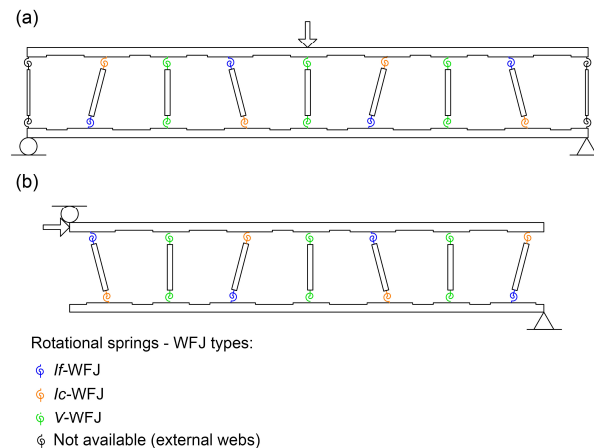
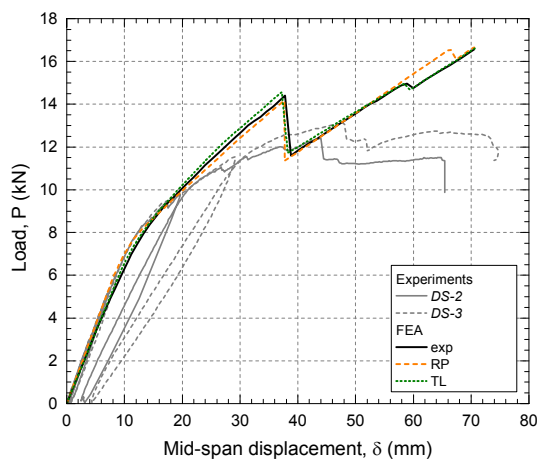


Figure 4.17 – Comparison of measured and calculated load-deflection behavior in four-module specimens subjected to three-point bending.



average load, was subsequently predicted, although at significantly higher loads (15.0–16.6 kN) than the experimental ones. The numerical simulations showed a further increasing load-bearing capacity, differing from the experimentally observed sustained load capacity. The differences between the experimental and the calculated behaviors were attributed to shortcomings of the modeling rather than to a lack of validity of the obtained $M-\phi$ relationships, namely: (i) the initial thickness of the laminates remained unchanged throughout the simulations, whereas cracking propagating from the WFJs' tensioned side towards the flange may have reduced the effective thickness of the latter; (ii) the adhesively-bonded profile-to-profile joints in the flanges were not considered; however, they may have affected the deck's global response – local tensile stresses may result in the opening at the edges of the adhesively-bonded joint and therefore in a reduction of the stiffness of the corresponding section; additional local deformations and hence increasing global deflections are expected; (iii) the $M-\phi$ relationships used in the modeling of the WFJs from the reinforced external webs were based on an uncorroborated hypothesis – no experimental data were available. The in-plane shear configuration, where (ii) and (iii) do not apply (the flanges were mainly under compression and the rotational behavior of all the WFJ types involved had been experimentally studied) can thus serve better to assess the validity of the proposed moment-rotation relationships.

The measured and calculated load-displacement responses of the deck for the in-plane shear configuration are shown in Figure 4.18. The differential shift between the deck's flange panels in the load application direction is displayed. Overall, the trends of the curves from the experiments and the numerical simulations compared well regardless of the $M-\phi$ relationships used, exhibiting initial linear behavior and subsequently pronounced nonlinear behavior up to the ultimate load, followed by a stepped descending branch showing moderately decreasing load with large displacement development. Good agreement existed between the experimental results and the predictions from the FE models using the experimentally-based $M-\phi$ relationships from Figure 4.12 (see *FEA exp* in Figure 4.18) – no approximations were made in the *exp* $M-\phi$ curves. The calculated initial stiffness, taken

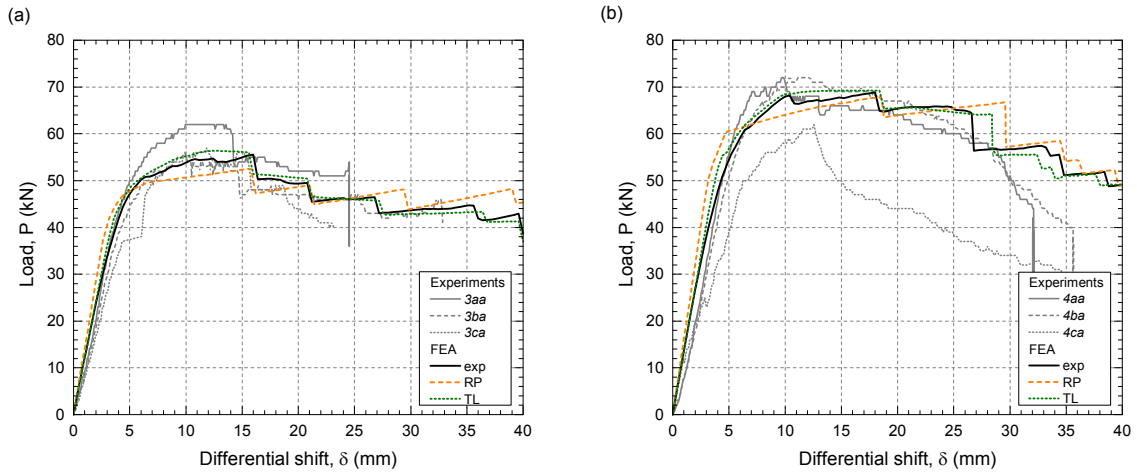


Figure 4.18 – Comparison of measured and calculated load-displacement behavior in (a) three-module and (b) four-module specimens subjected to in-plane shear.

as the slope of the P - δ curves, from the *exp* FE model (11.4/12.6 kN/mm for the three- and four-module specimens, respectively) overestimated the average experimental values (10.1/10.8 kN/mm) by 13–17%; the predicted ultimate load (56/69 kN) differed from the experimentally obtained load (59/69 kN) by a maximum of 6%. The good agreement between the experimental results and the predictions from the *exp* FE model supported the validity of the experimentally-based M - ϕ relationships. Only a fair agreement was found when the idealized *RP* M - ϕ relationships were used in the modeling: the predicted initial stiffnesses overestimated the mean experimental stiffnesses by 37–46% (initial perfectly rigid behavior was attributed to all WFJ types); the experimental and the modeling ultimate load values differed by up to 10%; the simulated P - δ responses moderately represented the pre-peak nonlinear behavior – an almost bilinear pre-peak response was obtained, see *FEA RP* in Figure 4.18. On the other hand, as good an agreement as with the *exp* M - ϕ curves was observed for the idealized *TL* M - ϕ relationships, as indicated by the almost coincident *FEA exp* and *FEA TL* P - δ plots shown in Figure 4.18. This suggested that the proposed trilinear model could be effectively used to represent the actual moment-rotation behavior of the WFJs when the deck's global performance is analyzed – local behaviors may show higher sensitivity.

4.5 Conclusions

The rotational behavior of the three web-flange junction (WFJ) types from a pultruded GFRP deck with trapezoidal cell cross section (*DS*) was investigated. The following conclusions were drawn:

1. An experimental procedure to characterize the WFJ rotational behavior based on three-point bending and cantilever experiments conducted on the web elements was established. The proposed procedure allows the determination of the rotational stiffness of the WFJs by conjointly using the measured load-deflection responses and simple analytical beam models. The developed experimental approach proved to be an effective method for evaluating the WFJ rotational behavior.

2. The rotational behavior of the three *DS* WFJ types, in two bending moment directions, was characterized. The WFJs generally exhibited non-rigid and nonlinear behavior. Two different overall trends were observed: (i) an initially linear or slightly nonlinear behavior up to the maximum bending moment, when abrupt failure occurred and was followed by constant moment-bearing capacity at a lower level; (ii) a markedly nonlinear behavior displaying progressive failure and sustained moment-bearing capacity at the peak bending moment level.
3. The rotational stiffness, strength and failure modes differed depending on the web type, the location of the WFJ within the deck profile, the initial imperfections observed and the direction of the local bending moment applied. This evidenced the relevance of characterizing the rotational response of all WFJ types separately, in the two possible bending directions for each of them.
4. The flexural strength of the *DS* WFJs was approximately 65–98% and 33–50% of the tensile and compressive strength values, respectively, of the flat web laminate. Thus, applying the latter to estimate the flexural capacity of the WFJs would lead to unconservative maximum bending moment values.
5. Numerical models of full-scale *DS* deck specimens subjected to bending and in-plane shear in their transverse-to-pultrusion direction were developed, incorporating the experimentally obtained rotational responses of the WFJs. Good agreement between numerical and experimental results demonstrated the validity of the calculated moment-rotation relationships.
6. Two simplified linearized relationships for the experimentally obtained rotational responses of the WFJs were proposed: a rigid-plastic model (*RP*) and a trilinear model (*TL*). Good agreement between the results of full-scale experiments conducted on the *DS* deck and predictions from the corresponding numerical models proved that the idealized *TL* model can be successfully used to represent the actual moment-rotation behavior of the *DS* WFJs.

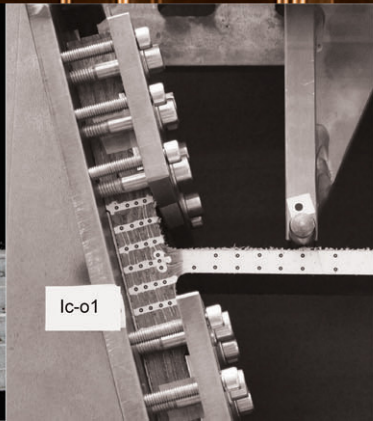
This investigation complements the basis for the assessment of the transverse behavior of pultruded GFRP decks provided in previous work.⁷ Further work will consider the results presented here for the entire characterization of the system's nonlinear transverse in-plane shear modulus up to failure and the subsequent evaluation of its effects on the global performances of both the slab and the hybrid girder.

References

1. Hollaway L. A review of the present and future utilisation of FRP composites in the civil infrastructure with reference to their important in-service properties. *Constr Build Mater* 2010;24(12):2419–2445.
2. Bakis CE, Bank LC, Brown VL, Cosenza E, Davalos JF, Lesko J, et al. Fiber-reinforced polymer composites for construction-state-of-the-art review. *J Compos Constr* 2002;6(2):73–87.
3. Keller T. *Use of fibre reinforced polymers in bridge construction*. Structural engineering documents, 7. Zürich: International Association for Bridge and Structural Engineering IABSE; 2003.

4. Cheng L, Karbhari VM. New bridge systems using FRP composites and concrete: a state-of-the-art review. *Prog Struct Eng* 2006;8(4):143–154.
5. Keller T, Schollmayer M. Plate bending behavior of a pultruded GFRP bridge deck system. *Compos Struct* 2004;64(3):285–295.
6. Gürtler HW. *Composite action of FRP bridge decks adhesively bonded to steel main girders* [PhD Thesis]. Ecole Polytechnique Fédérale de Lausanne, Switzerland; 2004.
7. Yanes-Armas S, de Castro, Keller T. System transverse in-plane shear stiffness of pultruded GFRP bridge decks. *Eng Struct* 2016; 107:34–46.
8. Yanes-Armas S, de Castro J, Keller T. Characterization of rotational behavior of web-flange junctions of pultruded GFRP bridge decks. In: Teng JG, Dai JG (eds.) *Proceedings of the Eighth International Conference on Fibre-Reinforced Polymer (FRP) Composites in Civil Engineering, CICE2016*, 14–16 December 2016, Hong Kong, China. Hong Kong: The Hong Kong Polytechnic University; 2016. p.618–623.
9. Barbero EJ, Raftoyiannis IG. Local buckling of FRP beams and columns. *J Mater Civ Eng* 1993;5(3):339–355.
10. Bank LC, Nadipelli M, Gentry TR. Local buckling and failure of pultruded fiber-reinforced plastic beams. *J Eng Mater Technol* 1994;116(2):233–237.
11. Turvey GJ, Zhang Y. A computational and experimental analysis of the buckling, postbuckling and initial failure of pultruded GRP columns. *Comput Struct* 2006;84(22–23):1527–1537.
12. Bai Y, Keller T, Wu C. Pre-buckling and post-buckling failure at web-flange junction of pultruded GFRP beams. *Mater Struct* 2013;46(7):1143–1154.
13. Ascione F, Mancusi G. The influence of the web-flange junction stiffness on the mechanical behaviour of thin-walled pultruded beams. *Compos Part B* 2013;55:599–606.
14. Mancusi G, Ascione F, Lamberti M. Pre-buckling behavior of composite beams: A mechanical innovative approach. *Compos Struct* 2014; 117:396–410.
15. Wu C, Bai Y. Web crippling behaviour of pultruded glass fibre reinforced polymer sections. *Compos Struct* 2014;108:789–800.
16. Borowicz DT, Bank LC. Behavior of pultruded fiber-reinforced polymer beams subjected to concentrated loads in the plane of the web. *J Compos Constr* 2011;15(2):229–238.
17. Mosallam AS. *Design guide for FRP composite connections*. ASCE manuals and reports on engineering practice, 102. Reston: American Society of Civil Engineers ASCE; 2011.
18. Park KT, Kim SH, Lee YH, Hwang YK. Pilot test on a developed GFRP bridge deck. *Compos Struct* 2005; 70(1):48–59.
19. Zi G, Kim BM, Hwang YK, Lee YH. An experimental study on static behavior of a GFRP bridge deck filled with a polyurethane foam. *Compos Struct* 2008;82(2):257–268.
20. Zi G, Kim BM, Hwang YK, Lee YH. The static behavior of a modular foam-filled GFRP bridge deck with a strong web-flange joint. *Compos Struct* 2008;85(2):155–163.
21. Turvey GJ, Zhang Y. Characterisation of the rotational stiffness and strength of web-flange junctions of pultruded GRP WF-sections via web bending tests. *Compos Part A* 2006;37(2):152–164.
22. Mosallam AS, Feo L, Elsadek A, Pul S, Penna R. Structural evaluation of axial and rotational flexibility and strength of web-flange junctions of open-web pultruded composites. *Compos Part B* 2014;66:311–327.
23. Turvey GJ, Zhang Y. Tearing failure of web-flange junctions in pultruded GRP profiles. *Compos Part A* 2005;36(2):309–317.
24. Turvey GJ, Zhang Y. Shear failure strength of web-flange junctions in pultruded GRP WF profiles. *Constr Build Mater* 2006;20(1–2):81–89.
25. Minghini F, Tullini N, Ascione F. Updating Italian design guide CNR DT-205/2007 in view of recent research findings: requirements for pultruded FRP profiles. *Am J Eng App Sci* 2016; 9(3):702–712.

26. Feo L, Mosallam AS, Penna R. Mechanical behavior of web-flange junctions of thin-walled pultruded I-profiles: An experimental and numerical evaluation. *Compos Part B* 2013;48:18–39.
27. Xin H, Mosallam A, Liu Y, Wang C and Zhang Y. Impact of hygrothermal aging on rotational behavior of web-flange junctions of structural pultruded composite members for bridge applications. *Compos Part B* 2017;110:279–297.
28. DARPA. Advanced composites for bridge infrastructure renewal - Phase II, Task 16 - Modular composite bridge. USA: Defense Advanced Research Projects Agency; 2000.
29. Yanes-Armas S, de Castro J and Keller T. Energy dissipation and recovery in web-flange junctions of pultruded GFRP decks. *Compos Struct* 2016;148:168–180.
30. Keller T, Schollmayer M. Through-thickness performance of adhesive joints between FRP bridge decks and steel girders. *Compos Struct* 2009;87(3):232–241.



Chapter 5

Long-term design of FRP-PUR web-core sandwich structures

5.1 Introduction

Sandwich structures constitute an efficient, versatile and lightweight structural system suitable for a wide variety of structural applications. Fiber-reinforced polymer (FRP) sandwich structures composed of FRP face sheets and relatively low-density core materials have been widely employed in various industries, e.g. aerospace, naval and automotive. Owing to their advantageous properties, the use of load-bearing FRP sandwich structures for civil infrastructure applications, in both the new construction and rehabilitation sectors, is also arousing increasing interest. Advantages of FRP sandwich constructions comprise high strength-to-weight and stiffness-to-weight ratios, rapid on-site assembly, reduced installation times, and design versatility – a vast choice of materials and geometrical options is available. The latter permits the integration into the structural sandwich components of non-structural functions that may be required for different applications, e.g. building physics functions and architectural features in building construction.¹⁻⁴ This merging of functions allows various design criteria to be met in single sandwich elements, thus reducing the number of construction components.

In this context, foam-core-based sandwich structures offer high potential in the building construction domain, as illustrated by successful applications for roof structures.^{2,5} The adoption of polymeric foams with low thermal conductivity as core material provides FRP structural sandwich panels with the thermal insulation characteristics required for roof and wall applications – this is widespread practice in conventional roof and cladding sandwich panels with metallic face sheets. In this respect, rigid polyurethane (PUR) foam is one of the most commonly used core materials on account of its relatively low cost, easy processing and possibility of free-form shaping. The

low stiffness and strength of low-density polymeric foams can however limit the structural performance of sandwich constructions – the core may govern both the deformation and load-bearing capacity of the structure, as several experimental studies have shown.^{6–9} An increase of the foam core density enhances the panel's structural performance – denser foams exhibit superior mechanical properties – but reduces its insulation efficiency.¹⁰ In order to increase the shear stiffness and strength of foam-core sandwich structures, web-core sandwich panels, in which the foam core is reinforced by internal FRP webs or ribs, have been proposed by several authors and the effectiveness of this system has been experimentally demonstrated.^{2,7,8,11,12} From a thermal performance point of view, the webs act as thermal bridges that reduce the insulation efficiency of the sandwich construction; hence, for building applications, the use of thin and widely spaced webs to avoid large conductive thermal losses across the panels is preferable.

The hybrid core of these web-core sandwich panels fulfills similar structural functions to those of a homogeneous core: (i) bears the overall shear force applied to the panel and (ii) prevents the relative slip, i.e. provides composite action between the panel's top and bottom face sheets. The contributions of the webs and foam core to these structural functions depend on several factors, e.g. the mechanical properties of the materials used, the relative dimensions of the components, the number and spacing of the webs. Additionally, a key function of the foam core is to laterally stabilize the thin webs, which are sensitive to local instabilities due to in-plane shear stresses, and prevent wrinkling of the compressed face sheet laminates.

FRP sandwich structures employed for civil infrastructure applications may be subjected to high long-term or permanent loads compared to their self-weight, especially when used for roofs and building floors, e.g. dead loads imposed by the increasingly used green roof solutions¹³ or certain functional purposes such as in the case of storage rooms or workshops.^{14,15} In addition, according to current regulations,¹⁴ imposed occupancy loads on buildings (e.g., normal use by persons, furniture and movable objects), which can also significantly exceed the self-weight of the lightweight sandwich components, are to be considered as medium-term loads, i.e. with up to six-months' accumulated duration. Furthermore, the working life required of building structures is typically equal to or higher than fifty years.¹⁷ In this context, it is therefore essential that creep be considered in structural design. FRP sandwich panels with polymeric foam cores subjected to sustained loads are prone to creep due to the viscoelastic character of both the foam and the FRP laminates, the latter owing to the polymeric nature of the matrix. Thus, creep constitutes a major concern regarding the application of FRP sandwich structures for building construction, and its effects must be appropriately taken into account in their design.

Creep of the FRP and foam constituent materials, affecting both their stiffness and strength, has several effects on the mechanical behavior of web-core sandwich panels. The effects of creep on the materials' stiffnesses influence the elastic stability of the sandwich structure (global) and its individual components (local). In particular, the stabilization provided by the

foam to the thin FRP laminates can significantly diminish over time due to creep of the former. Long-term creep deformations of the FRP face sheets and webs and foam core also result in an increase over time of the initial deflection of the sandwich structure. Shear creep of the core causes changes in the initial cross-sectional through-thickness stress distribution. Owing to the different creep behaviors of the web laminates and foam core components, their contributions to bearing shear forces can also vary with time. Furthermore, the overall shear strength provided by the hybrid core is influenced by creep – the individual material strengths under sustained loading (creep rupture strength) and stability of the web laminates are dependent on creep effects.

The creep of FRP materials is fundamentally a matrix-dominated phenomenon. The main factors affecting the magnitude of creep are related to the material itself (the polymer matrix and its curing degree, type and quantity of fiber reinforcement, fiber orientation in relation to applied loads, manufacturing process) and to the service conditions (exposure to temperature, moisture and/or aggressive environments, loading type, stress level).¹⁸ Extensive research on the creep behavior of FRP materials has been conducted during the last thirty years; comprehensive reviews on the subject can be found in the literature.^{19,20}

On the other hand, little research has been published^{21,22} regarding the creep behavior of polymeric foams, specifically of rigid PUR foams, in spite of its relevance for evaluating the long-term behavior of sandwich structures in which they are used as core material. Most of the experimental data available are based on flexural creep experiments concerning sandwich panels composed of PUR foam cores and metallic face sheets.^{23–27} The main objective of these studies was to assess long-term stiffness under sustained loading of the examined panels. The creep factor (related to the creep compliance) of the PUR foam core subjected to shear was estimated from the measured panels' creep deflections. No general analysis of the foam properties and creep behavior relevant to overall sandwich structural performance is however available.

Studies attempting to model the creep behavior of sandwich panels comprising viscoelastic materials have also focused on their creep deflection response.^{28–31} Analytical and numerical investigations concerning the redistribution of internal forces between the face sheets and core components^{28,31} – sandwich panels with homogeneous cores – and of shear forces between the web and foam components³² – hybrid cores – resulting from the viscoelastic behavior of the constituent materials have been conducted. Further focuses of research studies comprise the global^{28,33} and local³³ instability effects caused by the viscoelastic nature of the core material.

The current design framework for the consideration of sustained loading effects in FRP sandwich structures for civil engineering applications is somewhat limited. The available design recommendations or prospective guidelines for the design of FRP structures^{15,18,34,35} take into account the creep of FRP materials, both concerning stiffness and strength, via the application of time-dependent material safety factors, stiffness reduction factors or

conversion/modification factors. In contrast, although FRP sandwich design is covered by most of these recommendations, provisions for corresponding factors for the foam core material are generally not made, apart from in the German BÜV recommendation.¹⁵ This may constitute an obstacle for corresponding engineering designs. An assessment concerning aspects related to the foam core, relevant to the structural performance of FRP sandwich construction, is required in order to appropriately establish or select those factors and assist structural engineers, who are generally not familiar with the use of polymeric foams for structural purposes, in the designing process.

Of particular relevance for structural design is the approach adopted in the available design recommendations for considering creep effects on design aspects influenced by the web-core interaction, e.g. shear force distribution, web laminate instability, shear strength of the hybrid core. Given the different sets of material factors provided in each recommendation, in many cases unavailable for the foam core, the application of each of these may result in different corresponding designs, thus pinpointing the inconsistency and potential need for harmonisation between these guidelines.

The objective of this work is to address the structural design of FRP-PUR web-core sandwich structures subjected to sustained loading. A brief review of the creep behavior of PUR foams used as core materials and the relevant properties affecting the long-term structural performance of sandwich panels is provided in the first part. In the second part, the time-dependent behavior of web-core sandwich panels and specifically the aspects influenced by the web-core interaction, are analyzed. The effects of selecting particular guidelines for design are evaluated based on a case study. Lastly, design provisions for the cross-sectional design of the hybrid web-core are proposed.

5.2 Mechanical behavior of PUR foams used as sandwich core material

Rigid PUR foams are one of the most commonly used core materials for structural sandwich panels. An insight into specific aspects of their mechanical behavior that need to be taken into consideration when they are used for structural purposes is provided in this section. The two following subjects are particularly addressed: (i) the mechanical anisotropy and (ii) the creep behavior of PUR foams.

5.2.1 Anisotropy of rigid PUR foam properties

One of the main advantages offered by PUR foams for their use as sandwich core material is that they can be easily shaped or cut to adopt a selected geometry. This offers the possibility of constructing complex forms, e.g. to fulfill aesthetical architectural requirements in building applications. However, the mechanical behavior of PUR foams may not be isotropic, and therefore the orientation (and relevant mechanical properties) of the foam in relation to the acting forces needs to be taken into account in structural design. The understanding and assessment of the mechanical anisotropy of PUR foams are therefore necessary.

PUR foams consist of a polymeric solid phase (polyurethane, also referred to as urethane) and a gas phase. The bulk polyurethane polymer exhibits isotropic behavior, whereas the behavior of PUR foams can be anisotropic, since it is influenced by the properties of the solid and gas constituents and the cellular morphology of the foam material, which is in turn affected by the manufacturing process.

PUR foams are produced by mixing two main liquid components (a polyol and an isocyanate) and a blowing agent. Raw materials also include catalysts and surfactant additives, and may contain flame retardants, antioxidants, fillers and/or colorants. Both rigid PUR foams used in the construction domain and flexible PUR foams typically employed for cushioning, packaging and furnishing applications are based on a similar chemistry. However, rigid closed cell foams are produced from short-chain and highly branched polyols, whereas long-chain and lightly branched polyols are used for the production of flexible open cell foams; this results in a highly crosslinked and very stiff polyurethane structure in the former case compared to the latter. The production of PUR foams comprises two simultaneous phenomena: (i) the polymer formation, via the polyaddition reaction between the polyol and the isocyanate constituents, and (ii) the gas generation. Two types of gas generation methods, and their combinations, can be used depending on the selected blowing agent(s): (i) physical and (ii) chemical. In the former, blowing agents consist of liquids with low boiling points, inert to the polymer, which evaporate due to the heat release of the exothermic polyaddition reaction. In chemical gas generation, compounds whose chemical reaction with the isocyanate component results in the foaming gas phase are used as blowing agents.

The gas bubbles, which are spherical upon formation, expand during the foaming process. When the volume fraction of bubbles exceeds a certain amount corresponding to the most densely packed arrangement of spherical cells (74%),³⁶ the bubbles will cease to be spherical and adopt a polyhedral shape (pentagonal dodecahedra and tetradecahedra shapes have been reported). The final cellular structure of the PUR foam is reached at the end of the gel time of the reaction process, representing the transition of the reaction mix from the liquid to the solid state. The gas volume, which decreases with increasing foam density, is estimated to be approximately 98–80% for foams in the 30–240-kg/m³ density range.

The foam's cellular morphology is influenced by the foam's manufacturing process. Polymer foams produced by pouring the reaction mix into an open mold usually have cells that are mainly elongated in the rise direction, i.e., vertically oriented. For applications where stretched cells are not admissible, a mold closed on all sides can be used – the top cover prevents the foam from free rising and enables its compaction, thus counteracting vertical cell elongation. For the production of large PUR foam blocks or buns (slabstock foam), continuous manufacturing using a moving belt is selected. The reaction mix is applied into a continuous U-shape paper mold, open on its top side and lying on a conveyor belt, which serves as releasing agent and to transport the

developing bun; the side walls are also designed as conveyor belts which allow the block's shape to be maintained against the lateral pressure originating during the foam's expansion process. In order to impose a rectangular cross section onto the otherwise freely expanding foam and minimize material waste, a moving lid is also used on the top side in the rising foam zone. The foam has a flowing movement along the production line during the expansion phase; the flow resistance may result in a stretched cell geometry, elongated in the rise (vertical, through-thickness) direction – expansion in this direction may however be partially restrained by the top lid.

The geometrical anisotropy in the cell morphology can be expressed by the shape-anisotropy ratio, R , which represents the ratio of the largest cell dimension to the smallest. The minimum R value equals 1.0 and applies for isotropic foams; values of 10 or more can be obtained for highly anisotropic foams.³⁷ For polymeric foams, typical R values are approximately 1.3.³⁷ The cell morphology of rigid PUR foams with densities ranging from 32 to 160 kg/m³ was investigated by Huber and Gibson.³⁸ The cells were found to be roughly axisymmetric and oriented parallel to the foam rise direction, and a decreasing R from 1.47 to 1.19 with increasing density was obtained. According to the authors, for a given cell size, the thickness of the cell walls increases with increasing density; the gas pressure inside the cell cannot therefore raise the additional weight of the walls as high; as a result, the elongation of the cells in the rise direction is reduced. Comparable R values are reported in other studies conducted for different PUR foam formulations.^{39–42}

The foam's mechanical properties are significantly influenced by the shape-anisotropy ratio. The foam exhibits superior stiffness and strength properties in the direction parallel to cell elongation compared to those in the two perpendicular directions. The elastic modulus and plastic collapse strength are the two most sensitive properties to the cell shape.³⁸ Analogously to R , the elastic modulus or stiffness anisotropy ratio, R_E , and the strength anisotropy ratio, R_f , can be defined.

Several models have been proposed to relate the geometrical and mechanical anisotropy of polymer foams.^{38,39,43} According to the model presented by Huber and Gibson,³⁸ for axisymmetric cell morphology with R shape-anisotropy ratio, R_E and R_f (this applied to the collapse strength) increase as fast as R^2 and R , respectively.

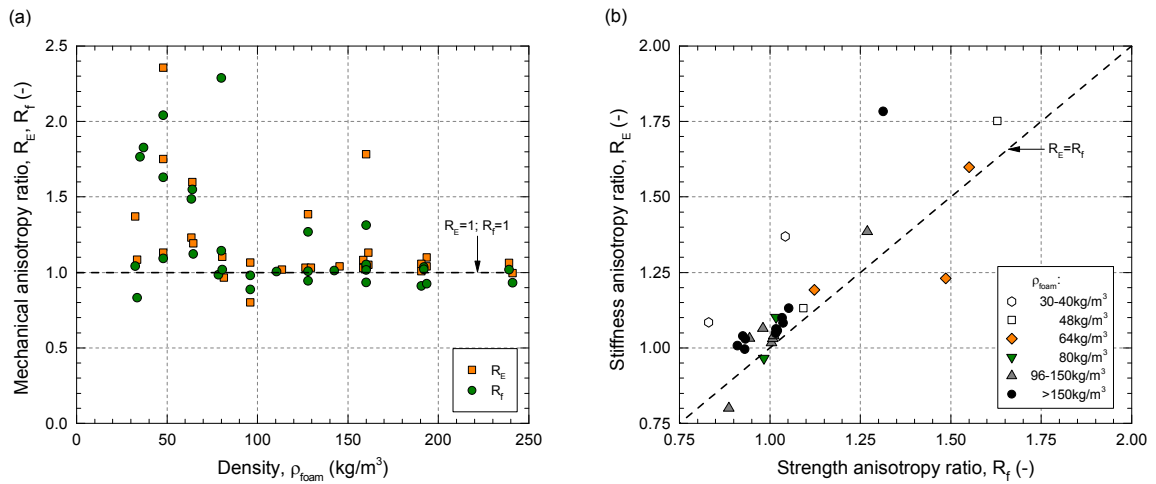
The R , R_E and R_f values experimentally obtained for different rigid PUR foams reported in several studies^{38–41} are shown in Table 5.1. Geometrical anisotropy ratio R results in generally equal or higher mechanical anisotropy ratios R_E and R_f , i.e., in $R_E/R \geq 1$ and $R_f/R \geq 1$ (results for compression from the study conducted by Kanakkanatt³⁹ deviate however from this trend). As suggested by Huber and Gibson,³⁸ the influence of R appears to be significantly higher on R_E than on R_f (results from the study by Esmaeilnezhad et al.⁴⁰ are however not consistent with this hypothesis).

Reference	Foam density ρ_{foam} (kg/m ³)	Loading type	Shape	Stiffness	Strength
			anisotropy ratio R	anisotropy ratio R_E	anisotropy ratio R_f
Huber and Gibson ³⁸	32/64/96/160	C	1.41/1.47/1.23/1.19	2.52/3.31/2.26/2.12	1.73/1.94/1.48/1.46 ^(a)
Kanakkanatt ³⁹	n/a	C	1.54/1.64/1.70	1.40/1.70/1.70	n/a
	n/a	T	1.54/1.64/1.70	2.20/2.60/2.80	n/a
Esmailnezhad et al. ⁴⁰	34-35	C	1.20/1.26/1.27/1.29	1.88/1.92/1.91/1.88	2.30/2.18/2.13/2.11 ^(b)
Ridha and Shim ⁴¹	23.3/29.5/35.2	T	2.5/2.0/1.7	17/9/4	3.0/2.2/2.0

C= compression, T= tension, in-plane

(a) Values obtained based on the collapse strength

(b) Values obtained based on the yield stress



^ Table 5.1 – Shape-anisotropy ratio and mechanical anisotropy of PUR foams.

√ Figure 5.1 – Compressive stiffness and strength anisotropy ratios of commercially available rigid PUR foams of 30–240 kg/m³: (a) influence of foam density; (b) comparison; from references 44–48.

Data presented in Table 5.1 are specific to the PUR foams examined in the relevant investigations. Moreover, the PUR foams referred to by Esmailnezhad et al.⁴⁰ and Ridha and Shim⁴¹ are of low density compared to those used for structural purposes (typically in the 40–150- kg/m³ range) and were specifically manufactured for the investigations by the hand-mixing method, whose reproducibility may be lower than for industrially machine-produced PUR foams. The direct applicability of these results for a particular engineering design may therefore be limited.

The compressive stiffness and strength anisotropy ratios of currently commercially available rigid PUR foams used for core applications and with densities (ρ_{foam}) in the 30–240-kg/m³ range are shown in Figure 5.1(a). The R_E and R_f values were calculated based on the *parallel*- and *perpendicular to rise* mechanical properties reported in the products' datasheets available from the manufacturers.^{44–48} Figure 5.1(a) shows that both R_E and R_f decrease with increasing foam density – this trend was expected since the shape-anisotropy ratio R also decreases with density, as mentioned above. The mechanical anisotropy is significantly higher for foams with densities below 80 kg/m³, with R_E and R_f values up to 2.36 and 2.04, respectively. A sharp decrease of mechanical anisotropy with increasing density is observed for this range. For higher densities, with smaller gas volumes, the mechanical anisotropy seems

not to be significantly influenced by the density: R_E and R_f values closer to 1 (representing isotropic behavior) are obtained regardless of ρ_{foam} .

Figure 5.1(b) shows the comparison between the compressive stiffness anisotropy ratio (R_E , on the ordinate) and the compressive strength anisotropy ratio (R_f , on the abscissa) of the examined foams. For most of the foams the R_f - R_E points lay above the straight line $R_E = R_f$, representing the equality of the stiffness and strength anisotropy ratios (see $R_E = R_f$ in Figure 5.1(b)). It can be inferred that given a certain foam shape-anisotropy ratio R , its influence on the foam's mechanical anisotropy, for compressive loading, is higher with reference to stiffness than to strength. This is in accordance with the model proposed by Huber and Gibson³⁸ for anisotropic cellular materials, and with the R_E and R_f values obtained by the same authors from the experiments conducted on PUR foams of different densities, see Table 5.1.

5.2.2 Creep behavior of rigid PUR foams

PUR foams exhibit viscoelastic behavior due to the polymeric nature of their solid phase material (polyurethane). Polyurethanes, and therefore PUR foams, exhibit creep at room temperature, which may limit their use for structural applications, especially in the case of long-term or permanent loads.

Many solid polymers are linear viscoelastic, i.e., the creep strains at a given time are directly proportional to the applied stress under constant load; the constant of proportionality is given by the time-dependent creep compliance, i.e. the inverse of the time-dependent elastic modulus $E(t)$ (time-dependent shear modulus, $G(t)$, in the case of shear creep). However, under the application of large strains or stresses or for long loading times, they may become nonlinear viscoelastic, i.e., the strain at a specific time is no longer linearly proportional to the applied stress. For engineering design purposes, time-dependent elastic moduli $E(t)$ and $G(t)$, independent of the stress level, can be applied provided that the linear viscoelastic limit is not exceeded. Furthermore, it is suggested that the stress level for long-term loading is limited in order to avoid excessive creep deformations and creep rupture. A limit value of 20% of the short-term strength for a 20-year service life is recommended for rigid PUR foams used as floor insulation and subjected to sustained loading.⁴⁹

The linear viscoelastic limit of rigid PUR foams with densities ranging between 32 and 96 kg/m³ and subjected to shear for durations of 1200 h at 23±1°C was found by Huang and Gibson²¹ to be greater than 40% of their short-term strength. In the experimental study conducted by Garrido et al.,²² lower stress limits for the linear viscoelastic behavior of a rigid 87-kg/m³ PUR foam under shear were observed. For different temperatures in the 20–28°C range, the foam exhibited linear viscoelastic behavior at stress levels of 11 and 22% of its strength; unlike results obtained by Huang and Gibson,²¹ the reported creep response for the 44% stress level was nonlinear. The creep response was also found to be highly dependent on temperature, despite the narrow temperature amplitude (8°C) considered.

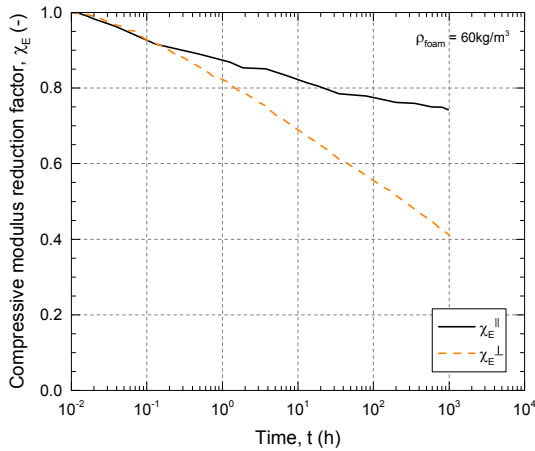
In the following, the effect of three factors (anisotropy of cell morphology, density, loading type) on the creep behavior of PUR foams is highlighted,

based on experimental creep data available in the literature. Considering the stress level and the temperature influence on the viscoelastic response of PUR foams, all selected data comply with a stress level lower than 25% of the material's short-term strength and are valid for room temperature, the latter in the range of 20–24°C. Data are presented in the form of moduli reduction factors (χ_E and χ_G for compression and shear, respectively). These are obtained as the ratio between the time-dependent modulus ($E(t)$ or $G(t)$ for compression and shear, respectively) and the relevant initial elastic moduli (E_0 or G_0) of the material for a given creep time, i.e. $\chi_E(t) = E(t)/E_0$ and $\chi_G(t) = G(t)/G_0$. Subsequently, the theoretical formulation for the creep response of rigid PUR foams in the linear viscoelastic range is presented. Finally, the current structural design approach proposed in the BÜV¹⁵ to take creep effects on PUR foams into account when used as core material of sandwich panels with FRP face sheets is addressed and discussed.

Effect of cell shape anisotropy, density and loading type

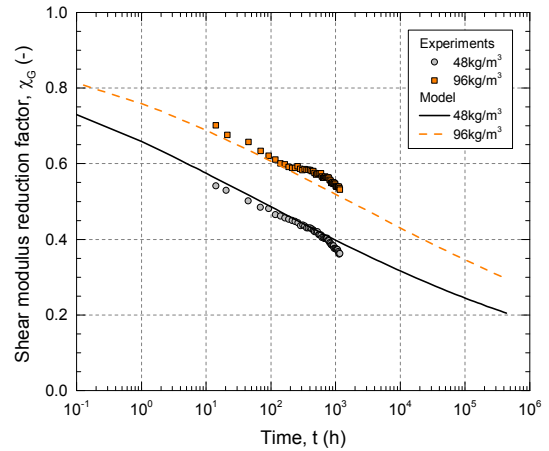
In the construction domain, densities in the range of 40–100 kg/m³ should be selected for rigid PUR foams acting as core material of structural sandwich panels with FRP face sheets, according to the BÜV¹⁵ (a higher low bound value of 50 kg/m³ is recommended in EUR 27666³⁵ and the use of PUR foam densities up to 145 kg/m³ is reported by Keller et al.).² PUR foams in this range exhibit anisotropic cell morphology, especially for the lowest densities, which results in anisotropic mechanical behavior (see Section 5.2.1). A different creep response is therefore expected depending on the relation between the direction of the applied load and the cellular structure of the material. In the study conducted by Schmidt,⁵⁰ compressive creep experiments for a duration of 1000 h were performed on a 60-kg/m³ rigid PUR foam applying the load both parallel to and perpendicular to the foam's rise direction (referred to as *parallel* and *perpendicular* in the following). For a given stress level, the measured deformations were higher for perpendicular loading than for parallel loading. This is partially explained by the higher stiffness of the foam in the parallel (rise) direction, aligned with the cell elongation, than in the perpendicular direction. In order to assess the effect of cell anisotropy on the creep behavior, the moduli reduction factors in both directions ($\chi_E^{\parallel}(t)$ and $\chi_E^{\perp}(t)$ for parallel and perpendicular, respectively) were calculated based on the reported deformation-time data for a stress level of 0.098 MPa. The results are shown in Figure 5.2. Lower values were obtained for $\chi_E^{\perp}(t)$ than for $\chi_E^{\parallel}(t)$ throughout the testing period. Furthermore, a faster decrease with time applies for $\chi_E^{\perp}(t)$. For a 1000-h loading period (equal to the duration of the experiments), reduction factors differ by 57% – values of $\chi_E^{\parallel}(1000 \text{ h}) = 0.74$ and $\chi_E^{\perp}(1000 \text{ h}) = 0.41$ apply. This suggests that for compressive loading foams may be more sensitive to creep when the load is applied perpendicular to the rise direction than parallel to it. It may therefore be necessary to take foam anisotropy into account for the designing of structural sandwich components in which the PUR foam is subjected to long-term loads.

The creep behavior of a PUR foam depends on the creep of the solid polymer. However, for a given solid polymer formulation, different creep



< Figure 5.2 – Effect of anisotropy on compressive creep behavior of a 60-kg/m³ PUR foam, calculated from Fig. 8 in reference 50.

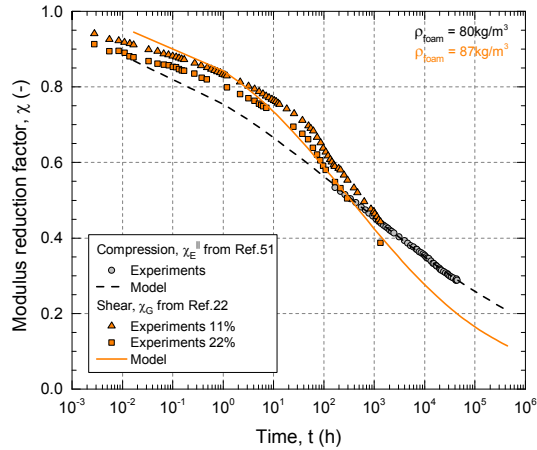
> Figure 5.3 – Effect of density on shear creep behavior of rigid PUR foams, calculated from Fig. 5 in reference 21.



behavior of the foamed material may be expected depending on the relative volume of the gas phase vs the solid phase, i.e. depending on the foam density. Huang and Gibson²¹ analyzed the linear viscoelastic behavior of polymer foams and provided expressions for the creep of the foam as a function of the creep of the solid polymer and the relative density of the foam. According to their model, in the linear viscoelastic range, the product of the creep compliance multiplied by the initial shear modulus of a foam ($J(t) \cdot G_0$), i.e. the ratio of the initial to the time-dependent shear modulus ($G_0/G(t)$), is a constant function of time, independent of the foam density. The same modulus reduction factor ($\chi_G(t) = G(t)/G_0$) would therefore be applicable for foams produced using the same solid polymer, regardless of the final density. Analogously, the same would apply for compressive creep and the Young's modulus. However, experimental data obtained from shear creep experiments performed by the same authors on PUR foams with different densities (32 to 160 kg/m³) showed that the $J(t) \cdot G_0$ product tends to decrease slightly with increasing foam density, which indicates that the shear modulus reduction factor increases with density and that denser foams are less prone to creep. The calculated modulus reduction factors for the 48-kg/m³ and the 96-kg/m³ foams at a stress level equal to 20% of their short-term strength are shown in Figure 5.3. Significantly lower $\chi_G(t)$ values were obtained for the 48-kg/m³ foam than for the 96-kg/m³ foam – e.g. 30% lower for a 1000-h time period. This suggests that PUR foams may be more sensitive to creep with decreasing density.

PUR foams used as cores of sandwich structural panels can be subjected to both shear and compressive stresses, i.e.: (i) the global shear force applied to a sandwich panel is borne by the core material; (ii) the panel may be subjected to concentrated loads perpendicular to it, e.g. at the supports. Also, local instability of the compressed sandwich face sheets is affected by both the shear and compressive stiffness properties of the core, which acts as an elastic foundation. To assess the behavior of the sandwich structural element under long-term loading, the shear and compressive creep responses of the foam are required. Figure 5.4 shows the compressive and shear moduli reduction factors of two rigid PUR foams of similar density. The compressive modulus reduction factor $\chi_E^{\parallel}(t)$ is shown for a 80-kg/m³ foam investigated at a stress level equal to 23% of the foam strength;⁵¹ the compressive load was applied parallel

Figure 5.4 – Comparison of compressive and shear creep behavior of rigid PUR foams, calculated from references 22 and 51.



to the foam rise direction, the experiments had a duration of approximately 45 000 h (≈ 5 years) and were performed at 23°C. The shear modulus reduction factor $\chi_G(t)$ is given for a 87-kg/m³ foam whose creep shear behavior at different temperatures and stress levels was experimentally investigated by Garrido et al.²² Data corresponding to experiments performed at 24°C and applying shear stress levels equal to 11 and 22% of the foam shear strength were selected for $\chi_G(t)$ shown in Figure 5.4. Slightly lower reduction factors apply for the 22% compared to the 11% stress level, despite the linear viscoelastic limit not being exceeded. In addition to the experimentally-based $\chi(t)$ values, which were calculated from the measured creep and elastic strains, the $\chi(t)$ values obtained from expressions presented in the relevant studies to model either the creep strain or the creep factor are also given. Experimentally-based $\chi(t)$ values for shear and compression are comparable in the time interval from one week to eight weeks of sustained loading (168–1344 h). However, for times longer than eight weeks, the trends of the experimentally-based $\chi(t)$ and model-based $\chi(t)$ suggest that PUR foams creep more under shear than under compressive loads applied parallel to the rise direction ($\chi_G < \chi_E^{\parallel}$). For compressive loads applied perpendicular to the rise direction, the opposite may apply, since shear can be considered as a biaxial compression-tension stress state, oriented at around 45° in relation to the parallel- and perpendicular-to-rise directions, and $\chi_E^{\perp} < \chi_E^{\parallel}$. For design purposes a distinction between these loading types should therefore be made.

Theoretical formulation

Numerous experimental investigations of the creep behavior of rigid PUR foams^{21,22,51–53} and sandwich panels with PUR foam cores and metallic face sheets^{23,24,26,27,29,54} have shown that the creep response of these foams in the linear viscoelastic range is well explained by a power law dependency of time. In particular, Findley's power law formulation⁵⁵ has been successfully used in most of these studies to model the foam's compressive or shear creep behavior. Further studies have extended Findley's formulation to include the temperature influence on the creep response of PUR foams.²² Findley's law is also used in the EN 1606 standard⁵⁶ for thermal insulating products, which include rigid PUR foams, to model creep experimental data and enable

extrapolation for the determination of a long-term deformation value due to compressive creep. There is general agreement on the validity of Findley's law to describe the creep behavior of polymeric foams.

The basic expression for Findley's power law formulation is given by:

$$\varepsilon(\sigma, t) = \varepsilon_0 + m \left(\frac{t}{t_0} \right)^n \quad (5.1)$$

where ε = total strain, σ = applied stress, t = time elapsed after load application, ε_0 = elastic strain, m = creep amplitude, t_0 = time unit considered and n = time exponent. The first term represents the elastic, instantaneous strain, while the second term represents the viscoelastic or creep (time-dependent) strain. The creep amplitude, m , is proportional to stress in the linear viscoelastic range and the time exponent, n , may be taken as a material constant for a given hygrothermal condition.

Provided that the foam creep behavior responds to Findley's power law, the modulus reduction factor, $\chi_E(t)$, can be expressed as follows:

$$\chi_E(t) = \frac{E(t)}{E_0} = \frac{\varepsilon_0(\sigma)}{\varepsilon(\sigma, t)} = \frac{1}{1 + \frac{m}{\varepsilon_0(\sigma)} \left(\frac{t}{t_0} \right)^n} \quad (5.2)$$

Since both m and $\varepsilon_0(\sigma)$ are proportional to stress (the constant of proportionality for the latter is given by E_0), $\chi_E(t)$ can be formulated as:

$$\chi_E(t) = \frac{1}{1 + a \left(\frac{t}{t_0} \right)^n} \quad (5.3)$$

where a = a constant and the term $a \cdot (t / t_0)^n$ is the creep factor or creep coefficient, $\phi(t)$, which equals the ratio of the creep strain, $m \cdot (t / t_0)^n$, over the elastic strain, ε_0 .

Analogous expressions to Equations (5.1)–(5.3) can be written in terms of shear strain (γ), shear stress (τ) and shear modulus (G) for the total shear strain under sustained loading and the corresponding shear modulus reduction factor, $\chi_G(t)$.

Based on Findley's law, representation of both the creep strain ($m \cdot (t / t_0)^n$) and the creep factor ($\phi(t) = a \cdot (t / t_0)^n$) over time on a double logarithmic scale plot results in straight lines of slope n and y -intercepts at m and a , respectively.^{23,24,26,27,54} This does not apply for the moduli reduction factors, since they are not described by a power law of time, see Equation (5.3).

Creep of PUR foams in structural design of sandwich panels

Several design recommendations or corresponding prospective guidelines (German BÜV,¹⁵ European EUR 27666,³⁵ Dutch CUR96+³⁴) are currently available for the structural design of sandwich panels consisting of FRP face sheets and foam core. All these recommendations highlight the relevance of taking creep effects into account in the design. In all of them long-term loading effects are included by applying to the material properties a reducing influence or conversion factor ($A_I / \eta_{cv} / \gamma_{ck}$ in the BÜV / EUR 27666 / CUR96+, respectively). However, among the abovementioned guidelines, only the BÜV

provides such influence factors for foams. EUR 27666 states that design data for core materials should be based on experiments. For creep behavior, the ASTM C480 standard⁵⁷ is referred to, but neither any indication on how to include the experimental results in the design nor any acceptance criterion is given.

The A_I influence factor in the BÜV, equivalent for stiffness to the inverse of the modulus reduction factor ($A_I^E(t) = 1/\chi_E(t)$ and $A_I^G(t) = 1/\chi_G(t)$), is formulated as:

$$A_I(t) = (A_{I,20J})^T \quad (5.4)$$

where $A_{I,20J}$ is the basic value for A_I after a 20-year loading time and the exponent T is calculated as:

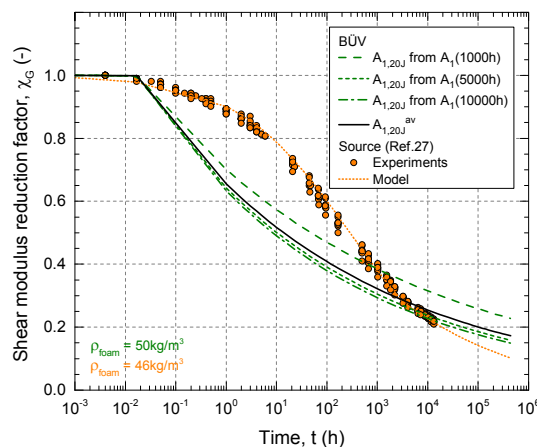
$$T = 0.253 + 0.142 \log(t) \quad (5.5)$$

with t in hours. Representation of the A_I influence factor against time in a double logarithmic scale plot results in a straight line. This also applies for the moduli reduction factors, since for stiffness $A_I(t) = 1/\chi(t)$.

The $A_{I,20J}$ values for PUR foams are not provided in the BÜV, presumably due to the absence of creep experimental data covering a 20-year period. Instead, A_I reference values for loading times of 1000, 5000 and 10 000 h are given. $A_{I,20J}$ can therefore be calculated by using those values conjointly with Equations (5.4) and (5.5). Different A_I reference values for stiffness are given depending on the foam density (50 and 100 kg/m³) and loading type (shear or compression). No distinctions are made however to consider the effect of the foam anisotropy on its creep behavior.

The shear modulus reduction factor $\chi_G(t)$ calculated according to the BÜV for a 50-kg/m³ PUR foam is shown in Figure 5.5. The $A_I(1000 \text{ h}) = 2.6$, $A_I(5000 \text{ h}) = 3.9$ and $A_I(10\,000 \text{ h}) = 4.4$ reference values (Table C-1 in the BÜV) and their corresponding loading times were replaced in Equation (5.4) to calculate $A_{I,20J}$. Three $A_{I,20J}$ values were thus obtained (4.08, 5.75 and 6.08, respectively). The resulting $\chi_G(t)$ curves for each calculated $A_{I,20J}$ and for the average, $A_{I,20J}^{av}$, are shown. For a 50-year load duration (438 000 h), considering the reference value corresponding to the shortest time, $A_I(1000 \text{ h})$, results in χ_G values that are 52 and 32% higher than if using the reference value from the longer time, $A_I(10\,000 \text{ h})$, or the average $A_{I,20J}^{av}$. Relia-

Figure 5.5 – Comparison of shear modulus reduction factor for 50-kg/m³ PUR foam calculated according to BÜV¹⁵ and experimentally determined from reference 27.



ble creep predictions for long-term scenarios may thus need longer experimental times (in EN 1606⁵⁶ extrapolation is permitted up to 30 times the testing time, which for a 50-year extrapolation would require experiments of approximately 15 000-h duration).

The experimental investigation of shear creep conducted by Just²⁷ on sandwich panels with a 46-kg/m³ PUR foam core and steel face sheets is the quoted source in the BÜV for the A_1^G values of the 50-kg/m³ foam. In order to assess the BÜV approach to obtain the time-dependent moduli, the $\chi_G(t)$ curves for the investigated 46-kg/m³ foam were obtained using the creep experimental data reported by Just²⁷ and the model proposed by the author to represent the creep factor, based on Findley's law. The latter was formulated as $\phi(t) = a \cdot t^n$ with $a = 0.11/0.34$ and $n = 0.39/0.25$ for time periods of under/over 3 000 h. A comparison of the $\chi_G(t)$ curves obtained by applying the BÜV and those calculated from reference 27 is shown in Figure 5.5. The two sets of curves show different trends: the decreasing rate of $\chi_G(t)$ in the curves from reference 27 is more pronounced with increasing time, whereas it stabilizes for those from the BÜV. As a result, for time periods shorter than approximately 3 000 h (equivalent to four months), the $\chi_G(t)$ values from the BÜV underestimate the experimentally-based values, by a maximum of 35% after a 24-h loading time for the average curve. For structures where a high ratio of short- to long-term loads applies and the short-term scenario governs the final design, the structure would be overdimensioned. However, for long-term scenarios, the $\chi_G(t)$ values from the BÜV are higher than the experimentally-based values (up to nearly 70% higher after a 50-year loading time for the average curve). For structures with high permanent loads, this may result in an unconservative design – at $t = 50$ years, the shear creep deformations of the PUR foam are underestimated by approximately 40%.

5.3 Time-dependent behavior of web-core sandwich panels

5.3.1 Distribution of shear forces

The shear forces applied to a sandwich panel are borne by the core material(s) or system. In web-core sandwich panels whose core is composed of PUR foam and FRP webs or ribs, the applied shear force is distributed between both elements of the hybrid core according to their shear stiffnesses,³² provided that there is adhesion between them and also to the face sheets. Given the viscoelastic behavior of both the PUR foam and the FRP laminates, sustained loading results in a reduction of the shear stiffness of both core constituents with increasing loading time. Since the PUR foam and FRP laminates exhibit different creep behavior, their individual contributions to the total shear stiffness of the hybrid core and therefore the distribution of shear forces between the FRP webs and the PUR foam are time-dependent.

In the following, the obtaining of the time-dependent contributions of the FRP webs and the PUR foam core to bearing the shear forces is briefly addressed. Subsequently, the influence of the selected $\chi_G(t)$ curves to take into account the creep behavior of the PUR foam and the effect of the foam's mechanical anisotropy on the shear distribution are assessed. This is done

based on a case study of a web-core sandwich roof composed of a PUR foam core and glass-FRP (GFRP) webs and face sheets.²

Theoretical formulation

According to Garrido et al.,³² the proportions of shear force borne by the GFRP webs (α_w^{GA}) and the PUR foam core (α_c^{GA}) may be estimated as follows:

$$\alpha_w^{GA}(t) = \frac{\chi_{G,w}(t) \cdot G_w \cdot A_{V,w}}{\chi_{G,c}(t) \cdot G_c \cdot A_{V,c} + \chi_{G,w}(t) \cdot G_w \cdot A_{V,w}} \quad (5.6)$$

$$\alpha_c^{GA}(t) = \frac{\chi_{G,c}(t) \cdot G_c \cdot A_{V,c}}{\chi_{G,c}(t) \cdot G_c \cdot A_{V,c} + \chi_{G,w}(t) \cdot G_w \cdot A_{V,w}} \quad (5.7)$$

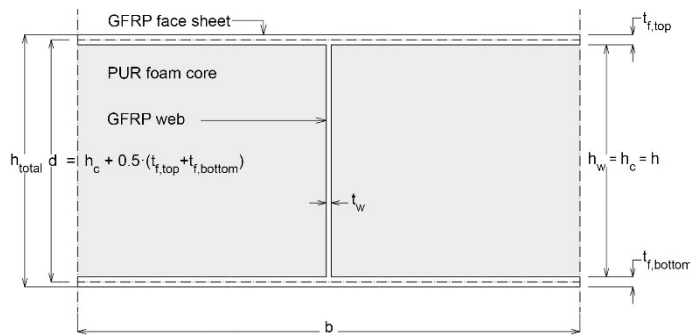
where G_w = in-plane shear modulus of the GFRP web, G_c = shear modulus of the PUR foam, $\chi_{G,w}(t)$ = shear modulus reduction factor of the GFRP web, $\chi_{G,c}(t)$ = shear modulus reduction factor of the PUR foam, $A_{V,w}$ = effective shear area of the web, $A_{V,c}$ = effective shear area of the core (calculated as $A_{V,c} = (b - t_w) \cdot d^2 / h_c$, where $(b - t_w)$ is the foam core width, d is the distance between the face sheets' centerlines and h_c is the core thickness, see Figure 5.6).

The formulation proposed by the authors is based on the following two assumptions: (i) $\alpha_c^{GA} + \alpha_w^{GA} = 1$, i.e. the only components participating in the shear stiffness of the web-core panels are the PUR foam and the GFRP webs, whereas the contribution of the face sheets is neglected; (ii) under sustained loading, these participations vary with time according to the time-dependent shear moduli of the materials (given by the relevant $\chi_G(t)$ factors).

Description of case study

A case study is presented in this section to assess the influence of the selected $\chi_{G,c}(t)$ curves on the predicted time-dependent shear distribution in the web-core sandwich panels subjected to sustained loading. The GFRP-PUR sandwich roof of the Novartis Campus Main Gate Building (Basel, Switzerland) is used.² The core of the sandwich structure consists of a PUR foam with three different densities (60, 80 and 145 kg/m³) and mechanical properties. The PUR core is reinforced by an internal grid of orthogonal GFRP webs spaced 925 mm apart. The roof structure can be modeled as a girder grid system of 925-mm-wide beams (width= b) beams consisting of the upper and lower face sheets as flanges and a hybrid GFRP-web/PUR-foam core. The cross-sectional configuration of the hybrid beam is schematically represented

Figure 5.6 – Cross-sectional geometry of web-core sandwich panel (not to scale).



in Figure 5.6. The following dimensions apply: face sheet thickness $t_{f,bottom} = t_{f,top} = 6-10.5$ mm, web thickness $t_w = 3-9$ mm, sandwich thickness $h_{total} = 70-620$ mm.²

For the current study, the GFRP-PUR sandwich at the support location, subjected to the maximum shear, was analyzed. The 80-kg/m³ PUR foam was adopted and web dimensions ($t_w \cdot h_w$) of 3·400 and 6·400 mm² were evaluated – the reduction of h_{total} resulting from the wedge-shaped cutouts over the supports was disregarded. The characteristic material properties, i.e. 5%-fractile values, of the GFRP web laminates and PUR foam core are given in Table 5.2. The average properties were obtained by dividing the relevant characteristic properties by a factor of 0.8.⁵⁸

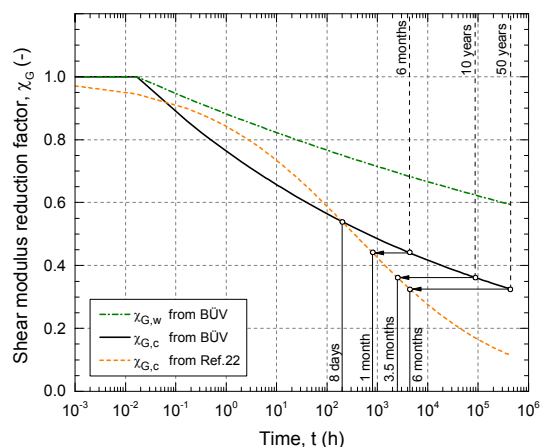
The shear moduli reduction factors of the GFRP webs ($\chi_{G,w}(t)$) and the PUR foam core ($\chi_{G,c}(t)$) to be applied in Equations (5.6) and (5.7) are shown in Figure 5.7. They were calculated according to the BÜV¹⁵ following the procedure described in Section 5.2.2. For the webs, the basic value for a 20-year loading time, $A_{I,20j}$, was calculated for a non-post-cured mixed laminate with a fiber weight fraction of $\delta = 0.43$, corresponding to a fiber volume fraction of $V_f = 29\%$ (the latter was estimated based on the fiber reinforcement type and fiber architecture referred by Keller et al.²). For the 80-kg/m³ PUR foam, a $A_{I,20j} = 2.90$ value was estimated by conjointly using Equations (5.4) and (5.5) with $A_I(1000\text{ h}) = 2.06$; this was obtained by linear interpolation between the $A_I(1000\text{ h})$ values provided for 50- and 100-kg/m³ density foams. Additionally, in order to assess the influence of the $\chi_{G,c}(t)$ curve selection on the expected shear distribution, the model for the $\chi_{G,c}(t)$ factor given by Garrido et al.²² for a 87-kg/m³ foam subjected to shear creep at a temperature of 24°C is also used. The proposed empirical model is based on Findley’s power law formulation, which results in different trends with time of $\chi_{G,c}(t)$ compared to the equivalent curves obtained from the BÜV, as highlighted in Section 5.2.2.

Table 5.2 – Characteristic material properties of GFRP web laminates and PUR foam core.²

Property	GFRP web laminates	PUR foam core
Elastic modulus	$E_{w,k} = 11\ 200$ MPa ^(a)	$E_{c,k} = 25$ MPa
Shear modulus	$G_{w,k} = 3000$ MPa	$G_{c,k} = 10$ MPa
Shear strength	$\tau_{w,k} = 47$ MPa	$\tau_{c,k} = 0.36$ MPa

^(a) Not available in reference 2, value for the face sheet laminates

Figure 5.7 – Shear moduli reduction factors for GFRP webs and PUR foam core.



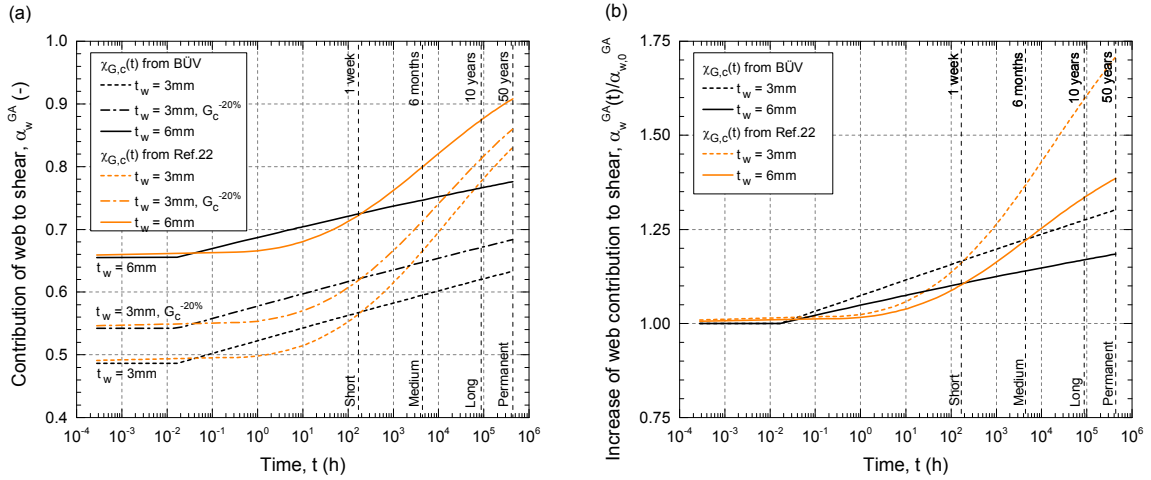


Figure 5.8 – (a) Time-dependent contribution of GFRP webs to bearing shear forces and (b) increase with time.

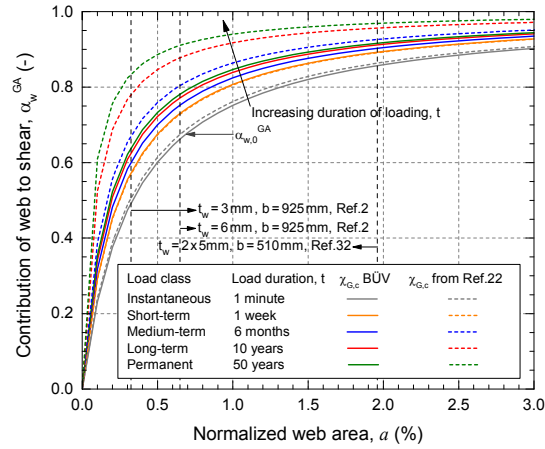
Resulting time-dependent shear distribution

The resulting contributions of the GFRP webs to bearing the shear forces during time, $\alpha_w^{GA}(t)$, are shown in Figure 5.8(a). The proportion of shear force borne by the webs increases with time, indicating that the shear load is partially transferred from the foam core to the webs over time – the PUR foam is more affected by creep than the GFRP laminates and the applicable shear modulus reduction factor is smaller for the former than for the latter, see Figure 5.7. Comparison of the $\alpha_w^{GA}(t)$ curves determined using $\chi_{G,c}(t)$ from the BÜV and from Garrido et al.²² shows that for instantaneous loading equal initial $\alpha_{w,0}^{GA}$ values are obtained in both cases – for $t = 0$ the distribution depends only on the relative area of webs/core and on the initial shear moduli of the components. However, different trends result over time: a linear increase of $\alpha_w^{GA}(t)$ with time (on the logarithmic scale) is obtained using $\chi_{G,c}(t)$ from the BÜV, whereas an increasing rate of $\alpha_w^{GA}(t)$ with time is observed when applying the experimentally-based $\chi_{G,c}(t)$ model from Garrido et al.²² The two sets of curves intersect at an approximately 8-day time point – $\chi_{G,c}(199 \text{ h})$ is the same in both cases, see Figure 5.7. As from this point, considering $\chi_{G,c}(t)$ from the BÜV results in significantly smaller $\alpha_w^{GA}(t)$, i.e. in less shear transfer from the core to the webs. For the 3-mm web thickness, the web contribution for instantaneous loading, $\alpha_{w,0}^{GA}$, is 49%; $\alpha_w^{GA}(t)$ increases to 63 or 83% for a 50-year load duration when selecting the $\chi_{G,c}(t)$ curve from the BÜV or Garrido et al.²² respectively.

The effect of the $\chi_{G,c}(t)$ curve selection on the shear distribution is further illustrated in Figure 5.8(b), which shows the ratio of the time-dependent $\alpha_w^{GA}(t)$ to the initial $\alpha_{w,0}^{GA}$ – this ratio represents the relative increase of the shear force borne by the web over time. For a given web thickness, the ratio corresponding to long-term to permanent loads is 1.14 to 1.31 times greater when using $\chi_{G,c}(t)$ from Garrido et al.²² than when using $\chi_{G,c}(t)$ calculated according to the BÜV, and the highest differences are obtained for the thinner webs. The $\chi_{G,c}(t)$ values from the BÜV may result in underestimating the shear force borne by the webs for long-term scenarios.

In order to assess the effect of the anisotropy of the PUR foam on the shear distribution, a 20% reduction of the foam shear modulus was applied, based

Figure 5.9 – Contribution of GFRP webs to bearing shear forces depending on normalized web area.



on the compressive stiffness anisotropy ratios (R_E) from Figure 5.1(a) for PUR foams of comparable density; the aforementioned shear moduli reduction factors were used. The resulting web contributions are denoted in Figure 5.8(a) by $G_c^{-20\%}$. For the analyzed case, a 20% reduction of G_c results in 10% higher initial contribution of the web to bearing the shear forces ($\alpha_{w,0}^{GA}$ of 0.54 instead of 0.49 for $t_w = 3\text{mm}$). The difference decreases over time, as in both cases the relative contribution of the core diminishes due to creep of the foam.

The α_w^{GA} values as a function of the normalized web area, a ($a = t_w/b$ for $h_w = h_c$ in Figure 5.6), are shown in Figure 5.9 for different durations of the sustained load, t . The selected t values correspond to the upper bounds of the load duration classes established in the BÜV¹⁵ and EUR 27666;³⁵ for permanent loads, an expected working life of 50 years was assumed. Figure 5.9 shows that for a given t , the increase of a results in greater α_w^{GA} values, i.e. in greater contribution of the webs to the shear stiffness of the hybrid core and thus to bearing the shear force. The α_w^{GA} - a relationship is not linear; higher increasing rates apply for lower normalized web areas. A higher increase of the shear force in the webs over time, indicated by the spacing of the α_w^{GA} - a curves, is obtained for lower a values – for higher a , the narrower spacing between the α_w^{GA} - a curves denotes a smaller time-dependent variation of $\alpha_w^{GA}(t)$. As a result, a higher shear transfer from the core to the webs over time is obtained for thinner webs, whose design may consequently be more critical. This is also illustrated in Figure 5.8(b), which shows that for a given $\chi_{G,c}(t)$ curve, higher $\alpha_w^{GA}(t)/\alpha_{w,0}^{GA}$ ratios over time are obtained for the 3-mm than for the 6-mm-thick web.

Figure 5.9 further demonstrates the effect of the $\chi_{G,c}(t)$ curve selection on the shear distribution. Similar $\alpha_w^{GA}(a)$ curves are obtained for 50-year and six-month loading periods when using $\chi_{G,c}(t)$ from the BÜV and Garrido et al.,²² respectively – a similar $\chi_{G,c}$ applies for those time scenarios in the relevant curves, see Figure 5.7. This confirms that the calculated shear distribution is highly dependent on the assumed creep behavior of the materials.

5.3.2 Shear resistance of webs

In web-core sandwich structures, the web components are mainly subjected to shear and their design at Ultimate Limit State (ULS) may be governed by their shear resistance. In many cases, however, the webs of these structural

elements are thin, and therefore sensitive to stability problems, i.e. shear buckling, which can limit their resistance. With a continuous core, e.g. the PUR foam, the web laminates are laterally stabilized by the core, which acts as an elastic foundation and prevents the webs from buckling. Nevertheless, shear wrinkling, a local buckling phenomenon or short wavelength buckling, may occur, especially in the case of flexible cores. Furthermore, under sustained loading, the web laminates become more prone to shear wrinkling due to creep of the foam, and shear buckling failure may be approached for slender webs.

Currently available design recommendations or corresponding prospective guidelines for FRP structures may be used for the structural design of web-core FRP-PUR sandwich panels. In the following, based on the case study presented in Section 5.3.1, the web components are designed for shear according to three different recommendations: Eurocomp,¹⁸ BÜV¹⁵ and EUR 27666.³⁵ The dissimilarities between them, the lacking information for design and the effects of selecting a particular recommendation on the resulting designs are discussed.

Material factors

In all the recommendations, the partial safety factors for materials, also denoted as material factors, comprise several partial coefficients (Eurocomp, EUR 27666) or are modified by additional influence or conversion factors (BÜV, EUR 27666). The partial coefficients and conversion factors take into account different effects on the material properties, which are summarized in Table 5.3. These effects are the source of the material properties, the type and quantity of fiber reinforcement, the matrix type (particularly its curing degree), the manufacturing process, environmental effects such as service temperature and exposure to humidity, the duration of loading and fatigue. In addition, in the BÜV and EUR 27666 they also take into account the verification type (strength or global/local stability), whereas no distinction is made in Eurocomp. Furthermore, influence/conversion factors in the BÜV

Table 5.3 – Effects taken into account in material factors by partial safety coefficients or influence/conversion factors.

	Eurocomp ¹⁸	BÜV ¹⁵	EUR 27666 ³⁵
Property source	γ_{m1}	No	γ_{M1}
Matrix type	γ_{m2} (post-curing) γ_{m3} (HDT ^(a))	A_1^* , A_2 , A_3^* (post-curing)	γ_{M2} , η_{cm} , η_{cv}^* (post-curing) η_{ct}^* ($T_g^{(b)}$)
Fiber architecture, fiber content	No	A_1^* (fiber architecture, $V_f^{(c)}$)	η_{cv}^* (fiber architecture, $V_f^{(c)}$)
Density	No	A_1^* , A_3^*	No
Manufacturing process	γ_{m2}	γ_M , A_1^*	γ_{M2} , η_{cv}^*
Temperature	γ_{m3}	A_2 , A_2 , A_3^* , A_3^*	η_{ct}^* , η_{cm}
Humidity	No	A_2 , A_2	η_{cm}
Load duration	γ_{m3}	A_1^* , A_1^*	η_{cv}^*
Fatigue	γ_{m4}	No	η_{cf}^*
Loading type	No	γ_M , A_1^* , A_3^*	γ_{M2}
Combination type	No	γ_M , γ_M	No
Verification type	No	γ_M , γ_M	γ_{M2} , γ_{M2} , η_{ct}^*

* Different values apply for stiffness and strength

Note: **in bold**, coefficients/factors for PUR foams

^(a) Heat distortion temperature

^(b) Glass transition temperature

^(c) Fiber volume fraction

and EUR 27666 referring to temperature (A_3, η_{ct}) and load duration (A_1, η_{cv}) adopt different values for stiffness and strength properties.

For the design of FRP-PUR sandwich panels, only the BÜV provides material and influence factors for PUR foams; different values are applied to stiffness/strength properties and depending on the loading type (shear/compression). In EUR 27666 the partial material factor γ_{M2} is provided for PUR foams, the conversion factors are not available however. No factors for foams are provided by Eurocomp. The overall structural design of FRP-PUR sandwich panels according to Eurocomp and EUR 27666 may therefore require the determination of material partial factors using other sources.

The partial coefficients, material factors and influence or conversion factors for the GFRP webs and PUR foam core used for the case study were determined, where available, according to the three recommendations. They are given in Tables 5.4 / 5.5 / 5.6 for Eurocomp / BÜV / EUR 27666. For the

^ Table 5.4 – Partial safety coefficients and material factors from Eurocomp¹⁸ applicable to case study.

Table 5.5 – Material and modification factors from BÜV¹⁵ applicable to case study.

√ Table 5.6 – Material and conversion factors from EUR 27666³⁵ applicable to case study.

Material	Time scenario	ULS			
		$\gamma_{m,1}^{(a)}$	$\gamma_{m,2}^{(b)}$	$\gamma_{m,3}^{(c)}$	$\gamma_m = \gamma_{m,1} \cdot \gamma_{m,2} \cdot \gamma_{m,3}$
GFRP web laminates	Short-term	1.15	2.00	1.00	2.30
	Long-term	1.15	2.00	2.50	5.75

^(a) Properties derived from experiments

^(b) Hand lay-up, not fully post-cured at works

^(c) Operating design temperature 25–50°C, Heat distortion temperature from the resin (HDT) > 90°C

Material	γ_M		$A_{mod} = A_1 \cdot A_2 \cdot A_3$		
	Strength	Local stability	A_{mod}^f	A_{mod}^E	A_{mod}^G
GFRP web laminates	1.50 ^(a)	2.00 ^(a)	1.20·1.57 ^T ^(b)	1.10·1.64 ^T ^(b) 1.10·√(1.64 ^T) ^(b, c)	1.10·1.64 ^T ^(b) 1.10·√(1.64 ^T) ^(b, c)
	1.50 ^(d) 1.20 ^(e)	1.70 ^(d) 1.40 ^(e)	1.32·2.38 ^T	1.37·2.53 ^T 1.37·√(2.53 ^T) ^(c)	1.32·2.90 ^T 1.32·√(2.90 ^T) ^(c)

^(a) Hand lay-up, variation coefficient $\nu = 0.17$

^(b) Mixed laminate with mass portion of fibers $\delta = 0.43$, not post-cured

^(c) Values for stability verifications, $\sqrt{A_i}$ is used

^(d) Shear

^(e) Compression

$T=0.253+0.142\log(t)$, with t = time in hours

Material	$\gamma_M = \gamma_{M1} \cdot \gamma_{M2}$			$\eta_c = \eta_{ct} \cdot \eta_{cm} \cdot \eta_{cv}$	
	γ_{M1}	γ_{M2} Strength	γ_{M2} Local stability	η_c^f	η_c^E, η_c^G
GFRP web laminates	1.15 ^(a)	1.92 ^(b)	2.40 ^(b)	0.90·0.637 ^T ^(c) 0.637 ^T ^(c, d)	0.90·0.610 ^T ^(c) 0.610 ^T ^(c, d)
	1.15 ^(a)	1.50 ^(e) 1.20 ^(f)	1.70 ^(e) 1.40 ^(f)	n/a	n/a

^(a) Properties derived from experiments

^(b) Production processes and properties of FRP with $0.10 < \nu \leq 0.17$, not post-cured

^(c) Mixed laminate with mass portion of fibers $\delta = 0.43$, not post-cured

^(d) Values for deformability and stability verifications

^(e) Shear

^(f) Compression

$T=0.253+0.142\log(t)$, with t = time in hours

BÜV and EUR 27666, only the combined modification (A_{mod}) or conversion factors (η_c), respectively, are given; these are calculated as the product of the individual influence/conversion factors. Factors applicable for strength are denoted by superscript f ; superscripts E or G are used to denote those applicable for stiffness.

Concerning sustained loading, it should be noted that Eurocomp only distinguishes between short- and long-term scenarios; no further indication about the corresponding load duration is given. However, both the BÜV and EUR 27666 provide expressions to determine the relevant influence/conversion factors over time (see T exponent in Tables 5.5 and 5.6).

Design value of shear resistance

The webs of GFRP-PUR web-core sandwich panels are designed to verify the ULS for shear. Additionally, the ULS for local stability (shear wrinkling) has to be verified – local wrinkling instability can limit the shear strength of webs, particularly when a flexible core is used (the lateral support it provides to the web laminates may not be sufficient) or under sustained loading (the stabilizing effect of the foam decreases due to creep).

All the recommendations provide similar expressions to verify the ULS for shear. The design shear resistance is defined as the product of the shear area, A_w , multiplied by the design shear strength, τ_d . The latter is calculated from the characteristic shear strength, τ_k , by applying the material factors and conversion factors relating to strength, see Table 5.7. The shear area equals the web cross-sectional area ($A_w = h_w \cdot t_w$) in all cases.

None of the recommendations provides expressions to obtain the shear wrinkling strength, $\tau_{wr,d}$, of FRP laminates; however, the design wrinkling strength under uniaxial compression, $\sigma_{wr,d}$, is defined in the BÜV and EUR 27666. According to Wiedemann,⁵⁹ a conservative lower bound value of the shear wrinkling strength may be estimated from the compressive wrinkling strength as $\tau_{wr,d} = 0.5 \cdot \sigma_{wr,d}$. Equations given in Table 5.7 for $\tau_{wr,d}$ are

Table 5.7 – Design shear, shear wrinkling and critical shear buckling strength equations.

	Eurocomp ¹⁸	BÜV ¹⁵	EUR 27666 ³⁵
τ_d	$\frac{\tau_k}{\gamma_m}$	$\frac{\tau_k}{\gamma_M \cdot A_{mod}^f}$	$\eta_c^f \frac{\tau_k}{\gamma_M}$
$\tau_{wr,d}$	$0.5 \cdot \left(\frac{0.50}{\gamma_m} \sqrt[3]{E_{w,k} \cdot E_{c,k} \cdot G_{c,k}} \right)^{(a)}$	$0.5 \cdot \left(0.82 \cdot \sqrt[3]{E_{w,d} \cdot E_{c,d} \cdot G_{c,d}} \right)$	$0.5 \cdot \left(\frac{0.50 \cdot \eta_c^f}{\gamma_{M2}} \sqrt[3]{E_{w,k} \cdot E_{c,k} \cdot G_{c,k}} \right)$
$\tau_{cr,d}$	$\frac{1}{\gamma_m} \frac{4k_1 (D_{x,k} D_{y,k}^3)^{0.25}}{(h_w^2 \cdot t_w)}$	$\frac{4k_2 (D_{x,d} D_{y,d}^3)^{0.25}}{(h_w^2 \cdot t_w)}^{(b)}$	$\frac{\eta_c^f}{\gamma_M} \frac{4k_2 (D_{x,k} D_{y,k}^3)^{0.25}}{(h_w^2 \cdot t_w)}^{(c)}$

(a) Not available in Eurocomp; adapted from EUR 27666

(b) From reference 60, reference 48 in BÜV¹⁵

(c) The material and conversion factor are omitted in EUR 27666 but not in its source of reference⁶¹

D_x = plate flexural rigidity in the X direction

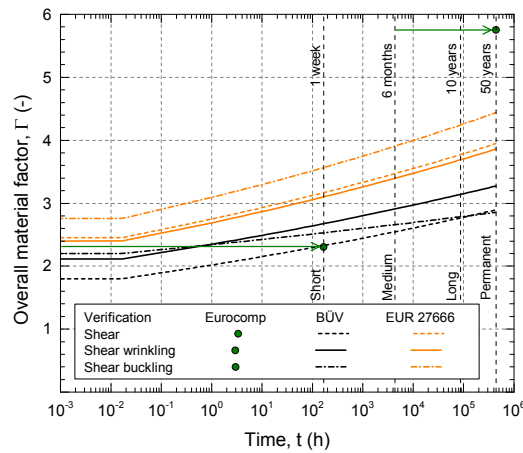
D_y = plate flexural rigidity in the Y direction

k_1 = 8 for orthotropic plates¹⁸

k_2 = 8.125+5.045K for $K > 1$ and

$$K = \frac{G_{xy}/6 + \nu_{xy} E_y / \left[12 \cdot (1 - \nu_{xy} \cdot \nu_{yx}) \right]}{\sqrt{E_x \cdot E_y / \left[12 \cdot (1 - \nu_{xy} \cdot \nu_{yx}) \right]^2}}$$

Figure 5.10 – Overall material factors over time applicable to GFRP webs in case study.

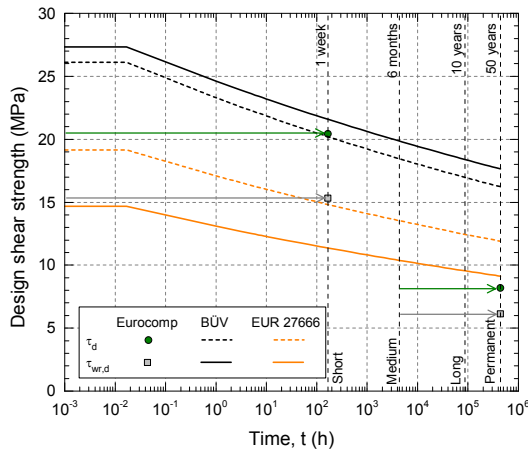


based on this assumption. It should be noted that the wrinkling strength depends on the stiffness properties of the FRP webs (E_w) and the PUR foam core (E_c , G_c). The obtaining of the design value differs in the BÜV and EUR 27666. The specific design values of each stiffness property ($E_{w,d}$, $E_{c,d}$, $G_{c,d}$) are used in the former, i.e., the different factors for the FRP laminates and PUR foam are considered. On the other hand, the characteristic stiffness properties are used in EUR 27666, and only the FRP factors are applied to the resulting (characteristic) strength. Therefore the absence of material/conversion factors for PUR foams in EUR 27666 does not prevent the wrinkling verification. For the design according to Eurocomp, the shear wrinkling expression provided in Table 5.7 was adapted from the expression given in EUR 27666.

For slender webs, the critical shear buckling strength, $\tau_{cr,d}$ may provide a low bound value for the shear strength of the web. Similar equations to verify the shear buckling resistance of FRP web components are available in the selected recommendations, see Table 5.7. They differ only in the shear buckling coefficients used (k_1 or k_2) and in the application of the material and modification/conversion factors to the stiffness properties (BÜV) or the resulting characteristic shear buckling strength (Eurocomp and EUR 27666).

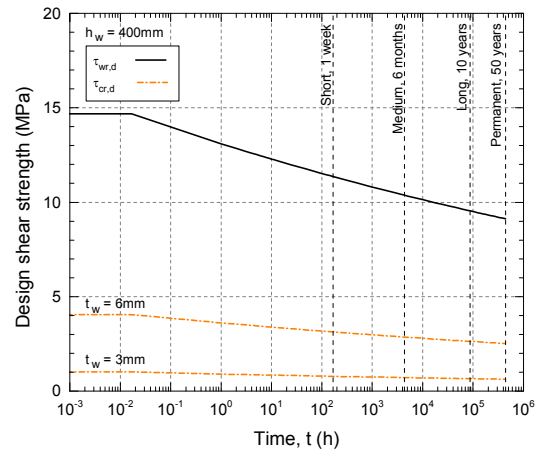
To compare the potential effects of the factor set selection on the web design, the overall material factors Γ (comprising the pertinent modification or conversion factors) for the three verifications were determined according to all recommendations and are shown in Figure 5.10.

Figure 5.10 shows that for the Eurocomp design the same overall factors (equal to γ_m in Table 5.4) apply regardless of the design verification, since no distinction for strength/stiffness properties and strength/stability verifications is made. The assignment of a particular loading time to the scenarios denoted as *short-* and *long-term* depends on the designer (indicative ranges are depicted in Figure 5.10). For short-term loading, the 2.30 factor is comparable to factors calculated according to the BÜV; for long-term loading, Eurocomp provides the most conservative value (5.75), 76 and 30% higher after a 50-year loading time than the maximum factors from the BÜV and EUR 27666, respectively. Unlike Eurocomp, both the BÜV and EUR 27666 allow the determination of the overall factors for any loading duration. A comparison between the two sets of curves shows that factors from EUR 27666 are globally



< Figure 5.11 – Design shear and shear wrinkling strength of GFRP webs from case study.

> Figure 5.12 – Design shear wrinkling and critical shear buckling strengths of GFRP webs from case study according to EUR 27666.³⁵



significantly higher than those calculated according to the BÜV: 36% higher for shear and up to 18% for shear wrinkling. Furthermore, for the latter case, the difference in the resulting $\tau_{wr,d}$ is even greater ($\tau_{wr,d}$ from the BÜV is approximately two times $\tau_{wr,d}$ from EUR 27666) due to the different formulations used for its calculation, see Table 5.7. A more conservative design therefore results when applying EUR 27666 instead of the BÜV.

The design shear and shear wrinkling strengths, τ_d and $\tau_{wr,d}$, over time obtained according to all the recommendations are shown in Figure 5.11. Different governing failure modes are obtained depending on the selected recommendation: shear for the BÜV and shear wrinkling for Eurocomp and EUR 27666. Moreover, significant differences in the resulting lowest design strengths are observed: 56% between τ_d (BÜV) and $\tau_{wr,d}$ (EUR 27666); 90% between τ_d (BÜV) and $\tau_{wr,d}$ (Eurocomp) for a 50-year loading time.

In the absence of the foam core, the shear buckling strength determines the shear resistance of slender webs. In web-core sandwich panels with a PUR foam core, the critical shear buckling strength may provide a low bound value for the shear resistance of slender webs subjected to permanent loads – the lateral support provided by the foam to the webs may be considerably diminished due to creep. To illustrate this phenomenon, the design shear wrinkling ($\tau_{wr,d}$) and shear buckling ($\tau_{cr,d}$) strengths obtained according to EUR 27666 for the web laminates of the case study are shown in Figure 5.12. In contrast to $\tau_{wr,d}$, $\tau_{cr,d}$ is geometry-dependent (dependency on the web height, h_w , and thickness, t_w , see Table 5.7). The critical buckling strengths given in Figure 5.12 correspond to selected web dimensions ($t_w \cdot h_w$) of 3·400 and 6·400 mm² as in Section 5.3.1. For a 50-year loading time, neglecting the PUR foam contribution would result in 3.6 (for $t_w = 6$ mm) and 14.5 (for $t_w = 3$ mm) times thicker webs than if considering its reduced contribution. A $\tau_{cr,d}$ -based design would be too conservative for the analyzed cases and selected design working life. Figure 5.12 shows however that $\tau_{wr,d}$ decreases over time at a faster rate than $\tau_{cr,d}$. This suggests that for a much longer loading duration, different material selection or geometrical configuration, the $\tau_{wr,d}$ and $\tau_{cr,d}$ curves may intersect, and the web's governing failure mode change from wrinkling to buckling.

5.4 Design of web and core dimensions

The shear forces applied to an FRP-PUR web-core sandwich panel are distributed between the web and core components of the hybrid core according to their shear rigidities (see Section 5.3.1). The shear resistance of the hybrid core depends therefore on the individual resistances provided by each of them. However, the shear strength and stiffness of each material are differently affected by creep. As a result, the overall shear resistance of the hybrid core considering creep effects cannot be estimated from the addition of the individual resistances over time of its components.

In the following, this subject is analyzed on the basis of the case study presented in Section 5.3.1. Based on this, design provisions for the resistance design of FRP-PUR web-cores taking creep effects into account are subsequently derived.

5.4.1 Shear resistance of hybrid FRP-PUR core

The shear resistance under sustained loading of a hybrid core consisting of an 80-kg/m³ PUR foam reinforced by GFRP webs spaced at $b = 925$ mm is evaluated (see Section 5.3.1). The web thickness of $t_w = 3$ mm is selected (for the sake of simplicity a normalized web area of $a = t_w / b = 0.3\%$, corresponding to $b = 1000$ mm, is considered). The material properties of the GFRP web laminates and PUR foam core are given in Table 5.2. The design was carried out according to the BÜV;¹⁵ the material and modification factors applicable are given in Table 5.5.

The contributions of the GFRP webs and PUR foam core to bearing the shear forces over time, $\alpha_w^{GA}(t)$ and $\alpha_c^{GA}(t)$ respectively, were calculated as indicated in Section 5.3.1 and are shown in Figure 5.13(a). The design values of the individual shear resistances over time provided by the webs and foam core, $V_{Rd,w}$ and $V_{Rd,c}$ respectively, can be obtained as follows:

$$V_{Rd,w}(t) = \tau_{Rd,w}(t) \cdot A_{V,w} = \tau_{Rd,w}(t) \cdot a \cdot b \cdot h \quad (5.8)$$

$$V_{Rd,c}(t) = \frac{\tau_{Rd,c}(t) \cdot A_{V,c}}{1.5} = \frac{\tau_{Rd,w}(t) \cdot (1-a) \cdot b \cdot h}{1.5} \quad (5.9)$$

where $\tau_{Rd,w}(t)$ = minimum time-dependent design strength of the GFRP web considering both shear (τ_d) and shear wrinkling ($\tau_{wr,d}$), see Section 5.3.2, $\tau_{Rd,c}(t)$ = time-dependent design shear strength of the PUR foam, $A_{V,w}$ = effective shear area of the web, $A_{V,c}$ = effective shear area of the core; the remaining variables are defined as previously. The 1.5 denominator in Equation (5.9) is applied in the BÜV to take into account the non-uniform distribution of shear stresses across the foam core.

The resulting design shear resistances normalized per unit area of the hybrid core ($b \cdot h$) are shown in Figure 5.13(b). Provided that under the shear distribution illustrated in Figure 5.13(a) failure occurred simultaneously in the web and core components, the design resistance of the hybrid core, $V_{Rd}(t)$, would be given by the addition of the individual shear resistances of the components, i.e. $V_{Rd}(t) = V_{Rd,w}(t) + V_{Rd,c}(t)$. However, since the decrease of the stiffness and strength properties of each material over time due to creep is different, failure will first occur in one of the components, governing the shear

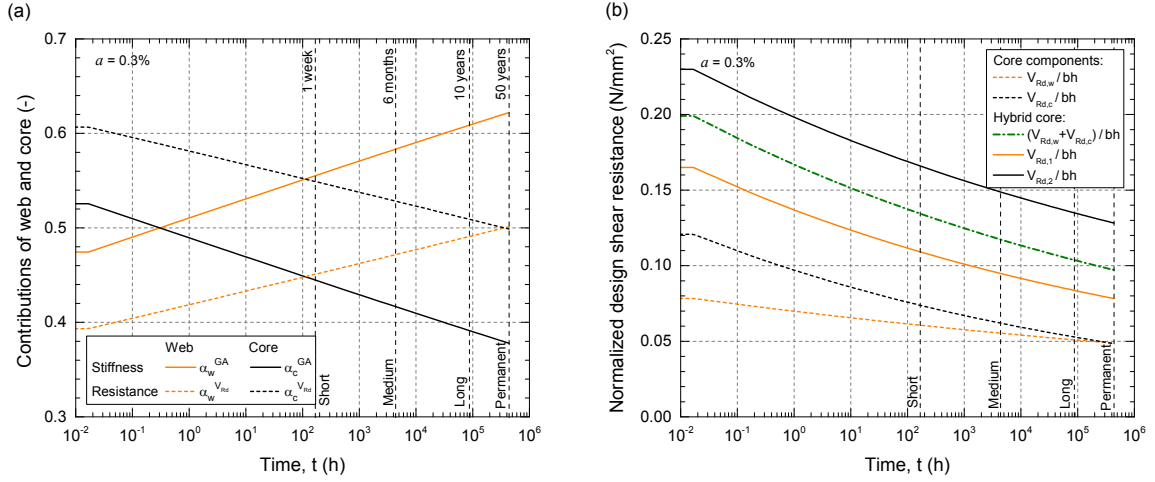


Figure 5.13 – (a) Time-dependent contribution of web-core components to shear stiffness and resistance; (b) time-dependent normalized shear resistance of hybrid core and individual components from case study.

capacity of the hybrid core. The design shear resistance of the hybrid core corresponding to web and core failures, $V_{Rd,1}(t)$ and $V_{Rd,2}(t)$ respectively, can be obtained as follows:

$$V_{Rd,1}(t) = \frac{V_{Rd,w}(t)}{\alpha_w^{GA}(t)} \quad (5.10)$$

$$V_{Rd,2}(t) = \frac{V_{Rd,c}(t)}{\alpha_c^{GA}(t)} \quad (5.11)$$

The design shear resistance of the hybrid core can therefore be expressed as:

$$V_{Rd}(t) = \min\{V_{Rd,1}(t), V_{Rd,2}(t)\} \quad (5.12)$$

The normalized shear resistance values corresponding to the addition of $(V_{Rd,w}(t) + V_{Rd,c}(t))$ as well as those resulting from Equations (5.10) and (5.11) are shown in Figure 5.13(b). Figure 5.13(b) shows that for the analyzed case the shear resistance of the hybrid core is governed by web failure for all load durations ($V_{Rd,1}(t) < V_{Rd,2}(t)$ for $t \geq 0$) and demonstrates that summing the components' individual resistances may result in an unsafe design – $V_{Rd,1}(t)$ is smaller than $(V_{Rd,w}(t) + V_{Rd,c}(t))$ by 17–20%. This can be further illustrated by obtaining the contributions of the GFRP webs and the PUR foam core to the $(V_{Rd,w}(t) + V_{Rd,c}(t))$ addition, denoted as $\alpha_w^{V_{Rd}}(t)$ and $\alpha_c^{V_{Rd}}(t)$ respectively:

$$\alpha_w^{V_{Rd}}(t) = \frac{V_{Rd,w}(t)}{V_{Rd,w}(t) + V_{Rd,c}(t)} \quad (5.13)$$

$$\alpha_c^{V_{Rd}}(t) = \frac{V_{Rd,c}(t)}{V_{Rd,w}(t) + V_{Rd,c}(t)} \quad (5.14)$$

The obtained values are given in Figure 5.13(a) together with the shear distribution coefficients. Figure 5.13(a) shows that the contribution of the web in terms of resistance is smaller than the relevant contribution for stiffness, i.e., $\alpha_w^{V_{Rd}}(t) < \alpha_w^{GA}(t)$. This implies that the resistance of the web component does not suffice to bear the corresponding proportion of shear load.

The governing failure mode of the hybrid core subjected to sustained loading can change over time. Figure 5.14 shows analogous plots correspond-

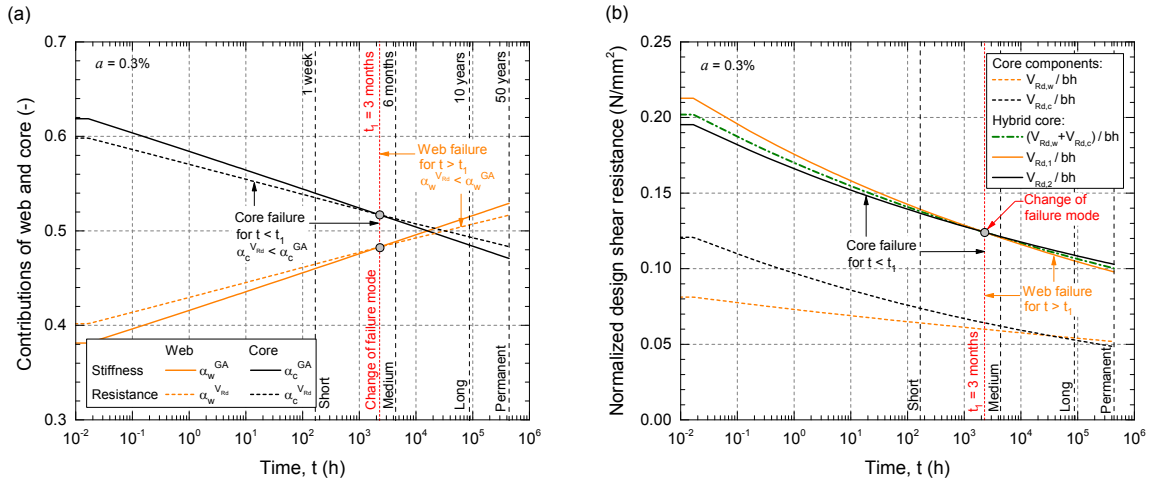


Figure 5.14 – (a) Time-dependent contribution of web-core components to shear stiffness and resistance; (b) time-dependent normalized shear resistance of hybrid core and individual components from case study 2.

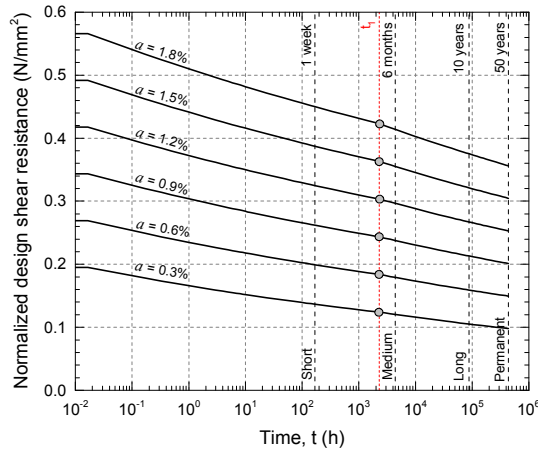
ing to another case study (case study 2) based on the one previously presented, in which slightly different material properties were considered for the GFRP webs. The average stiffness properties were estimated from the fiber architecture reported by Keller et al.² by conjointly using indicative ply properties provided in EUR 27666³⁵ and classical lamination theory (CLT). Values of $E_{w,m} = 13580$ MPa and $G_{w,m} = 2560$ MPa were obtained; the characteristic properties were calculated by applying a 0.8 factor to the relevant average values.⁵⁸ A characteristic shear strength of $\tau_k = 50$ MPa was used.⁵⁸

Figure 5.14(a) shows that the $\alpha^{GA}(t)$ curves intersect the pertinent $\alpha^{VRd}(t)$ curves at a $t = t_1 = 3$ -month loading time, representing the time at which under sustained loading the failure mode of the hybrid core changes from core to web failure – $\alpha_c^{VRd}(t) < \alpha_c^{GA}(t)$ for $t \leq t_1$ and $\alpha_w^{VRd}(t) < \alpha_w^{GA}(t)$ for $t \geq t_1$. This is further illustrated in Figure 5.14(b): $V_{Rd,1}/bh$, representing web failure, gives the lower envelope for the hybrid core resistance at $t \leq t_1$, while at $t \geq t_1$ this is given by $V_{Rd,2}/bh$, corresponding to core failure.

5.4.2 Design provisions

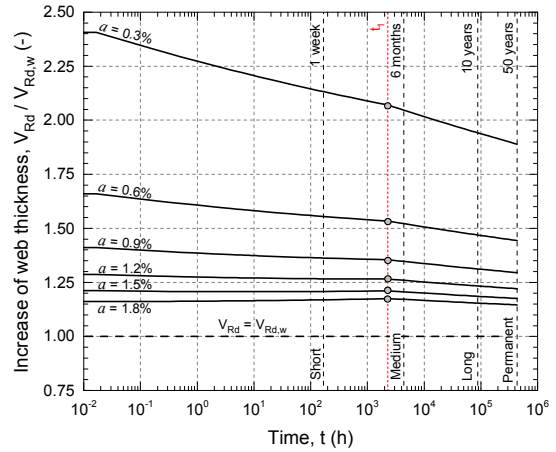
The design of the web-core dimensions (t_w, b) is an iterative process. First, for a preliminary geometry and selected material properties, the distribution of the design shear force between the web and core components should be obtained (see Section 5.3.1). Subsequently, strength verifications must be conducted for each of them (see Section 5.4.1). In case these are not fulfilled, the web-core dimensions need to be changed accordingly and the procedure repeated. Furthermore, this process has to be performed for every time scenario, considering the relevant loads and material properties.

To ease the design process, the procedure presented in Section 5.4.1 can be applied to obtain the normalized shear resistance over time for different a values (normalized web area); only the selection of the web and core materials and the design recommendations is required. The resulting curves for case study 2 and a values in the 0.3%–1.8% range are shown in Figure 5.15. It should be noted that t_1 , representing the switch from core to web failure, is independent of the normalized web area (a); t_1 is a function of the short-term strength and stiffness properties of the materials, the moduli reduction factors



< Figure 5.15 – Time-dependent normalized shear resistance of hybrid core from case study 2 depending on normalized web area.

> Figure 5.16 – Increase of web thickness in case study 2 resulting from neglect of foam core load-bearing capacity.



and the overall material factors, which are the same regardless of the considered a value. Then, for each time scenario, the normalized design shear force, V_d/bh , is obtained and represented in the normalized shear resistance-time plot (Figure 5.15). The lowest a value providing a normalized shear resistance exceeding the normalized shear force for any value of t is selected. The web thickness and spacing required to verify the ULS of shear strength over time can thus be determined.

A further design simplification would consist of neglecting the load-bearing capacity of the foam core, i.e., consider that the overall shear force is borne by the webs and that the foam core only contributes to laterally stabilize the web laminates. Consequently, a greater t_w value would be required to fulfill the shear resistance verification. The increase of web thickness can be obtained as the ratio between the shear resistance of the hybrid core, V_{Rd} , and that of the web, $V_{Rd,w}$. Figure 5.16 shows the increase of web thickness required for the presented case study for different a values. The surplus of t_w and hence of FRP material consumption, increases with decreasing a – for low a values, lower contributions of the web to shear stiffness and strength apply, therefore a higher increase of shear force needs to be assumed when neglecting the foam's contribution. For the a values applicable to the roof case study 2 ($a = 3.24/6.28\%$ corresponds to the 3/6-mm thickness webs), neglecting the load-bearing capacity of the foam core would result in 2.40/1.65 times thicker webs or in 60%/40% smaller web spacings.

5.5 Conclusions

The structural design of FRP-PUR web-core sandwich structures subjected to sustained loading was addressed in this study. The creep behavior of PUR foams and the relevant characteristics to be considered for their long-term structural performance were presented. The time-dependent behavior of web-core sandwich panels, and in particular the aspects influenced by the web-core interaction, were analyzed and the effects of selecting particular guidelines for the design were evaluated. The following main conclusions were drawn:

1. Rigid PUR foams used for structural purposes are mechanically anisotropic, especially in the case of low densities. The PUR foam anisotropy must be taken

into account for its use as core material of FRP sandwich structural components, relating to both its short- and long-term performance.

2. Anisotropic cellular morphology, density and loading type affect the creep behavior of PUR foams and should be taken into account in the design for long-term scenarios. Whereas the density and loading type of PUR foams are already referred to in design guidelines, no allusion to foam anisotropy is made.

3. Current design recommendations for FRP sandwich structures contain limited or no provisions for the consideration of PUR foam creep behavior in structural design. In addition, the comparison of structural designs using proposed creep parameters (BÜV) and equivalent experimental ones shows that the former may result in an unconservative design for long-term sustained loads.

4. The design shear resistance of the FRP web laminates, and therefore the web dimensions, depend significantly on the applied design recommendations. Regarding the performed case study, the BÜV provided the least conservative resistance and EUR 27666 the most conservative one, except for permanent loads, for which Eurocomp is more conservative. Furthermore, different governing failure modes are obtained depending on the applied recommendation.

5. The overall shear resistance of the hybrid FRP-web/PUR-foam core under sustained loading depends both on the varying shear stiffness and strength over time of the individual components and its load-bearing capacity is governed either by web or core failure. Considering the summation of the components' individual resistances results in an unsafe design. A straightforward procedure to take this into account and that is applicable to the design of the web and core dimensions is proposed.

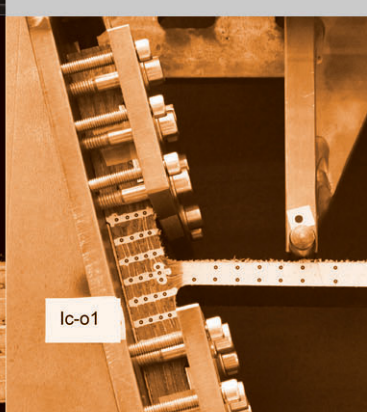
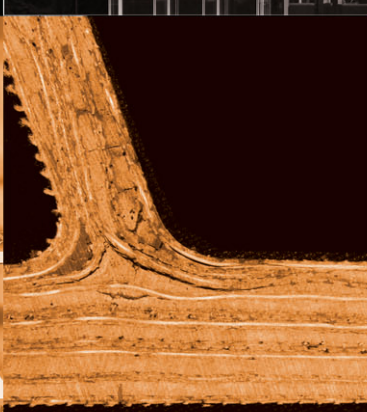
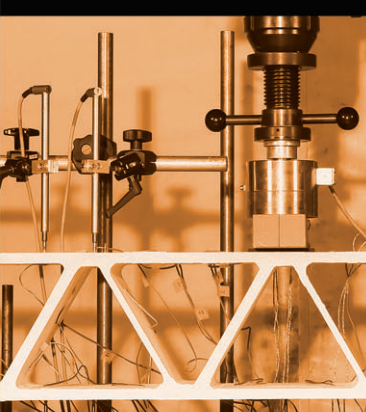
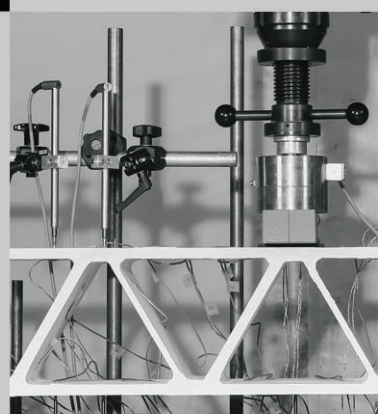
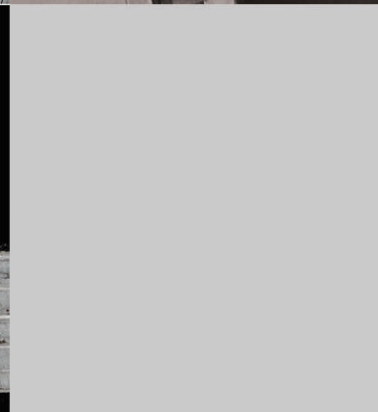
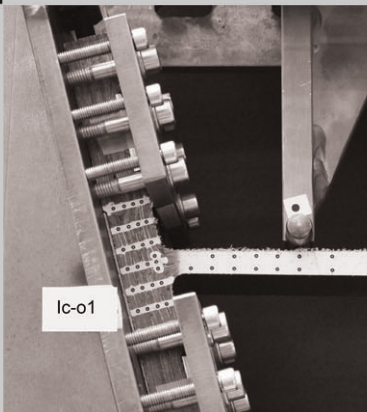
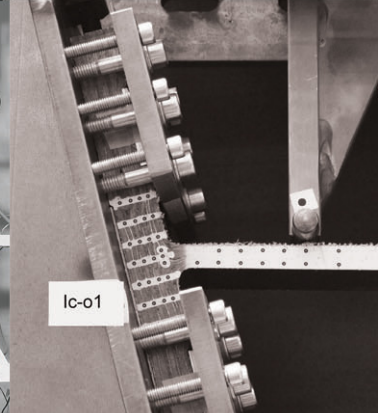
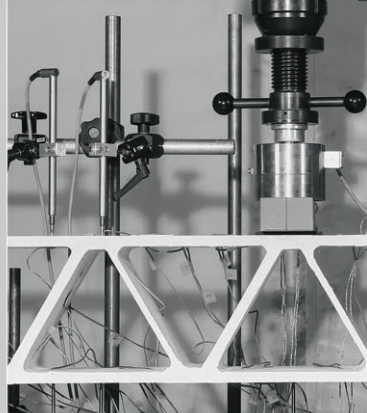
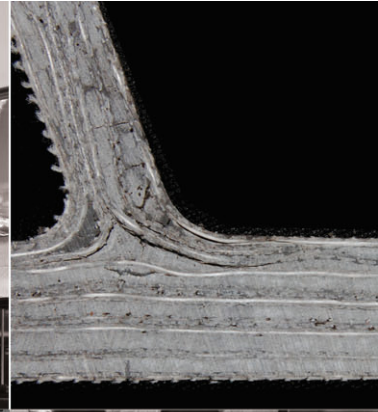
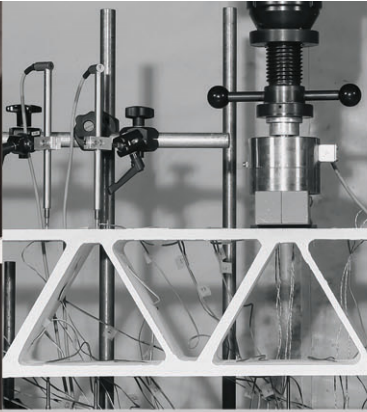
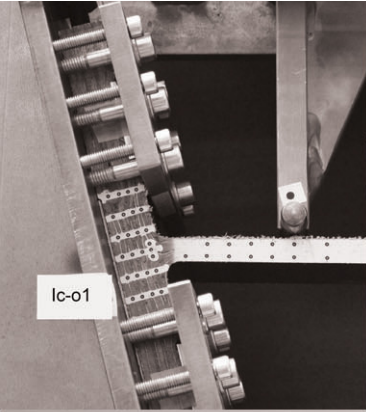
References

1. Davies JM (ed.) *Lightweight sandwich construction*. Oxford: Blackwell Science; 2001.
2. Keller T, Haas C, Vallée T. Structural concept, design, and experimental verification of a glass fiber-reinforced polymer sandwich roof structure. *J Compos Constr* 2008;12(4):454–468.
3. Keller T, Vassilopoulos AP, Manshadi BD. Thermomechanical behavior of multi-functional GFRP sandwich structures with encapsulated photovoltaic cells. *J Compos Constr* 2010;14(4):470–478.
4. Pascual C, de Castro J, Schueler A, Keller T. Integration of dye solar cells in load-bearing translucent glass fiber-reinforced polymer laminates. *J Compos Mater* 2017;51(7):939–953.
5. Durand S, Billaudeau E, Chapelle H and Lubineau G. Design analysis of GRP panels for the roof of the Haramain High Speed Railway Jeddah Station. In: Casari P *Proceedings of the 10th International Conference on Sandwich Structures, ICSS-10, 27–29 August 2012, Nantes, France*. p.119–120.
6. Mathieson H, Fam A. Static and fatigue behavior of sandwich panels with GFRP skins and governed by soft-core shear failure. *J Compos Constr* 2013;18(2):04013046.
7. Correia JR, Garrido M, Gonilha JA, Branco FA and Reis LG. GFRP sandwich panels with PU foam and PP honeycomb cores for civil engineering structural applications: Effects of introducing strengthening ribs. *Int J Struct Integrity* 2012; 3(2):127–147.
8. Fam A, Sharaf T. Flexural performance of sandwich panels comprising polyurethane core and GFRP skins and ribs of various configurations. *Compos Struct* 2010;92(12):2927–2935.

9. Mousa MA, Uddin N. Flexural behavior of full-scale composite structural insulated floor panels. *Adv Compos Mater* 2011;20(6):547–567.
10. Sharaf T, Shawkat W, Fam A. Structural performance of sandwich wall panels with different foam core densities in one-way bending. *J Compos Mater* 2010;44(19):2249–2263.
11. Wang L, Liu W, Fang H, Wan L. Behavior of sandwich wall panels with GFRP face sheets and a foam-GFRP web core loaded under four-point bending. *J Compos Mater* 2015;49(22):2765–2778.
12. Tuwair H, Volz J, ElGawady MA, Mohamed M, Chandrashekhara K, Birman V. Testing and evaluation of polyurethane-based GFRP sandwich bridge deck panels with polyurethane foam core. *J Bridge Eng* 2015;21(1):04015033.
13. Yanes-Armas S, Keller T. Structural concept and design of a GFRP-polyurethane sandwich roof structure. In: Teng JG, Dai JG (eds.) *Proceedings of the Eighth International Conference on Fibre-Reinforced Polymer (FRP) Composites in Civil Engineering, CICE2016*, 14–16 December 2016, Hong Kong, China. Hong Kong: The Hong Kong Polytechnic University; 2016. p.1318–1323.
14. European Committee for Standardization (CEN). EN 1995-1-1:2004. *Eurocode 5: Design of timber structures- Part 1-1: General - Common rules and rules for buildings*. Brussels: CEN; 2004.
15. Bau-Überwachungsverein (BÜV e.V.) (ed.) *Tragende Kunststoffbauteile : Entwurf – Bemessung – Konstruktion*. Wiesbaden: Springer Vieweg; 2014.
16. European Committee for Standardization (CEN). EN 1991-1-1:2002. *Eurocode 1: Actions on structures - Part 1-1: General actions - Densities, self-weight, imposed loads for buildings*. Brussels: CEN; 2002.
17. European Committee for Standardization (CEN). EN 1990:2002. *Eurocode - Basis of structural design*. Brussels: CEN; 2002.
18. Clarke JL (ed.) *Structural design of polymer composites: Eurocomp design code and handbook*. London: E & FN Spon; 1996.
19. Scott DW, Lai JS, Zureick AH. Creep behavior of fiber-reinforced polymeric composites: a review of the technical literature. *J Reinf Plast Compos* 1995;14(6):588–617.
20. Sá MF, Gomes AM, Correia JR, Silvestre N. Creep behavior of pultruded GFRP elements—Part 1: Literature review and experimental study. *Compos Struct* 2011;93(10):2450–2459.
21. Huang JS, Gibson LJ. Creep of polymer foams. *J Mater Sci* 1991;26(3):637–647.
22. Garrido M, Correia JR, Keller T. Effect of service temperature on the shear creep response of rigid polyurethane foam used in composite sandwich floor panels. *Constr Build Mater* 2016;118:235–244.
23. Just M. *Beitrag zum Langzeitverhalten von Stützelementen mit einem Stützkern aus freongetriebenem Polyurethan-Hartschaumstoff* [PhD Thesis]. Universität Dresden, Germany; 1974.
24. Burkhardt S. *Zeitabhängiges Verhalten von Sandwichelementen mit Metalldeckschichten und Stützkernen aus Polyurethanhartschaumstoffen*. Karlsruhe: Versuchsanstalt für Stahl, Holz und Steine der Universität Fridericiana; 1988. Report No.4(20).
25. Schulz U, Burkhardt S. *Langzeituntersuchungen an Sandwichelementen mit Metalldeckschichten und Kunststoffschäumen. Abschlußbericht*. Karlsruhe: Versuchsanstalt für Stahl, Holz und Steine. Amtliche Materialprüfungsanstalt der Universität Karlsruhe; 1988.
26. Just M, Gerbet, Wienert. *Experimentelle Untersuchungen zum Langzeitverhalten von Sandwichplatten mit Stahldeckschichten und FCKW-reduzierten Stützkernen im Hinblick auf die Sicherung und Erweiterung der Anwendung von Sandwichplatten in Stahlleichtbau*. Dresden: IMA Materialforschung und Anwendungstechnik; 1993.
27. Just M. *Abschlußbericht zum AiF-Forschungsvorhaben 10011B. Untersuchungen zum Langzeitverhalten von Sandwichplatten mit CO₂-getriebenen Polyurethan-Schaumstoffkernen*. Dresden: IMA Materialforschung und Anwendungstechnik; 1996. Report No. B85/4.

28. Ackermann G. Zum zeitabhängigen Tragverhalten dreischichtiger Träger unter Quer- und Längsbelastung. *Bauplanung—Bautechnik* 1985; 39(7):319–324.
29. Huang JS, Gibson LJ. Creep of sandwich beams with polymer foam cores. *J Mater Civ Eng* 1990;2(3):171–182.
30. Garrido M, Correia JR, Branco FA, Keller T. Creep behaviour of sandwich panels with rigid polyurethane foam core and glass-fibre reinforced polymer faces: Experimental tests and analytical modelling. *J Compos Mater* 2014;48(18):2237–2249.
31. Ramezani M, Hamed E. Coupled thermo-mechanical creep behavior of sandwich beams – Modeling and analysis. *Eur J of Mech A Solids* 2013;42:266–279.
32. Garrido M, Correia JR, Keller T, Cabral-Fonseca S. Creep of sandwich panels with longitudinal reinforcement ribs for civil engineering applications: experiments and composite creep modeling. *J Compos Constr* 2017;21(1):04016074.
33. Hamed E, Frostig Y. Influence of creep on the geometrically nonlinear behavior of soft core sandwich panels. *Int J Mech Sci* 2016;105:398–407.
34. CUR96+. *Revised CUR96 FRP composite structures. Draft for updating CUR96:2003*. Utrecht: CUR; Utrecht; 2012.
35. Ascione L, Caron J-F, Godonou P, Van IJselmuiden K, Knippers J, Mottram T, et al. *Prospect for new guidance in the design of FRP: Support to the implementation, harmonization and further development of the Eurocodes*. Publications Office of the European Union; 2016. Report No.EUR 27666 EN.
36. Sonnenschein MF. *Polyurethanes - science, technology, markets, and trends*. Wiley series on polymer engineering and technology. Hoboken: Wiley; 2015
37. Gibson LJ, Ashby MF. *Cellular solids: structure & properties*. International series on materials science & technology. Oxford: Pergamon Press; 1988.
38. Huber AT, Gibson LJ. Anisotropy of foams. *J Mater Sci* 1988;23(8):3031–3040.
39. Kanakkanatt SV. Mechanical anisotropy of open-cell foams. *Cell Plast* 1973;9(1):50–53.
40. Esmaeilnezhad E, Rezaei M, Razavi MK. The effect of alternative blowing agents on microstructure and mechanical characteristics of rigid polyurethane foam. *Iran Polym J* 2009;18(7):569–579.
41. Ridha M, Shim VPW. Microstructure and tensile mechanical properties of anisotropic rigid polyurethane foam. *Exp Mech* 2008;48(6):763–776.
42. Burteau A, N'Guyen F, Bartout JD, Forest S, Bienvenu Y, Saberi S, et al. Impact of material processing and deformation on cell morphology and mechanical behavior of polyurethane and nickel foams. *Int J Solids Struct* 2012;49(19):2714–2732.
43. Gibson LJ, Ashby MF. The mechanics of three-dimensional cellular materials. *P Roy Soc Lond A Mat* 1982;382(1782):43–59.
44. General Plastics Manufacturing Company. Product information available from: <https://www.generalplastics.com/rigid-foams> [Accessed 13th April 2017].
45. Australian Urethane Systems PTY Limited. Product information available from: <http://www.total-insulation.com.au/pdf/AUSTHANE%20BF35RigidFRPUFoam-July2007> [Accessed 13th April 2017].
46. Insulpro Insulation Products. Product information available from: <http://insulationproductssa.co.za/products/polyurethane-foam/> [Accessed 13th April 2017].
47. ITW Insulation Systems. Product information available from: http://www.itwinsulation.com/Trymer/library/Data_Sheets/ITW_TRYMER_2000_XP.pdf [Accessed 13th April 2017].
48. SAITEC. Datasheet Saitpur free 080 (SPF 080). Challans: SAITEC; 2015.
49. Kleser J. *Zeitstand-Druckverhalten von PUR-Hartschaum*. IVPU - Industrieverband Polyurethan-Hartschaum e.V.; 2002.

50. Schmidt W. Eigenschaften und Prüfung von mit harten Polyurethanschaumstoffen hergestellten Leichtkern-Verbundplatten. *Materialprüfung* 1968;10(3):81–87.
51. Krollmann N. *Determination of compressive creep behaviour of PUR rigid foam products*. Ludwigshafen: BASF; 2002. Report No. 298.4386.
52. Badstube M. Kriechgesetze von Polyurethan-Hartschaumstoffen. *Plaste Kautsch* 1979;26(12):703–706.
53. Yourd RA. Compression creep and long-term dimensional stability in appliance rigid foam. *J Cell Plast* 1996;32(6):601–616.
54. Just M. Ergebnisse experimenteller Untersuchungen zum Langzeitverhalten von PUR-Hartschaumstoff-Stützkernbauteilen und Schlußfolgerungen für die Anwendung. *IfL Mitt* 1983;22(3):95–104.
55. Findley WN. *Mechanisms and mechanics of creep plastics and stress relaxation and combined stress creep of plastics*. Rhode Island: Division of Engineering, Brown University; 1960.
56. European Committee for Standardization (CEN). EN 1606:2013. *Thermal insulating products for building applications — Determination of compressive creep*. Brussels: CEN; 2013.
57. American Society for Testing and Materials (ASTM). ASTM C480/C480M-16. *Standard test method for flexure creep of sandwich constructions*. West Conshohocken: ASTM; 2016.
58. German Institute for Standardization (DIN). DIN 18820-2. *Glass fibre reinforced unsaturated polyester (GF-UP) and phenacrylic (GF-PHA) resin structural composites. Characteristic values of standard composites*. Berlin: DIN; 1991.
59. Wiedemann J. *Leichtbau 1: Elemente*. Berlin: Springer; 1996.
60. Bank LC. *Composites for construction: structural design with FRP materials*. Hoboken: John Wiley & Sons; 2006.
61. National Research Council of Italy (CNR). CNR-DT 205/2007, 2008. *Guide for the design and construction of structures made of FRP pultruded elements*. Rome: CNR; 2008.



Chapter 6

Conclusions and future work

6.1 Conclusions

The main conclusions of this thesis related to local structural effects in pultruded GFRP bridge decks and GFRP-foam web-core sandwich structures are presented below. These conclusions are categorized based on the objectives of the thesis, explained in Section 1.2.

6.1.1 Effect of core geometry of pultruded GFRP decks on their transverse behavior

Two pultruded GFRP bridge deck designs of comparable dimensions with trapezoidal and triangular cellular cross-sectional geometries were experimentally investigated in their transverse-to-pultrusion direction via static three-point bending experiments. The analysis and comparison of their structural behavior concerning stiffness, strength, failure modes and load-transfer mechanisms showed that the transverse structural performance, which affects the deck's response to concentrated loading (orthotropy ratio) and its contribution as top chord of the main girders, depends on the cell geometry.

Systems with triangular cells exhibit truss-governed behavior; failure occurs abruptly due to the absence of static indeterminacy of the system. On the other hand, trapezoidal cells result in the transverse behavior being frame-governed; due to the local bending moments in the components, significantly higher strains and lower failure loads are reached. However, in contrast to the triangular core, the trapezoidal core provides system redundancy, resulting in a nonlinear behavior with progressive failure.

The analysis of the transverse apparent bending and in-plane shear stiffness of both decks demonstrated that the trapezoidal core provides a very low degree (less than 4%) of composite action between the deck flanges, thus resulting in a much less stiff panel in the transverse direction compared to the deck with triangular core. A triangular core allows a much higher degree of composite action between the flanges (approximately 60%). This may result in

a more pronounced bi-directional behavior of the deck, i.e. a larger number of profiles contributing to bearing the concentrated loads applied to the deck, and a higher stiffness of the composite main girders.

6.1.2 Energy dissipation capacity and recovery of web-flange junctions of pultruded GFRP decks

The energy dissipation capacity and recovery subsequent to unloading of the web-flange junctions (WFJs) of a pultruded GFRP bridge deck were experimentally investigated by means of cantilever bending experiments conducted on the web components. Two WFJ types with similar geometry and fiber architecture but different initial imperfections were investigated. The reported experimental responses demonstrated the sensitivity of the WFJs' local structural behavior to initial imperfections of the components, e.g. deviations from fiber architecture design, wrinkling of fabrics, resin pockets and pre-cracks. Dissimilar imperfections can change the local bending response of the WFJs from brittle to ductile and affect their load-bearing capacity owing to the different resulting sequences of crack formation.

The WFJs displaying ductile behavior exhibited significant deflection recovery (77%). The recovery and accumulated damage rates were constant regardless of the load levels and loading/unloading rates. In spite of the viscoelastic nature of the GFRP material, the viscoelastic effects on the deflection recovery of the WFJs and on the energy dissipation mechanisms were small. For the investigated configuration, approximately 93% of the total recovery occurred instantaneously (elastic recovery) and crack development was the primary energy dissipation mechanism, except at low deflection levels.

6.1.3 Rotational behavior of web-flange junctions of pultruded GFRP decks

The rotational behavior of the WFJs of a pultruded GFRP deck was characterized based on small-scale three-point bending and cantilever experiments conducted on the web elements. The investigation comprised three WFJ types, each was studied in two bending directions. The overall moment-rotation relationships, rotational stiffness, strength and failure modes vary for each WFJ type and bending direction; this confirmed that the characterization of the WFJs' rotational response has to be separately conducted for each WFJ type and loading direction. Parameters affecting the rotational behavior are the web type, location of the WFJ within the deck profile, existing initial imperfections and direction of the bending moment applied.

In order to simulate the global response of the deck in the transverse-to-pultrusion direction, WFJs can be modeled as rotational springs responding to the experimental moment-rotation ($M-\phi$) curves. To facilitate the modeling and structural analysis of the deck system, the actual rotational behavior of the WFJs can also be represented by simplified empirically-based $M-\phi$ relationships.

6.1.4 Creep effects on the load-bearing behavior of web-core sandwich structures

The behavior of GFRP-PUR web-core sandwich structures for building construction subjected to sustained loading was investigated. Based on experimental results obtained from the literature, the mechanical behavior of rigid PUR foams used as core material was analyzed, with emphasis on creep.

The study showed that rigid PUR foams used for structural purposes are mechanically anisotropic, especially for low densities, and that to assess the structural performance of the web-core sandwich, both for short- and long-term scenarios, the foam anisotropy must be considered. The foam density and loading type applied constitute further parameters that need to be taken into account in order to evaluate the sandwich panel's creep performance, regarding the influence of the foam creep on both the distribution of forces between the GFRP and foam components and local instability effects occurring in the GFRP laminates.

Unlike the foam anisotropy, reference to these two factors is already made in currently available design guidelines; however, comparison of the creep parameters established in the guidelines and experimentally obtained equivalent parameters revealed that they respond to different trends and that using the former may result in an unconservative structural design for long-term sustained loads.

A design case study using an existing GFRP-PUR web-core sandwich roof (Novartis Campus Main Gate Building) demonstrated that the design shear resistance of the GFRP web laminates under sustained loading – and therefore their dimensions – and the governing failure mode are determined by the applied design recommendations. This demonstrates that design recommendations are not consistent and underscores the necessity for harmonization. The overall shear resistance of the hybrid GFRP-web/PUR-foam core is lower than the summation of the individual components' resistances, since it is dependent on both the varying shear stiffness and strength of the components over time. Unless the foam contribution to shear resistance is neglected, which would result in significantly thicker webs or smaller web spacing, this interaction should be considered in order to prevent an unsafe design.

6.2 Original contributions

The original contributions of this thesis with regard to the research topic are the following:

1. The influence of the cellular cross-sectional geometry of pultruded GFRP deck systems on their static transverse behavior has been investigated by three-point bending experiments. This approach, which takes into consideration global bending effects from out-of-plane loads applied to the deck, is of significance for its structural performance as a slab.
2. The transverse in-plane shear stiffness of pultruded GFRP decks and the composite action between the flanges of these decks have been quantified based on the deflection results from three-point bending experiments and existing analytical methods for composite beams with flexible shear connections. In comparison to the determination by means of in-plane shear experiments, the developed approach more accurately takes into account the axial forces in the deck flanges and is not affected by the eccentricity of the load application.

3. The energy dissipation capacity and ductility of the web-flange junctions (WFJs) of pultruded GFRP components were demonstrated by cyclic local bending experiments and the influence of existing imperfections in the components on the resulting behavior was identified. This provided additional knowledge and understanding to overcome the lack of inherent ductility of FRP materials for their use in structural applications.
4. An experimental approach to ascertain the rotational stiffness of WFJs by means of symmetric three-point bending and cantilever experiments and relevant analytical beam models was developed and successfully used to characterize the rotational behavior of all WFJ types present in a pultruded GFRP bridge deck. The established procedure is applicable to other WFJ configurations of pultruded elements and overcomes the limitations of existing experimental approaches with the same purpose.
5. A design procedure for hybrid FRP-web/PUR-foam cores subjected to sustained loading has been developed. The procedure allows the straightforward consideration of the dependence of the overall shear resistance of the hybrid core on both the time-dependent shear stiffness and strength of each of the components, i.e. the fact that the load-bearing capacity of the hybrid core is governed by failure in one of the individual components and lower than the summation of the components' individual resistances.

6.3 Recommendations for future work

Research topics regarding future prospects for the development of the current work are presented in the following.

6.3.1 GFRP bridge decks as top chord of main girders

As described in Chapter 2, GFRP bridge decks can act as the top chord of the underlying main girders when there is sufficient composite action between the girder and deck. The contribution of the GFRP deck depends on the shear transmission within the deck itself (from its bottom to its top flange), which in turn is dependent on its transverse in-plane shear stiffness and load transfer mechanisms.

The present research considered the characterization, in the linear elastic range, of the in-plane shear modulus of the deck system. As shown in Chapter 2, the system's in-plane shear modulus can be nonlinear. Its complete characterization up to failure is therefore required. This would allow evaluation of the effects of the deck's transverse behavior on the global performance of composite girders at the ultimate limit state (ULS).

Currently available analytical models for composite girders with FRP decks with flexible cores acting as top chord only consider the constant in-plane shear modulus of the deck.¹ Their extension to consider the nonlinear in-plane shear stiffness of the deck is recommended. The approach could furthermore be applied to GFRP-balsa sandwich decks, since the in-plane shear behavior of balsa panels may also be nonlinear.²

6.3.2 Ductility of pultruded GFRP members

In spite of the absence of inherent ductility of FRP materials, it was shown in Chapter 3 that pultruded GFRP components could dissipate internal energy through viscoelastic losses, particularly at low damage levels. In order to better exploit this energy dissipation capability derived from the material viscoelasticity, e.g. for impact loading or seismic actions, further research would be required. In particular, for the analyzed WFJs, the performance under cyclic loading could be evaluated.

In addition, it has been shown that the ductile behavior of FRP components is influenced by the characteristics of the composite material on the mesoscopic scale, such as local defects in the fiber architecture. A detailed investigation of the characteristics of the fiber arrangement resulting in improved (pseudo-)ductility of pultruded FRP elements could result in the design of components with enhanced ductile performance, an advantage for their application in bridge and building structures.

6.3.3 Standardized experimental methods for WFJ behavior characterization

The global structural performance of pultruded profiles, for both steel-like open-/closed-section elements and multicellular closed-section shapes for bridge decks, is governed to a large extent by the local behavior of their WFJs. However, no standardized procedures are available to determine the WFJ strength and stiffness in order to include them in the structural element design. The development of standardized experimental methods for this purpose, including tensile, shear and bending moment loading, would provide a common framework for manufacturers and designers to design pultruded FRP elements and structures.

In this investigation, an experimental procedure for the characterization of the rotational behavior of WFJs has been proposed. Nonetheless, it is only applicable to uniform local bending moment along the WFJ – concentrated forces and their spread would require further consideration.

6.3.4 Wrinkling strength of GFRP laminates subjected to sustained loading

In GFRP-PUR sandwich panels, the wrinkling strength and governing failure mode of GFRP components subjected to sustained compressive and shear loads is influenced by creep of the foam core material, resulting in a reduction of its contribution as lateral support for the thin GFRP laminates. Experimentally validated analytical methods to evaluate the short-term strength of the laminates exist and have been included in currently available guidelines applicable to the design of FRP sandwich structures. In order to consider creep effects, design recommendations establish reduction factors applicable to material properties in the case of sustained loading. Approaches based on the high-order sandwich theory (HSAPT), also considering geometrical nonlinearities, have been presented in the literature.³ However, to the author's best knowledge, no experimental validation of these approaches has been conducted. An experimental investigation of the compressive and shear creep behavior of GFRP laminates laterally stabilized by foam core

material is therefore necessary to assess their validity and if necessary modify existing models or develop new ones.

6.3.5 Partial safety factors for core materials

Existing design recommendations or prospective guidelines for the structural design of FRP sandwich structures generally do not make provisions for partial safety factors for core materials, despite their being required for engineering design – only the BÜV⁴ includes these factors for PUR foams. The definition of partial safety factors for materials commonly used as cores of sandwich structures in building and bridge construction (e.g. PUR foam, PET foam, balsa wood) is therefore necessary and may also promote a more widespread application of this structural system.

6.3.6 Shear resistance of web-core sandwich structures

The design procedure presented in Chapter 5 for evaluation of the shear resistance of FRP-web/foam-core sandwich structures subjected to sustained loading has to be experimentally and/or numerically validated. The developed procedure is based on currently available provisions for the design of FRP structures and assumes that the distribution of shear forces between the web and core components depends on their relative shear stiffnesses, that perfect adherence between the individual components exist and that the contributing width of the foam core is equal to the spacing between the FRP webs. The validity of the shear distribution assumption, the long-term performance of the FRP-foam adherence and the effective width of the hybrid FRP-foam element remain to be studied.

References

1. Gürtler HW. *Composite action of FRP bridge decks adhesively bonded to steel main girders* [PhD Thesis]. Ecole Polytechnique Fédérale de Lausanne, Switzerland; 2004.
2. Osei-Antwi M. *Structural performance of complex core systems for FRP-balsa composite sandwich bridge decks* [PhD Thesis]. Ecole Polytechnique Fédérale de Lausanne, Switzerland; 2014.
3. Hamed E, Frostig Y. Influence of creep on the geometrically nonlinear behavior of soft core sandwich panels. *Int J Mech Sci* 2016;105:398–407.
4. Bau-Überwachtungsverein (BÜV e.V.) (ed.) *Tragende Kunststoffbauteile : Entwurf – Bemessung – Konstruktion*. Wiesbaden: Springer Vieweg; 2014.

Appendices

Appendix A | Equations for beams with flexible shear connections

Appendix B | *DS* beam experiments

Appendix C | *AS* beam experiments

Appendix D | *DS* web three-point bending experiments

Appendix E | *DS* web-flange junction cantilever experiments

Appendix F | Summary of experimental studies of the creep behavior of PUR foams

Appendix A

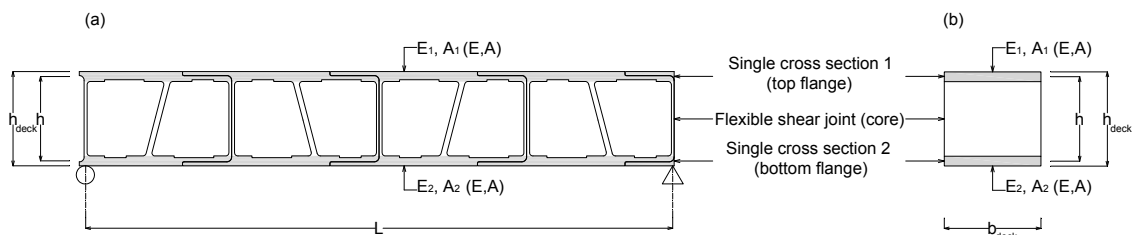
Equations for beams with flexible shear connections

A.1 Introduction

In Chapter 2, the low bound values for the transverse in-plane shear moduli of the *DS* and *AS* pultruded GFRP bridge deck systems are estimated from the experimental deflection results. In their transverse direction, pultruded decks can be modeled as two-component composite beams with a partial or flexible shear connection, see Figure A.1. The cross section of the GFRP transverse beams is composed of two partial cross sections corresponding to the top – *single cross section 1* – and bottom – *single cross section 2* – flanges of the deck. The core structure of the deck, which connects the upper and lower flanges, can be considered as a flexible shear connection.

The transverse in-plane shear stiffness of the deck is calculated by conjointly using the experimental load-deflection data, material and geometrical properties together with existing deflection equations for composite beams with flexible shear connections. In particular, the analytical method developed by Natterer and Hoefft¹ for single-span timber-concrete composite beams is used. Appendix A presents the method's deflection equations applicable to single-span beams loaded in a three-point bending configuration, conforming to the experimental set-up of the *DS* and *AS* beams investigated in Chapter 2.

Figure A.1 – GFRP/GFRP composite beam; (a) elevation; (b) cross section.



A.2 Equations for beams with flexible shear connections

The differential equation (Equation (A.1)) for the deflection of a two-component composite girder, according to Natterer and Hoefl, is:¹

$$\delta^{VI} - b^2 \cdot \delta^{IV} = \frac{1}{E_1 I_1 + E_2 I_2} \cdot (q'' - \omega^2 \cdot q) \quad (\text{A.1})$$

The factors ω^2 and b^2 are calculated using Equations (A.2) and (A.3) as follows:

$$\omega^2 = \frac{(E_1 A_1 + E_2 A_2) \cdot k}{E_1 A_1 \cdot E_2 A_2} \quad (\text{A.2})$$

$$b^2 = \omega^2 + \frac{k \cdot h^2}{E_1 I_1 + E_2 I_2} \quad (\text{A.3})$$

where δ = beam deflection; E_1 = elastic modulus of *single cross section 1 (SC1)*; E_2 = elastic modulus of *single cross section 2 (SC2)*; I_1 = moment of inertia of SC1; I_2 = moment of inertia of SC2; q = distributed load; A_1 = area of SC1; A_2 = area of SC2; h = distance between neutral axes of SC1 and SC2; k = shear stiffness of the connection between SC1 and SC2.

Since the experimental beams studied here are composed of two identical partial cross sections – top and bottom flanges of the deck – Equations (A.2) and (A.3) can be simplified as indicated in Equations (A.4) and (A.5), respectively:

$$\omega^2 = \frac{2k}{EA} \quad (\text{A.4})$$

$$b^2 = \omega^2 + \frac{kh^2}{2EI} \quad (\text{A.5})$$

where E = elastic modulus of SC1 and SC2, I = moment of inertia of SC1 and SC2, A = area of SC1 and SC2.

For a GFRP deck in its transverse direction, k (Equation (A.6)) can be expressed, according to Keller and Gürtler,² as:

$$k = b_{deck} \frac{G_{yz}}{h_{deck}} \quad (\text{A.6})$$

where b_{deck} = effective deck width, G_{yz} = transverse system in-plane shear modulus, and h_{deck} = depth of the deck.

Natterer and Hoefl solved Equation (A.1) for different loading configurations. For a composite beam composed of two equal partial cross sections and subject to three-point bending at mid-span, the deflections at quarter-span ($\delta_{1/4}$) and mid-span ($\delta_{1/2}$) are calculated using Equations (A.7) to (A.11):

$$\delta_{1/4} = \frac{PL^3}{48B} \left\{ \frac{a^2}{1-a^2} \frac{24}{\lambda^2} \left[\frac{1}{4} - \frac{1}{\lambda} \frac{\text{Sinh}(\lambda/4)}{\text{Cosh}(\lambda/2)} \right] + \frac{11}{16} \right\} \quad (\text{A.7})$$

$$\delta_{1/2} = \frac{PL^3}{48B} \left\{ \frac{a^2}{1-a^2} \frac{24}{\lambda^2} \left[\frac{1}{2} - \frac{1}{\lambda} \frac{\text{Sinh}(\lambda/2)}{\text{Cosh}(\lambda/2)} \right] + 1 \right\} \quad (\text{A.8})$$

$$B = 2EI + \frac{EAh^2}{2} \quad (\text{A.9})$$

$$\frac{a^2}{1-a^2} = \frac{Ah^2}{4I} \quad (\text{A.10})$$

$$\lambda^2 = b^2L^2 \quad (\text{A.11})$$

where P = concentrated load of the three-point bending configuration, L = span length, B = bending stiffness of the full cross section assuming full composite action, a^2 = non-dimensional factor that represents Steiner contribution to bending stiffness of the full cross section, and λ = degree of composite action ($\lambda = 0$ signifies no composite action and $\lambda \rightarrow \infty$ represents full composite action).

Equations (A.7) and (A.8) were conjointly used with experimental load-deflection data to back calculate the in-plane shear stiffness k of both deck systems. Equation (A.6) was then applied to calculate their transverse in-plane shear moduli G_{yz} . All parameters used are listed in Table A.1 for both deck series.

Table A.1 – Parameters of composite beams for DS and AS series.

Parameter	Units	DS Deck system	AS Deck system
L	mm	1210	1495
h_{deck}	mm	194.6	225
b_{deck}	mm	200	200
h	mm	176.1	209.4
A	mm ²	3 710	3 120
I	mm ⁴	106 385	63 274
E	MPa	12 975	19 000
B	Nmm ²	7.49·10 ¹¹	13.02·10 ¹¹
$a^2/(1-a^2)$	-	270	541

References

1. Natterer J, Hoefft M. *Zum Tragverhalten von Holz-Beton-Verbundkonstruktionen*. Lausanne: Ecole Polytechnique Fédérale de Lausanne, Chaire de Construction en Bois; 1987. Report No.1345.
2. Keller T, Gürtler H. Design of hybrid bridge girders with adhesively bonded and compositely acting FRP deck. *Compos Struct* 2006;74(2):202–212.

Appendix B

DS beam experiments

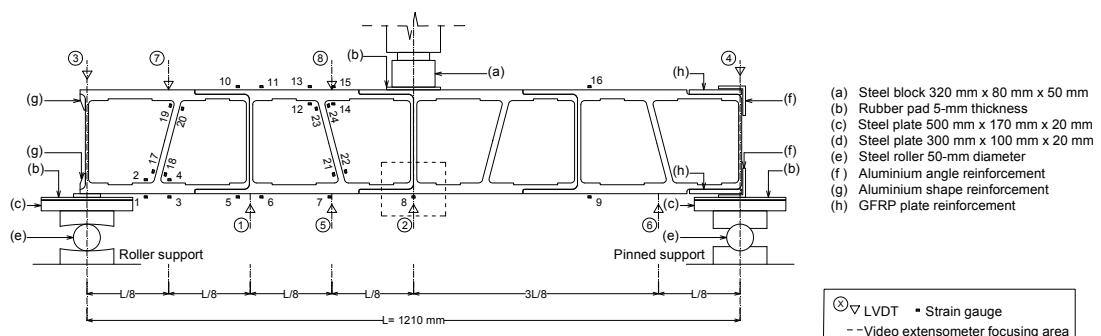
B.1 Introduction

Appendix B presents supplementary results from the experiments conducted on the DS beams (described in Chapter 2).

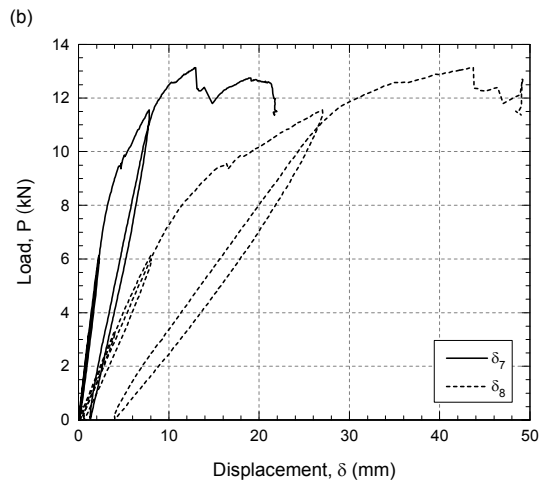
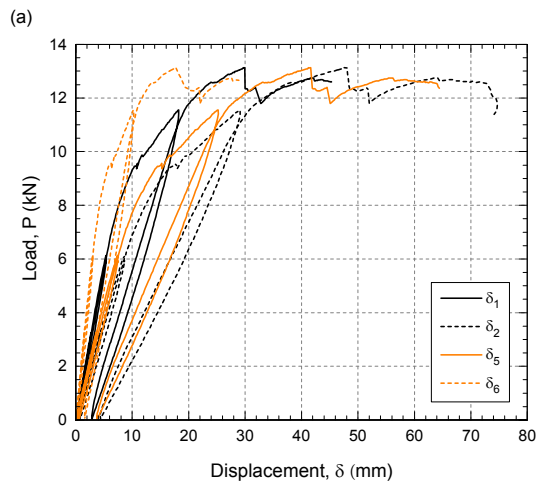
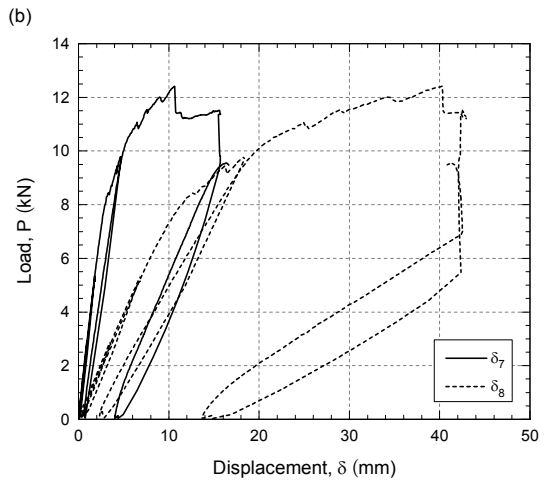
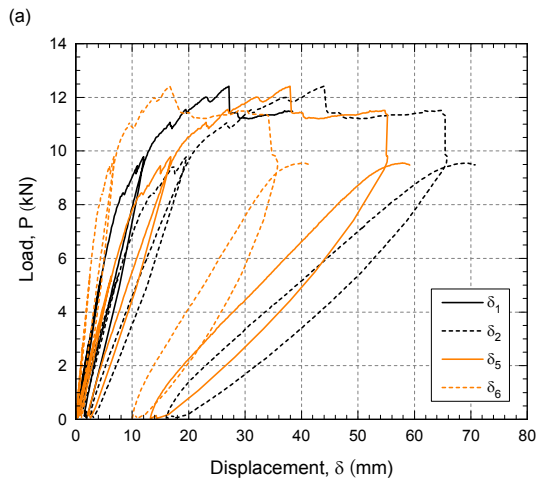
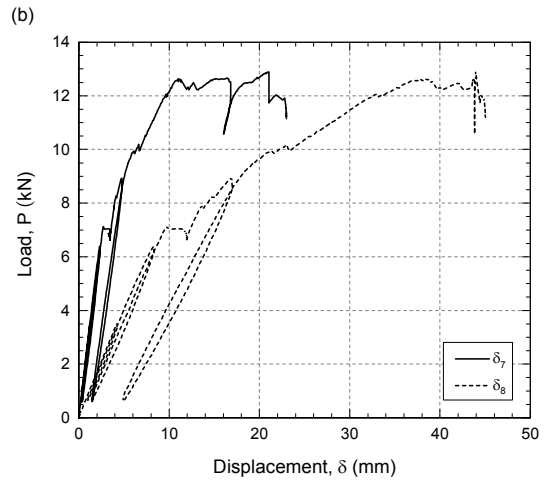
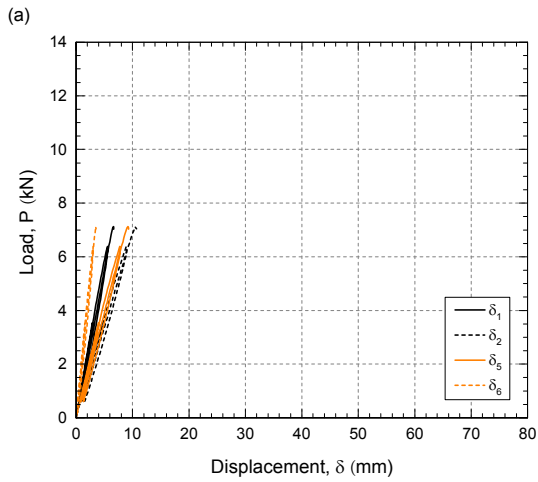
The experimental program was conducted on three beams from the DuraSpan¹ (DS) deck: DS-1, DS-2, DS-3. The DS specimens consisted of four DS unit module profiles adhesively bonded with a structural polyurethane adhesive.² The DS specimens' global length, height and width were 1230, 194.6 and 200 mm, respectively (see Figure B.1). The DS beams were loaded in a three-point bending configuration with a 1210-mm clear span length. Specimens were equipped with linear vertical displacement transducers (LVDTs) and 120- Ω -resistance/6-mm-length electrical strain gages, the latter positioned parallel to span. The experimental set-up and instrumentation of the DS specimens is shown in Figure B.1.

The measured load-deflection and load-strain responses, the failure modes and the behavior of the adhesively-bonded joints between adjacent unit profiles are presented in the following.

Figure B.1 – Experimental set-up for DS beams.



B.2 Load-deflection curves



∧ Figure B.2 – Load-deflection behavior of specimen *DS-1*; measured deflections on (a) bottom and (b) top surfaces.

Figure B.3 – Load-deflection behavior of specimen *DS-2*; measured deflections on (a) bottom and (b) top surfaces.

∨ Figure B.4 – Load-deflection behavior of specimen *DS-3*; measured deflections on (a) bottom and (b) top surfaces.

B.3 Load-strain curves

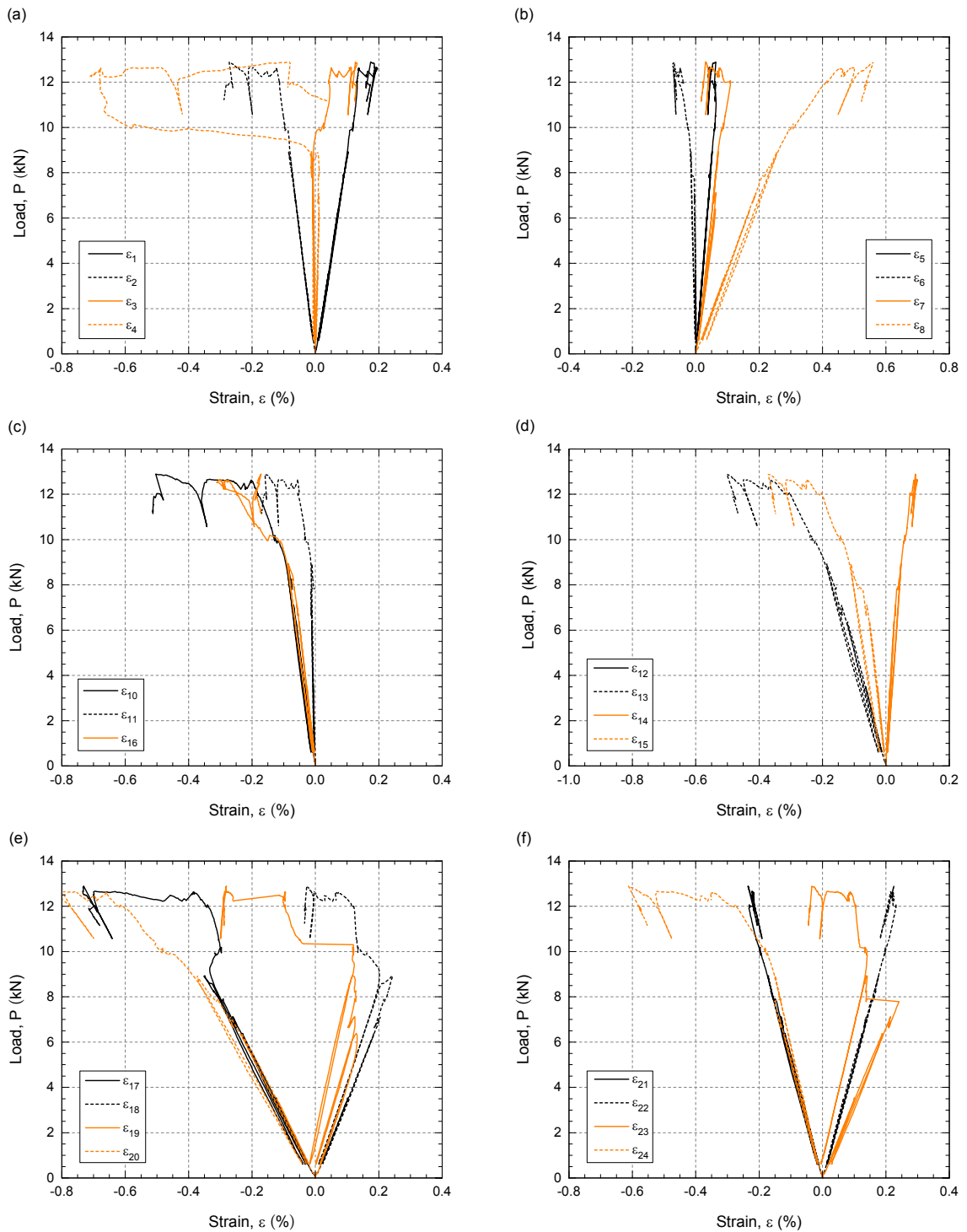


Figure B.5 – Load-strain behavior of specimen DS-1; measured strains on (a–b) bottom flange; (c–d) top flange and (e–f) webs.

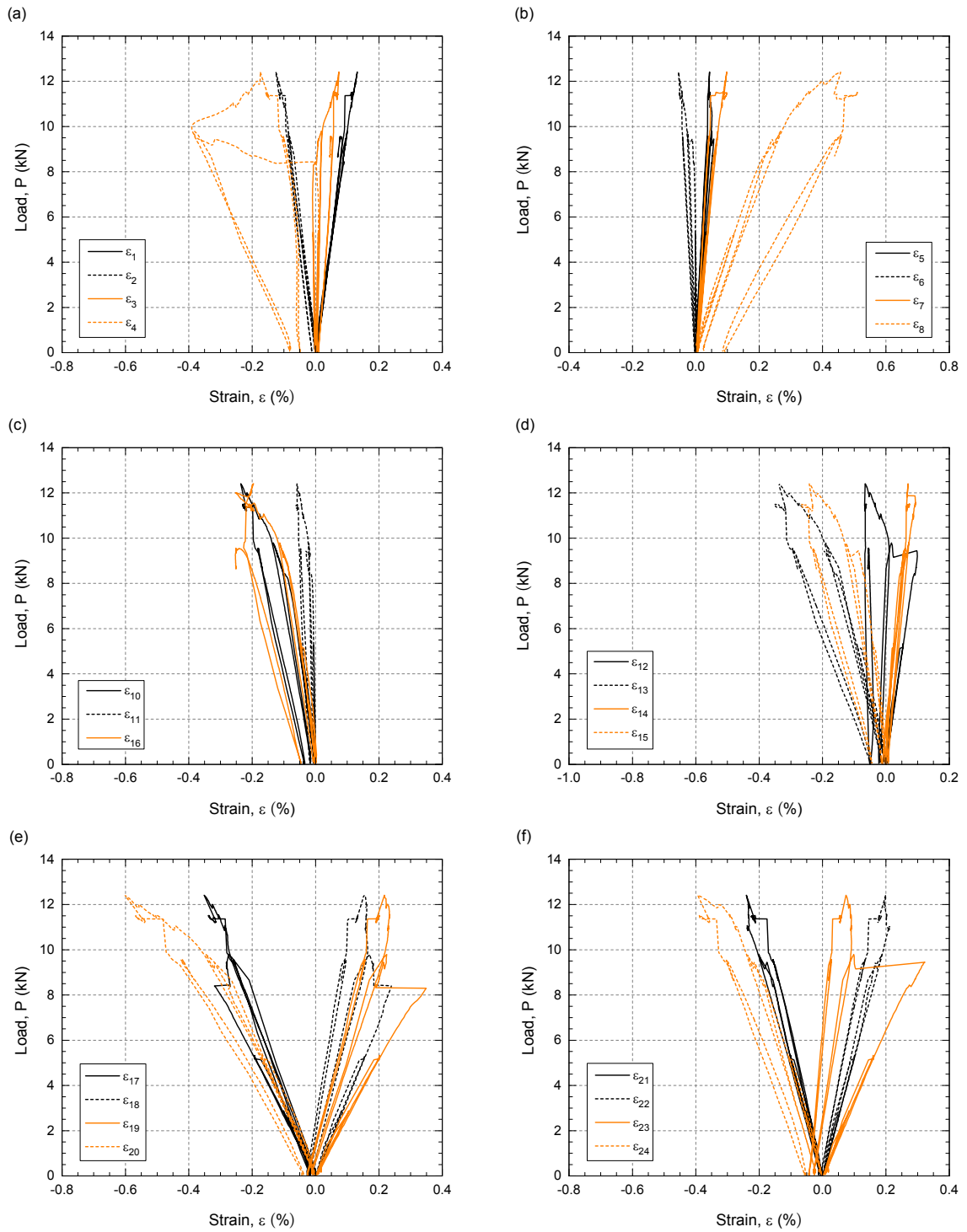


Figure B.6 – Load-strain behavior of specimen DS-2; measured strains on (a–b) bottom flange; (c–d) top flange and (e–f) webs.

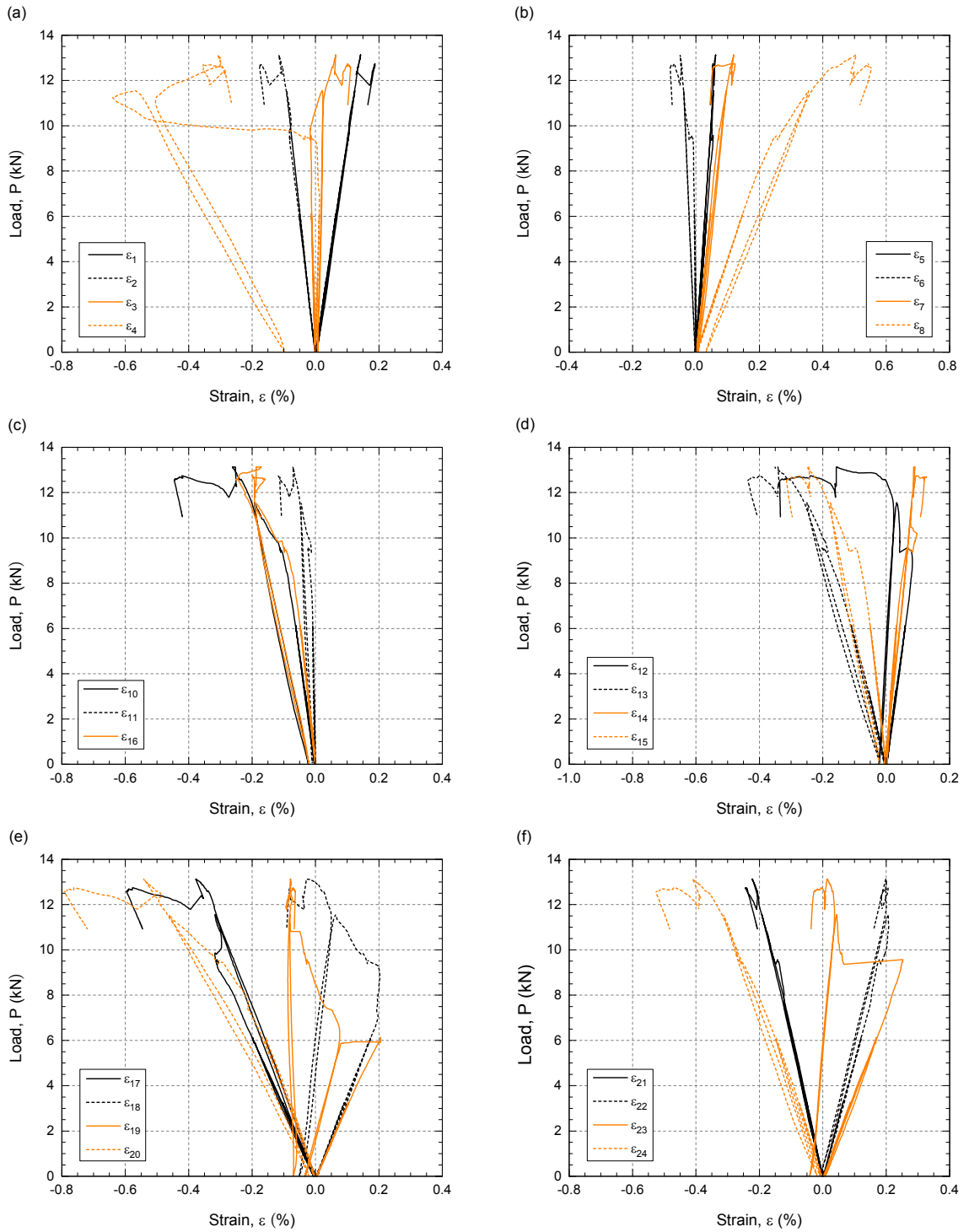
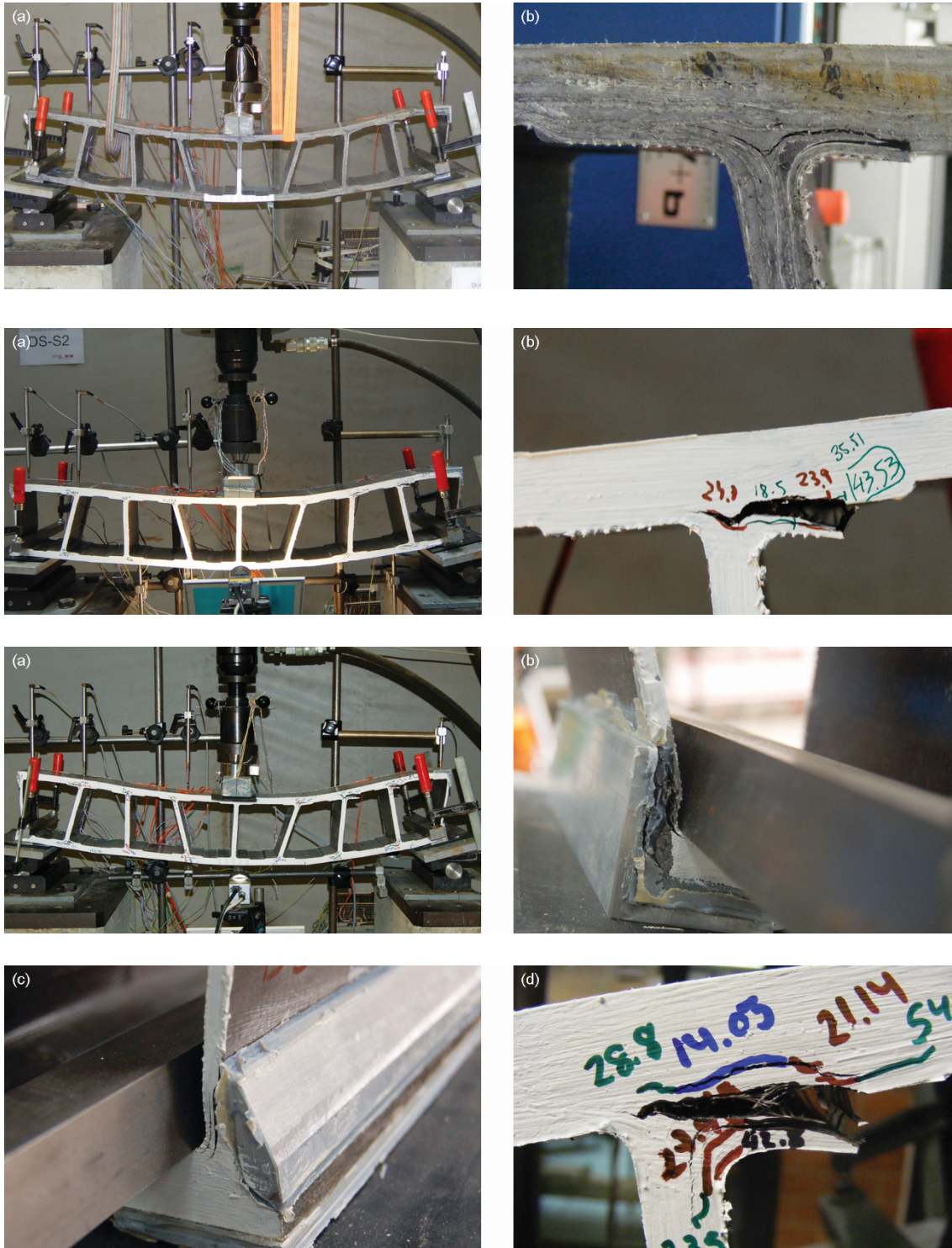


Figure B.7 – Load-strain behavior of specimen DS-3; measured strains on (a–b) bottom flange; (c–d) top flange and (e–f) webs.

B.4 Failure mode



△ Figure B.8 – Failure pattern of specimen *DS-1*; (a) deformed shape; (b) local failure in 8th web-top flange junction.

Figure B.9 – Failure pattern of specimen *DS-2*; (a) deformed shape; (b) local failure in 8th web-top flange junction.

▽ Figure B.10 – Failure pattern of specimen *DS-3*; (a) deformed shape; (b) first local failure in 9th web-bottom flange junction, view from back side; (c) second local failure in 1st web-bottom flange junction, view from back side; (d) third local failure in 8th web-top flange junction.

B.5 Adhesively-bonded joint behavior

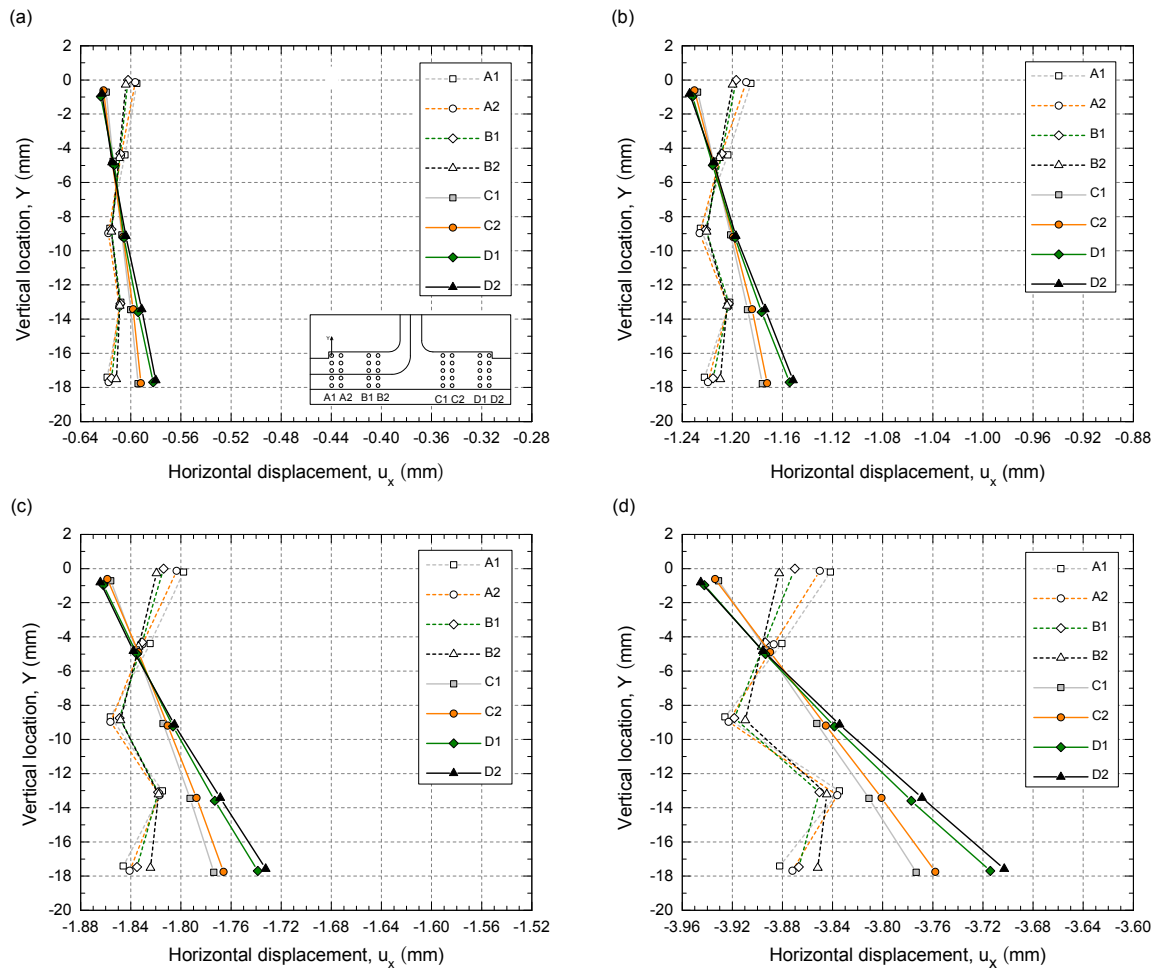


Figure B.11 – Horizontal displacement across bottom flange at mid-span in specimen DS-2 at (a) 3-kN; (b) 6-kN; (c) 9-kN and (d) 12-kN load.

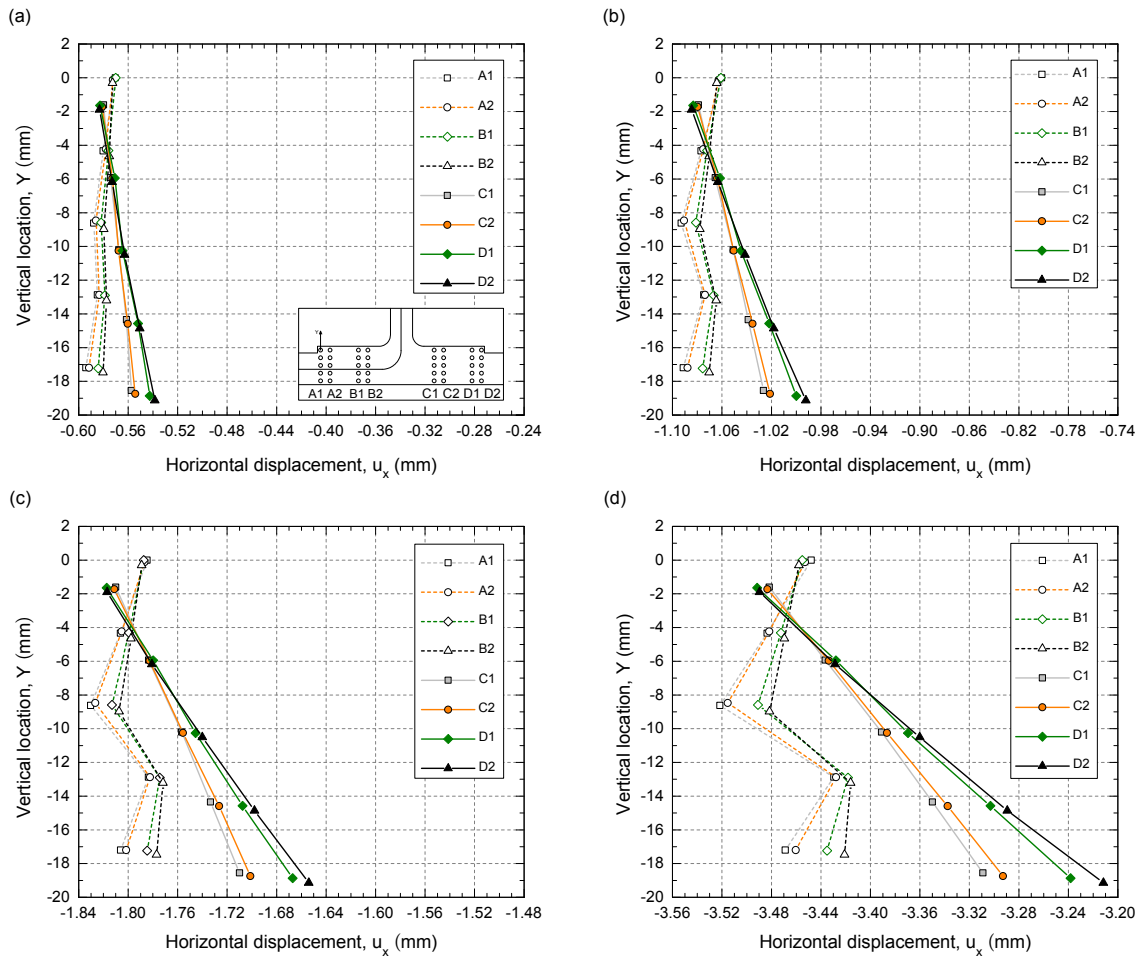


Figure B.12 – Horizontal displacement across bottom flange at mid-span in specimen *DS-3* at (a) 3-kN; (b) 6-kN; (c) 9-kN and (d) 12-kN load.

References

1. DARPA. Advanced composites for bridge infrastructure renewal - Phase II, Task 16 - Modular composite bridge. USA: Defense Advanced Research Projects Agency; 2000.
2. Ashland. *Data Sheet Pliogrip 6660*. Columbus: Ashland; 1999.

Appendix C

AS beam experiments

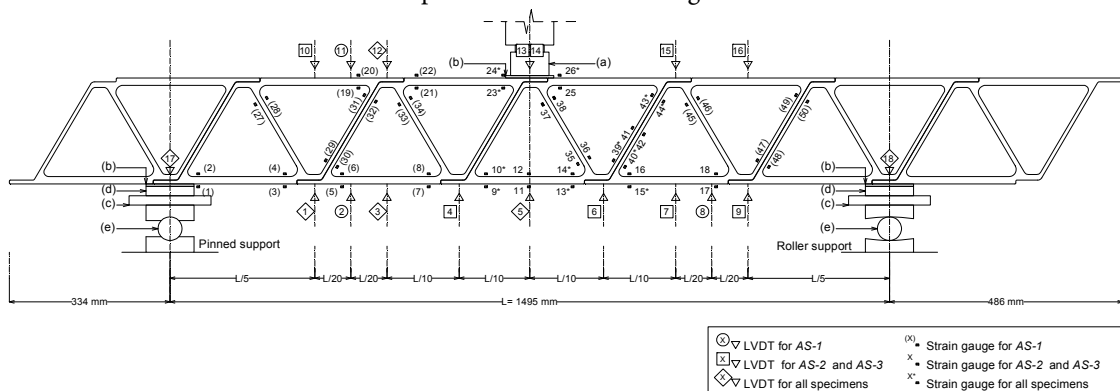
C.1 Introduction

Appendix C presents supplementary results from the experiments conducted on the AS beams (described in Chapter 2).

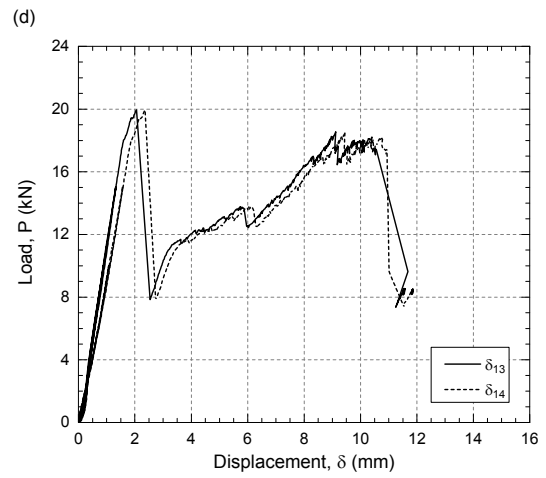
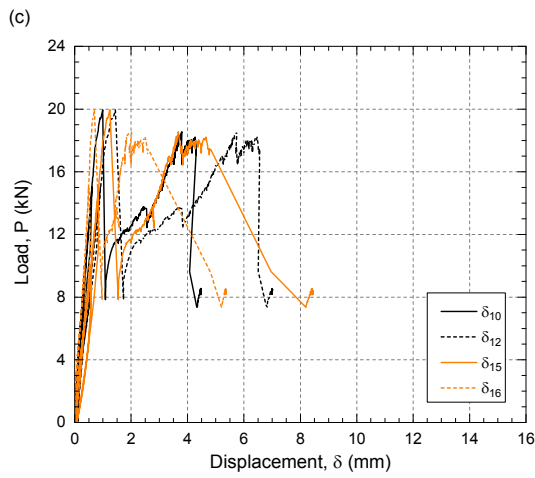
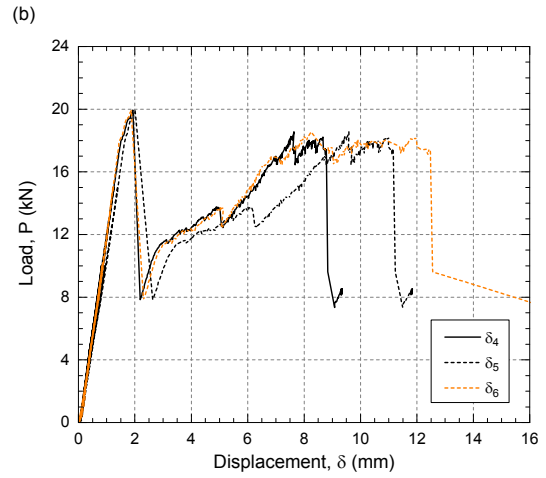
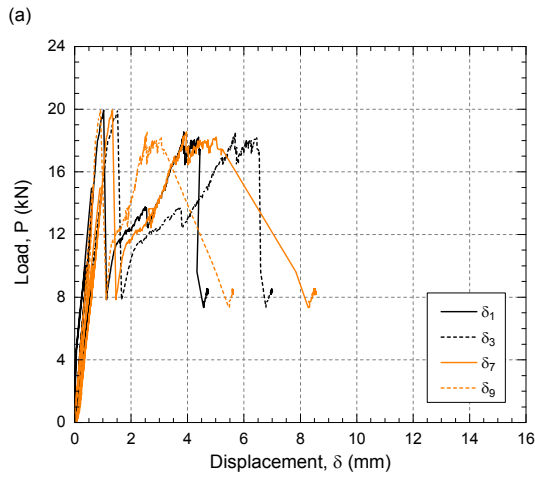
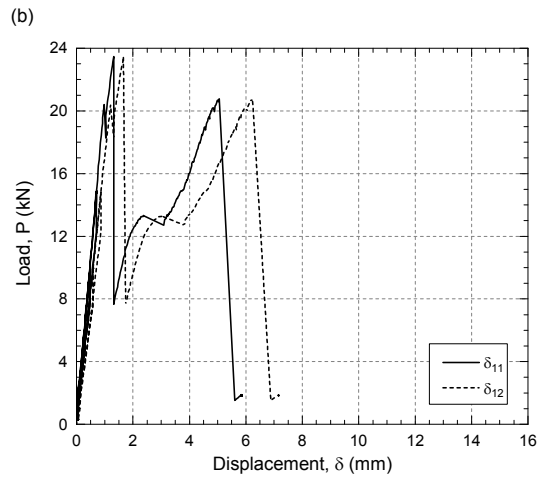
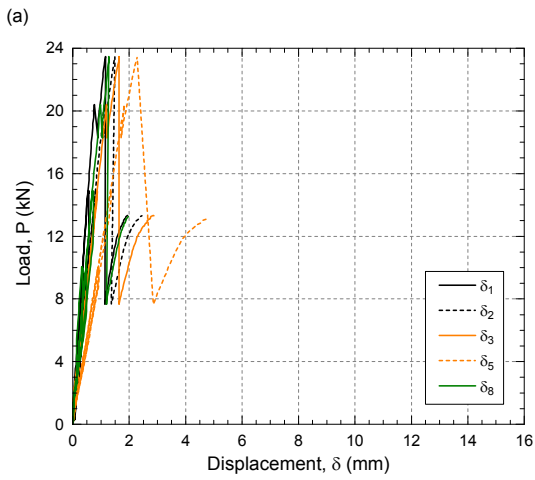
The experimental program was conducted on three beams from the AS deck: AS-1, AS-2, AS-3. The AS specimens consisted of seven Asset¹ single profile units adhesively bonded with a structural two-component epoxy adhesive. The AS specimens' global length, height and width were 2315, 225 and 200 mm, respectively. The AS beams were loaded in a three-point bending configuration with a 1495-mm clear span length, see Figure C.1. Specimens were equipped with linear vertical displacement transducers (LVDTs) and 120- Ω -resistance/6-mm-length electrical strain gages, the latter positioned parallel to span. In addition, an instrumentation system to take pictures in the expected failure area and allow their correlation with the recorded data was used for specimens AS-2 and AS-3, as presented in Chapter 2. The experimental set-up and instrumentation of the AS specimens is shown in Figure C.1.

Figure C.1 – Experimental set-up for AS beams.

The measured load-deflection and load-strain responses and the failure modes are presented in the following.



C.2 Load-deflection curves



^ Figure C.2 – Load-deflection behavior of specimen AS-1; measured deflections on (a) bottom and (b) top surfaces.

✓ Figure C.3 – Load-deflection behavior of specimen AS-2; measured deflections on (a–b) bottom and (c–d) top surfaces.

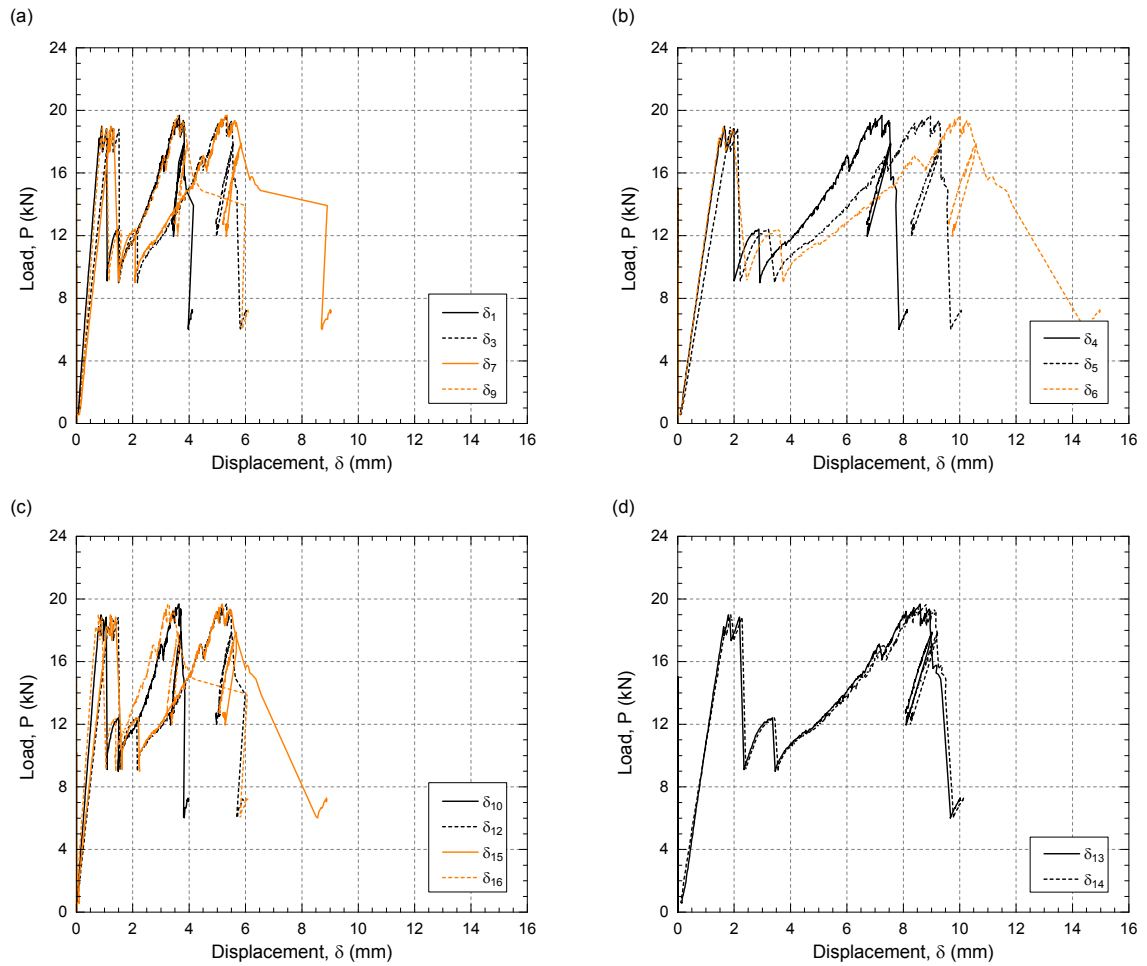


Figure C.4 – Load-deflection behavior of specimen AS-3; measured deflections on (a–b) bottom and (c–d) top surfaces.

C.3 Load-strain curves

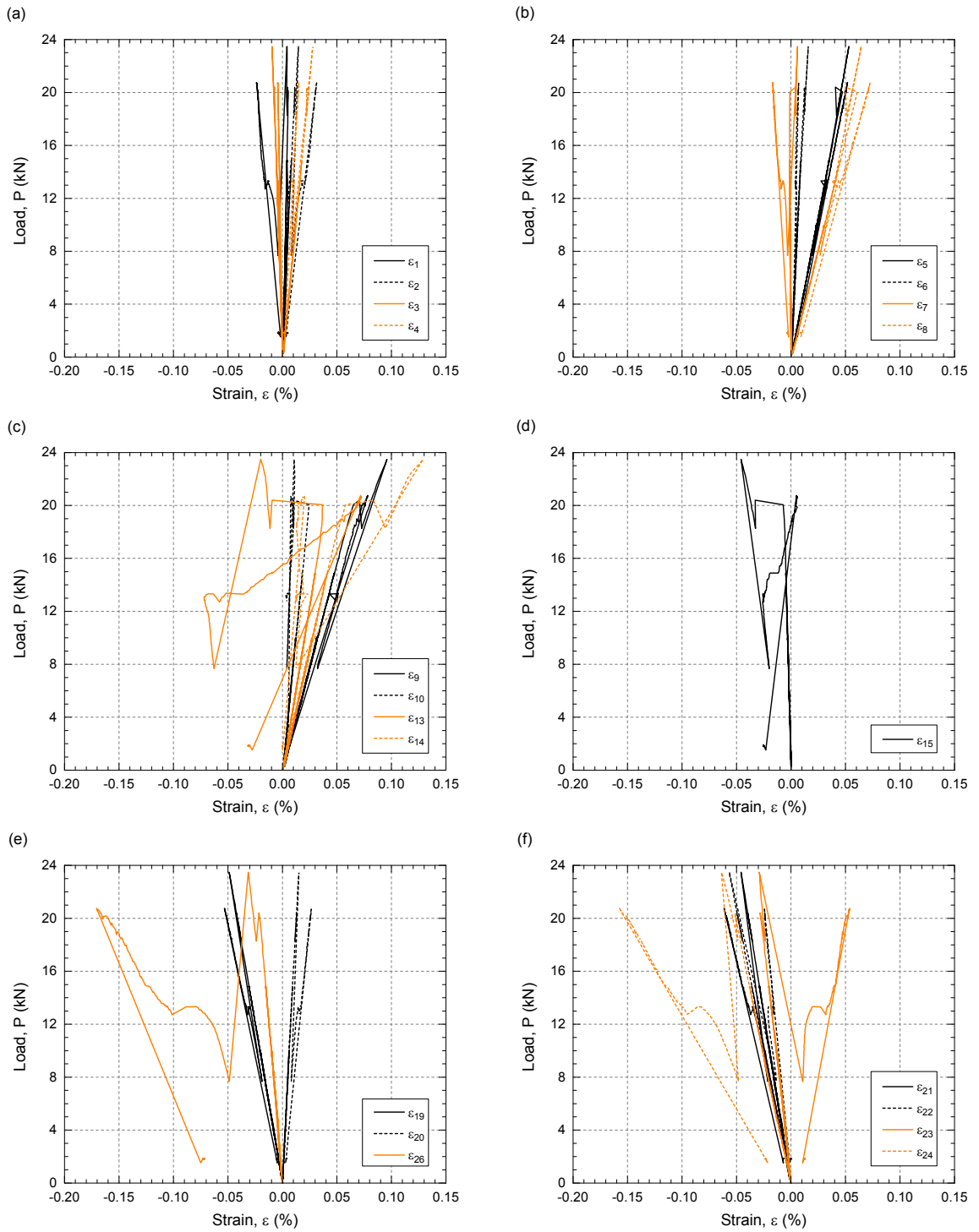


Figure C.5 – Load-strain behavior of specimen AS-1; measured strains on (a–d) bottom flange and (e–f) top flange.

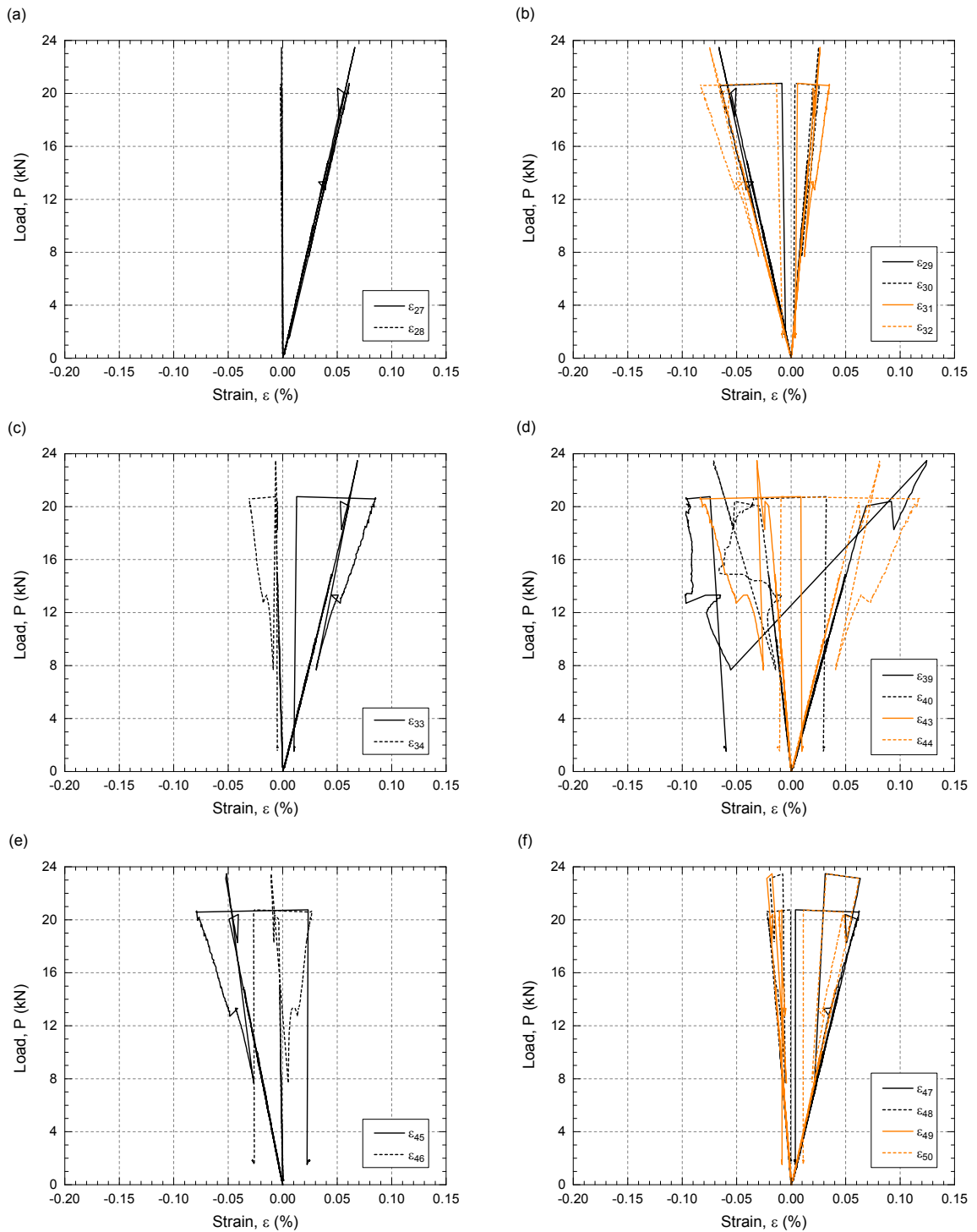


Figure C.6 – Load-strain behavior of specimen AS-7; measured strains on (a) 4th; (b) 5th; (c) 6th; (d) 9th; (e) 10th and (f) 11th webs.

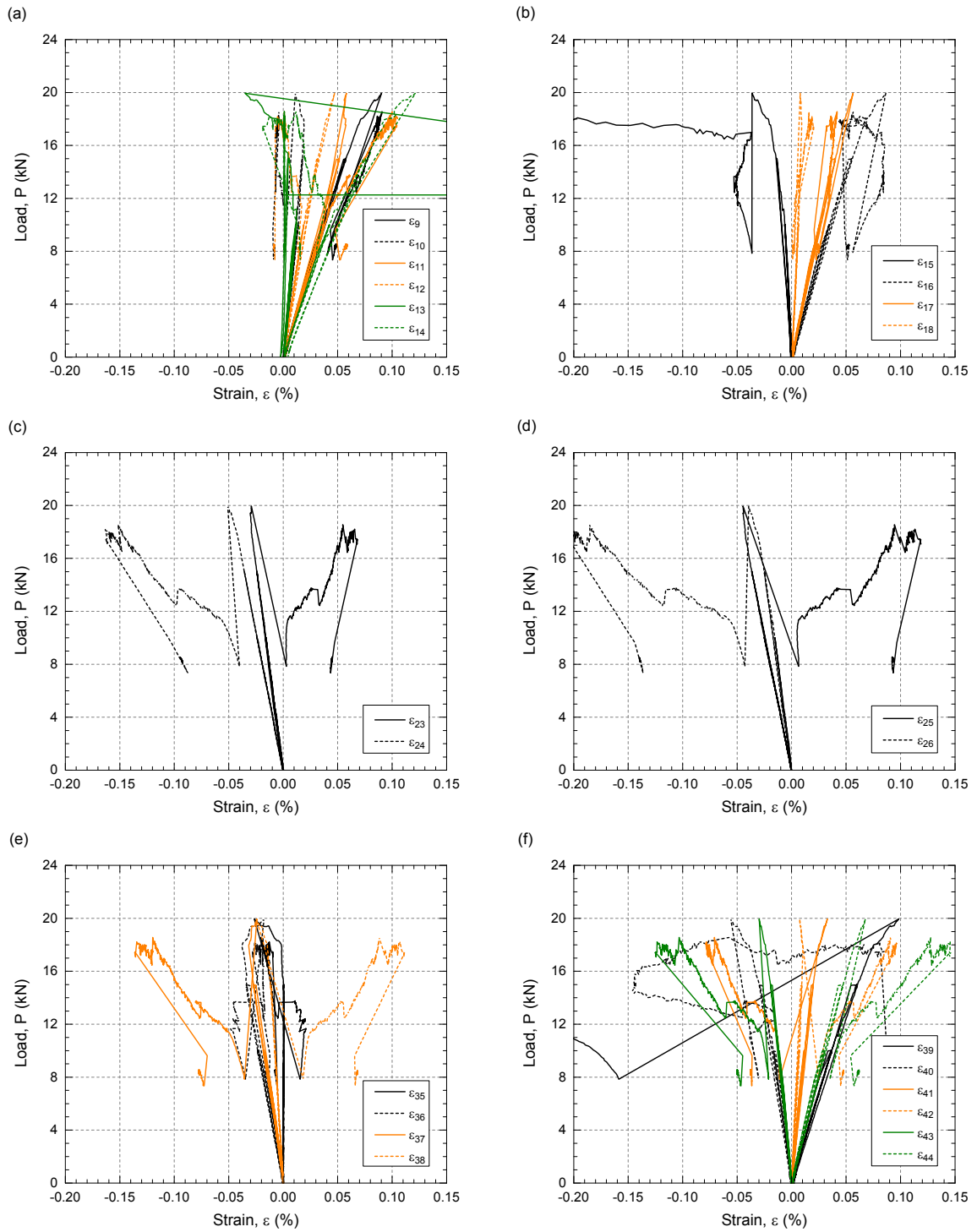


Figure C.7 – Load-strain behavior of specimen AS-2; measured strains on (a–b) bottom flange; (c–d) top flange; (e) 8th and (f) 9th webs.

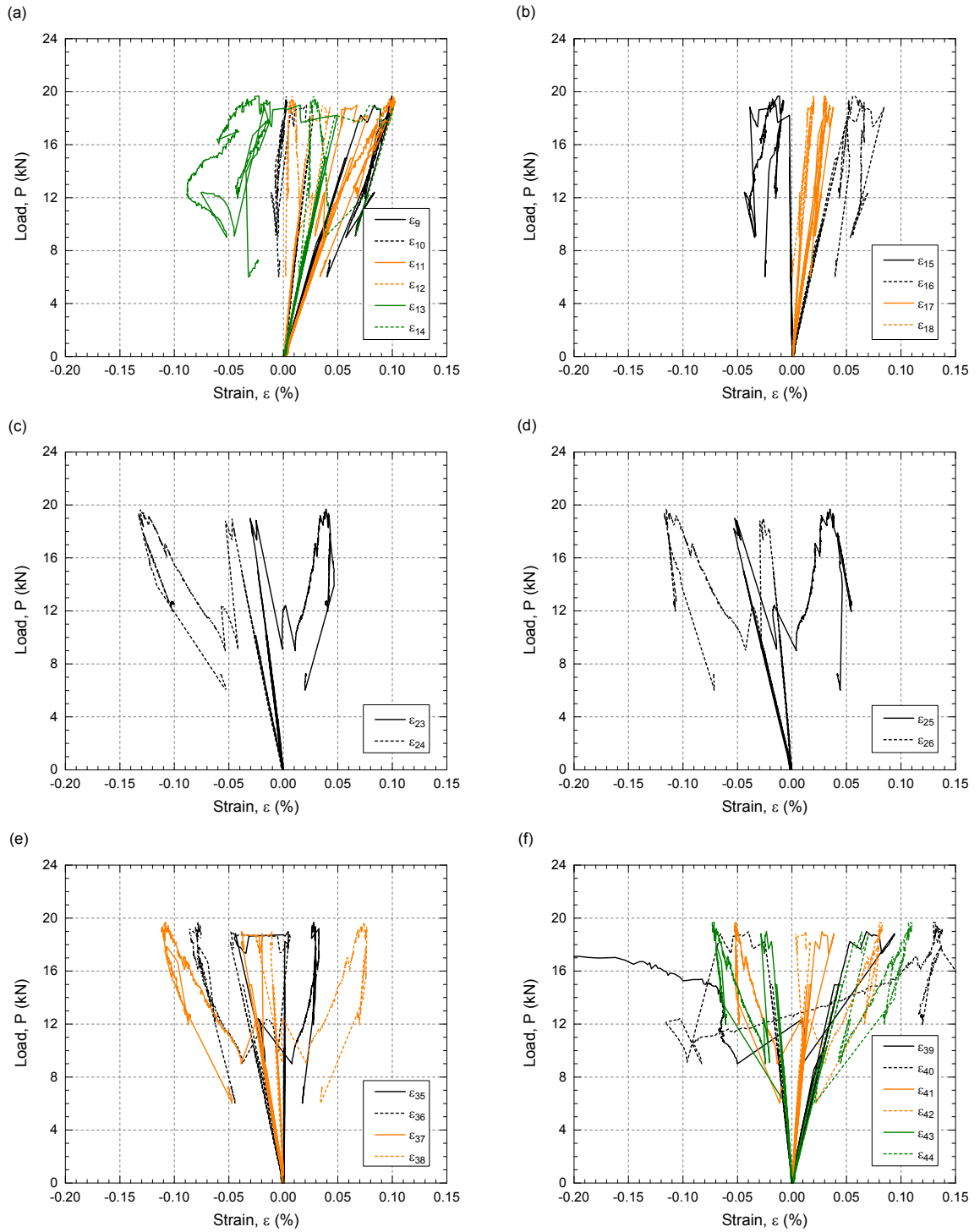


Figure C.8 – Load-strain behavior of specimen AS-3; measured strains on (a–b) bottom flange; (c–d) top flange; (e) 8th and (f) 9th webs.

C.4 Failure modes

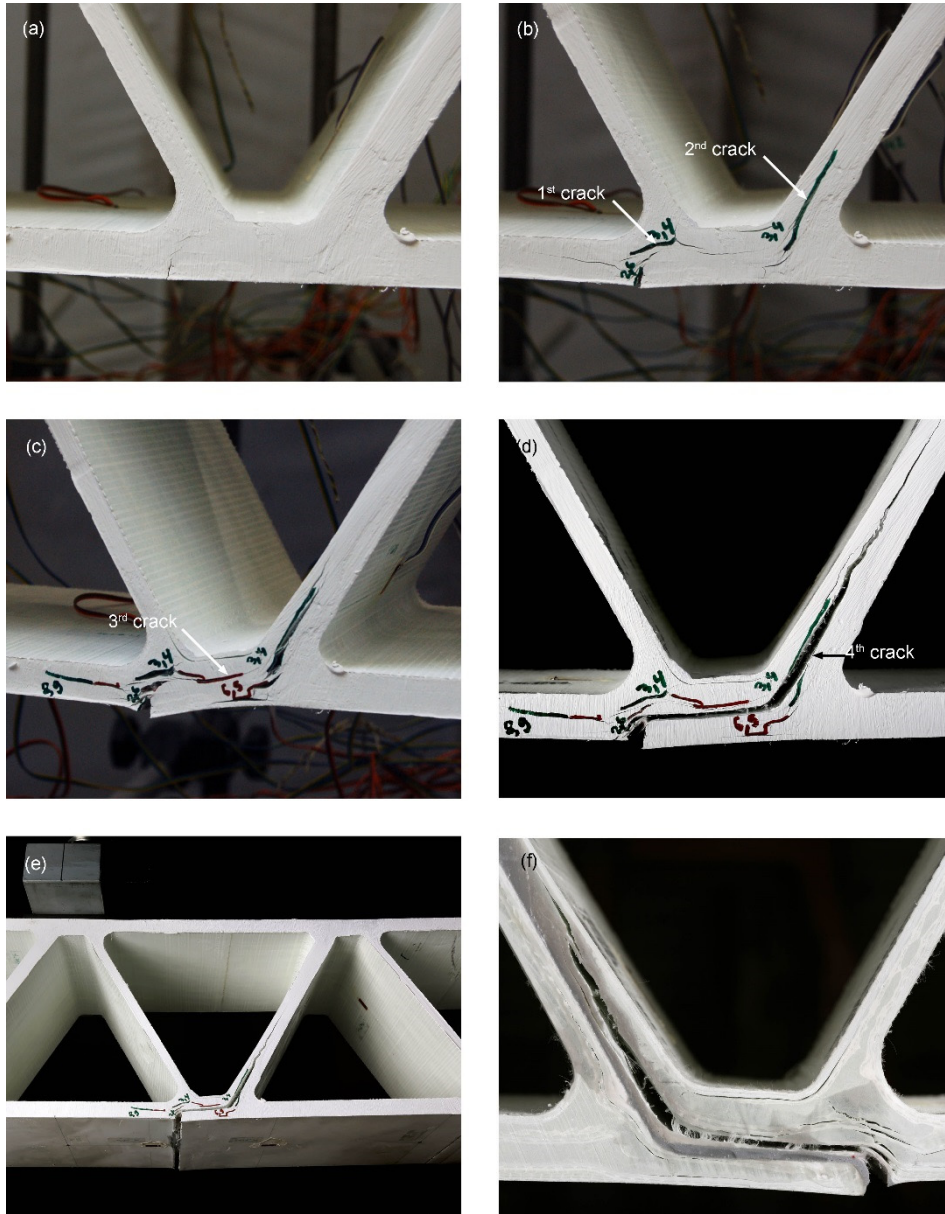


Figure C.9 – Failure pattern of specimen AS-1; (a) opening of adhesively-bonded joint at 20.4 kN; (b) crack pattern at first failure at 23.5 kN; (c) crack pattern at 13 kN after first failure; (d) final failure; view (e) across width and (f) from back face.

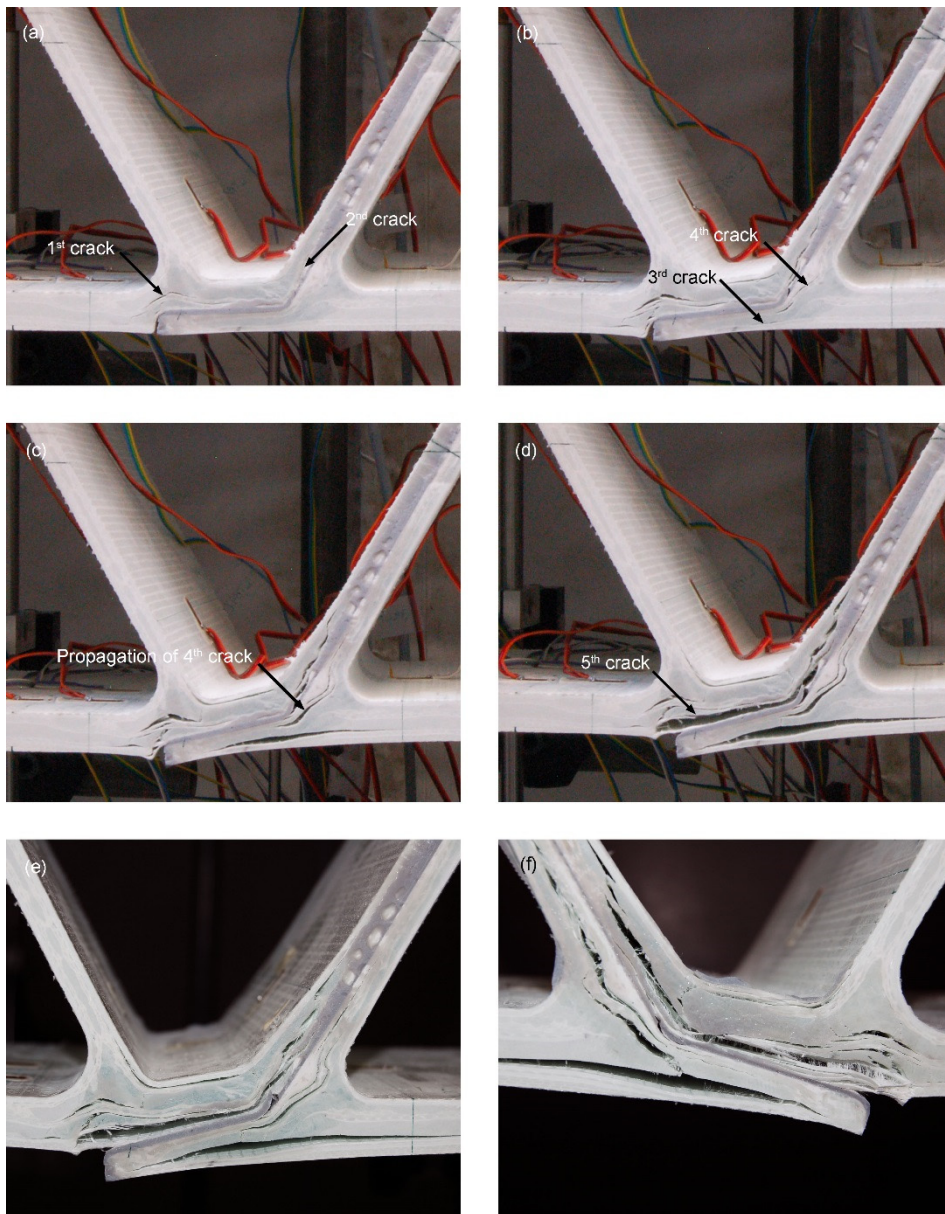


Figure C.10 – Failure pattern of specimen AS-2; (a) crack pattern at first failure at 20.0 kN; (b) crack pattern at 13.7 kN after first failure; (c) crack pattern at 18.6 kN after first failure; (d) final failure; view from (e) front and (f) back faces.

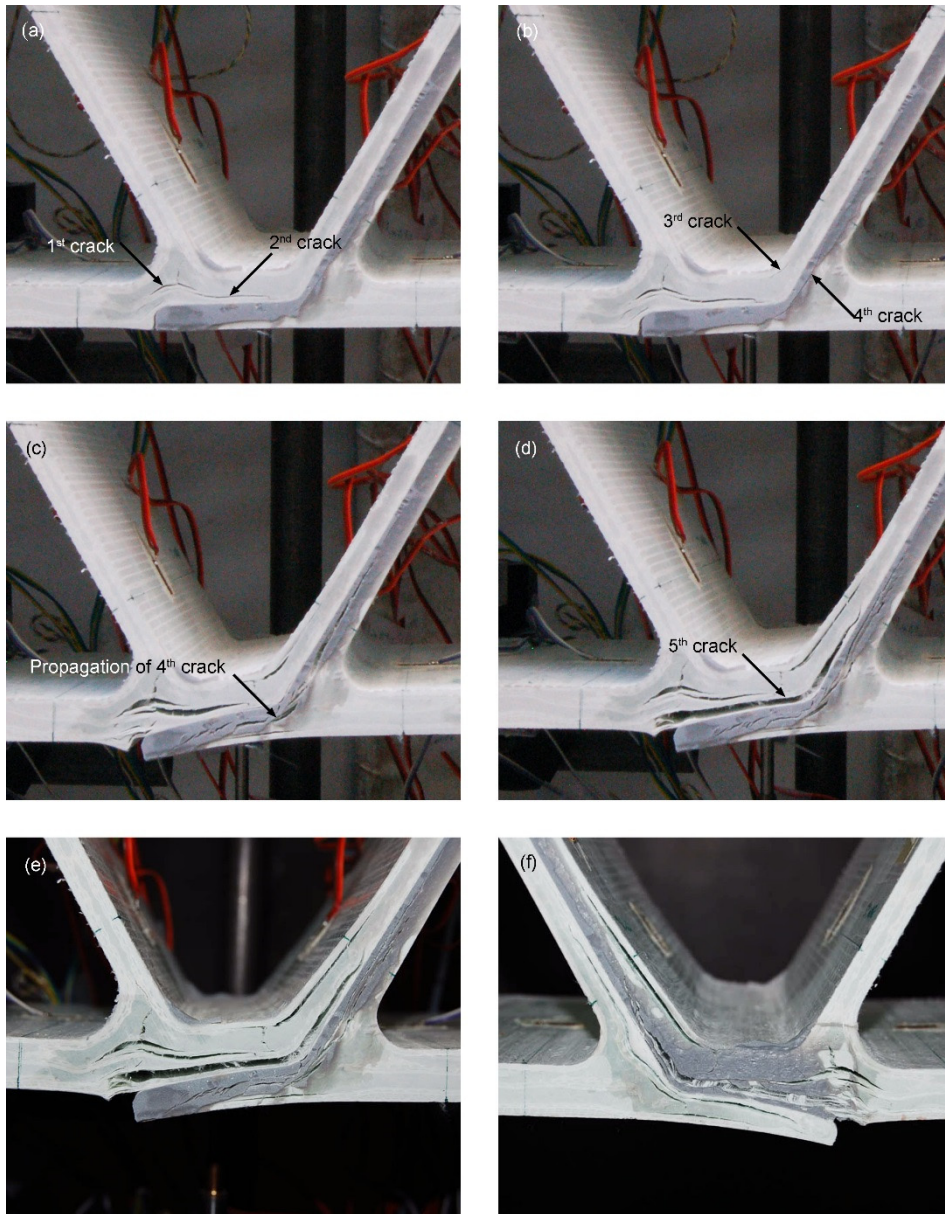


Figure C.11 – Failure pattern of specimen AS-3; (a) crack pattern at first failure at 18.8 kN; (b) crack pattern at 12.4 kN after first failure; (c) crack pattern at 17.8 kN after first failure; (d) final failure; view from (e) front and (f) back faces.

References

1. Fiberline Composites. Product information available from: <https://fiberline.com/fbd600-asset-bridge-deck-product-data> [Last accessed 16th May 2017].

Appendix D

DS web three-point bending experiments

D.1 Introduction

Appendix D presents supplementary results from the small-scale three-point bending experiments conducted on the web elements of the DS deck and described in detail in Chapter 4. Conjointly with cantilever experiments performed on the deck's web-flange junctions (WFJs), they allowed the characterization of the rotational stiffness of the DS WFJs.

The experimental program was performed on three 50-mm-wide specimens from each of the six WFJ series (*If-o*, *If-a*, *Ic-o*, *Ic-a*, *V-d*, *V-s*). The specimens' geometry, global dimensions and location within the DS deck are shown in Figure D.1. Table D.1 lists the detailed width (b) and thickness (t_w) dimensions of the specimens' web components.

The webs of the WFJ specimens were subjected to symmetric three-point bending with a clear span length of 130 mm. The experimental set-up is illustrated in Figure D.2. Each specimen was instrumented with a 120- Ω -resistance/6-mm-length electrical strain gage in the soffit of the web at mid-span, see Figure D.3. A video extensometer was used to measure the vertical deflections and rotations; the arrangement of the target points monitored is shown in Figure D.3.

In the following, the measured load-strain and load-deflection responses for all specimens are presented. The average deflections at a given location (see X in Figure D.3) are shown. The rotation of the specimens at the left and right supports are also presented – these were measured to demonstrate that the web behavior was symmetric despite the attachment of the WFJ on one of its sides. The elastic flexural moduli of the web components in the deck's transverse-to-pultrusion direction, calculated from the measured load-strain responses, are also reported, see Table D.2.

Figure D.1 – (a) WFJ specimens; (b) location of WFJ specimens within DS deck panel when subjected to transverse bending (local bending moments in webs are shown); dimensions in mm.

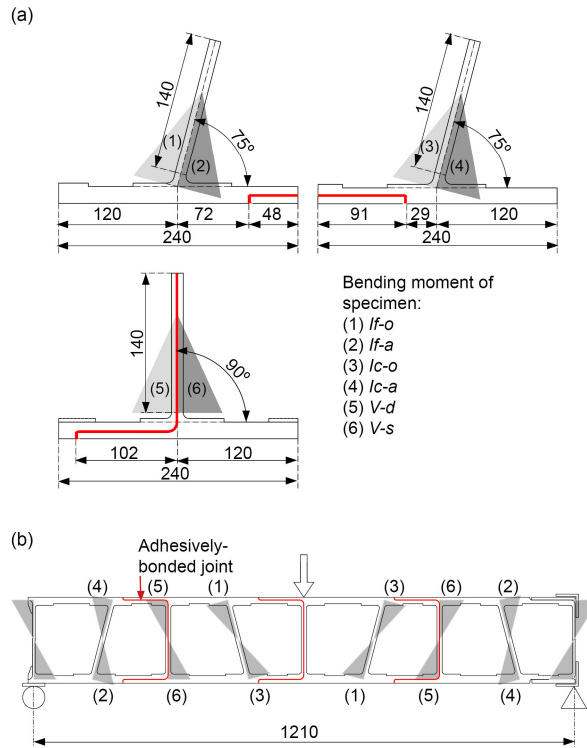


Table D.1 – Dimensions of WFJ specimens.

Series	Specimen	Web width b (mm)	Web thickness t_w (mm)
<i>If-o</i>	<i>If-o1</i>	49.4	11.4
	<i>If-o2</i>	49.6	11.4
	<i>If-o3</i>	49.3	11.5
	Mean	$49.4 \pm 0.2^{(a)}$	$11.4 \pm 0.1^{(a)}$
<i>If-a</i>	<i>If-a1</i>	50.2	11.4
	<i>If-a2</i>	51.3	11.4
	<i>If-a3</i>	49.9	11.5
	Mean	$50.5 \pm 0.7^{(a)}$	$11.4 \pm 0.1^{(a)}$
<i>Ic-o</i>	<i>Ic-o1</i>	51.4	11.4
	<i>Ic-o2</i>	49.2	11.4
	<i>Ic-o3</i>	49.6	11.4
	Mean	$50.1 \pm 1.2^{(a)}$	$11.4 \pm 0.0^{(a)}$
<i>Ic-a</i>	<i>Ic-a1</i>	50.6	11.4
	<i>Ic-a2</i>	50.0	11.4
	<i>Ic-a3</i>	51.1	11.4
	Mean	$50.6 \pm 0.6^{(a)}$	$11.4 \pm 0.0^{(a)}$
<i>V-d</i>	<i>V-d1</i>	50.0	12.6
	<i>V-d2</i>	51.4	12.6
	<i>V-d3</i>	49.4	12.5
	Mean	$50.3 \pm 1.0^{(a)}$	$12.6 \pm 0.1^{(a)}$
<i>V-s</i>	<i>V-s1</i>	50.1	12.3
	<i>V-s2</i>	51.3	12.3
	<i>V-s3</i>	49.9	12.5
	Mean	$50.4 \pm 0.8^{(a)}$	$12.4 \pm 0.1^{(a)}$

^(a) Standard deviation

Figure D.2 – Set-up for three-point bending experiments; (a) general view (*lc-o* specimen); (b) front view (*lc-a* specimen); (c) cross section; dimensions in mm.

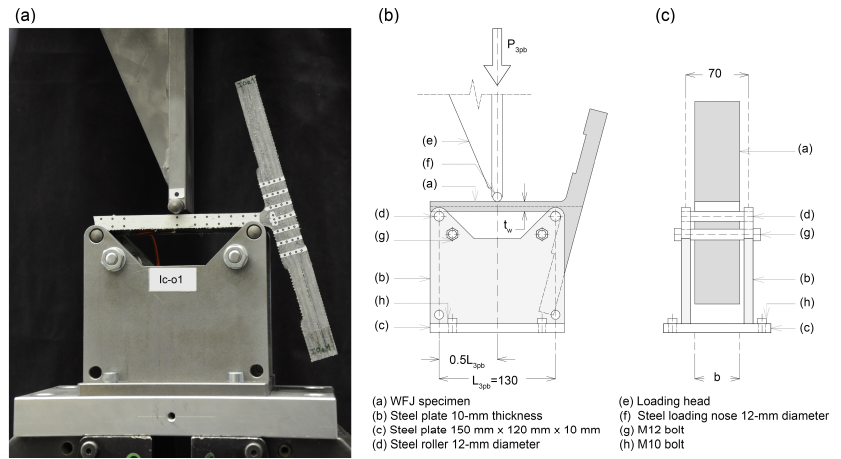
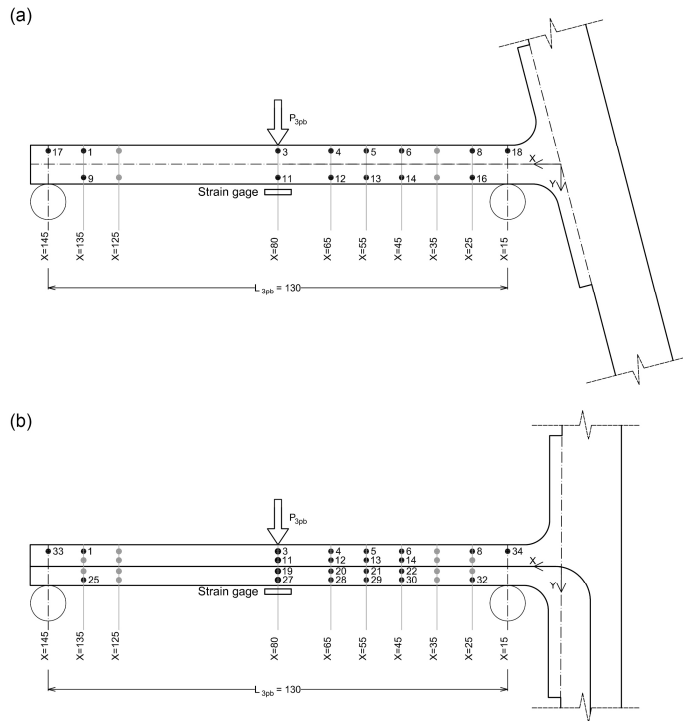


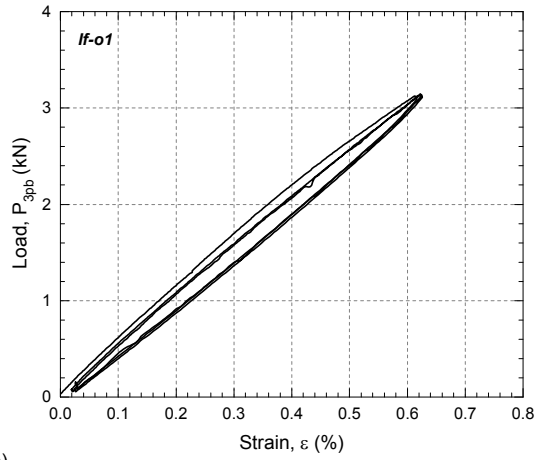
Figure D.3 – Instrumentation for three-point bending experiments in (a) *I* specimens and (b) *V* specimens; dimensions in mm.



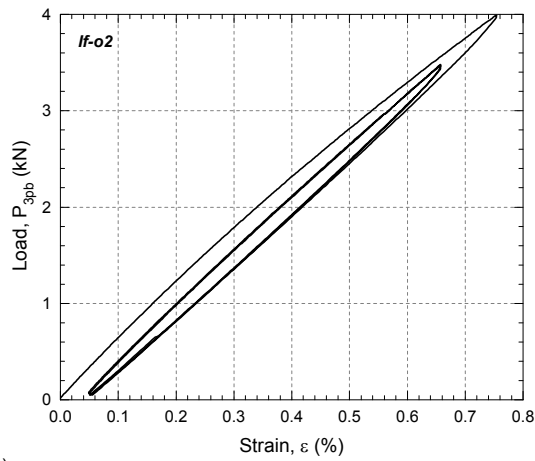
D.2 Load-strain curves

If-o series

(a)



(b)



(c)

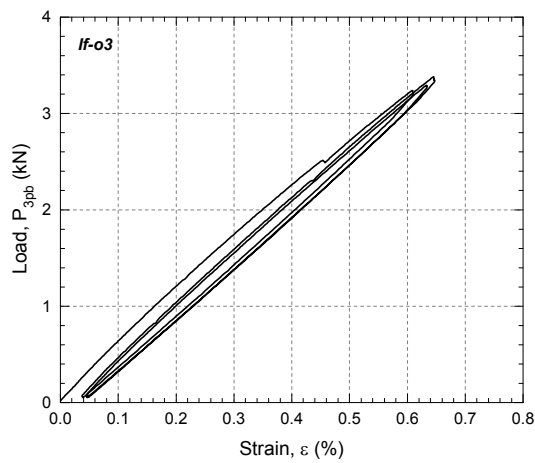
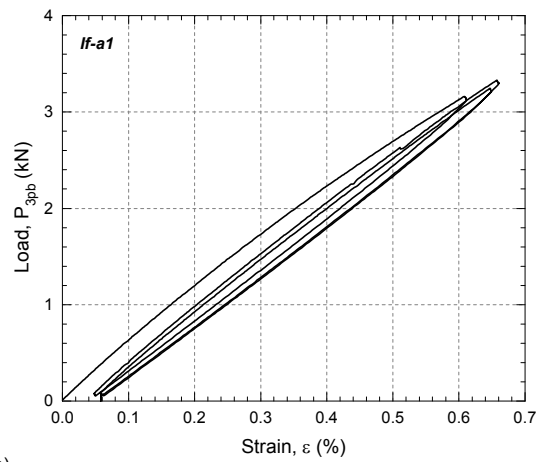


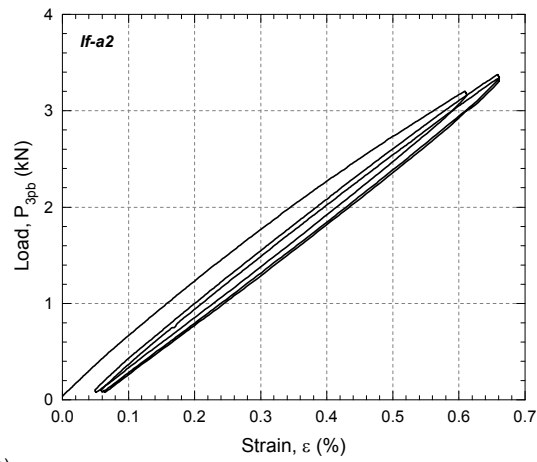
Figure D.4 – Load-strain behavior of specimens (a) *If-o1*, (b) *If-o2* and (c) *If-o3*.

If-a series

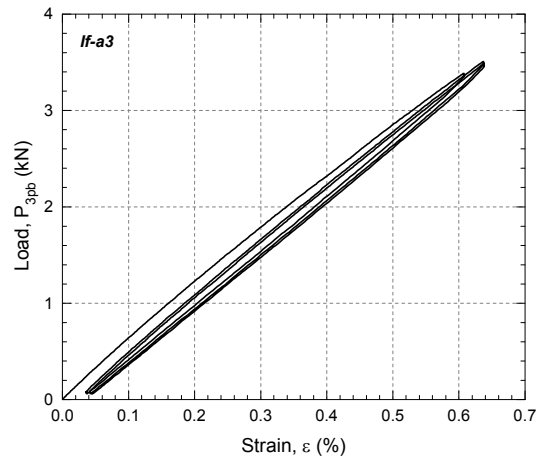
(a)



(b)

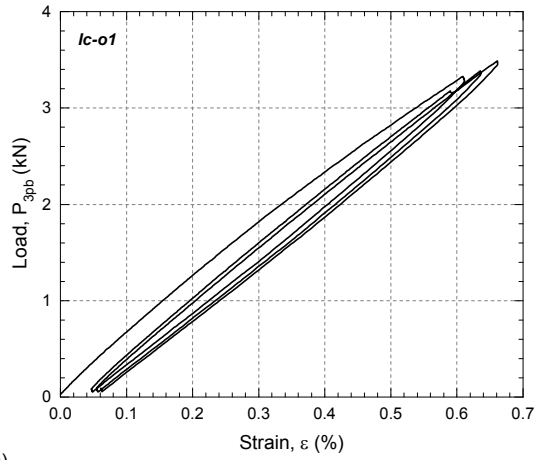


(c)

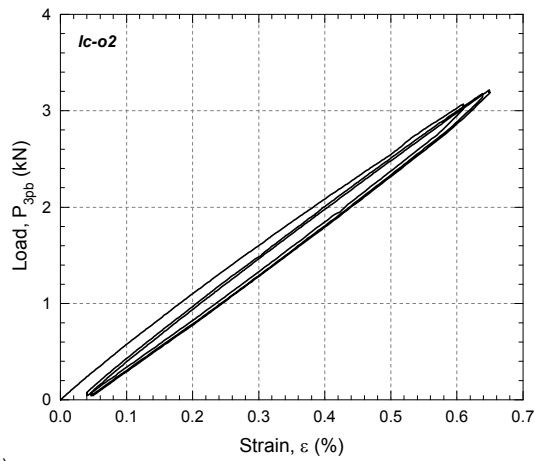
Figure D.5 – Load-strain behavior of specimens (a) *If-a1*, (b) *If-a2* and (c) *If-a3*.

lc-o series

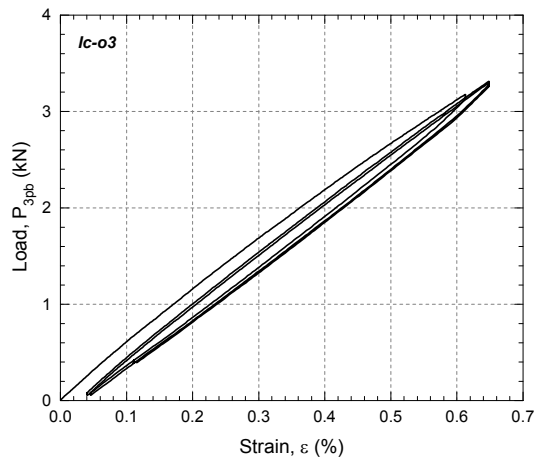
(a)



(b)

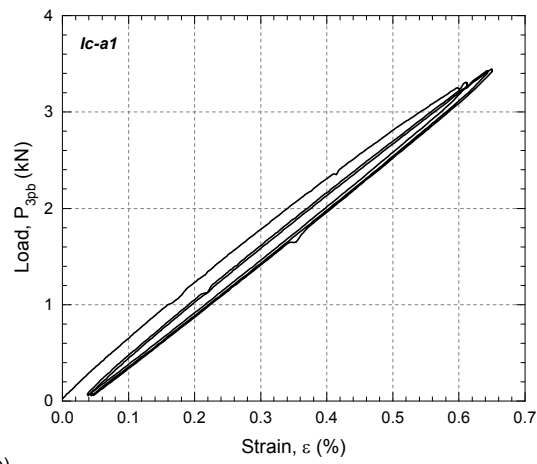


(c)

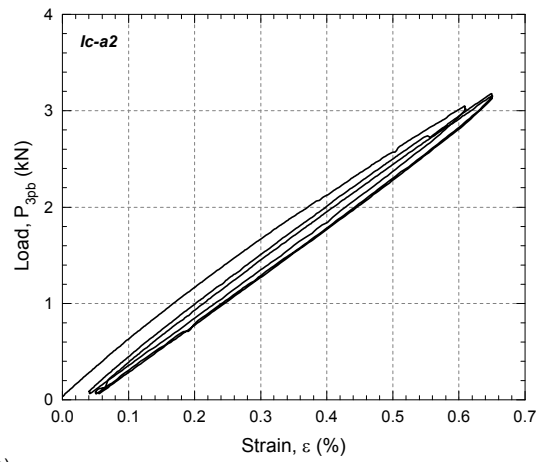
Figure D.6 – Load-strain behavior of specimens (a) *lc-o1*, (b) *lc-o2* and (c) *lc-o3*.

lc-a series

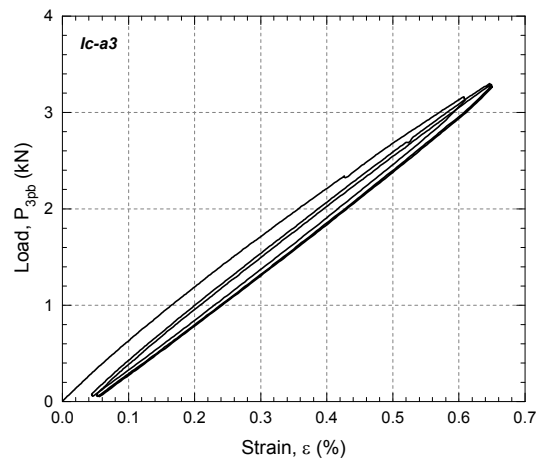
(a)



(b)

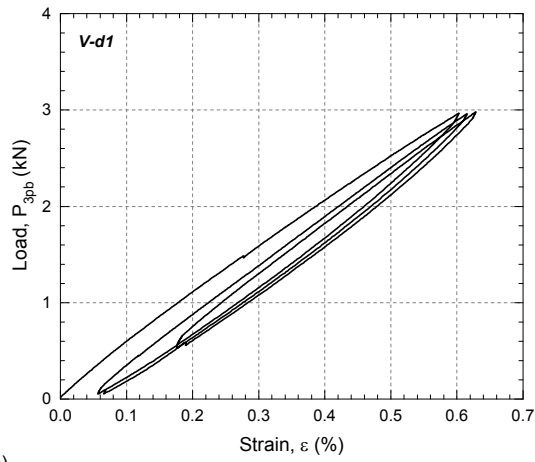


(c)

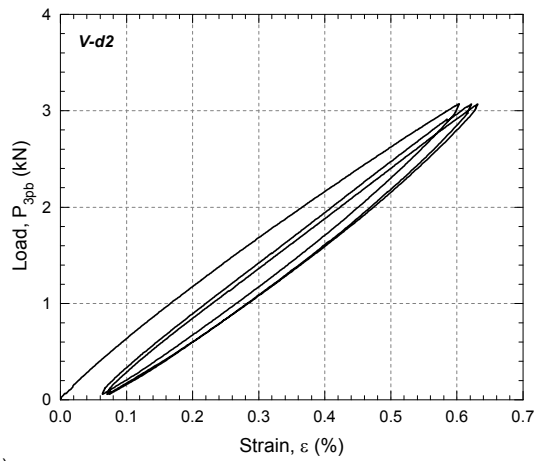
Figure D.7 – Load-strain behavior of specimens (a) *lc-a1*, (b) *lc-a2* and (c) *lc-a3*.

V-d series

(a)



(b)



(c)

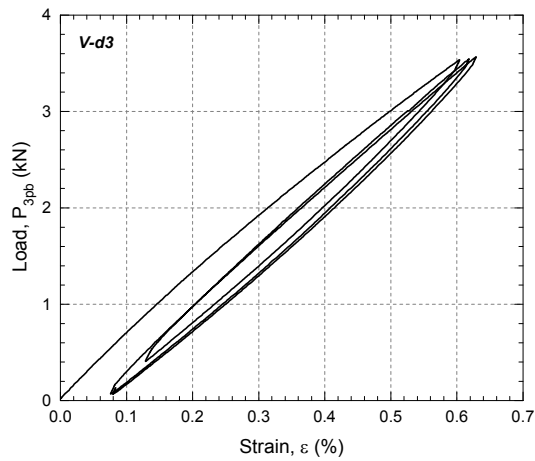
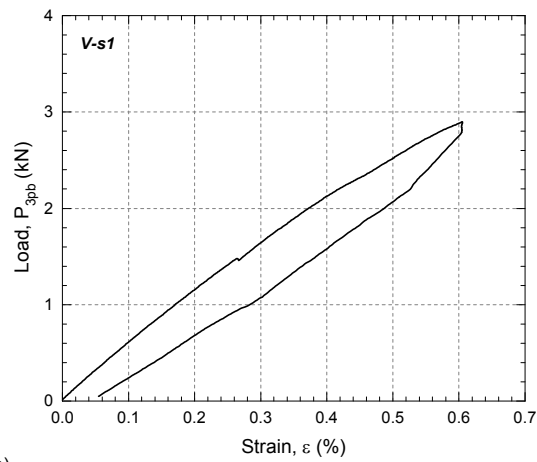


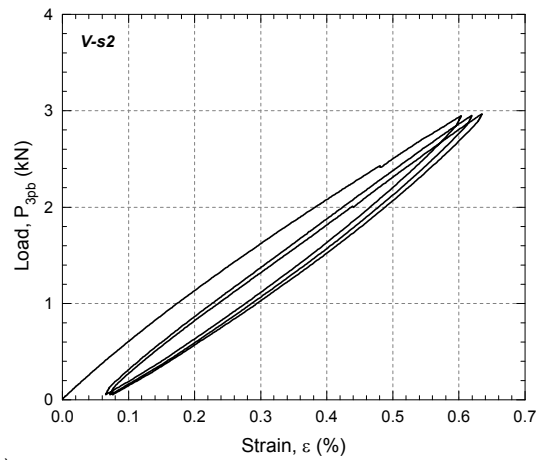
Figure D.8 – Load-strain behavior of specimens (a) V-d1, (b) V-d2 and (c) V-d3.

V-s series

(a)



(b)



(c)

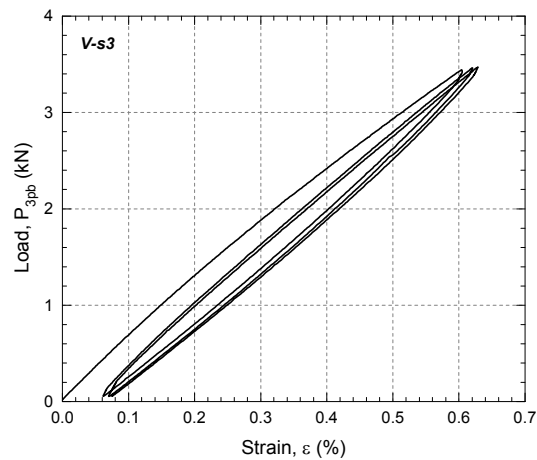
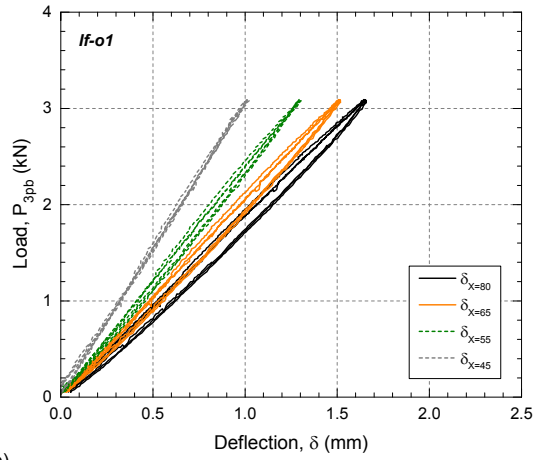


Figure D.9 – Load-strain behavior of specimens (a) V-s1, (b) V-s2 and (c) V-s3.

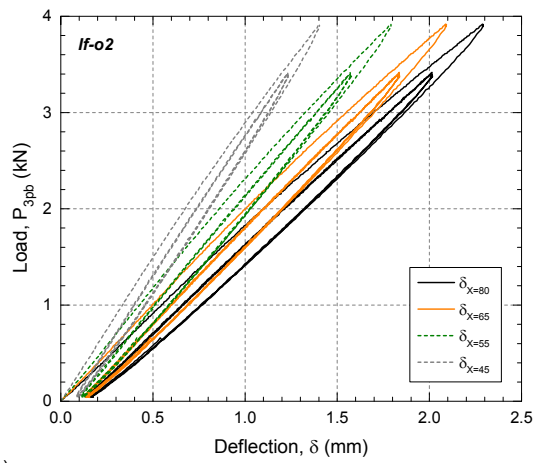
D.3 Load-deflection curves

If-o series

(a)



(b)



(c)

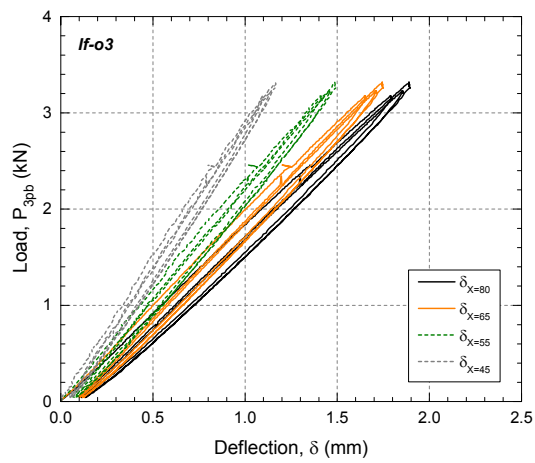
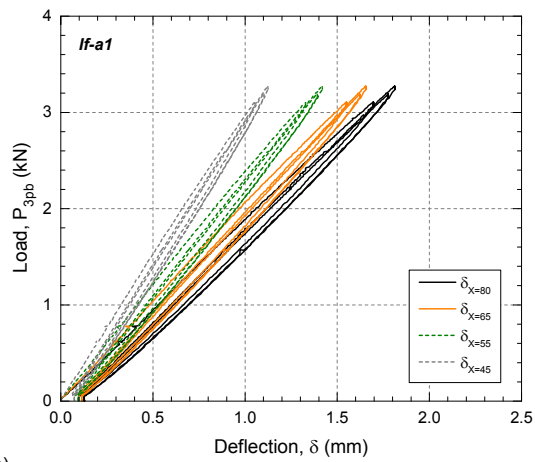


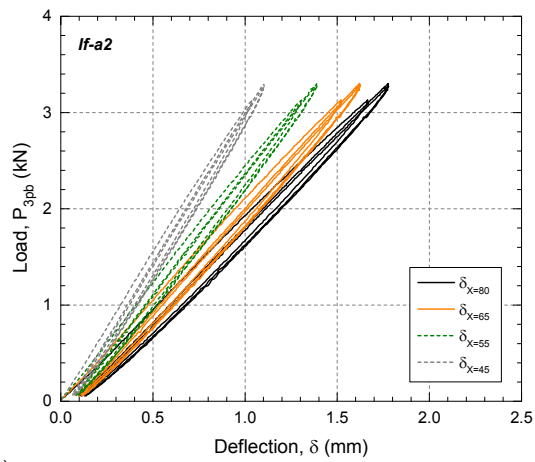
Figure D.10 – Load-deflection behavior of specimens (a) *If-o1*, (b) *If-o2* and (c) *If-o3*.

If-a series

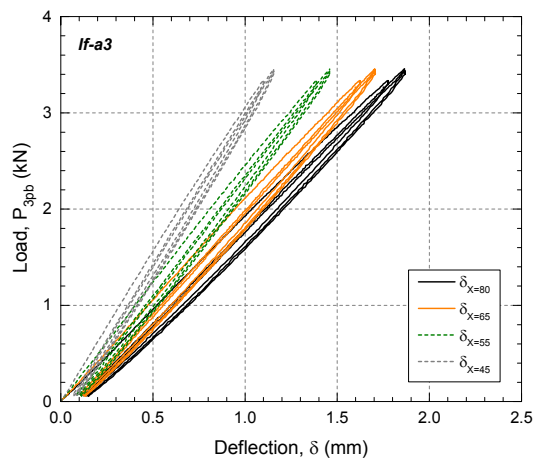
(a)



(b)

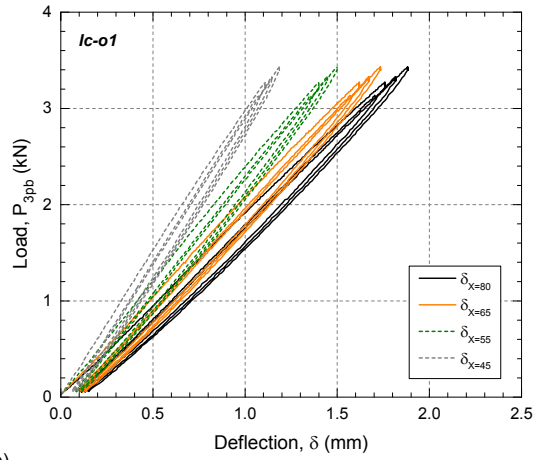


(c)

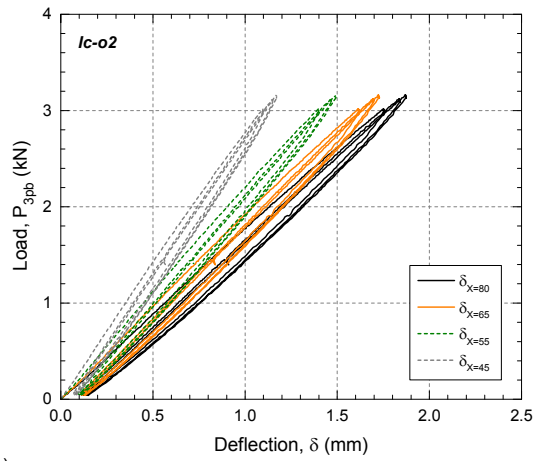
Figure D.11 – Load-deflection behavior of specimens (a) *If-a1*, (b) *If-a2* and (c) *If-a3*.

***lc-o* series**

(a)



(b)



(c)

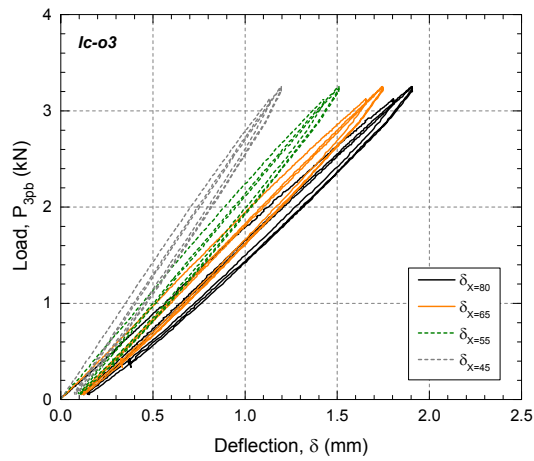
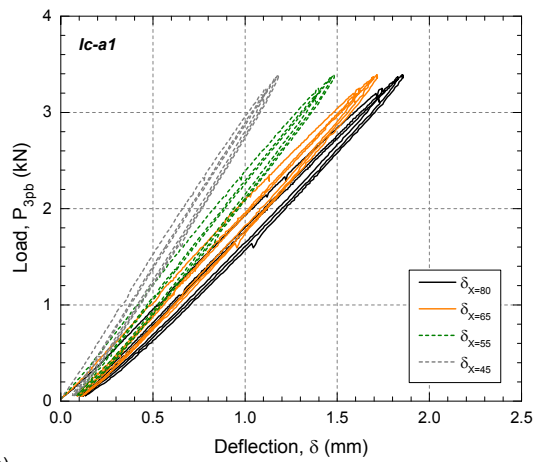


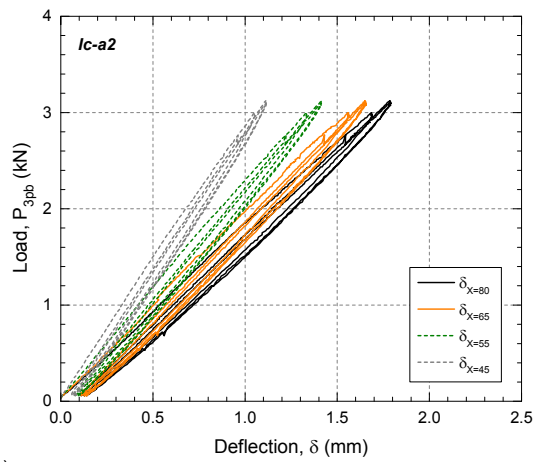
Figure D.12 – Load-deflection behavior of specimens (a) *lc-o1*, (b) *lc-o2* and (c) *lc-o3*.

lc-a series

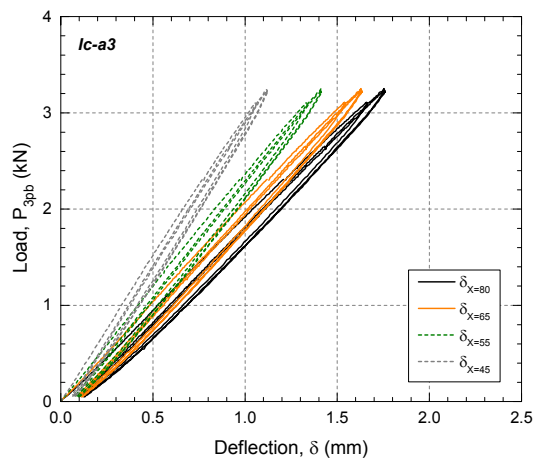
(a)



(b)

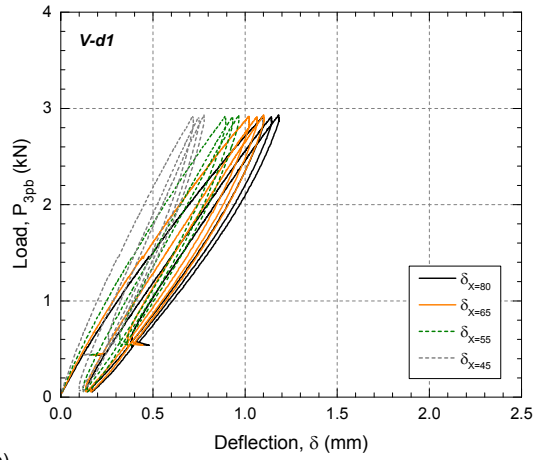


(c)

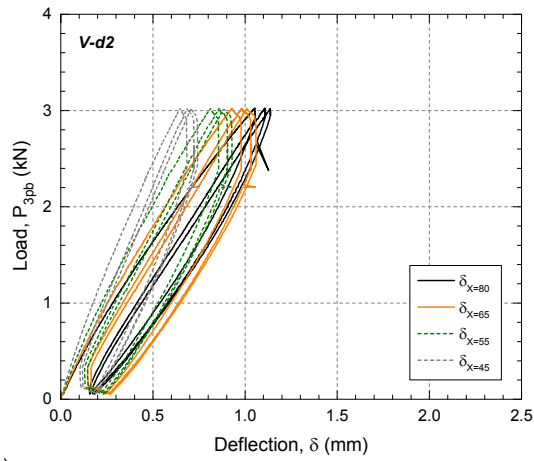
Figure D.13 – Load-deflection behavior of specimens (a) *lc-a1*, (b) *lc-a2* and (c) *lc-a3*.

V-d series

(a)



(b)



(c)

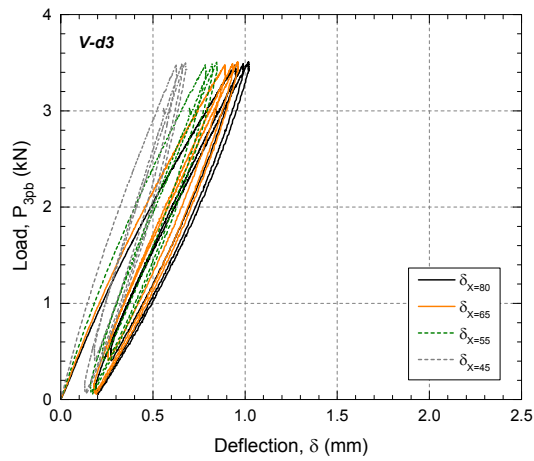
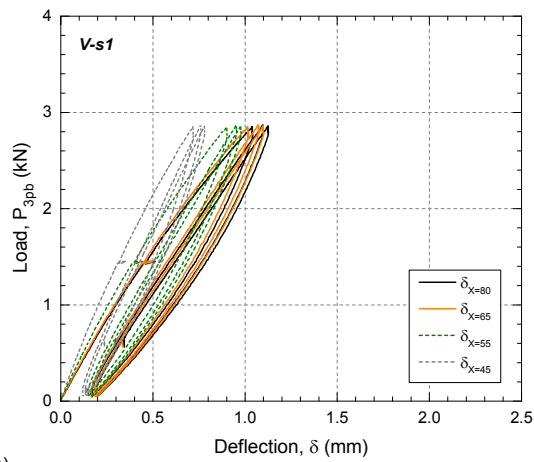


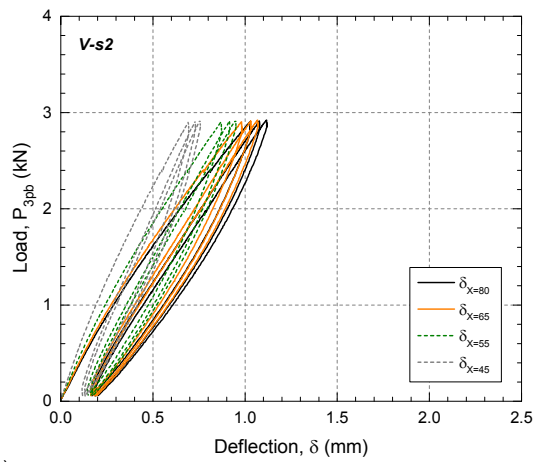
Figure D.14 – Load-deflection behavior of specimens (a) V-d1, (b) V-d2 and (c) V-d3.

V-s series

(a)



(b)



(c)

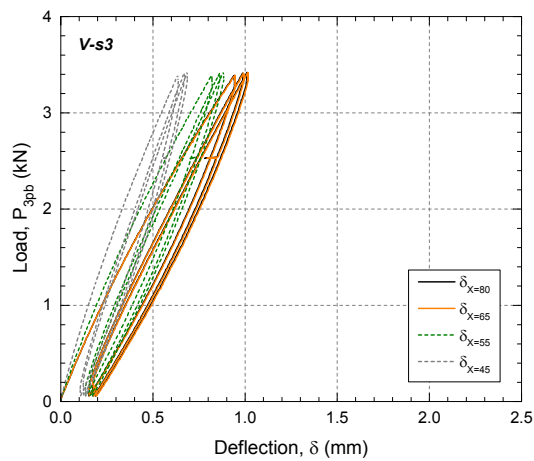
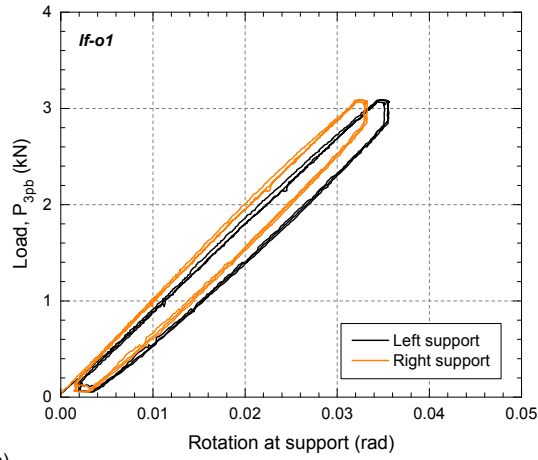


Figure D.15 – Load-deflection behavior of specimens (a) V-s1, (b) V-s2 and (c) V-s3.

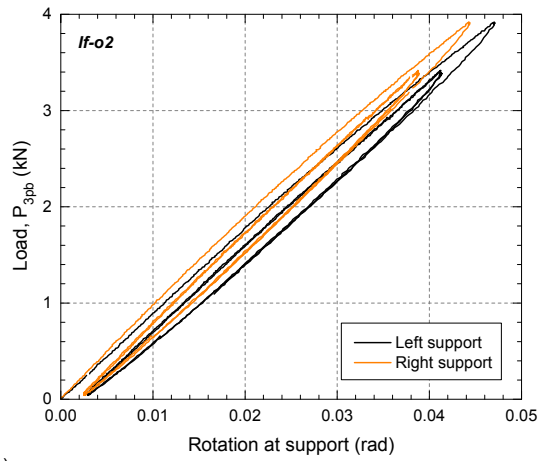
D.4 Rotation at supports

If-o series

(a)



(b)



(c)

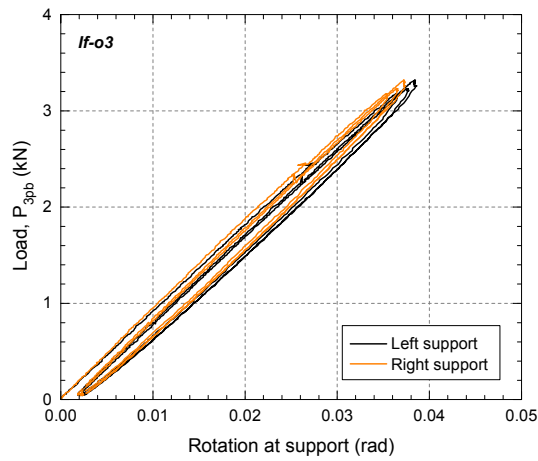
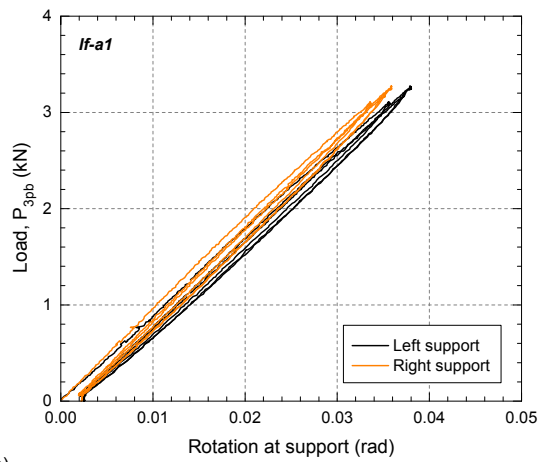


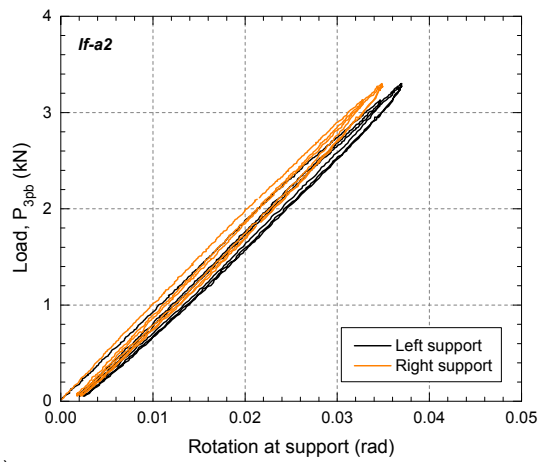
Figure D.16 – Rotation at supports of specimens (a) *If-o1*, (b) *If-o2* and (c) *If-o3*.

If-a series

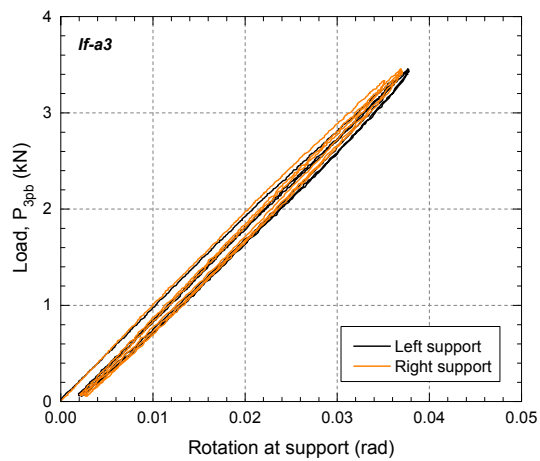
(a)



(b)

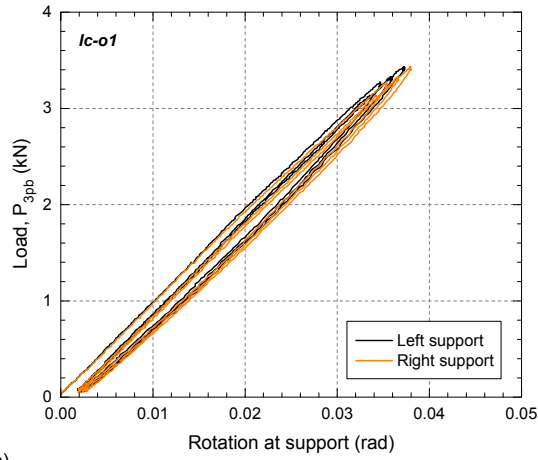


(c)

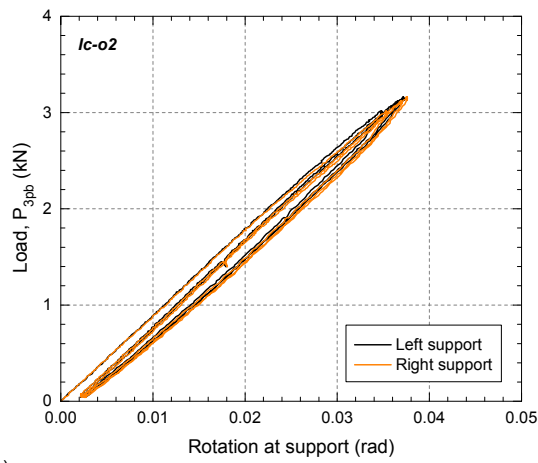
Figure D.17 – Rotation at supports of specimens (a) *If-a1*, (b) *If-a2* and (c) *If-a3*.

***lc-o* series**

(a)



(b)



(c)

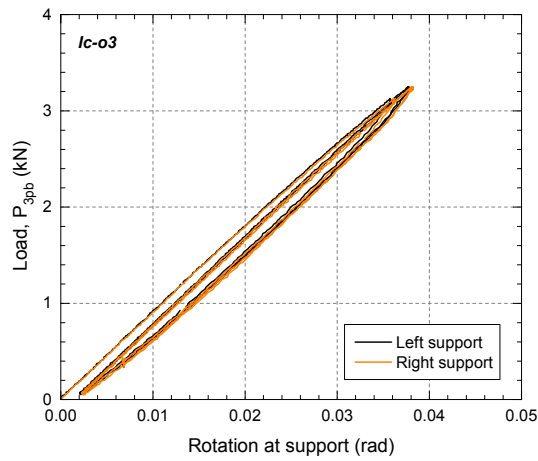
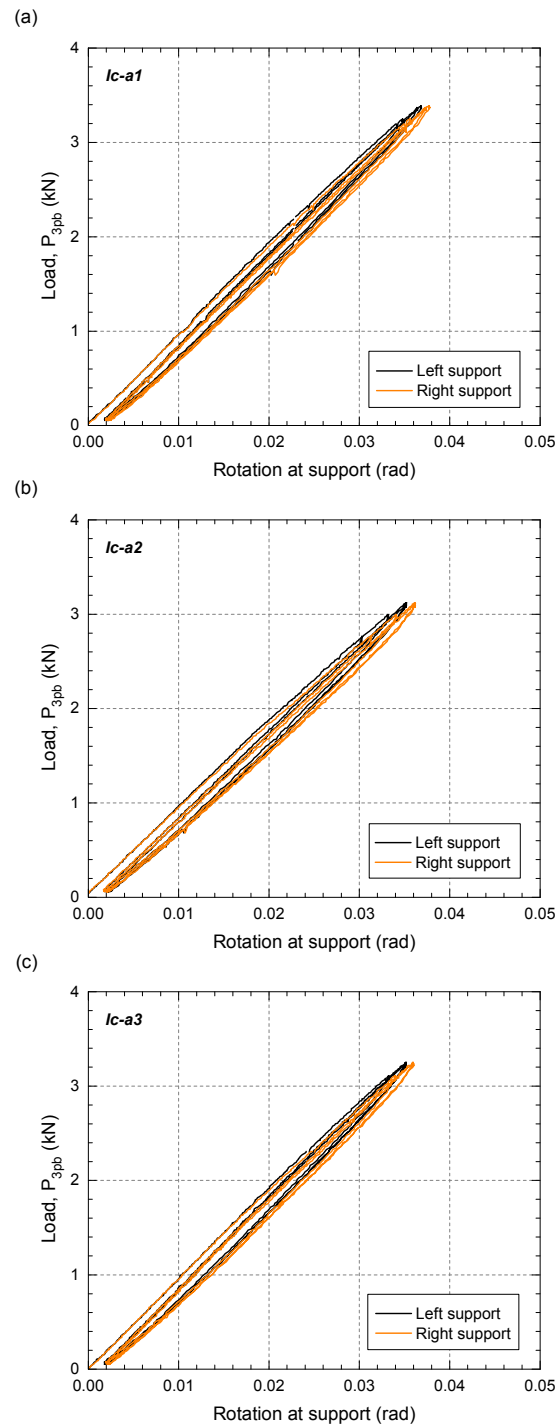
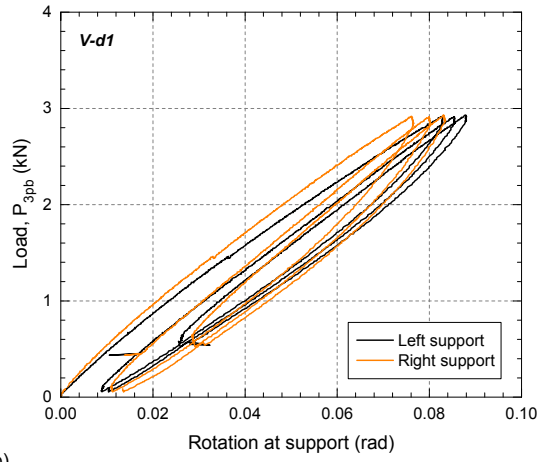


Figure D.18 – Rotation at supports of specimens (a) *lc-o1*, (b) *lc-o2* and (c) *lc-o3*.

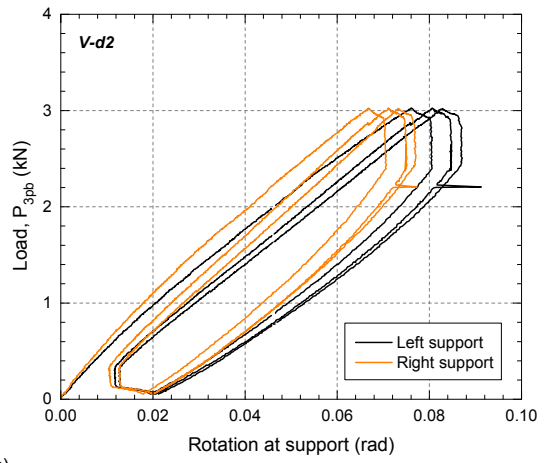
lc-a seriesFigure D.19 – Rotation at supports of specimens (a) *lc-a1*, (b) *lc-a2* and (c) *lc-a3*.

V-d series

(a)



(b)



(c)

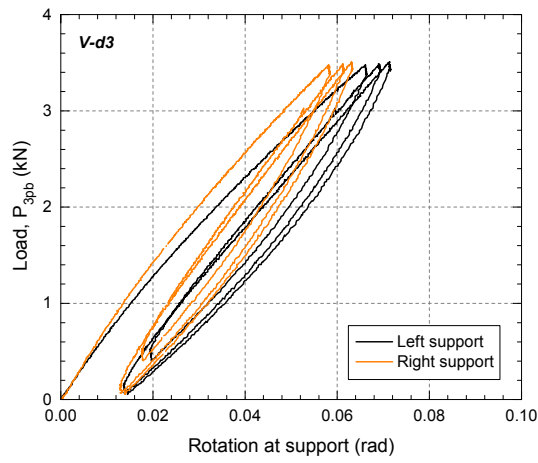
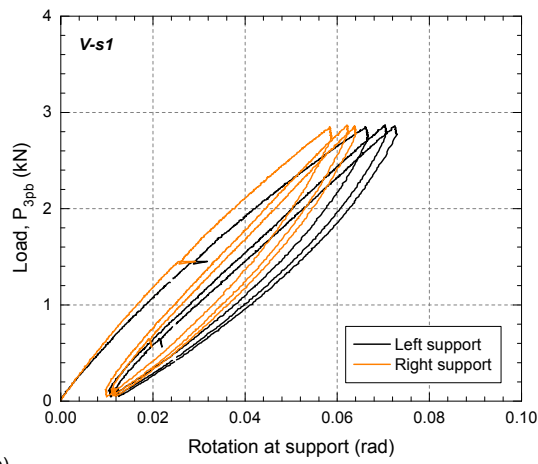


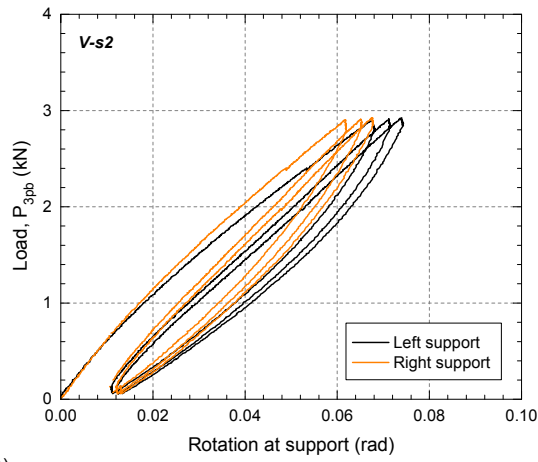
Figure D.20 – Rotation at supports of specimens (a) V-s1, (b) V-d2 and (c) V-d3.

V-s series

(a)



(b)



(c)

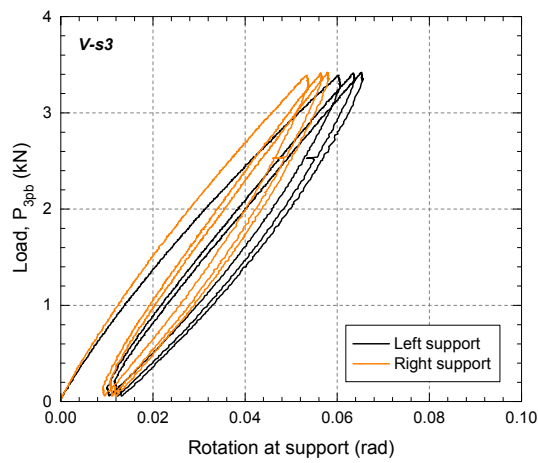


Figure D.21 – Rotation at supports of specimens (a) V-s1, (b) V-s2 and (c) V-s3.

D.5 Elastic flexural moduli

Series	Specimen	$E_{f,y}$ (MPa)
<i>If-o</i>	<i>If-o1</i>	17 150
	<i>If-o2</i>	18 360
	<i>If-o3</i>	17 870
	Mean	17 790±610 ^(a)
<i>If-a</i>	<i>If-a1</i>	17 770
	<i>If-a2</i>	17 470
	<i>If-a3</i>	18 110
	Mean	17 780±320 ^(a)
<i>Ic-o</i>	<i>Ic-o1</i>	17 960
	<i>Ic-o2</i>	16 850
	<i>Ic-o3</i>	17 450
	Mean	17 420±560 ^(a)
<i>Ic-a</i>	<i>Ic-a1</i>	17 730
	<i>Ic-a2</i>	17 060
	<i>Ic-a3</i>	17 460
	Mean	17 420±340 ^(a)
<i>V-d</i>	<i>V-d1</i>	13 370
	<i>V-d2</i>	13 810
	<i>V-d3</i>	16 700
	Mean	14 630±1 810 ^(a)
<i>V-s</i>	<i>V-s1</i>	14 660
	<i>V-s2</i>	14 190
	<i>V-s3</i>	16 120
	Mean	14 990±1 010 ^(a)

^(a) Standard deviation

Table D.2 – Calculated transverse elastic flexural moduli of web laminates.

Appendix E

DS web-flange junction cantilever experiments

E.1 Introduction

Appendix E presents supplementary results from the small-scale cantilever experiments conducted on the web-flange junctions (WFJs) of the *DS* deck and described in detail in Chapters 3 and 4. Based on these experiments, the energy dissipation capacity and recovery of two WFJ series (*If-o* and *Ic-o*) were studied in Chapter 3. In Chapter 4, the results of the WFJ cantilever experiments were conjointly used with those of web three-point bending experiments (see Appendix D) to characterize the rotational stiffness of the six WFJ types of the *DS* deck.

Within the framework of Chapter 4, the experimental program was performed on three 50-mm-wide specimens from each WFJ series (*If-o*, *If-a*, *Ic-o*, *Ic-a*, *V-d*, *V-s*). The specimens' geometry, global dimensions and location within the *DS* deck are shown in Figure E.1. Table E.1 lists the detailed width (b) and thickness (t_w) dimensions of the specimens' web components. For the study conducted in Chapter 3, five additional *Ic-o* specimens were used.

The webs of the WFJ specimens were subjected to bending in a cantilever configuration with a 65-mm lever arm. The experimental set-up is illustrated in Figure E.2. A video extensometer was used to measure the vertical deflections and rotations of the web and flange components; the arrangement of the target points monitored for that purpose is illustrated in Figure E.3.

In the following, the measured load-deflection responses and observed crack patterns are presented for all specimens. The average deflections at a given locations (see X in Figure E.3) are shown. Corresponding to the investigation conducted in Chapter 4, the experimental peak loads and corresponding displacement, the calculated flexural strength of the WFJs and the moment-rotation behavior of all specimens are also presented, see Tables E.2 and E.3.

Figure E.1 – (a) WFJ specimens; (b) location of WFJ specimens within DS deck panel when subjected to transverse bending (local bending moments in webs are shown); dimensions in mm.

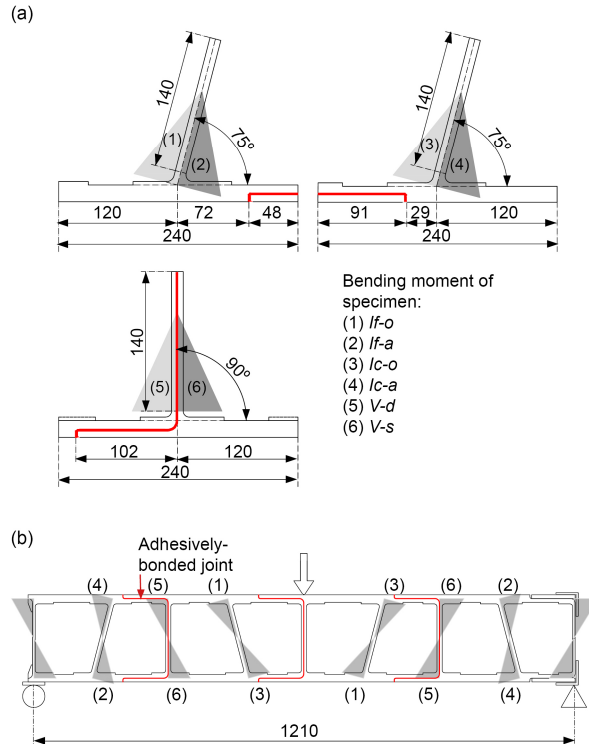
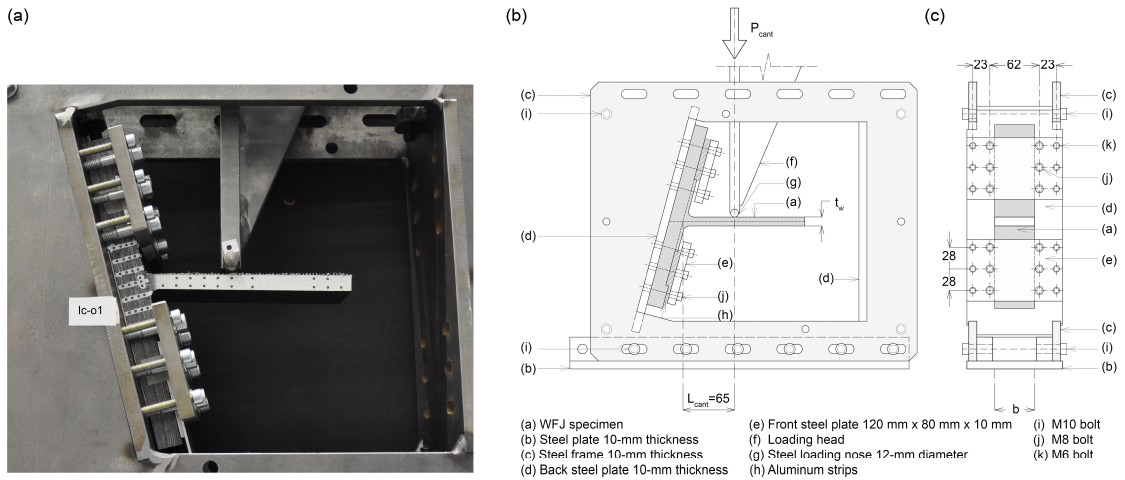


Table E.1 – Dimensions of WFJ specimens.

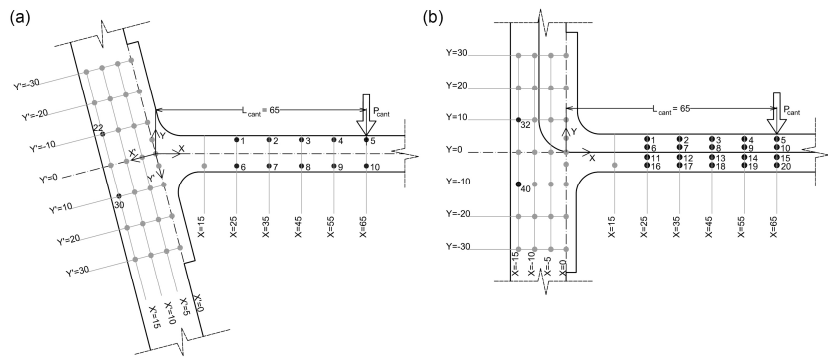
Series	Specimen	Web width <i>b</i> (mm)	Web thickness <i>t_w</i> (mm)
<i>If-o</i>	<i>If-o1</i>	49.4	11.4
	<i>If-o2</i>	49.6	11.4
	<i>If-o3</i>	49.3	11.5
	Mean	49.4±0.2 ^(a)	11.4±0.1 ^(a)
<i>If-a</i>	<i>If-a1</i>	50.2	11.4
	<i>If-a2</i>	51.3	11.4
	<i>If-a3</i>	49.9	11.5
	Mean	50.5±0.7 ^(a)	11.4±0.1 ^(a)
<i>Ic-o</i>	<i>Ic-o1</i>	51.4	11.4
	<i>Ic-o2</i>	49.2	11.4
	<i>Ic-o3</i>	49.6	11.4
	Mean	50.1±1.2 ^(a)	11.4±0.0 ^(a)
<i>Ic-a</i>	<i>Ic-a1</i>	50.6	11.4
	<i>Ic-a2</i>	50.0	11.4
	<i>Ic-a3</i>	51.1	11.4
	Mean	50.6±0.6 ^(a)	11.4±0.0 ^(a)
<i>V-d</i>	<i>V-d1</i>	50.0	12.6
	<i>V-d2</i>	51.4	12.6
	<i>V-d3</i>	49.4	12.5
	Mean	50.3±1.0 ^(a)	12.6±0.1 ^(a)
<i>V-s</i>	<i>V-s1</i>	50.1	12.3
	<i>V-s2</i>	51.3	12.3
	<i>V-s3</i>	49.9	12.5
	Mean	50.4±0.8 ^(a)	12.4±0.1 ^(a)

^(a) Standard deviation



^ Figure E.2 – Set-up for cantilever experiments; (a) general view (*Ic-o* specimen); (b) front view (*Ic-a* specimen); (c) cross section; dimensions in mm.

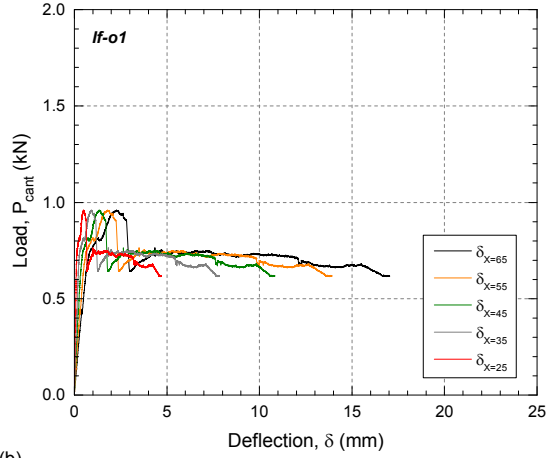
> Figure E.3 – Video extensometer target arrangement for cantilever experiments in (a) *I* specimens and (b) *V* specimens; dimensions in mm.



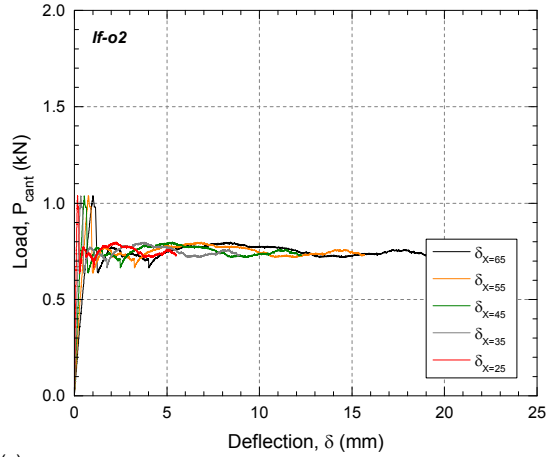
E.2 Load-deflection curves

If-o series

(a)



(b)



(c)

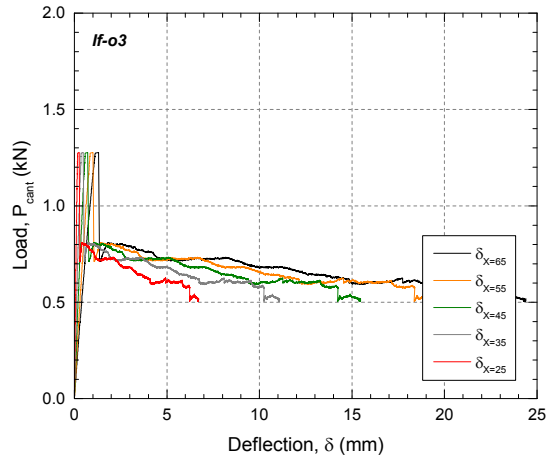
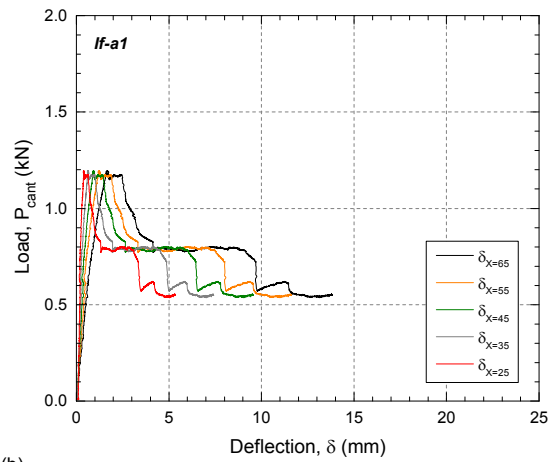


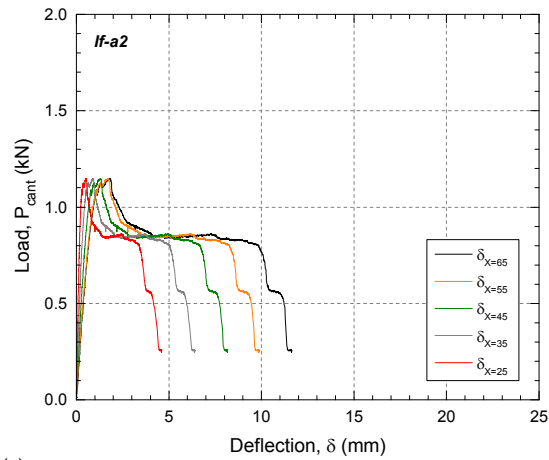
Figure E.4 – Load-deflection behavior of specimens (a) *If-o1*, (b) *If-o2* and (c) *If-o3*.

If-a series

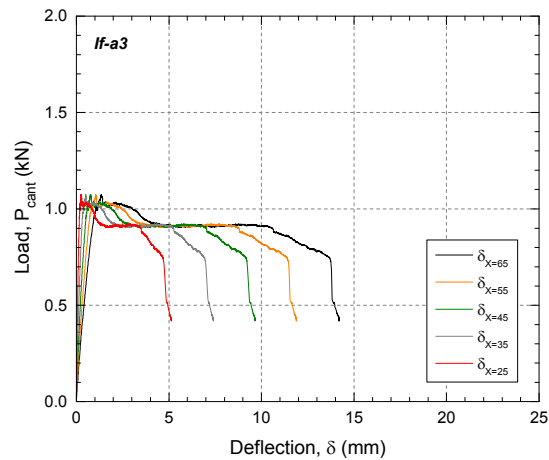
(a)



(b)

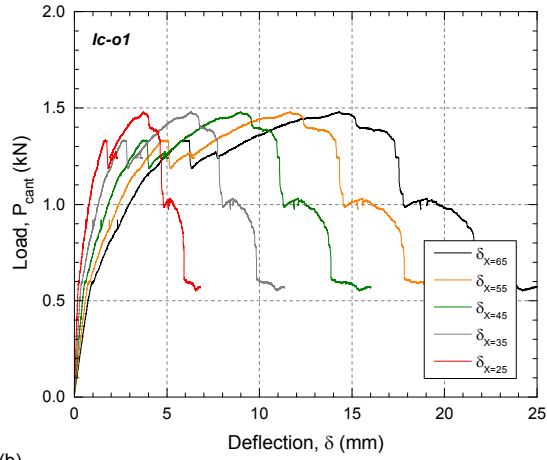


(c)

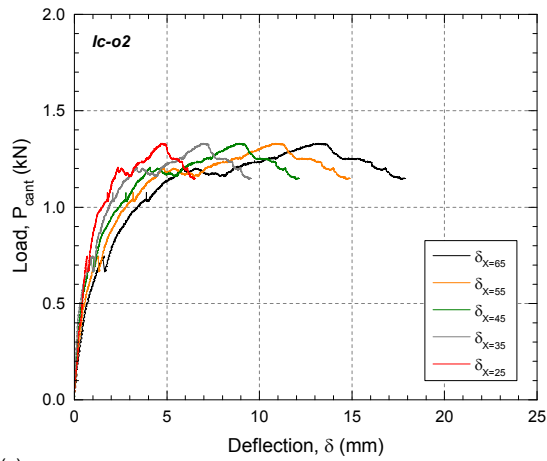
Figure E.5 – Load-deflection behavior of specimens (a) *If-a1*, (b) *If-a2* and (c) *If-a3*.

lc-o series

(a)



(b)



(c)

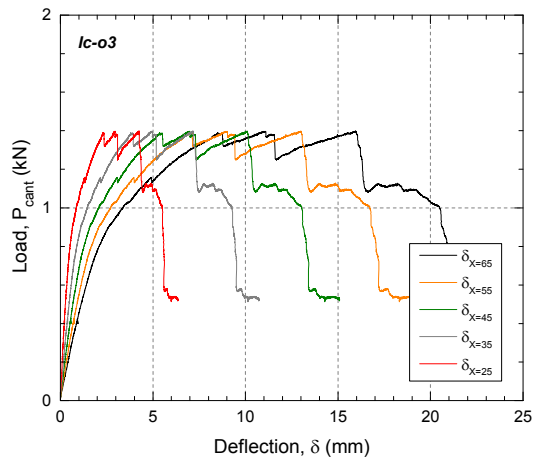
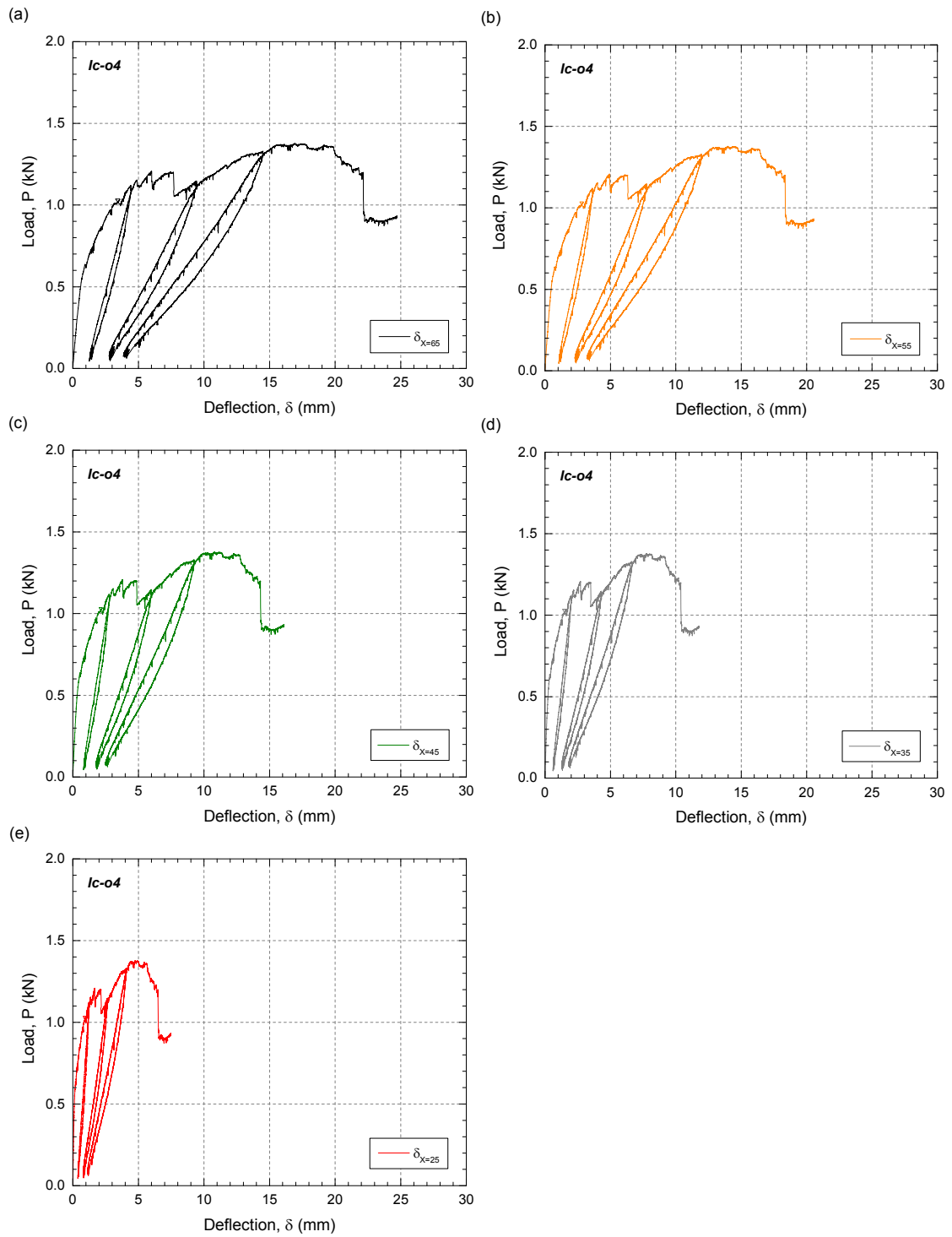
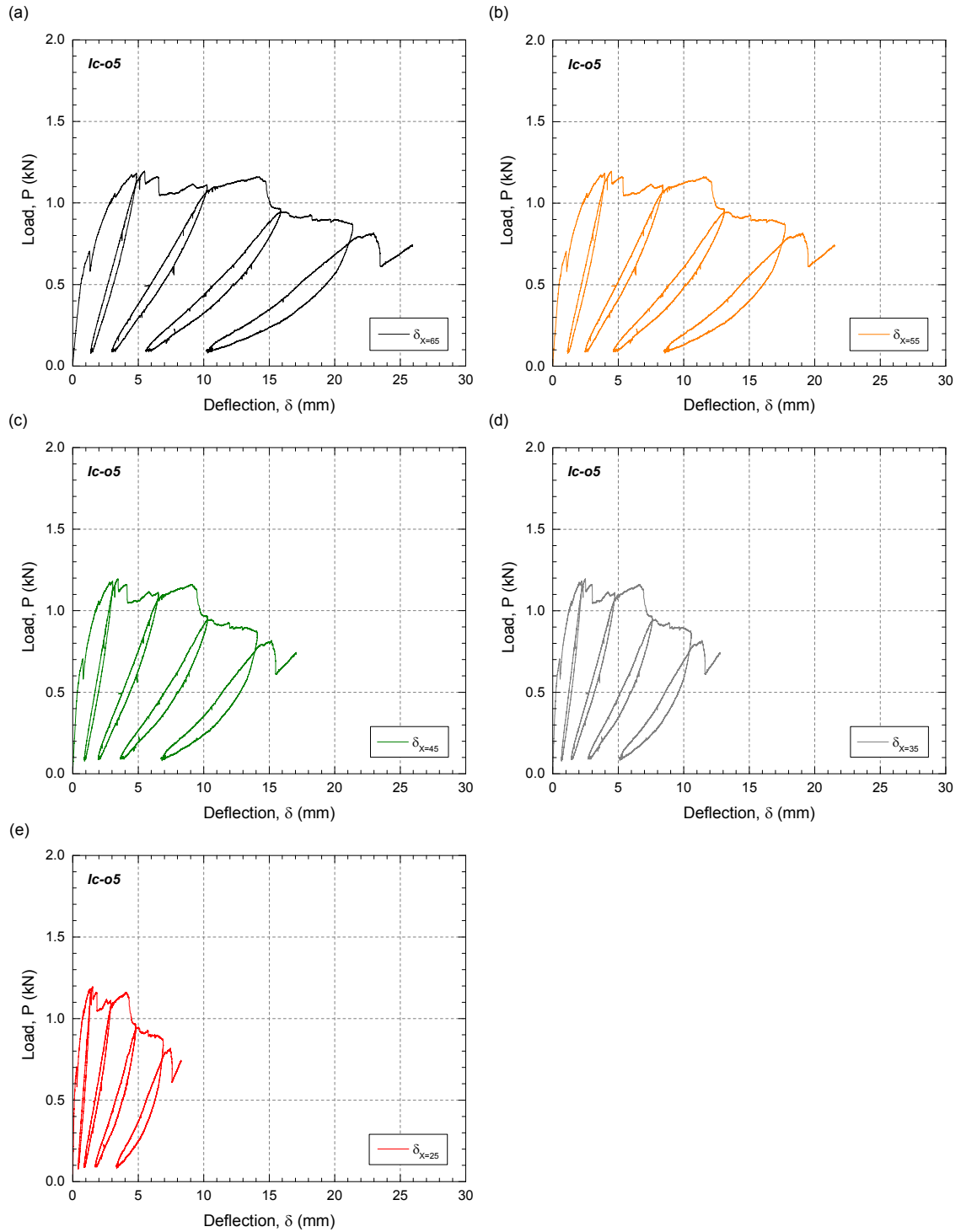
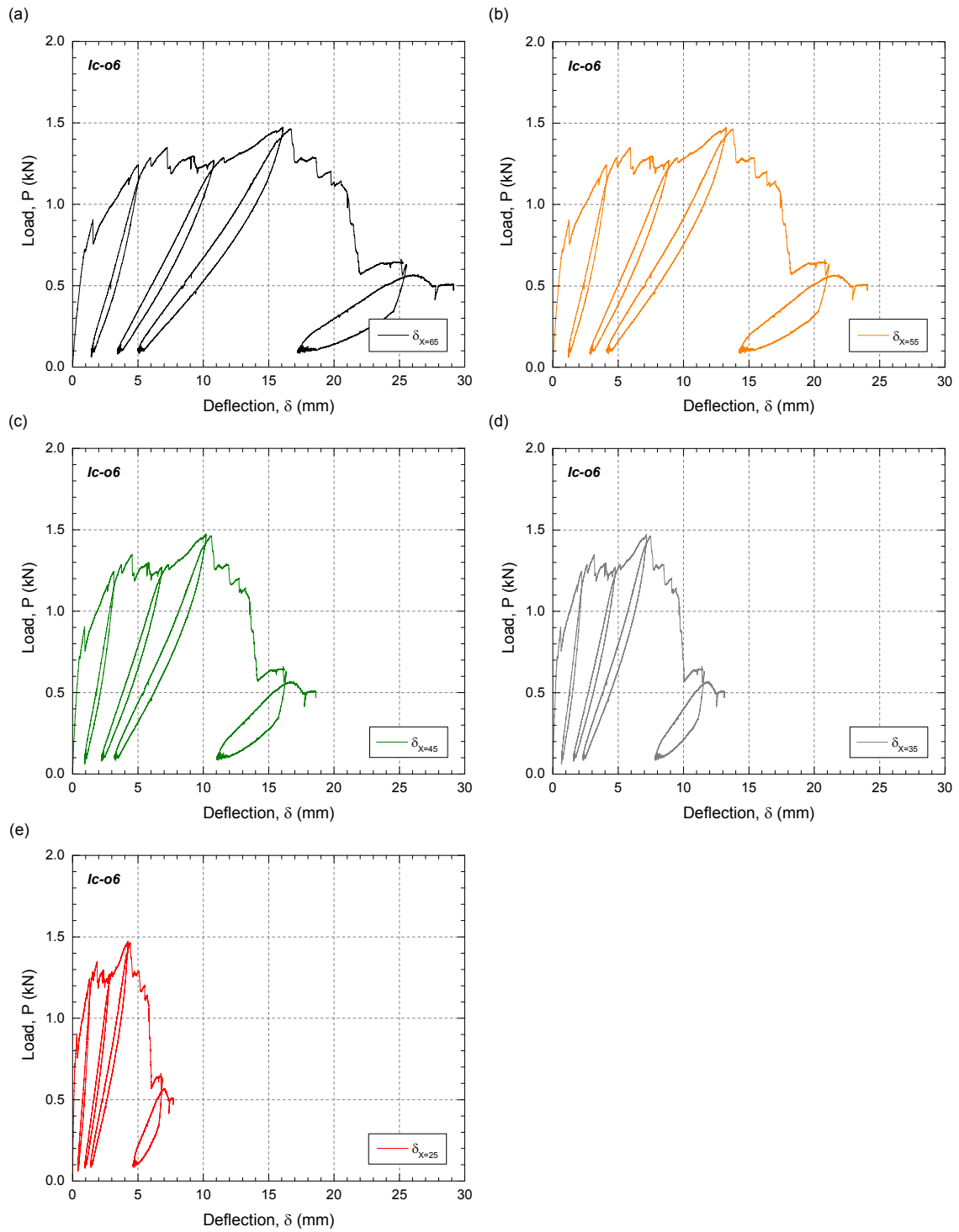


Figure E.6 – Load-deflection behavior of specimens (a) *lc-o1*, (b) *lc-o2* and (c) *lc-o3*.

Figure E.7 – Load-deflection behavior of specimen *Ic-04*.

Figure E.8 – Load-deflection behavior of specimen *lc-o5*.

Figure E.9 – Load-deflection behavior of specimen *Ic-06*.

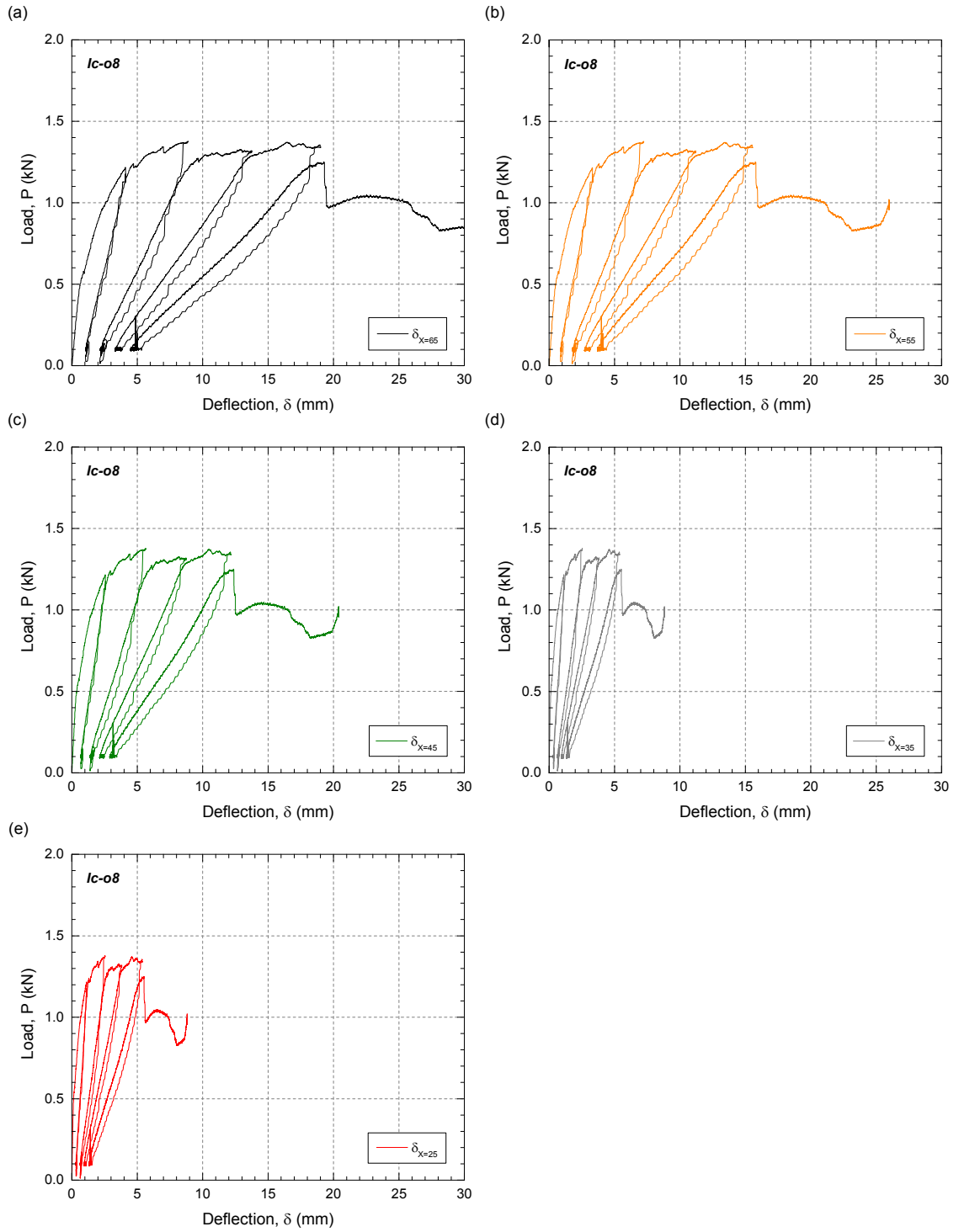
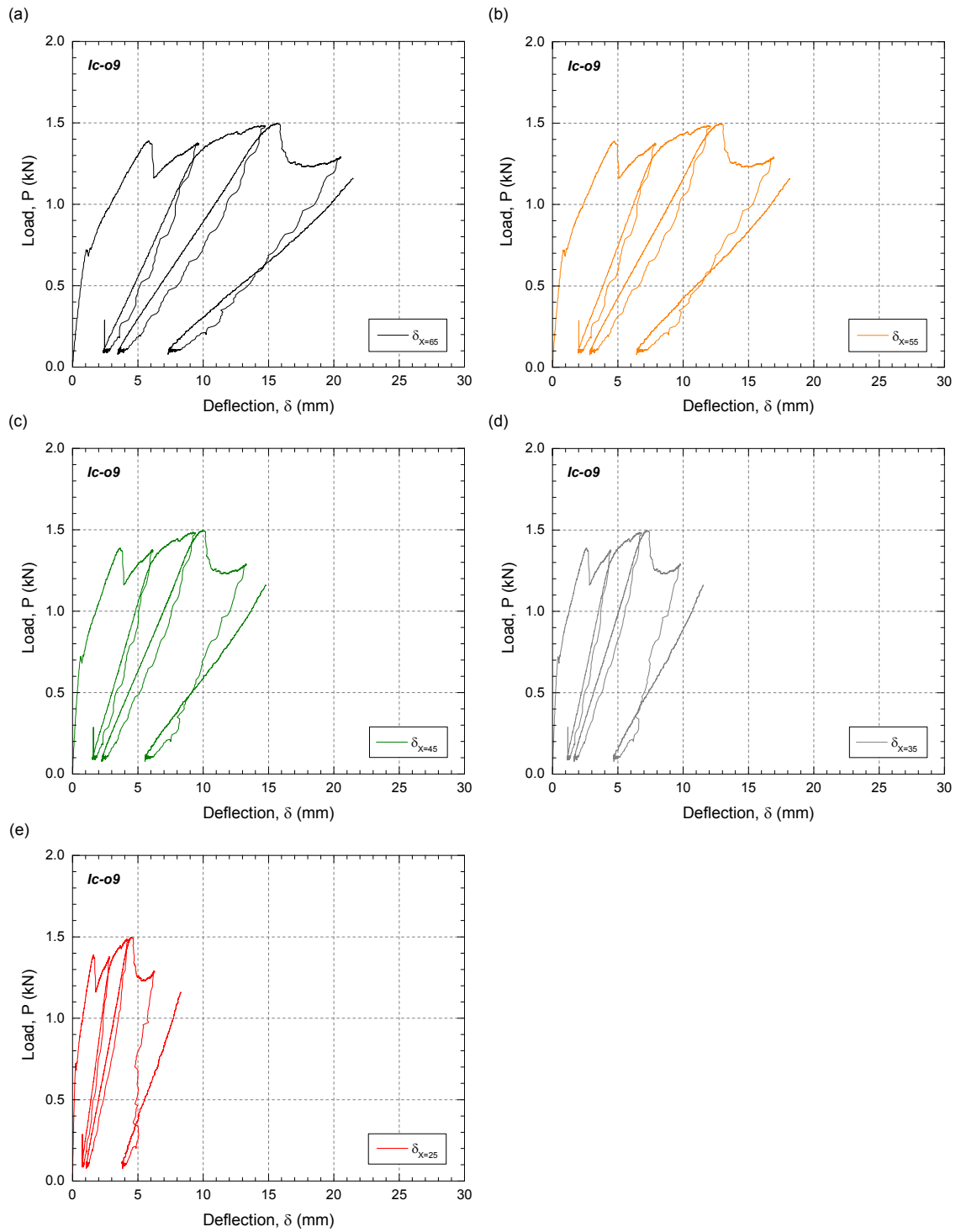
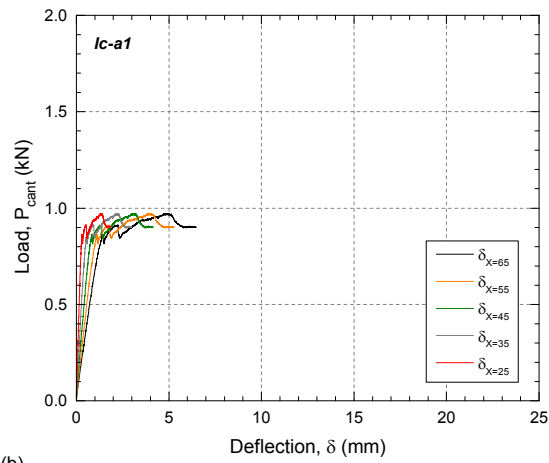


Figure E.10 – Load-deflection behavior of specimen *lc-08*.

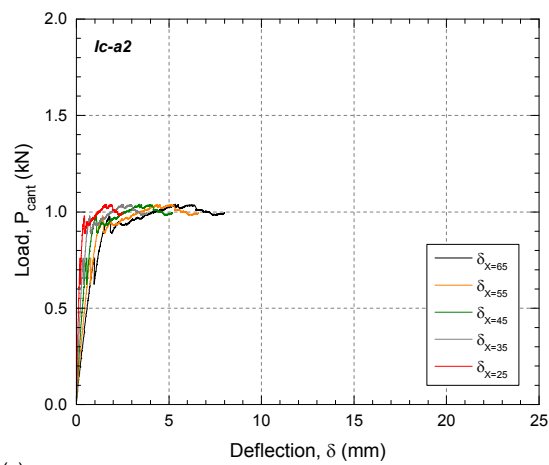
Figure E.11 – Load-deflection behavior of specimen *Ic-09*.

lc-a series

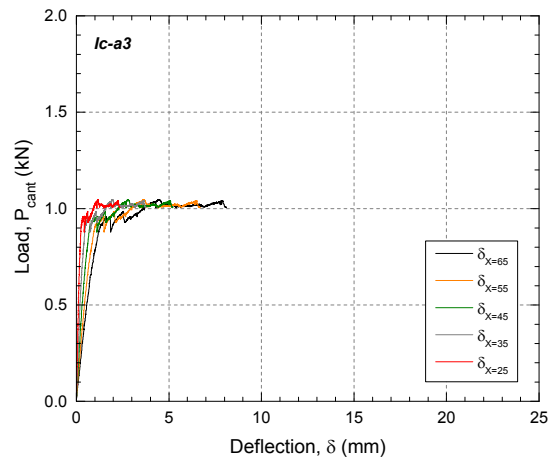
(a)



(b)

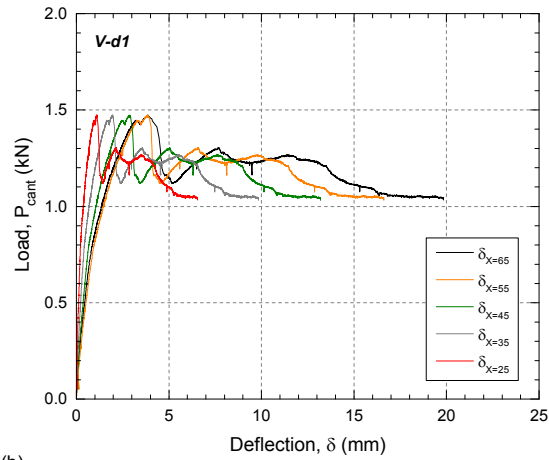


(c)

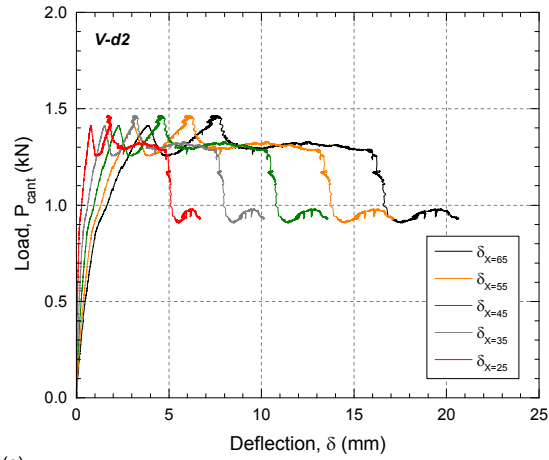
Figure E.12 – Load-deflection behavior of specimens (a) *lc-a1*, (b) *lc-a2* and (c) *lc-a3*.

V-d series

(a)



(b)



(c)

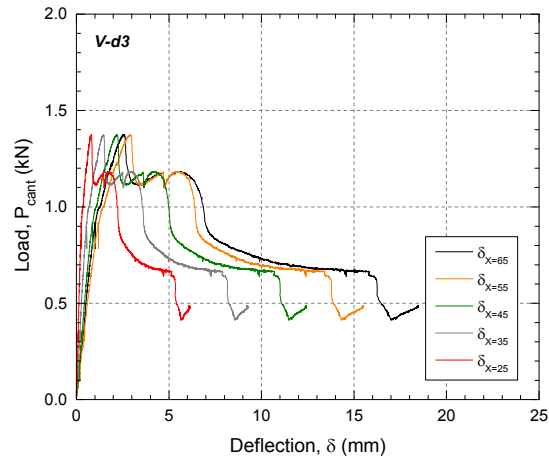
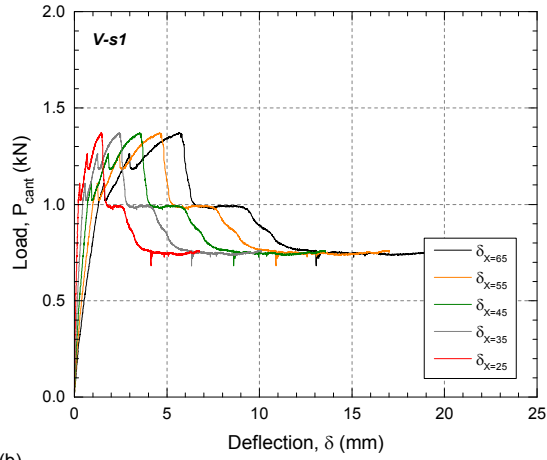


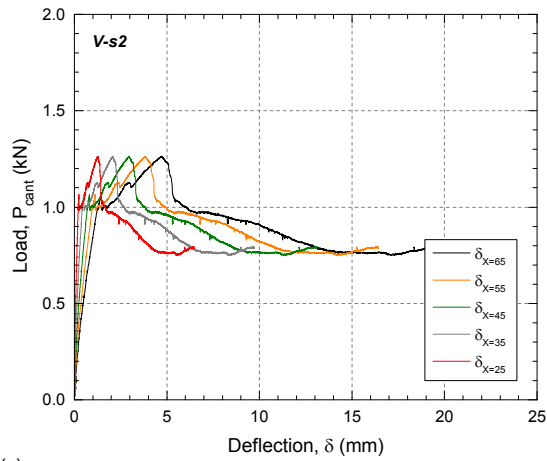
Figure E.13 – Load-deflection behavior of specimens (a) V-d1, (b) V-d2 and (c) V-d3.

V-s series

(a)



(b)



(c)

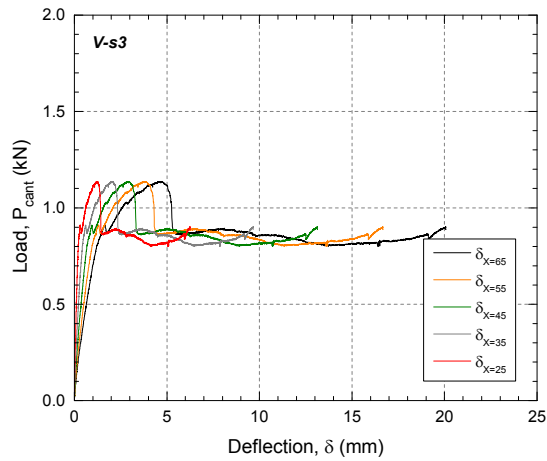


Figure E.14 – Load-deflection behavior of specimens (a) V-s1, (b) V-s2 and (c) V-s3.

E.3 Peak loads, corresponding displacements and flexural strength

Series	Specimen	P_{ult} (kN)	δ_{ult} (mm)	P_{ult}/b (N/mm)	σ_f (MPa)
<i>If-o</i>	<i>If-o1</i>	0.96	2.8	19.5	55.4
	<i>If-o2</i>	1.05	1.1	21.1	59.9
	<i>If-o3</i>	1.28	1.3	25.9	72.1
	Mean		1.7±0.9 ^(a)	22.2±3.3 ^(a)	62.5±8.7 ^(a)
<i>If-a</i>	<i>If-a1</i>	1.20	1.6	23.8	67.5
	<i>If-a2</i>	1.15	1.8	22.4	63.4
	<i>If-a3</i>	1.08	1.6	21.5	60.0
	Mean		1.6±0.1 ^(a)	22.6±1.2 ^(a)	63.6±3.8 ^(a)
<i>Ic-o</i>	<i>Ic-o1</i>	1.48	14.3	28.8	81.6
	<i>Ic-o2</i>	1.33	13.2	27.1	76.7
	<i>Ic-o3</i>	1.40	15.9	28.2	79.9
	Mean		14.5±1.4 ^(a)	28.0±0.9 ^(a)	79.4±2.5 ^(a)
<i>Ic-a</i>	<i>Ic-a1</i>	0.97	4.9	19.2	54.4
	<i>Ic-a2</i>	1.04	5.3	20.8	58.9
	<i>Ic-a3</i>	1.05	4.4	20.5	58.1
	Mean		4.9±0.5 ^(a)	20.2±0.8 ^(a)	57.1±2.4 ^(a)
<i>V-d</i>	<i>V-d1</i>	1.47	3.8	29.5	68.5
	<i>V-d2</i>	1.47	7.4	28.5	66.3
	<i>V-d3</i>	1.38	2.6	27.8	65.7
	Mean		4.6±2.5 ^(a)	28.6±0.8 ^(a)	66.8±1.4 ^(a)
<i>V-s</i>	<i>V-s1</i>	1.37	5.7	27.4	66.7
	<i>V-s2</i>	1.26	4.7	24.6	60.0
	<i>V-s3</i>	1.14	4.6	22.8	53.8
	Mean		5.0±0.6 ^(a)	24.9±2.3 ^(a)	60.2±6.5 ^(a)

^(a) Standard deviation

Table E.2 – Experimental peak loads and corresponding displacements; calculated flexural strength of WFJs.

E.4 Crack patterns

If-o series

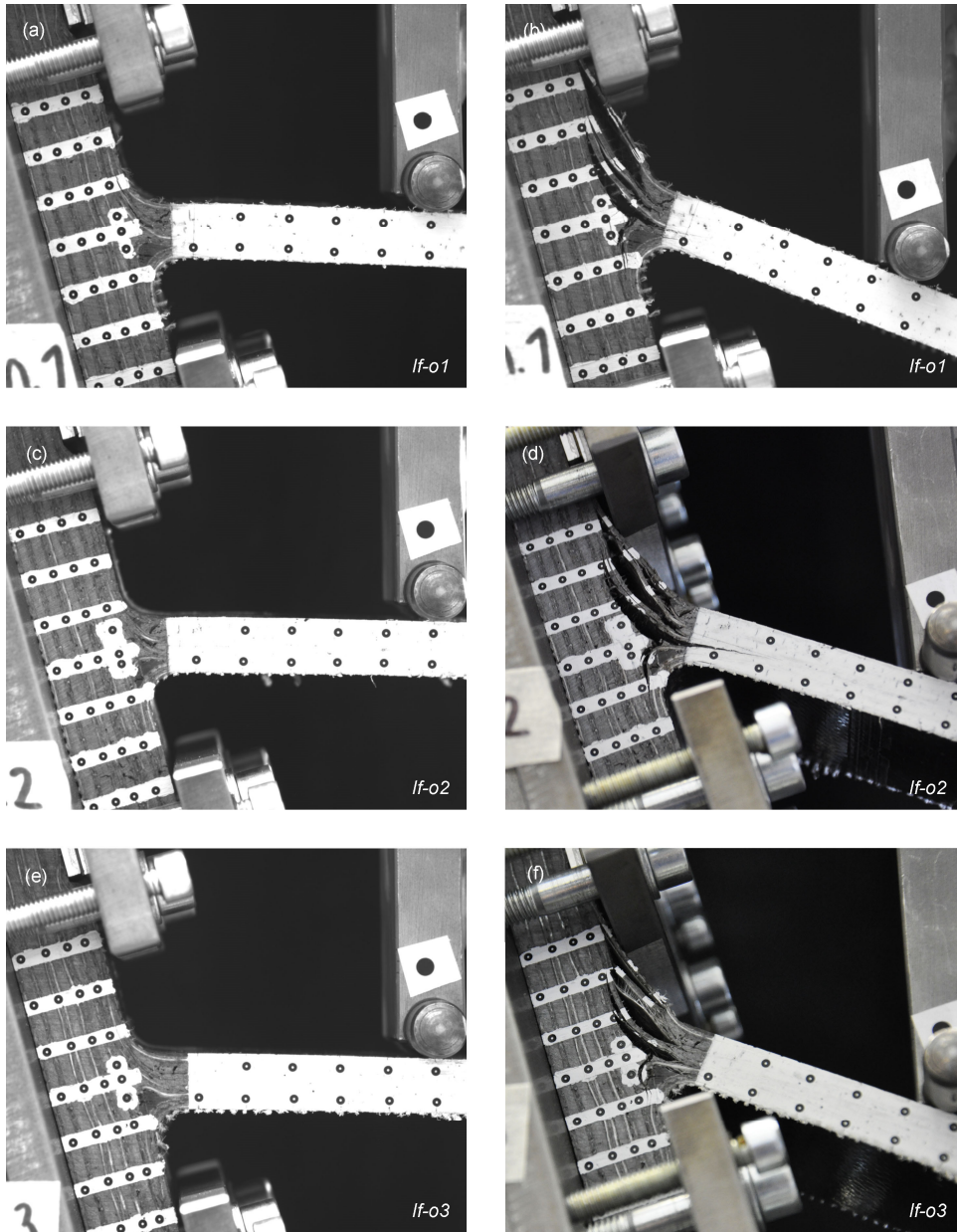


Figure E.15 – Crack pattern at peak load (a, c, e) and post-peak crack pattern (b, d, f) of *If-o* series.

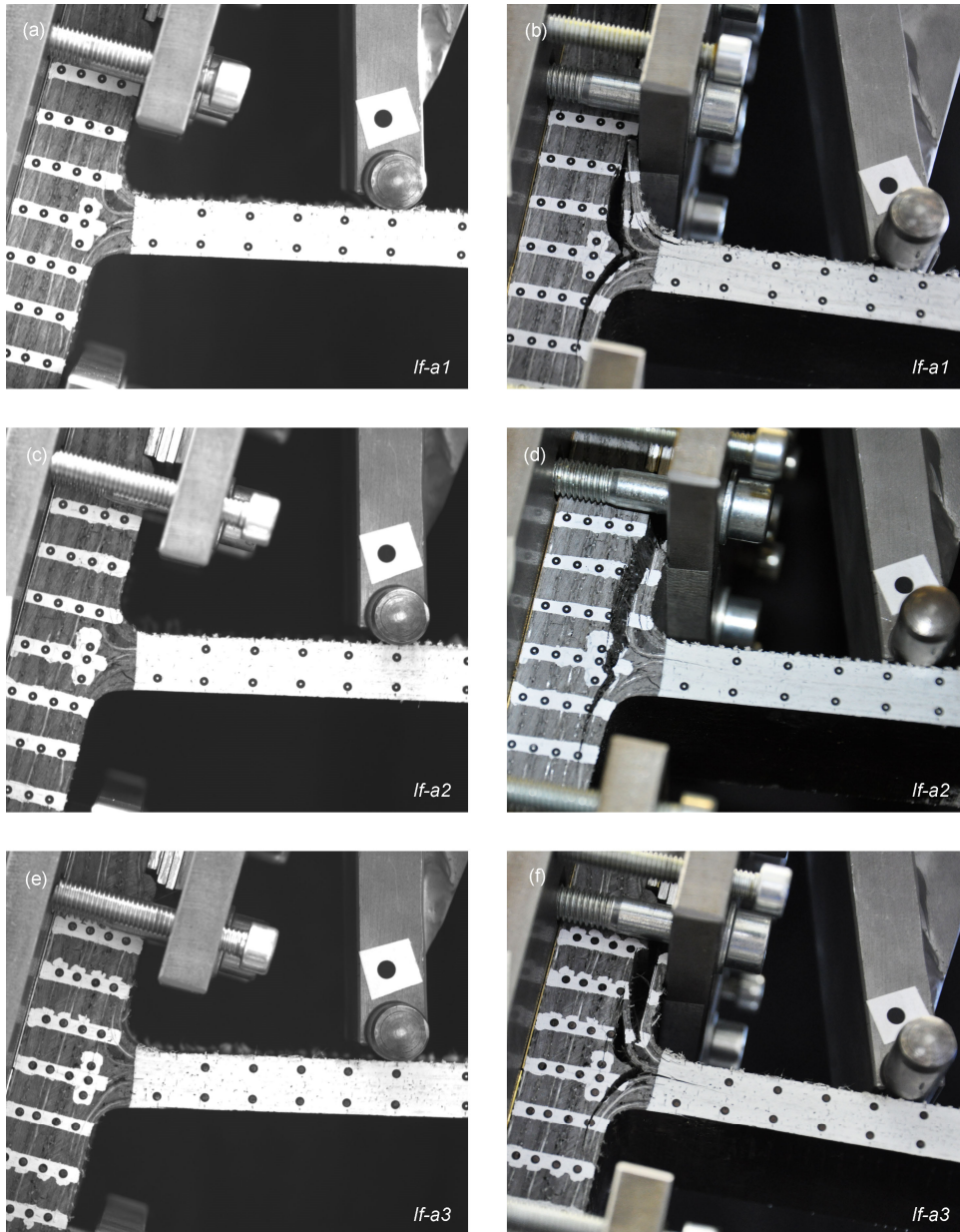
If-a series

Figure E.16 – Crack pattern at peak load (a, c, e) and post-peak crack pattern (b, d, f) of If-a series.

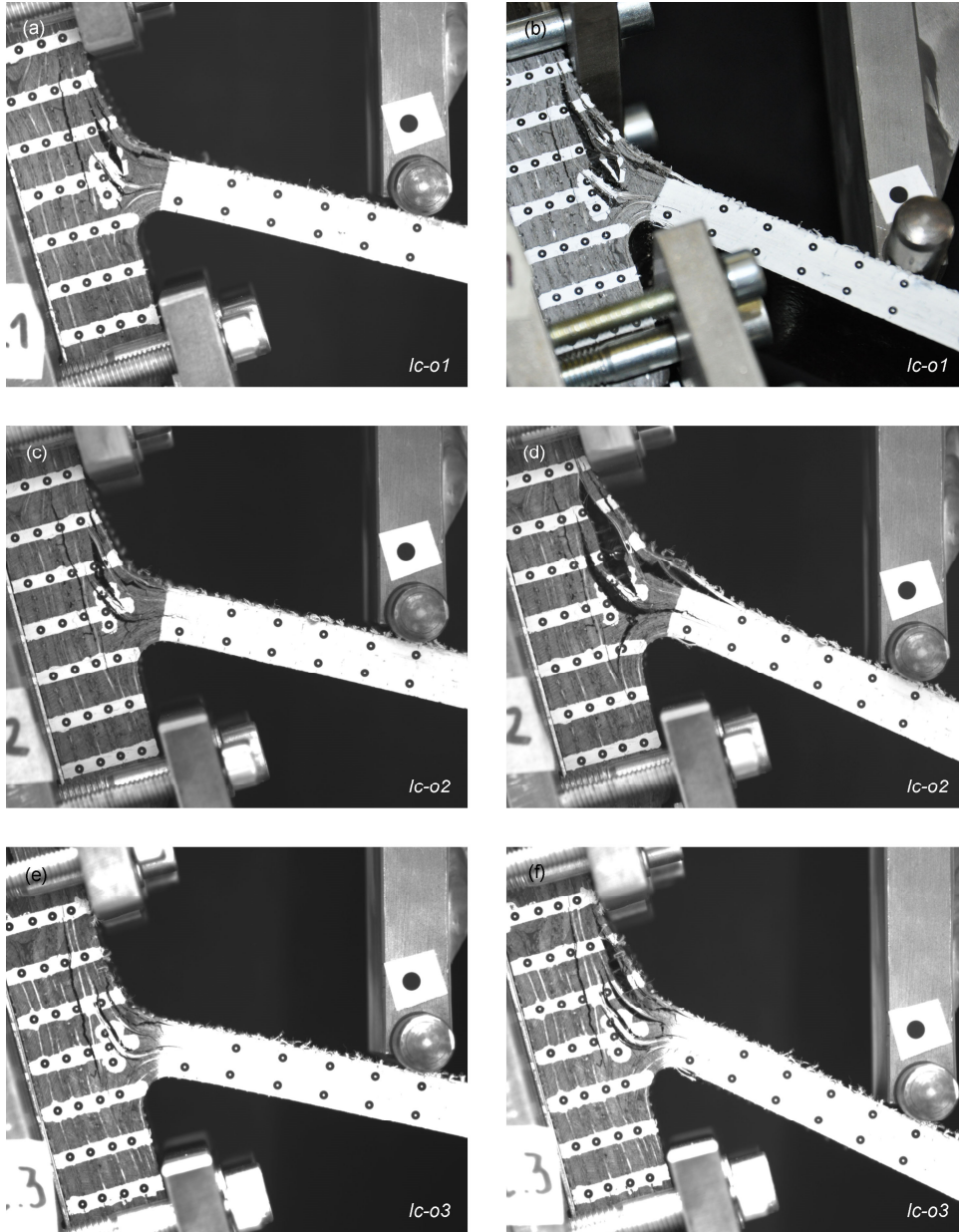
lc-o series

Figure E.17 – Crack pattern at peak load (a, c, e) and post-peak crack pattern (b, d, f) of specimens *lc-01*, *lc-02* and *lc-03*.

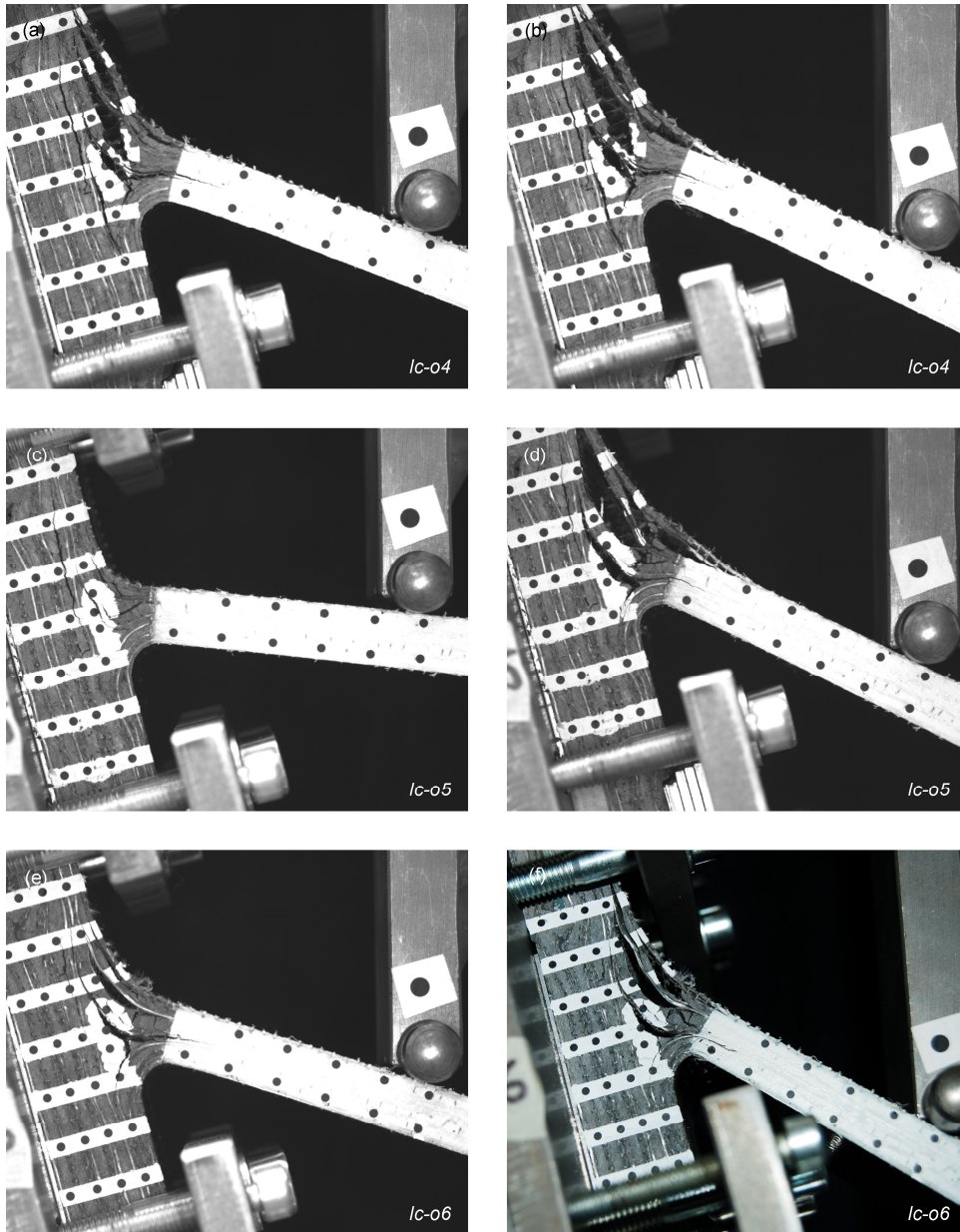


Figure E.18 – Crack pattern at peak load (a, c, e) and post-peak crack pattern (b, d, f) of specimens *lc-04*, *lc-05* and *lc-06*.

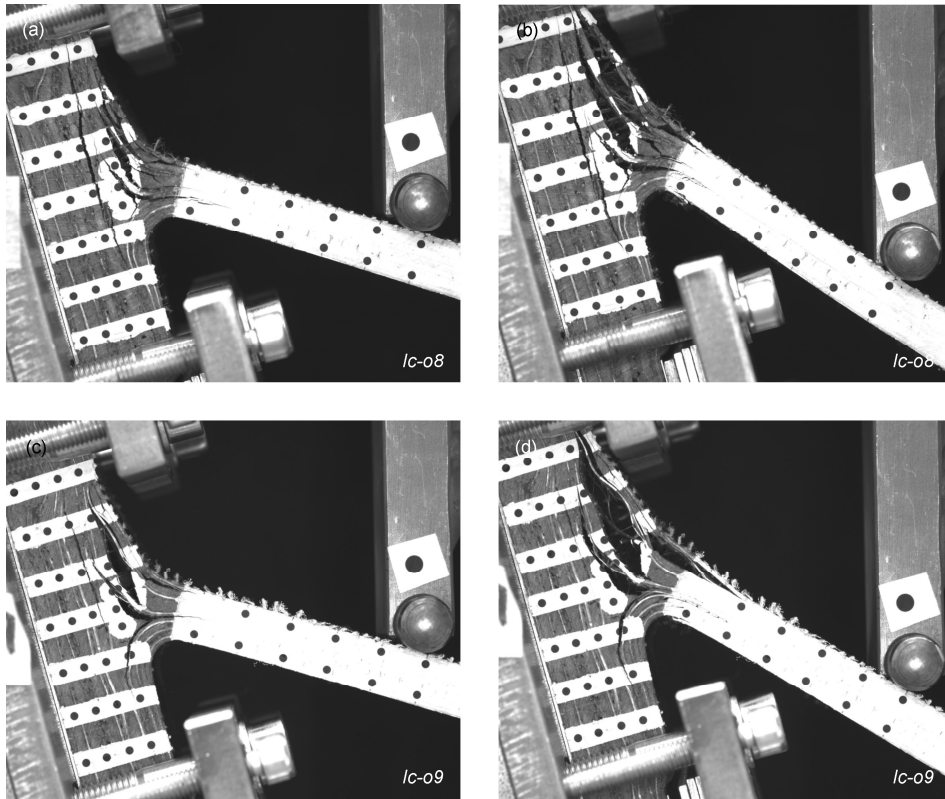


Figure E.19 – Crack pattern at peak load (a, c, e) and post-peak crack pattern (b, d, f) of specimens *Ic-08* and *Ic-09*.

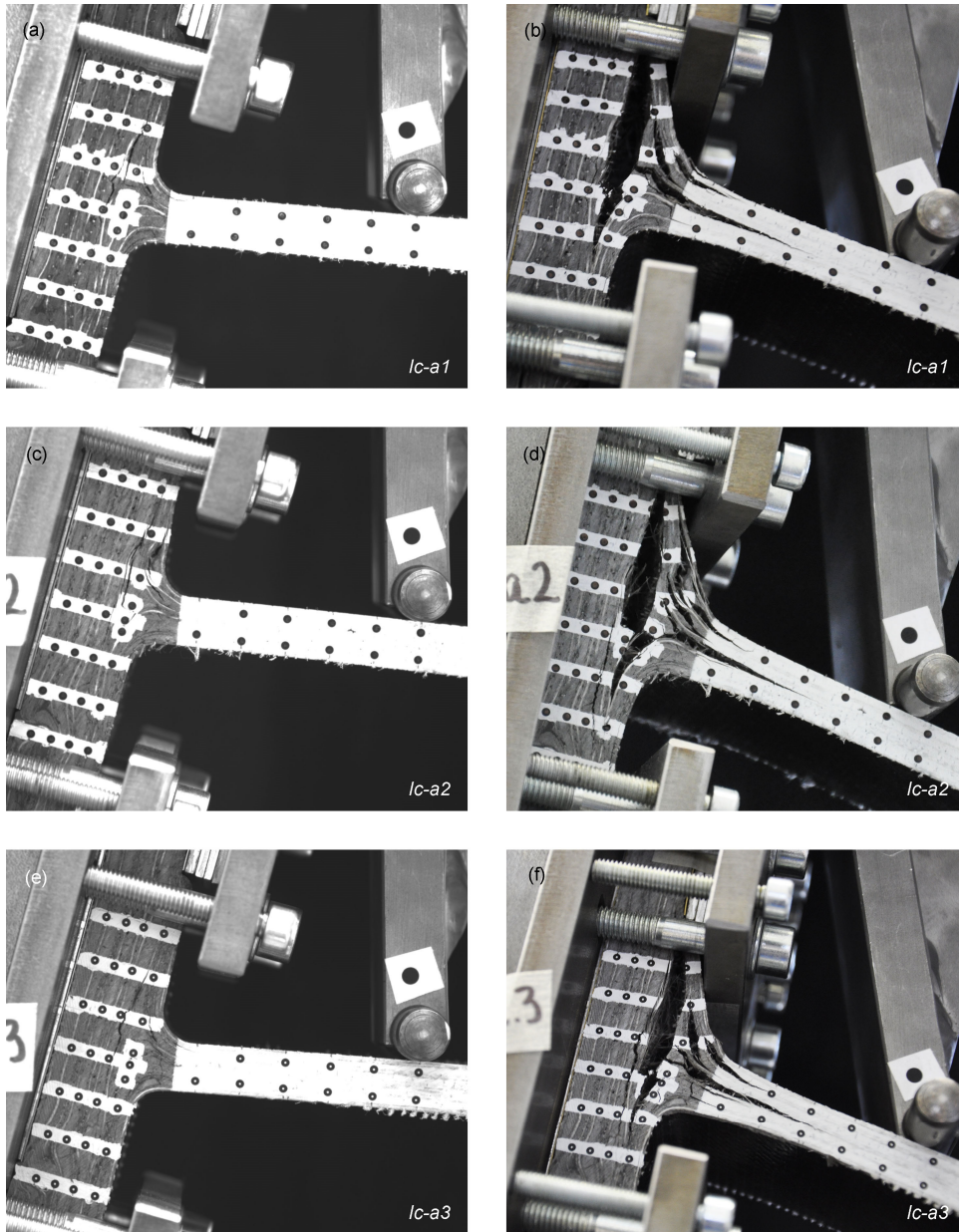
Ic-a series

Figure E.20 – Crack pattern at peak load (a, c, e) and post-peak crack pattern (b, d, f) of *Ic-a* series.

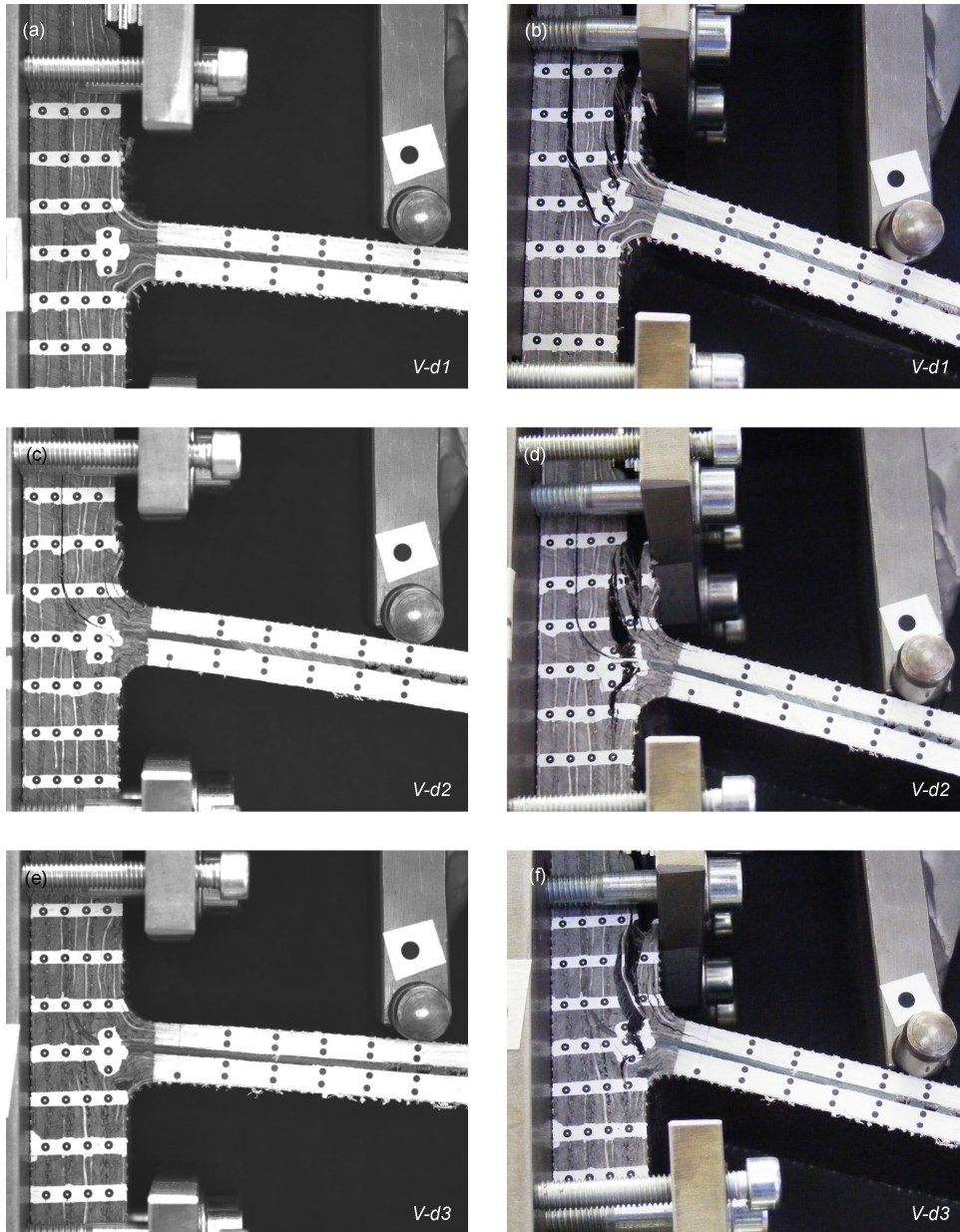
V-d series

Figure E.21 – Crack pattern at peak load (a, c, e) and post-peak crack pattern (b, d, f) of V-d series.

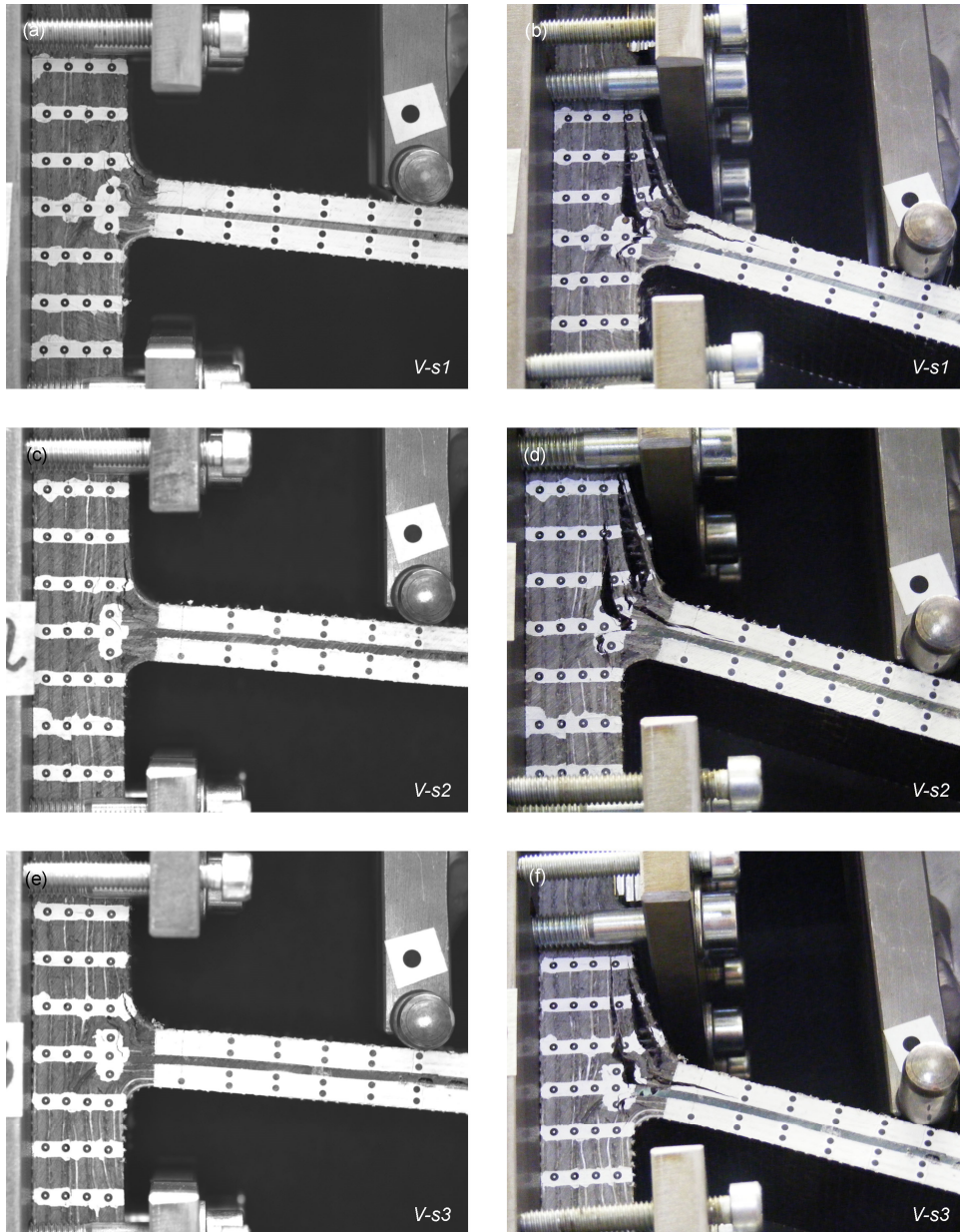
V-s series

Figure E.22 – Crack pattern at peak load (a, c, e) and post-peak crack pattern (b, d, f) of V-s series.

E.5 Moment-rotation behavior

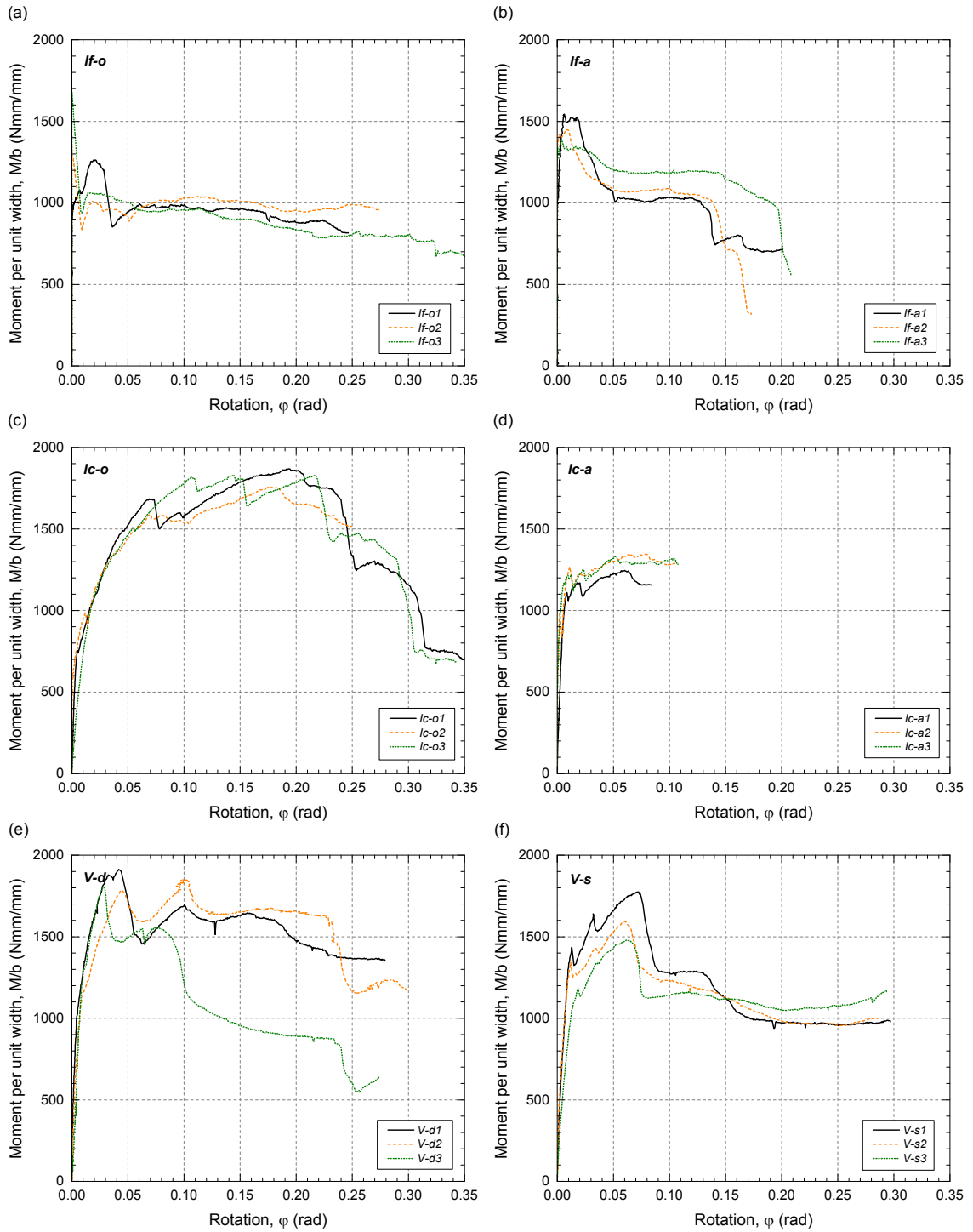


Figure E.23 – Calculated moment-rotation behavior of (a) *If-o*, (b) *If-a*, (c) *Ic-o*, (d) *Ic-a*, (e) *V-d* and (f) *V-s* WFJs.

Series	Specimen	M_{ult}/b (Nmm/mm)	$\varphi_{M,ult}$ (rad)	K_{θ}^{rot}/b (kN/rad)	K_r^{rot}/b (kN/rad)
<i>If-o</i>	<i>If-o1</i>	1 270	0.020	∞	∞
	<i>If-o2</i>	1 375	0.000	∞	∞
	<i>If-o3</i>	1 684	0.000	∞	∞
	Mean	1 443±215 ^(a)	0.007±0.011 ^(a)	∞	∞
<i>If-a</i>	<i>If-a1</i>	1 549	0.006	∞	∞
	<i>If-a2</i>	1 455	0.010	∞	∞
	<i>If-a3</i>	1 400	0.004	∞	∞
	Mean	1 468± 75 ^(a)	0.006±0.003 ^(a)	∞	∞
<i>Ic-o</i>	<i>Ic-o1</i>	1 872	0.193	205	46
	<i>Ic-o2</i>	1 758	0.173	268	73
	<i>Ic-o3</i>	1 832	0.217	93	57
	Mean	1 821± 57 ^(a)	0.195±0.022 ^(a)	189±87 ^(a)	59±14 ^(a)
<i>Ic-a</i>	<i>Ic-a1</i>	1 247	0.060	310	146
	<i>Ic-a2</i>	1 351	0.065	759	345
	<i>Ic-a3</i>	1 332	0.051	817	294
	Mean	1 310± 55 ^(a)	0.059±0.007	628±277 ^(a)	262±104 ^(a)
<i>V-d</i>	<i>V-d1</i>	1 915	0.042	284	190
	<i>V-d2</i>	1 854	0.098	226	137
	<i>V-d3</i>	1 809	0.029	125	153
	Mean	1 859± 53 ^(a)	0.056±0.037 ^(a)	212±80 ^(a)	160±27 ^(a)
<i>V-s</i>	<i>V-s1</i>	1 779	0.072	194	128
	<i>V-s2</i>	1 600	0.060	215	130
	<i>V-s3</i>	1 480	0.062	126	72
	Mean	1 620±150 ^(a)	0.064±0.007 ^(a)	178±46 ^(a)	110±33 ^(a)

^(a) Standard deviation

Table E.3 – Calculated ultimate moments and corresponding rotations; calculated rotational stiffness.

Appendix F

Summary of experimental studies of the creep behavior of PUR foams

F.1 Introduction

Within the framework of Chapter 5, the mechanical behavior of polyurethane (PUR) foams, particularly regarding creep, was analyzed to assess the long-term design of sandwich structures with PUR foam cores for building applications. Experimental results obtained from the literature were used for this purpose. Appendix F presents a summary of experimental studies of the creep behavior of polyurethane (PUR) foams reported in the literature, which served as a basis for the investigation conducted in Chapter 5.

Table F.1 lists the studies included in this Appendix. For each investigation reported, the type of sustained loading applied to the PUR foam (compression, tension, shear, bending), mention of whether the relevant creep investigation focuses on the material's strength (σ , τ) or stiffness (E , G), and parameters analyzed relating to the material's properties or the experimental conditions are indicated. Details of the experimental program performed and results provided in each study are subsequently given in Tables F.2 to F.35.

Creep experimental investigation													
Reference	Compression		Tension		Shear		Bending		Studied parameters				Table
	$\sigma_c^{(a)}$	$E_c^{(b)}$	$\sigma_t^{(a)}$	$E_t^{(b)}$	$\tau^{(a)}$	$G^{(b)}$	$\sigma_f^{(a)}$	$E_f^{(b)}$	Foam density	Blowing agent	Load level	Temperat. and/or humidity	
Hartsock ¹						(X)						X	F.2-F.4
Traeger ²		X							X				F.5
Schmidt ³		X				(X)				X			F.6-F.7
Stamm ⁴						(X)		X		X			F.8
Müller ⁵		X					X	X		X			F.9-F.10
Just ⁶						(X)		X		X	X		F.11-F.13
Basu ⁷		X		X		(X) (X*)		X		X			F.14-F.15
Badstube ⁸		X											F.16
Höninger and Reichelt ⁹		X					X	X		X	X		F.17
Just ¹⁰						(X)					X		F.18-F.19
Holmijoki ¹¹						(X)				X	X		F.20
Burkhardt ¹²					(X)	(X)				X	X		F.21-F.24
Schulz and Burkhardt ¹³						(X)				X	X		F.25-F.27
Huang and Gibson ¹⁴						(X)		X		X			F.28
Huang and Gibson ¹⁵						X		X		X			F.29
Just et al. ¹⁶						(X)			X	X	X		F.30-F.31
Just ¹⁷						(X)				X			F.32
Yourd ¹⁸		X							X	X			F.33
Krollmann ¹⁹		X						X					F.34
Garrido et al. ²⁰						X				X	X		F.35

(a) Creep investigation focused on material's strength

(b) Creep investigation focused on material's stiffness

(X) The shear creep behavior is investigated by bending experiments performed on sandwich panels or foam beam specimens

(X*) The shear creep behavior is investigated by torsion experiments performed on tubular foam specimens

Table F.1 – Summary of experimental studies of creep behavior of PUR foams reported in literature.

F.2 Summary of experimental studies

Hartsock (1967),¹ 1 of 3

Investigation of shear creep behavior of four rigid PUR foam systems	
Material properties	
PUR foams	Four PUR foam systems (A, B, C, D)
Foam density	A: 29 kg/m ³ B: 25 kg/m ³ C: 29 kg/m ³ D: 24 kg/m ³
Blowing agent	n/a
Manufacturing process	In-place foaming between sandwich face sheets
Application	Building structures
Experimental program	
Specimens	
- Number	24
- Type	Sandwich beams with 0.9-mm-thick steel face sheets
- Dimensions	$L = 368 \text{ mm}$, $b = 51 \text{ mm}$, $t = 25 \text{ mm}$
Loading conditions	
- Loading type	Three-point bending
- Loading direction	Through-thickness (sandwich panel)
- Load level	Six load levels per foam system resulting in shear stresses in the PUR foam in the following ranges: A: $0.007 \text{ MPa} \leq \tau \leq 0.045 \text{ MPa}$ B: $0.007 \text{ MPa} \leq \tau \leq 0.043 \text{ MPa}$ C: $0.006 \text{ MPa} \leq \tau \leq 0.042 \text{ MPa}$ D: $0.008 \text{ MPa} \leq \tau \leq 0.047 \text{ MPa}$
- Loading duration	57 days (creep) 50 days (recovery)
Environmental conditions	
- Temperature	23°C
- Relative humidity	50%
Results	
	Deflection-Time plots Elastic deflection, tabulated values Elastic recovery, tabulated values Initial shear modulus, tabulated values Time-dependent shear modulus, tabulated values Model for creep deflection
Reference	1

Table F.2 – Summary of experimental study by Hartsock, 1967 (1 of 3).¹

Hartsock (1967),¹ 2 of 3

	Investigation of shear creep behavior of one rigid PUR foam under different relative humidity conditions
Material properties	
PUR foams	One PUR foam system (A)
Foam density	A: 35–41 kg/m ³
Blowing agent	n/a
Manufacturing process	In-place foaming between sandwich face sheets
Application	Building structures
Experimental program	
Specimens	
- Number	9
- Type	Sandwich beams with 0.9-mm-thick steel face sheets
- Dimensions	$L = 368 \text{ mm}$, $b = 51 \text{ mm}$, $t = 25 \text{ mm}$
Loading conditions	
- Loading type	Three-point bending
- Loading direction	Through-thickness (sandwich panel)
- Load level	Three load levels per relative humidity level resulting in shear stresses in the PUR foam in the following range: A: $0.010 \text{ MPa} \leq \tau \leq 0.032 \text{ MPa}$
- Loading duration	371 days (creep)
Environmental conditions	
- Temperature	24°C
- Relative humidity	The behavior at three RH levels is investigated: 15% / 35% / 81%
Results	
	Deflection-Time plots Elastic deflection, tabulated values Elastic recovery, tabulated values Initial shear modulus, tabulated values Time-dependent shear modulus, tabulated values Model for creep deflection
Reference	1

Table F.3 – Summary of experimental study by Hartsock, 1967 (2 of 3).¹

Hartsock (1967),¹ 3 of 3

Investigation of shear creep behavior of one rigid PUR foam under high temperature	
Material properties	
PUR foams	One PUR foam system (A)
Foam density	A: 36–43 kg/m ³
Blowing agent	n/a
Manufacturing process	Discontinuous manufacturing (in-place foaming between sandwich face sheets)
Application	Building structures
Experimental program	
Specimens	
- Number	4
- Type	Sandwich beams with 0.9-mm-thick steel face sheets
- Dimensions	$L = 368 \text{ mm}$, $b = 51 \text{ mm}$, $t = 25 \text{ mm}$
Loading conditions	
- Loading type	Three-point bending
- Loading direction	Through-thickness (sandwich panel)
- Load level	Two load levels per temperature resulting in shear stresses in the PUR foam in the following range: A: $0.010 \text{ MPa} \leq \tau \leq 0.020 \text{ MPa}$
- Loading duration	76 days (creep)
Environmental conditions	
- Temperature	The behavior at two temperature levels is investigated: 24°C / 93°C
- Relative humidity	35%
Results	
	Deflection-Time plots
	Elastic deflection, tabulated values
	Initial shear modulus, tabulated values
Reference	1

Table F.4 – Summary of experimental study by Hartsock, 1967 (3 of 3).¹

Traeger (1967)²

Investigation of compressive creep behavior of five PUR foams	
Material properties	
PUR foams	Five PUR foam systems
Foam density	32–400 kg/m ³
Blowing agent	n/a
Manufacturing process	Hand-mixing method
Application	n/a
Experimental program	
Specimens	
- Number	n/a
- Type	n/a
- Dimensions	n/a
Loading conditions	
- Loading type	Compression
- Loading direction	Parallel to rise direction (foam)
- Load level	Up to 95% of the short-term compressive stress corresponding to a 10% strain
- Loading duration	231 days
Environmental conditions	
- Temperature	24°C
- Relative humidity	n/a
Results	
	Creep rate - Stress plots
Reference	2

Table F.5 – Summary of experimental study by Traeger, 1967.²

Schmidt (1968),³ 1 of 2

	Investigation of compressive creep behavior of one rigid PUR foam in directions parallel and perpendicular to rise direction
Material properties	
PUR foams	One PUR foam system
Foam density	60 kg/m ³
Blowing agent	n/a
Manufacturing process	n/a
Application	Building construction
Experimental program	
Specimens	
- Number	n/a
- Type	n/a
- Dimensions	n/a
Loading conditions	
- Loading type	Compression
- Loading direction	Parallel and perpendicular to rise direction (foam)
- Load level	Three stress levels are investigated: $\sigma = 0.010 \text{ MPa} / 0.098 \text{ MPa} / 0.196 \text{ MPa}$
- Loading duration	42 days (maximum)
Environmental conditions	
- Temperature	20°C
- Relative humidity	55%
Results	
	Strain-Time plots
Reference	3

Table F.6 – Summary of experimental study by Schmidt, 1968 (1 of 2).³

Schmidt (1968),³ 2 of 2

Investigation of flexural creep behavior of sandwich panels with rigid PUR foam core and metallic face sheets

Material properties	
PUR foams	n/a
Foam density	50 kg/m ³
Blowing agent	n/a
Manufacturing process	n/a
Application	Building construction
Experimental program	
Specimens	
- Number	11
- Type	Sandwich beams with 0.5-mm-thick steel face sheets
- Dimensions	$L = 4500 \text{ mm}, b = 1000 \text{ mm}, t = 35 \text{ mm}$ (4 specimens) $L = 4500 \text{ mm}, b = 1000 \text{ mm}, t = 60 \text{ mm}$ (3 specimens) $L = 2000 \text{ mm}, b = 1000 \text{ mm}, t = 35 \text{ mm}$ (2 specimens) $L = 2000 \text{ mm}, b = 1000 \text{ mm}, t = 60 \text{ mm}$ (2 specimens)
Loading conditions	
- Loading type	Three-point bending
- Loading direction	Through-thickness (sandwich panel)
- Load level	Load levels resulting in shear stresses in the PUR foam in the following range: $0.003 \text{ MPa} \leq \tau \leq 0.010 \text{ MPa}$
- Loading duration	Approximately 125 days
Environmental conditions	
- Temperature	20°C
- Relative humidity	55%
Results	
	Deflection-Time plots
Reference	3

Table F.7 – Summary of experimental study by Schmidt, 1968 (2 of 2).³

Stamm (1970)⁴

Investigation of shear creep behavior of rigid PUR foams with two different densities by bending experiments on sandwich panels

Material properties	
PUR foams	Two PUR foam types
Foam density	50 and 100 kg/m ³
Blowing agent	n/a
Manufacturing process	n/a
Application	Building construction
Experimental program	
Specimens	
- Number	16
- Type	Sandwich beams with 1-mm-thick steel face sheets
- Dimensions	$L = 2800$ mm, $b = n/a$, $t = 50$ mm (6 specimens) n/a (10 specimens)
Loading conditions	
- Loading type	Three-point bending
- Loading direction	Through-thickness (sandwich panel)
- Load level	Load levels resulting in shear stress (τ) to short-term shear strength (τ_{ult}) ratios in the PUR foam in the following range: $18\% \leq \tau/\tau_{ult} \leq 67\%$
- Loading duration	231 days
Environmental conditions	
- Temperature	Ambient temperature (5–20°C)
- Relative humidity	n/a
Results	
	Creep factor at selected times, tabulated values (selected specimens)
Reference	4

Table F.8 – Summary of experimental study by Stamm, 1970.⁴

Müller (1970),⁵ 1 of 2

Investigation of compressive behavior of rigid PUR foams with three different densities	
Material properties	
PUR foams	Three PUR foam types
Foam density	40, 70 and 230 kg/m ³
Blowing agent	n/a
Manufacturing process	Continuous manufacturing of slabstock foam
Application	Building construction
Experimental program	
Specimens	
- Number	n/a
- Type	Prismatic foam specimens (2 types)
- Dimensions	$L = 50 \text{ mm}, b = 50 \text{ mm}, t = 50 \text{ mm}$ $L = 50 \text{ mm}, b = 50 \text{ mm}, t = 25 \text{ mm}$
Loading conditions	
- Loading type	Compression
- Loading direction	n/a
- Load level	Compressive stresses in the following range: $0.025 \text{ MPa} \leq \sigma_c \leq 0.735 \text{ MPa}$
- Loading duration	21 days – 2 years
Environmental conditions	
- Temperature	n/a
- Relative humidity	n/a
Results	
	Strain-Time plots (selected specimens)
	Creep rate-Time plots (selected specimens)
Reference	5

Table F.9 – Summary of experimental study by Müller, 1970 (1 of 2).⁵

Müller (1970),⁵ 2 of 2

Investigation of flexural creep behavior of rigid PUR foams with three different densities	
Material properties	
PUR foams	Three PUR foam types
Foam density	40, 70 and 230 kg/m ³
Blowing agent	n/a
Manufacturing process	Continuous manufacturing of slabstock foam
Application	Building construction
Experimental program	
Specimens	
- Number	n/a
- Type	Foam beam specimens
- Dimensions	$L = 120 \text{ mm}$, $b = 25 \text{ mm}$, $t = 20 \text{ mm}$
Loading conditions	
- Loading type	Three-point bending
- Loading direction	n/a
- Load level	Flexural stresses in the following range: $0.049 \text{ MPa} \leq \sigma_f \leq 1.471 \text{ MPa}$
- Loading duration	416 days
Environmental conditions	
- Temperature	n/a
- Relative humidity	n/a
Results	
	Creep rate-Foam density plot
	Creep rate-stress level plot
	Deflection-Time plot (one density)
	Deflection recovery-Time plot (one density)
Reference	5

Table F.10 – Summary of experimental study by Müller, 1970 (2 of 2).⁵

Investigation of shear creep behavior of four PUR foam systems via bending experiments on sandwich panels	
Material properties	
PUR foams	Four PUR foam systems (A, B, C, D)
Foam density	A: 65 kg/m ³ B: 80 kg/m ³ C: 140 kg/m ³ D: 55 kg/m ³
Blowing agent	CFC-11
Manufacturing process	Discontinuous manufacturing
Application	Building structures
Experimental program	
Specimens	
- Number	38
- Type	Sandwich beams with aluminum, GFRP or steel face sheets: A: 1-mm-thick aluminum face sheets 2–3-mm-thick GFRP face sheets 0.8-mm steel face sheets (22 specimens in total) B: 1-mm-thick aluminum face sheets (5 specimens) C: 1.5-mm-thick aluminum face sheets (7 specimens) D: 0.8-mm-thick aluminum face sheets (4 specimens)
- Dimensions	A : $L = 1500$ mm, $b = 440$ – 470 mm, $t = 50$ – 55 mm B : $L = 1500$ mm, $b = 225$ – 250 mm, $t = 51$ – 52 mm C : $L = 1500$ mm, $b = 209$ mm, $t = 51$ – 53 mm D : $L = 1500$ mm, $b = 270$ mm, $t = 49$ mm
Loading conditions	
- Loading type	Three-point bending
- Loading direction	Through-thickness (sandwich panel)
- Load level	Load levels resulting in shear stress (τ) to short-term shear strength (τ_{ult}) ratios in the PUR foam in the following range: $2\% \leq \tau/\tau_{ult} \leq 22\%$
- Loading duration	83 days–2.5 years (creep) 125 days–500 days (recovery)
Environmental conditions	
- Temperature	20°C
- Relative humidity	Variable in the 40–85% range
Results	
	Elastic total and shear deflections, tabulated values Creep shear deflection-Time plots Deflection recovery-Time plots Creep factors at different times, tabulated values Recovery factors at different times, tabulated values Expression for creep factor as a function of time
Reference	6

Table F.11 – Summary of experimental study by Just, 1974 (1 of 3).⁶

Just (1974),⁶ 2 of 3

Investigation of shear creep behavior at elevated temperatures of four PUR foam systems via bending experiments on sandwich panels

Material properties	
PUR foams	Four PUR foam systems (A, B, C, D)
Foam density	A: 65 kg/m ³ B: 80 kg/m ³ C: 140 kg/m ³ D: 55 kg/m ³
Blowing agent	CFC-11
Manufacturing process	Discontinuous manufacturing
Application	Building structures
Experimental program	
Specimens	
- Number	20
- Type	Sandwich beams with aluminum face sheets: A: 1-mm-thick aluminum face sheets (7 specimens) B: 1-mm-thick aluminum face sheets (6 specimens) C: 1.5-mm-thick aluminum face sheets (3 specimens) D: 0.8-mm-thick aluminum face sheets (4 specimens)
- Dimensions	$L = 920 \text{ mm}$, $b = 200 \text{ mm}$, $t = 49\text{--}52 \text{ mm}$
Loading conditions	
- Loading type	Three-point bending
- Loading direction	Through-thickness (sandwich panel)
- Load level	Load levels resulting in shear stress (τ) to short-term shear strength at room temperature (τ_{ult}) ratios in the PUR foam in the following range: $2\% \leq \tau/\tau_{ult} \leq 17\%$
- Loading duration	16 days–25 days (creep) 23 days–42 days (recovery)
Environmental conditions	
- Temperature	The behavior at three temperature levels is investigated: 35°C / 49°C / 64°C
- Relative humidity	10% / 20% / 20% respectively for the above-mentioned temperatures
Results	
	Elastic total and shear deflections, tabulated values Creep shear deflection-Time plots Deflection recovery-Time plots Creep factors at different times, tabulated values Recovery factors at different times, tabulated values Creep factor-Time plots Expression for creep factor as a function of time
Reference	6

Table F.12 – Summary of experimental study by Just, 1974 (2 of 3).⁶

Investigation of shear creep behavior in outdoor conditions of four PUR foam systems via bending experiments on sandwich panels

Material properties	
PUR foams	Four PUR foam systems (A, B, C, D)
Foam density	A: 65 kg/m ³ B: 80 kg/m ³ C: 140 kg/m ³ D: 55 kg/m ³
Blowing agent	CFC-11
Manufacturing process	Discontinuous manufacturing
Application	Building structures
Experimental program	
Specimens	
- Number	23
- Type	Sandwich beams with aluminum, GFRP or steel face sheets: A: 1-mm-thick aluminum face sheets 2–3-mm-thick GFRP face sheets 0.8-mm steel face sheets (18 specimens in total) B: 1-mm-thick aluminum face sheets (1 specimens) C: 1.5-mm-thick aluminum face sheets (2 specimens) D: 0.8-mm-thick aluminum face sheets (2 specimens)
- Dimensions	$L = 920 \text{ mm}$, $b = 200 \text{ mm}$, $t = 49\text{--}52 \text{ mm}$
Loading conditions	
- Loading type	Three-point bending
- Loading direction	Through-thickness (sandwich panel)
- Load level	Load levels resulting in shear stress (τ) to short-term shear strength at room temperature (τ_{ult}) ratios in the PUR foam in the following range: $4\% \leq \tau/\tau_{ult} \leq 22\%$
- Loading duration	2 years
Environmental conditions	
- Temperature	Outdoor temperature (Dresden, Germany)
- Relative humidity	Outdoor relative humidity (Dresden, Germany)
Results	
	Elastic total and shear deflections, tabulated values Creep factors at different times, tabulated values
Reference	6

Table F.13 – Summary of experimental study by Just, 1974 (3 of 3).⁶

Basu (1976),⁷ 1 of 2

Investigation of tensile, compressive and torsion creep behavior of PUR foams with two densities

Material properties	
PUR foams	One PUR foam type
Foam density	55 and 80 kg/m ³
Blowing agent	CFC-11
Manufacturing process	Discontinuous manufacturing, free foaming
Application	Building construction
Experimental program	
Specimens	
- Number	n/a
- Type	Tension experiments: cylindrical specimens (50-kg/m ³ foam), cubic specimens (80-kg/m ³ foam) Compression experiments: tubular specimens Torsion experiments: tubular specimens
- Dimensions	Tension experiments: 50-kg/m ³ foam: $\phi = 43.5$ mm, $h = 50$ mm 80-kg/m ³ foam: $b = 50$ mm Compression experiments: $\phi_{ext} = 43.5$ mm, $\phi_{int} = 8$ mm, $h = 50$ mm Torsion experiments: $\phi_{ext} = 66$ mm, $\phi_{int} = 48.5$ mm, $h = 100-120$ mm
Loading conditions	
- Loading type	Tension, compression and torsion
- Loading direction	n/a
- Load level	Load levels resulting in tensile (σ_t), compressive (σ_c) or shear (τ) stress in the following range: 50-kg/m ³ foam: $0.049 \text{ MPa} \leq \sigma_t \leq 0.196 \text{ MPa}$ $0.049 \text{ MPa} \leq \sigma_c \leq 0.196 \text{ MPa}$ $0.049 \text{ MPa} \leq \tau \leq 0.196 \text{ MPa}$ 80-kg/m ³ foam: $0.029 \text{ MPa} \leq \sigma_t \leq 0.294 \text{ MPa}$ $0.049 \text{ MPa} \leq \sigma_c \leq 0.196 \text{ MPa}$ $0.098 \text{ MPa} \leq \tau \leq 0.392 \text{ MPa}$
- Loading duration	50-kg/m ³ foam: Tension, torsion: 42 days (minimum) Compression: 4–42 days 80-kg/m ³ foam: Tension, torsion: approximately 42 days Compression: 42 days (minimum)
Environmental conditions	
- Temperature	20°C
- Relative humidity	n/a
Results	
	Strain-Time plots Strain recovery-Time plots (80-kg/m ³ foam, tension)
Reference	7

Table F.14 – Summary of experimental study by Basu, 1976 (1 of 2).⁷

Basu (1976),⁷ 2 of 2

Investigation of shear creep behavior of one PUR foam type by bending experiments on sandwich panels with metallic face sheets

Material properties	
PUR foams	One PUR foam type
Foam density	40–115 kg/m ³ (variable across panel thickness)
Blowing agent	CFC-11
Manufacturing process	Discontinuous (in-place foaming between face sheets) and continuous manufacturing of sandwich panels
Application	Building construction
Experimental program	
Specimens	
- Number	n/a
- Type	Sandwich beams with PUR foam core and steel face sheets
- Dimensions	$L = 1000$ mm, $b =$ variable, $t =$ variable
Loading conditions	
- Loading type	Four-point bending
- Loading direction	Through-thickness (sandwich panel)
- Load level	Load levels resulting in shear stress (τ) in the PUR foam core in the following range: $0.010 \text{ MPa} \leq \tau \leq 0.078 \text{ MPa}$
- Loading duration	5–208 days (generally 42 days)
Environmental conditions	
- Temperature	20°C
- Relative humidity	n/a
Results	
	Shear strain-Time plots
	Strain recovery-Time plots (80-kg/m ³ foam, tension)
Reference	7

Table F.15 – Summary of experimental study by Basu, 1976 (2 of 2).⁷

Badstube (1979)⁸

Investigation of compressive creep behavior of two rigid PUR foam systems with similar densities

Material properties	
PUR foams	Two PUR foam systems (A, B)
Foam density	A: 48 kg/m ³ B: 50 kg/m ³
Blowing agent	n/a
Manufacturing process	Continuous manufacturing of sandwich panels
Application	Building construction
Experimental program	
Specimens	
- Number	12
- Type	Prismatic specimens from sandwich panels with steel of GFRP face sheets
- Dimensions	$L = 50 \text{ mm}$, $b = 50 \text{ mm}$, $t = 120 \text{ mm}$
Loading conditions	
- Loading type	Compression
- Loading direction	n/a
- Load level	n/a
- Loading duration	42 days
Environmental conditions	
- Temperature	20°C
- Relative humidity	65%
Results	
	Isochronous plots (creep strain-elastic strain at different loading times)
Reference	8

Table F.16 – Summary of experimental study by Badstube, 1979.⁸

Höniger and Reichelt (1982)⁹

Investigation of shear or flexural creep behavior of several commercially available PUR foam systems with different compositions and densities

Material properties	
PUR foams	Five PUR foam systems (A, B, C, D, E)
Foam density	A: 60 kg/m ³ B: 106 kg/m ³ C: 381–415 kg/m ³ , 646 kg/m ³ D, E: 646 kg/m ³
Blowing agent	n/a
Manufacturing process	n/a
Application	Building construction
Experimental program	
Specimens	
- Number	n/a
- Type	Compression experiments: cubic specimens Bending experiments: foam beam specimens
- Dimensions	Compression specimens: $b = 50$ mm Bending specimens: $L = 150\text{--}320$ mm, $b = 30\text{--}50$ mm, $t = 10\text{--}20$ mm
Loading conditions	
- Loading type	Constant stress and constant strain experiments under: A, B: Compression C, D, E: Four-point bending
- Loading direction	n/a
- Load level	Constant stress experiments: load levels resulting in compressive (σ_c) or flexural (σ_f) stresses in the ranges: A: $0.050 \text{ MPa} \leq \sigma_c \leq 0.200 \text{ MPa}$ B: $0.050 \text{ MPa} \leq \sigma_c \leq 0.300 \text{ MPa}$ C (381–415 kg/m ³): $1 \text{ MPa} \leq \sigma_f \leq 4 \text{ MPa}$ C (646 kg/m ³), D, E: $2 \text{ MPa} \leq \sigma_f \leq 12 \text{ MPa}$ Constant strain experiments: Load levels resulting in compressive (ϵ_c) or flexural (ϵ_f) strains in the ranges: A: $0.2\% \leq \epsilon_c \leq 0.8\%$ B: $0.1\% \leq \epsilon_c \leq 0.5\%$ C (381–415 kg/m ³): $0.1\% \leq \epsilon_f \leq 0.8\%$ C (646 kg/m ³), D, E: $0.2\% \leq \epsilon_f \leq 1\%$
- Loading duration	42 days (generally)
Environmental conditions	
- Temperature	23°C (also 50°C for A foam)
- Relative humidity	50%
Results	
	Strain-Time plots (constant stress experiments) Stress-Time plots (constant strain experiments) Isochronous plots (Stress-Strain) Elastic modulus-Time plots Elastic modulus and stress reduction factors
Reference	10

Table F.17 – Summary of experimental study by Höniger and Reichelt, 1982.⁹

Just (1983),¹⁰ 1 of 2

Investigation of shear creep behavior of five PUR foam systems with different densities by bending experiments on sandwich panels

Material properties	
PUR foams	Five PUR foam systems (A, B, C, D, E)
Foam density	n/a (presumably as in reference 6)
Blowing agent	CFC-11
Manufacturing process	n/a (presumably as in reference 6)
Application	Building construction
Experimental program	
Specimens	
- Number	n/a
- Type	Sandwich beams with PUR foam core and steel, aluminum, GFRP or asbestos face sheets
- Dimensions	$L = 1500 \text{ mm}$, $b = 220 \text{ mm}$, $t = \text{n/a}$
Loading conditions	
- Loading type	Three-point bending
- Loading direction	Through-thickness (sandwich panel)
- Load level	Load levels resulting in shear stress (τ) to short-term shear strength (τ_{ult}) ratios in the PUR foam in the following range: $\tau/\tau_{ult} \leq 11\%$
- Loading duration	10 years
Environmental conditions	
- Temperature	20°C
- Relative humidity	60%±20%
Results	
	Shear creep deflection-Time plots
	Creep factor-Time plots
	Expression for creep factor as a function of time
Reference	10

Table F.18 – Summary of experimental study by Just, 1983 (1 of 2).¹⁰

Just (1983),¹⁰ 2 of 2

Investigation of shear creep behavior of one PUR foam system in outdoor environment via bending experiments on sandwich panels

Material properties	
PUR foams	One PUR type
Foam density	65 kg/m ³
Blowing agent	CFC-11
Manufacturing process	n/a (presumably as in reference 6)
Application	Building construction
Experimental program	
Specimens	
- Number	n/a
- Type	Sandwich beams with PUR foam core and aluminum face sheets
- Dimensions	$L = 1450 \text{ mm}$, $b = 440 \text{ mm}$, $t = 54 \text{ mm}$
Loading conditions	
- Loading type	Three-point bending
- Loading direction	Through-thickness (sandwich panel)
- Load level	Load levels resulting in shear stress (τ) in the PUR foam core $\tau = 0.024 \text{ MPa}$
- Loading duration	10 years
Environmental conditions	
- Temperature	Outdoor temperature (Dresden, Germany)
- Relative humidity	Outdoor relative humidity (Dresden, Germany)
Results	
	Shear creep deflection-Time plots
Reference	
	10

Table F.19 – Summary of experimental study by Just, 1983 (2 of 2).¹⁰

Holmijoki (1984)¹¹

Investigation of shear creep behavior of one low-density PUR foam under elevated temperature by bending experiments on sandwich panels with metallic face sheets

Material properties	
PUR foams	One PUR type
Foam density	45 kg/m ³
Blowing agent	n/a
Manufacturing process	Continuous manufacturing of sandwich panels
Application	Building construction
Experimental program	
Specimens	
- Number	60
- Type	Sandwich beams with PUR foam core and steel face sheets
- Dimensions	$L = 1440 \text{ mm}$, $b = 180\text{--}230 \text{ mm}$, $t = 80 \text{ mm}$
Loading conditions	
- Loading type	Four-point bending
- Loading direction	Through-thickness (sandwich panel)
- Load level	Load levels resulting in shear stress (τ) in the PUR foam core in the following range: $0.020 \text{ MPa} \leq \tau \leq 0.080 \text{ MPa}$
- Loading duration	Variable, depending on the temperature level: 208 days for $T = 20^\circ\text{C}$ 83 days for $T = 40^\circ\text{C}$ 42 days for $T = 53^\circ\text{C}$
Environmental conditions	
- Temperature	The behavior at three temperature levels is investigated: 20°C / 40°C / 53°C
- Relative humidity	40–45%
Results	
	Shear creep deflection-Time plots
Reference	
	11

Table F.20 – Summary of experimental study by Holmijoki, 1984.¹¹

Burkhardt (1988),¹² 1 of 4

Investigation of shear creep behavior of four PUR foam systems with similar densities by bending experiments on sandwich panels with metallic face sheets

Material properties	
PUR foams	Four PUR systems (b, f, g, h)
Foam density	b: 45–46 kg/m ³ f: 42–47 kg/m ³ g: 45 kg/m ³ h: 42 kg/m ³
Blowing agent	n/a
Manufacturing process	n/a
Application	Building construction
Experimental program	
Specimens	
- Number	48 b: 16 specimens f: 12 specimens g: 12 specimens h: 8 specimens
- Type	Sandwich beams with metallic face sheets
- Dimensions	b: $L = 1000$ mm, $b = 150$ mm, $t = 40$ – 60 mm f: $L = 1000$ mm, $b = 100$ – 150 mm, $t = 57$ – 181 mm g: $L = 1000$ mm, $b = 150$ mm, $t = 100$ mm h: $L = 1000$ mm, $b = 150$ mm, $t = 100$ mm
Loading conditions	
- Loading type	Four-point bending
- Loading direction	Through-thickness (sandwich panel)
- Load level	Load levels resulting in shear stress (τ) to short-term shear strength (τ_{ult}) ratios in the following range: b: $70\% \leq \tau/\tau_{ult} \leq 90\%$ f: $30\% \leq \tau/\tau_{ult} \leq 90\%$ g: $10\% \leq \tau/\tau_{ult} \leq 30\%$ h: $10\% \leq \tau/\tau_{ult} \leq 30\%$
- Loading duration	92 days (maximum)
Environmental conditions	
- Temperature	23±3°C
- Relative humidity	60±5%
Results	
	Creep factor-Time plots Expression for creep factor as a function of time Recovery factor-Time plots Expression for recovery factor as a function of time
Reference	11

Table F.21 – Summary of experimental study by Burkhardt, 1988 (1 of 4).¹²

Burkhardt (1988),¹² 2 of 4

Investigation of shear creep behavior at low temperature of two PUR foam systems with similar densities by bending experiments on sandwich panels with metallic face sheets

Material properties	
PUR foams	Two PUR systems (g, h)
Foam density	g: 45 kg/m ³ h: 42 kg/m ³
Blowing agent	n/a
Manufacturing process	n/a
Application	Building construction
Experimental program	
Specimens	
- Number	7 g: 3 specimens h: 4 specimens
- Type	Sandwich beams with metallic face sheets
- Dimensions	g: $L = 1000$ mm, $b = 150$ mm, $t = 100$ mm h: $L = 1000$ mm, $b = 150$ mm, $t = 100$ mm
Loading conditions	
- Loading type	Four-point bending
- Loading direction	Through-thickness (sandwich panel)
- Load level	Load levels resulting in shear stress (τ) to short-term shear strength (τ_{ult}) ratios in the PUR foam in the following range: g: $10\% \leq \tau/\tau_{ult} \leq 30\%$ h: $10\% \leq \tau/\tau_{ult} \leq 30\%$
- Loading duration	92 days
Environmental conditions	
- Temperature	0°C
- Relative humidity	n/a
Results	
	Creep factor-Time plots Expression for creep factor as a function of time Recovery factor-Time plots
Reference	12

Table F.22 – Summary of experimental study by Burkhardt, 1988 (2 of 4).¹²

Burkhardt (1988),¹² 3 of 4

Investigation of shear creep behavior in outdoor environment of two PUR foam systems with similar densities by bending experiments on sandwich panels with metallic face sheets

Material properties	
PUR foams	Two PUR systems (g, h)
Foam density	g: 45 kg/m ³ h: 42 kg/m ³
Blowing agent	n/a
Manufacturing process	n/a
Application	Building construction
Experimental program	
Specimens	
- Number	7 g: 3 specimens h: 4 specimens
- Type	Sandwich beams with metallic face sheets
- Dimensions	g: $L = 1000$ mm, $b = 150$ mm, $t = 100$ mm h: $L = 1000$ mm, $b = 150$ mm, $t = 100$ mm
Loading conditions	
- Loading type	Four-point bending
- Loading direction	Through-thickness (sandwich panel)
- Load level	Load levels resulting in shear stress (τ) to short-term shear strength (τ_{ult}) ratios in the PUR foam in the following range: g: $10\% \leq \tau/\tau_{ult} \leq 30\%$ h: $10\% \leq \tau/\tau_{ult} \leq 30\%$
- Loading duration	117 days
Environmental conditions	
- Temperature	Outdoor temperature (Karlsruhe, Germany)
- Relative humidity	Outdoor relative humidity (Karlsruhe, Germany)
Results	
	Creep factor-Time plots Expression for creep factor as a function of time Recovery factor-Time plots
Reference	12

Table F.23 – Summary of experimental study by Burkhardt, 1988 (3 of 4).¹²

Burkhardt (1988),¹² 4 of 4

Investigation of shear creep rupture of three PUR foam systems with similar densities by bending experiments on sandwich panels with metallic face sheets

Material properties	
PUR foams	Three PUR systems (a, b, c)
Foam density	a: 35–38 kg/m ³ b: 45–46 kg/m ³ c: 43 kg/m ³
Blowing agent	n/a
Manufacturing process	n/a
Application	Building construction
Experimental program	
Specimens	
- Number	37 a: 9 specimens b: 19 specimens c: 9 specimens
- Type	Sandwich beams with metallic face sheets
- Dimensions	a: $L = 1000$ mm, $b = 140$ mm, $t = 34$ – 64 mm b: $L = 1000$ mm, $b = 150$ mm, $t = 40$ – 60 mm c: $L = 1000$ mm, $b = 100$ mm, $t = 57$ – 67 mm
Loading conditions	
- Loading type	Four-point bending
- Loading direction	Through-thickness (sandwich panel)
- Load level	Load levels resulting in shear stress (τ) to short-term shear strength (τ_{ult}) ratios in the PUR foam in the following range: a: $60\% \leq \tau/\tau_{ult} \leq 90\%$ b: $70\% \leq \tau/\tau_{ult} \leq 90\%$ c: $60\% \leq \tau/\tau_{ult} \leq 90\%$
- Loading duration	Up to failure
Environmental conditions	
- Temperature	23±3°C
- Relative humidity	60±5%
Results	
	Time to failure, tabulated values Stress level-Time to failure plots
Reference	12

Table F.24 – Summary of experimental study by Burkhardt, 1988 (4 of 4).¹²

Schulz and Burkhardt (1988),¹³ 1 of 3

	Investigation of cyclic shear creep behavior of three PUR foam systems with similar densities by bending experiments on sandwich panels with metallic face sheets
Material properties	
PUR foams	Three PUR systems (a, b, c)
Foam density	a: 36–38 kg/m ³ b: 41–43 kg/m ³ c: 42–47 kg/m ³
Blowing agent	n/a
Manufacturing process	Continuous manufacturing of sandwich panels
Application	Building construction
Experimental program	
Specimens	
- Number	72 a: 18 specimens b: 27 specimens c: 27 specimens
- Type	Sandwich beams with metallic face sheets
- Dimensions	$L = 1000$ mm, $b = 150$ mm, $t = 100$ – 105 mm
Loading conditions	
- Loading type	Four-point bending
- Loading direction	Through-thickness (sandwich panel)
- Load level	Load levels resulting in shear stress (τ) to short-term shear strength (τ_{ult}) ratios in the PUR foam in the following range: $10\% \leq \tau/\tau_{ult} \leq 30\%$
- Loading duration	6 days (loading) + 6 days (recovery), 7 cycles 21 days (loading) + 21 days (recovery), 6 cycles 83 days (loading) + 83 days (recovery), 2 cycles 2 years (loading)
Environmental conditions	
- Temperature	Room temperature (n/a)
- Relative humidity	Room relative humidity (n/a)
Results	
	Deflection-Time plots Deflection recovery-Time plots Creep factor-Time plots Expression for creep factor as function of time, tabulated parameters
Reference	13

Table F.25 – Summary of experimental study by Schulz and Burkhardt, 1988 (1 of 3).¹³

Schulz and Burkhardt (1988),¹³ 2 of 3

	Investigation of shear creep behavior at low temperature of two PUR foam systems with similar densities by bending experiments on sandwich panels with metallic face sheets
Material properties	
PUR foams	Two PUR systems (b, c)
Foam density	b: 41–43 kg/m ³ c: 42–47 kg/m ³
Blowing agent	n/a
Manufacturing process	Continuous manufacturing of sandwich panels
Application	Building construction
Experimental program	
Specimens	
- Number	18 b: 9 specimens c: 9 specimens
- Type	Sandwich beams with metallic face sheets
- Dimensions	$L = 1000 \text{ mm}$, $b = 150 \text{ mm}$, $t = 100\text{--}105 \text{ mm}$
Loading conditions	
- Loading type	Four-point bending
- Loading direction	Through-thickness (sandwich panel)
- Load level	Load levels resulting in shear stress (τ) to short-term shear strength (τ_{ult}) ratios in the PUR foam in the following range: $10\% \leq \tau/\tau_{ult} \leq 30\%$
- Loading duration	92 days
Environmental conditions	
- Temperature	0°C
- Relative humidity	n/a
Results	
	Deflection-Time plots Deflection recovery-Time plots Creep factor-Time plots Expression for creep factor as function of time, tabulated parameters
Reference	13

Table F.26 – Summary of experimental study by Schulz and Burkhardt, 1988 (2 of 3).¹³

Schulz and Burkhardt (1988),¹³ 3 of 3

	Investigation of shear creep behavior at elevated temperature of two PUR foam systems with similar densities by bending experiments on sandwich panels with metallic face sheets
Material properties	
PUR foams	Two PUR systems (b, c)
Foam density	b: 41–43 kg/m ³ c: 42–47 kg/m ³
Blowing agent	n/a
Manufacturing process	Continuous manufacturing of sandwich panels
Application	Building construction
Experimental program	
Specimens	
- Number	18 b: 9 specimens c: 9 specimens
- Type	Sandwich beams with metallic face sheets
- Dimensions	$L = 1000 \text{ mm}$, $b = 150 \text{ mm}$, $t = 100\text{--}105 \text{ mm}$
Loading conditions	
- Loading type	Four-point bending
- Loading direction	Through-thickness (sandwich panel)
- Load level	Load levels resulting in shear stress (τ) to short-term shear strength (τ_{ult}) ratios in the PUR foam in the following range: $10\% \leq \tau/\tau_{ult} \leq 30\%$
- Loading duration	129 days
Environmental conditions	
- Temperature	40°C
- Relative humidity	n/a
Results	
	Deflection-Time plots Deflection recovery-Time plots Creep factor-Time plots Expression for creep factor as function of time, tabulated parameters
Reference	13

Table F.27 – Summary of experimental study by Schulz and Burkhardt, 1988 (3 of 3).¹³

Huang and Gibson (1990)¹⁴

	Investigation of shear creep behavior of PUR foam systems with different densities by bending experiments on sandwich panels with metallic face sheets
Material properties	
PUR foams	PUR foams with four different densities
Foam density	32 kg/m ³ , 48 kg/m ³ , 64 kg/m ³ , 96 kg/m ³
Blowing agent	n/a
Manufacturing process	n/a for the foam; bonding of face sheets to the PUR core for the sandwich panels
Application	Building construction
Experimental program	
Specimens	
- Number	16 (4 specimens per density)
- Type	Sandwich beams with aluminum face sheets
- Dimensions	n/a
Loading conditions	
- Loading type	Three-point bending
- Loading direction	Through-thickness (sandwich panel)
- Load level	Load levels resulting in shear stress (τ) to short-term shear strength (τ_{ult}) ratios in the PUR foam in the following range: $5\% \leq \tau/\tau_{ult} \leq 20\%$
- Loading duration	50 days (loading) 19 days (recovery)
Environmental conditions	
- Temperature	23°C
- Relative humidity	20%
Results	
	Deflection-Time plots Deflection recovery-Time plots
Reference	14

Table F.28 – Summary of experimental study by Huang and Gibson, 1990.¹⁴

Huang and Gibson (1991)¹⁵

Investigation of shear creep behavior of PUR foam systems with different densities

Material properties	
PUR foams	PUR foams with four different densities
Foam density	32 kg/m ³ , 48 kg/m ³ , 64 kg/m ³ , 96 kg/m ³
Blowing agent	n/a
Manufacturing process	n/a
Application	Building construction
Experimental program	
Specimens	
- Number	16 (4 specimens per density)
- Type	Foam shear specimens
- Dimensions	n/a
Loading conditions	
- Loading type	Shear
- Loading direction	Shear in the most isotropic plane of the foam
- Load level	Shear stress (τ) to short-term shear strength (τ_{ult}) ratios in the PUR foam in the following range: $10\% \leq \tau/\tau_{ult} \leq 40\%$
- Loading duration	50 days (loading) 19 days (recovery)
Environmental conditions	
- Temperature	23°C
- Relative humidity	20%
Results	
	Shear strain-Time plots Creep shear strain-Time plots Shear compliance-Time plots Shear strain recovery-Time plots Expression for shear strain as a function of time, tabulated parameters
Reference	15

Table F.29 – Summary of experimental study by Huang and Gibson, 1991.¹⁵

Just et al. (1993),¹⁶ 1 of 2

	Investigation of shear creep behavior of five PUR foam systems with different blowing agents by bending experiments on sandwich panels with metallic face sheets
Material properties	
PUR foams	Five PUR foam systems (A, B, C, F, W)
Foam density	n/a
Blowing agent	A: CFC-11 + CO ₂ B: CFC-22 + CO ₂ C: HCFC-141b + CO ₂ F: Pentane + CO ₂ W: CO ₂
Manufacturing process	A, B, C, F: Continuous manufacturing of sandwich panels W: Discontinuous manufacturing of sandwich panels
Application	Building construction
Experimental program	
Specimens	
- Number	15 (3 specimens per foam system)
- Type	Sandwich beams with 1-2-mm-thick aluminum face sheets
- Dimensions	$L = 1500$ mm, $b = 150\text{--}200$ mm, $t = 80$ mm
Loading conditions	
- Loading type	Three-point bending
- Loading direction	Through-thickness (sandwich panel)
- Load level	Load levels resulting in shear stress (τ) to short-term shear strength (τ_{ult}) ratios in the PUR foam in the following range: $5\% \leq \tau/\tau_{ult} \leq 15\%$
- Loading duration	83–417 days
Environmental conditions	
- Temperature	20°C
- Relative humidity	65%
Results	
	Creep shear deflection-Time plots Creep factor-Time plots Time-dependent shear modulus – Time plots Expression for creep factor as a function of time, tabulated values Creep shear deflection, creep factor and time-dependent shear modulus at different loading times, tabulated values
Reference	16

Table F.30 – Summary of experimental study by Just et al., 1993 (1 of 2).¹⁶

	Investigation of shear creep behavior in outdoor environment of five PUR foam systems with different blowing agents by bending experiments on sandwich panels with metallic face sheets
Material properties	
PUR foams	Five PUR foam systems (A, B, C, F, W)
Foam density	n/a
Blowing agent	A: CFC-11 + CO ₂ B: CFC-22 + CO ₂ C: HCFC-141b + CO ₂ F: Pentane + CO ₂ W: CO ₂
Manufacturing process	A, B, C, F: Continuous manufacturing of sandwich panels W: Discontinuous manufacturing of sandwich panels
Application	Building construction
Experimental program	
Specimens	
- Number	15 (3 specimens per foam system)
- Type	Sandwich beams with 1-2-mm-thick aluminum face sheets
- Dimensions	$L = 1500$ mm, $b = 150$ – 200 mm, $t = 80$ mm
Loading conditions	
- Loading type	Three-point bending
- Loading direction	Through-thickness (sandwich panel)
- Load level	Load levels resulting in shear stress (τ) to short-term shear strength (τ_{ult}) ratios in the PUR foam in the following range: $5\% \leq \tau/\tau_{ult} \leq 15\%$
- Loading duration	Approximately 480 days
Environmental conditions	
- Temperature	Outdoors temperature (Dresden, Germany)
- Relative humidity	Outdoors relative humidity (Dresden, Germany)
Results	
	Creep shear deflection-Time plots Creep factor-Time plots Time-dependent shear modulus – Time plots Expression for creep factor as a function of time, tabulated values Creep shear deflection, creep factor and time-dependent shear modulus at different loading times, tabulated values
Reference	16

Table F.31 – Summary of experimental study by Just et al., 1993 (2 of 2).¹⁶

Just (1996),¹⁷ 1 of 1

	Investigation of shear creep behavior of one PUR foam by bending experiments on sandwich panels with metallic face sheets
Material properties	
PUR foams	One PUR foam type
Foam density	46 kg/m ³
Blowing agent	CO ₂
Manufacturing process	Continuous manufacturing of sandwich panels
Application	Building construction
Experimental program	
Specimens	
- Number	8
- Type	Sandwich beams with 0.7-mm-thick steel face sheets
- Dimensions	$L = 1450 \text{ mm}, b = 135 \text{ mm}, t = 80 \text{ mm}$
Loading conditions	
- Loading type	Three-point bending
- Loading direction	Through-thickness (sandwich panel)
- Load level	Load levels resulting in shear stress (τ) to short-term shear strength (τ_{ult}) ratios in the PUR foam in the following range: $5\% \leq \tau/\tau_{ult} \leq 15\%$
- Loading duration	Approximately 542 days (1.5 years)
Environmental conditions	
- Temperature	23°C
- Relative humidity	50%
Results	
	Creep shear deflection-Time plots
	Creep factor-Time plots
	Expression for creep factor as a function of time, tabulated values
	Creep shear deflection and creep factor at different loading times, tabulated values
Reference	17

Table F.32 – Summary of experimental study by Just, 1996.¹⁷

Yourd (1996)¹⁸

Investigation of compressive creep behavior of two PUR foams using different blowing agents

Material properties	
PUR foams	Two PUR foam types (A, B)
Foam density	27–28 kg/m ³
Blowing agent	A: CFC-11 + CO ₂ B: HCFC-141b + CO ₂
Manufacturing process	Discontinuous manufacturing of sandwich panels
Application	Appliance
Experimental program	
Specimens	
- Number	16 (one per foam type and load level)
- Type	Prismatic foam specimens
- Dimensions	$L = 50.8 \text{ mm}$, $b = 50.8 \text{ mm}$, $t = 25.4 \text{ mm}$
Loading conditions	
- Loading type	Compression
- Loading direction	Through-thickness (sandwich panel)
- Load level	Load levels resulting in compressive stresses (σ_c) in the following range: $0.040 \text{ MPa} \leq \sigma_c \leq 0.100 \text{ MPa}$ These correspond to ratios of σ_c to $\sigma_{c,ult}$ (short-term compressive strength): $28\% \leq \sigma_c / \sigma_{c,ult} \leq 74\%$
- Loading duration	8 days (maximum)
Environmental conditions	
- Temperature	23°C
- Relative humidity	50%
Results	
	Compressive strain-Time plots Compressive creep strain-Time plots Expression for creep strain as a function of time, tabulated values
Reference	18

Table F.33 – Summary of experimental study by Yourd, 1996.¹⁸

Krollmann (2002)¹⁹

Investigation of compressive creep behavior of four PUR foams	
Material properties	
PUR foams	Four PUR foam types (A, B, C, D)
Foam density	A: 80 kg/m ³ B: 35 kg/m ³ C: 35 kg/m ³ D: 45 kg/m ³
Blowing agent	n/a
Manufacturing process	A: Slabstock foam, manufacturing process n/a B, C: Continuous manufacturing of sandwich panels D: Sandwich panel with metallic face sheets, manufacturing process n/a
Application	Building construction
Experimental program	
Specimens	
- Number	12 (three per foam type)
- Type	Prismatic specimens from sandwich panels (the face sheets were kept for D foam only)
- Dimensions	A: $L = 50$ mm, $b = 50$ mm, $t = 50$ mm B: $L = 50$ mm, $b = 50$ mm, $t = 40$ mm C: $L = 50$ mm, $b = 50$ mm, $t = 50$ mm D: $L = 100$ mm, $b = 100$ mm, $t = 60$ mm
Loading conditions	
- Loading type	Compression
- Loading direction	A: n/a B, C: Through-thickness (sandwich panel) D: n/a
- Load level	Load levels resulting in compressive stresses (σ_c) in the following range: $0.040 \text{ MPa} \leq \sigma_c \leq 0.200 \text{ MPa}$ These correspond to ratios of σ_c to $\sigma_{c,ult}$ (short-term compressive strength): $14\% \leq \sigma_c / \sigma_{c,ult} \leq 23\%$
- Loading duration	2 years (two specimens per series) 5 years (one specimen per series)
Environmental conditions	
- Temperature	23°C
- Relative humidity	50%
Results	
	Compressive deformation, compressive strain and creep displacement, tabulated values Compressive deformation-Time plots Expression for creep deformation as a function of time
Reference	19

Table F.34 – Summary of experimental study by Krollmann, 2002.¹⁹

Garrido et al. (2016)²⁰

Investigation of shear creep behavior of one PUR foam under different temperatures

Material properties	
PUR foams	One PUR foam type
Foam density	87 kg/m ³
Blowing agent	n/a
Manufacturing process	n/a
Application	Building construction
Experimental program	
Specimens	
- Number	9 (one per temperature and load level)
- Type	Prismatic specimens from sandwich panels
- Dimensions	$L = 250 \text{ mm}$, $b = 250 \text{ mm}$, $t = 120 \text{ mm}$
Loading conditions	
- Loading type	Shear
- Loading direction	Shear in the plane containing the through-thickness direction of the sandwich panels
- Load level	Load levels resulting in shear stresses (τ) in the following range: $0.035 \text{ MPa} \leq \tau \leq 0.143 \text{ MPa}$ These correspond to ratios of τ to τ_{ult} (short-term shear strength): $11\% \leq \tau / \tau_{ult} \leq 44\%$
- Loading duration	54–88 days
Environmental conditions	
- Temperature	The behavior at three temperature levels is investigated: 20°C / 24°C / 28°C
- Relative humidity	63% / 50% / 50% respectively for the above-mentioned temperatures
Results	
	Shear strain-Time plots Creep shear strain-Time plots Expressions for shear strain, shear modulus and creep factor as a function of time and temperature
Reference	20

Table F.35 – Summary of experimental study by Garrido et al., 2016.²⁰

References

1. Hartsock JA. Experiments on the creep of rigid urethane foam in shear. *J Cell Plast* 1967;3(2):81–90.
2. Traeger RK. Physical properties of rigid polyurethane foams. *J Cell Plast* 1967;3(9):405–418.
3. Schmidt W. Eigenschaften und Prüfung von mit harten Polyurethanschaumstoffen hergestellten Leichtkern-Verbundplatten. *Materialprüfung* 1968;10(3):81–87.
4. Stamm K. Grundsatzversuche an ebenen und trapezprofilierten Sandwichbalken. *HOESCH Berichte aus Forschung und Entwicklung unserer Werke* 70(4): 185–201.
5. Müller D. Kunststoff-Hartschäume unter langzeitiger statischer Belastung. *Gummi – Asbest – Kunststoffe* 12/1970.
6. Just M. *Beitrag zum Langzeitverhalten von Stützkernelementen mit einem Stützkern aus freongetriebenem Polyurethan-Hartschaumstoff* [PhD Thesis]. Universität Dresden, Germany; 1974.
7. Basu AK. *Zur Herstellung und zum Werkstoffverhalten von Sandwichtragwerken des Werkstoffverbundsystems Stahlblech-Polyurethan-Hartschaum* [PhD Thesis]. Technischen Hochschule Darmstadt, Germany; 1976.
8. Badstube M. Kriechgesetze von Polyurethan-Hartschaumstoffen. *Plaste Kautsch* 1979;26(12):703–706.
9. Höninger H, Reichelt E. *Langzeit-Deformationsverhalten von Plastwerkstoffen: 352 Diagramme für 56 Plastwerkstoffe des DDR-Sortiments*. Dresden: Institut für Leichtbau und ökonomische Verwendung von Werkstoffen IfL; 1982. Materialökonomie 32.
10. Just M. Ergebnisse experimenteller Untersuchungen zum Langzeitverhalten von PUR-Hartschaumstoff-Stützkernbauteilen und Schlußfolgerungen für die Anwendung. *IfL Mitt* 1983;22(3):95–104.
11. Holmijoki O. *Shear strength and shear creep properties of rigid polyurethane foam determined by sandwich beam tests* [Master Thesis]. Helsinki University of Technology, Finland; 1984.
12. Burkhardt S. *Zeitabhängiges Verhalten von Sandwichelementen mit Metalldeckschichten und Stützkernen aus Polyurethanhartschaumstoffen*. Karlsruhe: Versuchsanstalt für Stahl, Holz und Steine der Universität Fridericiana; 1988. Report No.4(20).
13. Schulz U, Burkhardt S. *Langzeituntersuchungen an Sandwichelementen mit Metalldeckschichten und Kunststoffschäumen. Abschlußbericht*. Karlsruhe: Versuchsanstalt für Stahl, Holz und Steine. Amtliche Materialprüfungsanstalt der Universität Karlsruhe; 1988.
14. Huang JS, Gibson LJ. Creep of sandwich beams with polymer foam cores. *J Mater Civ Eng* 1990;2(3):171–182.
15. Huang JS, Gibson LJ. Creep of polymer foams. *J Mater Sci* 1991;26(3):637–647.
16. Just M, Gerbet, Wienert. *Experimentelle Untersuchungen zum Langzeitverhalten von Sandwichplatten mit Stahldeckschichten und FCKW-reduzierten Stützkernen im Hinblick auf die Sicherung und Erweiterung der Anwendung von Sandwichplatten in Stahlleichtbau*. Dresden: IMA Materialforschung und Anwendungstechnik; 1993.
17. Just M. *Abschlußbericht zum AiF-Forschungsvorhaben 10011B. Untersuchungen zum Langzeitverhalten von Sandwichplatten mit CO₂-getriebenen Polyurethan-Schaumstoffkernen*. Dresden: IMA Materialforschung und Anwendungstechnik; 1996. Report No. B85/4.
18. Yourd RA. Compression creep and long-term dimensional stability in appliance rigid foam. *J Cell Plast* 1996;32(6):601–616.
19. Krollmann N. *Determination of compressive creep behaviour of PUR rigid foam products*. Ludwigshafen: BASF; 2002. Report No. 298.4386.
20. Garrido M, Correia JR, Keller T. Effect of service temperature on the shear creep response of rigid polyurethane foam used in composite sandwich floor panels. *Constr Build Mater* 2016;118:235–244.

Curriculum Vitae

SONIA YANES ARMAS

✉ sonia.yanes.armas@gmail.com

Birth date: March 15, 1985

Nationality: Spanish

EDUCATION

- 2013–2017** **PhD candidate, Civil Engineering**
Composite Construction Laboratory (CCLab), Prof. Thomas Keller
Ecole Polytechnique Fédérale de Lausanne (EPFL), Lausanne, Switzerland
- 2009-2010** **Postgraduate Master in Building Structures**
Universidad Politécnica de Madrid (UPM), Madrid, Spain
- 2003-2009** **Master in Architecture**
Universidad Politécnica de Madrid (UPM), Madrid, Spain

ADDITIONAL EDUCATION

- 2011–2012** **Training for University Teaching**
Universidad Politécnica de Madrid (UPM), Madrid, Spain
20-ECTS course
- 2010 (Summer)** **Introduction to Research, Teaching and Scientific Innovation**
Universidad Internacional Menéndez Pelayo (UIMP), Santander, Spain
33-h course, participation granted by open and competitive call

WORK EXPERIENCE

- 2013–2017** **Research and teaching assistant at the CCLab-EPFL, Lausanne, Switzerland**
Research and consulting projects on FRP bridge and building structures
Teaching assistance for “Structures and Materials” (Bachelor in Architecture)
Co-organizing of symposium “FRP sandwich structures in bridge and building construction” at CICE 2016 conference
Member of Organizing Committee of 12th International Conference on Sandwich Structures (ICSS-12, ongoing)
- 2011-2012** **Teaching trainee at Escuela Técnica Superior de Arquitectura-UPM, Madrid, Spain**
Assistance in exercise sessions for “Solid and Structural Mechanics” (Bachelor in Architecture)
- 2010-2012** **Research assistant at Instituto de Ciencias de la Construcción Eduardo Torroja-CSIC, Madrid, Spain**
Research on FRP structures
- 2009 (Summer)** **Architect, De Lapuerta + Asensio Arquitectos Asociados, Madrid, Spain**
Architectural design and production of drawings for architecture competitions

PUBLICATIONS

- Journal papers**
- Yanes-Armas S, de Castro J, Keller T. Long-term design of FRP-PUR web-core sandwich structures in building construction. Submitted to *Compos Struct* in June 2017.
- Yanes-Armas S, de Castro J, Keller T. Rotational stiffness of web-flange junctions of pultruded GFRP decks. *Eng Struct* 2017;140:373–389.
- Yanes-Armas S, de Castro J, Keller T. Energy dissipation and recovery in web-flange junctions of pultruded GFRP decks. *Compos Struct* 2016;148:168–180.
- Yanes-Armas S, de Castro J, Keller T. System transverse in-plane shear stiffness of pultruded GFRP bridge decks. *Eng Struct* 2016;107:34–46.
- Conference papers**
- Yanes-Armas S, Keller T. Structural concept and design of a GFRP-polyurethane sandwich roof structure. In: *Proceedings of CICE 2016*, 14–16 December 2016, Hong Kong, China.
- Yanes-Armas S, de Castro J, Keller T. Characterization of rotational behavior of web-flange junctions of pultruded GFRP bridge decks. In: *Proceedings of CICE 2016*, 14–16 December 2016, Hong Kong, China.
- Yanes-Armas S, Keller T. FRP sandwich structures in bridge and building construction. In: *Proceedings of ICSS-11*, 20–22 March 2016, Fort Lauderdale, USA.
- Yanes-Armas S, de Castro J, Keller T. Performance in transverse direction of fiber-reinforced polymer bridge decks. In: *Proceedings of IABSE Conference 2015*, 23–25 September 2015, Geneva, Switzerland.
- Yanes-Armas S, de Castro J, Keller T. Energy dissipation in web-flange junctions of pultruded GFRP decks. In: *Proceedings of ICCM20*, 19–24 July 2015, Copenhagen, Denmark.
- Yanes-Armas S, de Castro J, Vassilopoulos AP, Keller T. Static performance in transverse direction of pultruded GFRP bridge decks. In: *Proceedings of CICE 2014*, 20–22 August 2014, Vancouver, Canada.

AWARDS AND SCHOLARSHIPS

- 2012** **JAE-PreDOC Mobility Grant, Spanish National Research Council (CSIC)**
Funding for three-months scientific visit to EPFL, Switzerland
- 2010** **JAE-PreDOC Scholarship, Spanish National Research Council (CSIC)**
Four years of funding for pre-doctoral research
- 2009** **National Award for Excellence in Academic Performance, First Prize for Architecture Degree, Spanish Ministry of Education**
Award granted to students with the best academic performance in their corresponding degrees
- 2009** **Graduation Prize, Award for Excellence, Escuela Técnica Superior de Arquitectura-UPM**
Award granted to graduated student with the best academic performance
- 2003–2007** **Graduate Scholarship, Comunidad Autónoma de Madrid**
Five years of funding during undergraduate studies, awarded to high level students

